THE USE OF MATHEMATICALLY EXACT SOLUTIONS OF STRUCTURAL DYNAMICS MODELS FOR STRUCTURAL CONTROL DESIGN

by

VICTOR D. LUPI

S.B., Massachusetts Institute of Technology (1988)
S.M., Massachusetts Institute of Technology (1990)

SUBMITTED TO THE DEPARTMENT OF AERONAUTICS AND ASTRONAUTICS IN PARTIAL FULFILLMENT OF THE REQUIREMENTS FOR THE DEGREE OF

DOCTOR OF PHILOSOPHY IN AERONAUTICS AND ASTRONAUTICS

at the

MASSACHUSETTS INSTITUTE OF TECHNOLOGY
June, 1992

Signature of Author _____
Department of Aeronautics and Astronautics
1, 1992

Certified by _____
Professor Wallace E. Vander Velde
Thesis Committee Chairman, Department of Aeronautics and Astronautics

Certified by _____
Professor Steven R. Hall
Department of Aeronautics and Astronautics

Certified by _____
Professor Andres von Flotow
Department of Aeronautics and Astronautics

Certified by _____
Dr. Hon M. Chun
Photon Research Associates

Certified by _____
Dr. James D. Turner
Photon Research Associates

Accepted by _____
Professor Harold Y. Wachman
Chairman, Department Graduate Committee

THE USE OF MATHEMATICALLY EXACT SOLUTIONS OF STRUCTURAL DYNAMICS MODELS FOR STRUCTURAL CONTROL DESIGN

by

VICTOR D. LUPI

Submitted to the Department of Aeronautics and Astronautics
on May 11, 1992 in partial fulfillment of the
requirements for the Degree of Doctor of Philosophy in
Aeronautics and Astronautics

ABSTRACT

This thesis investigates the utilization of mathematically exact solutions of common structural models for structural analysis and control design. The solutions developed in this research are mathematically exact at all frequencies, unlike modal solutions derived from finite element models. As a result, control designs based on these exact solutions are presumed to be less susceptible to spillover and instability.

Two methods of manipulating the exact solutions of the governing partial differential equations are presented. In the first (called Transform Element Modelling, or TEM), the Laplace transform is utilized to transform the equation describing the dynamics behavior of the structural element into the frequency-domain. This leads to mathematically exact dynamic stiffness matrices, which can be assembled to form an exact global structural model. This approach is applied to general one-dimensional and axisymmetric two-dimensional structural elements. The TEM methodology is shown to be, in some cases, superior to traditional finite element techniques in terms of both numerical accuracy and computation speed. Based on this approach, an open-loop optimal control algorithm for small angle slews of flexible structures is developed. The numerical solution of the optimal control problem is obtained by expressing the control inputs in terms of a finite set of basis functions. The algorithm is applied to two structural models and succeeds in minimizing the post-maneuver residual kinetic energy. The issue of closed-loop control using the TEM methodology is also addressed.

The second technique presented (called the direct approach) deals with the original partial differential equations describing the dynamics of the structural elements, expressed in the time-domain. An extended state-space representation is used to develop a distributed full state feedback control solution for simple one-dimensional systems, and numerical algorithms are formulated to determine the distributed feedback gains. The control solution is applied to a Bernoulli-Euler beam, and the feedback gains are determined for various control and deformation penalties. The results are validated with both discrete structural models and analytical results for a beam of infinite length. A novel algorithm for simulating the closed-loop response of the controlled beam is presented. The distributed control theory is also applied to a plate of infinite extent.

A hybrid control design, which takes advantage of the favorable properties of both modelling methods, is proposed. In this design, the distributed controller exerts low-authority control to achieve active damping augmentation. The TEM-based controller exerts high-authority control, and is designed to meet the performance specifications for the structural system.

Thesis Supervisor: Dr. Wallace E. Vander Velde

Title: Professor of Aeronautical and Astronautical Engineering

ACKNOWLEDGEMENTS

First and foremost, I would like to thank Professors Wallace VanderVelde, Steve Hall, and Andy von Flotow of MIT for their patience, understanding, and wisdom. I also wish to express my appreciation for the guidance and encouragement provided by Drs. Hon Chun, Jim Turner, and Keto Soosar of Photon Research Associates, Inc. Thanks to Terri, Jennie, Liz and Caroline for their administrative help in dealing with all the #@&! that came along. Finally, thanks to Debi for hanging in there - we both made it !

Now the formal stuff ... The author wishes to thank Dr. D.J. Wilcox for his advice on implementation of the inverse Laplace transform algorithm. Some of the calculations required for this research were performed on the MIT CRAY 2 supercomputer. This work has been partially sponsored by the AFOSR, under contract #49620-89-C-0082.

This thesis is dedicated to my parents, Nino and Lydia, who have always supported my educational endeavors.

And if you feel that you can't go on, in the light you will find the road ....

TABLE OF CONTENTS

ABSTRACT 2

ACKNOWLEDGEMENTS 3

LIST OF FIGURES 7

LIST OF TABLES 10

NOMENCLATURE 11

1 Introduction 15

1.1 The Control-Structure Interaction (CSI) Problem 15
1.2 The Current Control Design Approach 17
1.3 Summary of Related Research 20
1.4 Overview of the Thesis 22

2 The Transform Element Modelling Approach 26

2.1 Advantages of the Transform Element Method 27
2.2 Inverse Laplace Transform Algorithm 29
2.3 One-dimensional element models 34
2.3.1 Stiffness matrix formulation 36
2.3.2 Interpolation 38
2.3.3 Internal energy formulation 40
2.3.4 Axial rod example 43
2.3.5 Bernoulli-Euler beam example 47
2.3.6 Higher order elements 51
2.4 Two-dimensional elements 55
2.4.1 Axisymmetric elements 55
2.4.2 Plate bending element 61
2.4.3 Plane stress element 64
2.5 Assembly Procedure 68
2.6 Applications 71
2.6.1 Modal frequencies 71
2.6.2 Frequency response and transfer functions 71
2.6.3 Time-domain simulation 77

3 Transform Element Formulation for Arbitrary Motions 80

3.1 Mathematical Model 80
3.1.1 Equations of Motion 80
3.1.2 Solution of the Integral-Partial Differential Equations 88
3.2 Foreshortening Effects 97
3.3 Discussion 99

4 Control Design Based on Transform Element Models 100

4.1 Open-Loop Control 100
4.1.1 Finite-basis control approximation 101
4.1.2 Solution without minimization 103
4.1.3 Minimization with point constraints 103
4.1.4 Minimization of flexible energy 112
4.2 Closed-loop control 114
4.3 Limitations of the Transform Element Control Design Methodology 121

5 Direct Partial Differential Equation Modelling 123

5.1 One-dimensional elements 124
5.1.1 General Formulation 124
5.1.2 Bernoulli-Euler Beam Example 125
5.1.2.1 Normalization of Equations of Motion 125
5.1.2.2 The Case of Curvature Actuation 128
5.1.2.3 Numerical Simulation Using Laplace Transform 129
5.2 Two-dimensional elements 136
5.2.1 Membrane model 138
5.2.2 Plate model 138
5.2.3 Complexity Issues 139
5.3 Multiple Element Formulation 139

6 Control Design Based on Direct Partial Differential Equation Models 142

6.1 Linear Quadratic Optimal Control Theory in the 1-D Case 143
6.2 Distributed Control of a Finite Beam 148
6.2.1 Cost Functional 149
6.2.2 Derivation of the Necessary Conditions 150
6.2.3 Numerical Solution of the Riccati Equations 151
6.2.3.1 Solution of the First Riccati Equation 151
6.2.3.2 Solution of the Second Riccati Equation 154
6.2.3.3 Comparison With Discretized Beam Model 157
6.2.4 The Case of Curvature Actuation 160
6.2.5 Closed-Loop Simulation Results 162
6.3 Distributed Control of an Infinite Beam 167
6.3.1 Spatially Transformed Dynamics and Cost Functional 167
6.3.2 Optimal Control Solution 169
6.3.3 The Case of Curvature Actuation 173
6.4 Distributed Control of 2-D Systems 174
6.4.1 Structures of Finite Dimensions 175
6.4.2 Structure of Infinite Dimensions 177
6.5 Discussion 180

7 Hybrid Modelling Approach for High Authority/Low Authority Control Design 184

8 Conclusion 189

8.1 Summary of Key Results 189
8.2 Contributions of this Thesis 193
8.3 Recommendations for Future Research 198

APPENDIX A High Frequency Transform Elements 201
A.1 Mindlin-Herrmann Rod 201
A.2 Timoshenko Beam 202

APPENDIX B Steady-State Solution for Rotating Mass/Appendage System 205

APPENDIX C Finite-Difference Equations for the Bernoulli-Euler Beam Subject to Non-Homogeneous Boundary Conditions 207

APPENDIX D Simulation of Beam with Curvature Actuation 211

APPENDIX E Simulation of a Timoshenko Beam 213

APPENDIX F Derivation of Adjoint Operators 215

APPENDIX G Optimal Costs for Distributed Control Systems 217

REFERENCES 219

LIST OF FIGURES

Fig. 1-1: Collocated feedback for an undamped system. 18

Fig. 1-2: Collocated feedback for a damped system. 18

Fig. 1-3: Common types of structural dynamics solution techniques used for control design. 21

Fig. 2-1: The integration contour used in calculating the inverse Laplace transform. 31

Fig. 2-2: (a) Frequency-domain sampling used in the inverse Laplace transform algorithm, (b) Resulting time-domain samples. 31

Fig. 2-3: Time-domain responses generated by the inverse transform algorithm. 35

Fig. 2-4: Axial rod model. 44

Fig. 2-5: Bernoulli-Euler beam model. 44

Fig. 2-6: Mindlin-Herrmann rod model. 52

Fig. 2-7: Dispersion curves associated with the Mindlin-Herrmann model. 52

Fig. 2-8: Timoshenko beam model. 54

Fig. 2-9: Timoshenko beam dispersion characteristics (α_I=4x10^{-4}, α_E=2.8). 54

Fig. 2-10: Typical two-dimensional element with three generalized displacements and forces at each boundary point. 56

Fig. 2-11: Response of a membrane impacted at center (r=0). 59

Fig. 2-12: Assembly of simple, four element structure. 69

Fig. 2-13: Transfer functions of simple cantilevered element with various frequency-domain damping models. 73

Fig. 2-14: Schematic of the SCOLE structural system with flexible antenna model. 74

Fig. 2-15: Transfer functions from yaw torque on shuttle to various points on SCOLE model as determined by TEM and FEM models. 75

Fig. 2-16: Comparison between simple axial rod and Mindlin-Herrmann rod models. 78

Fig. 2-17: Time-domain impulse responses of free-free beam element impacted with unit transverse force on left boundary (α_I=4x10^{-4}, α_E=2.8). 79

Fig. 3-1: Beam cantilevered to arbitrarily moving rigid mass. 81

Fig. 3-2: The foreshortening phenomenon arising from finite transverse deformation. 87

Fig. 3-3: Comparison of TEM and DISCOS simulations of mass/appendage system (first run). 93

Fig. 3-4: Comparison of TEM and DISCOS simulations of mass/appendage system (second run). 94

Fig. 3-5: Comparison of TEM and DISCOS simulations of mass/appendage system (third run). 95

Fig. 3-6: Comparison of TEM and DISCOS simulations of mass/appendage system (fourth run). 96

Fig. 4-1: Simple mass/flexible appendage structural model used in the open-loop optimal control demonstrations. 105

Fig. 4-2: Results of optimal maneuver of mass/flexible appendage system. 107

Fig. 4-3: Results of optimal maneuver of mass/flexible appendage system with reduced axial stiffness. 108

Fig. 4-4: Optimal rotational slew of SCOLE structure with four control inputs (see text). 109

Fig. 4-5: Optimal rotational slew of SCOLE structure with nine control inputs (see text). 110

Fig. 4-6: Linear slew maneuver with residual energy cost functional and terminal velocity of 0 m/sec. 115

Fig. 4-7: Linear slew maneuver with residual energy cost functional and terminal velocity of 1 m/sec. 116

Fig. 4-8: Rotational slew maneuver with residual energy cost functional and terminal angular velocity of 0 rad/sec. 117

Fig. 4-9: Rotational slew maneuver with residual energy cost functional and terminal angular velocity of 0.1 rad/sec. 118

Fig. 4-10: The prototypical control problem posed in the standard form. 120

Fig. 5-1: Bernoulli-Euler beam models. 126

Fig. 5-2: Uncontrolled response of beam with initial displacement $v_0(x)=\sin(2\pi x)$. 134

Fig. 5-3: Response of uniform beam to unit impulse applied at center-span. 135

Fig. 5-4: Response of free-free beam to unit impulse applied at x=0. 137

Fig. 5-5: Schematic of multi-element truss structure. 141

Fig. 6-1: Curvature feedback kernels for uniform beam. 155

Fig. 6-2: Velocity feedback kernels for uniform beam. 158

Fig 6-3: Feedback gains for tapered beam (Beam diameter varies linearly from 1.0 at x=0 to 0.75 at x=1). 159

Fig. 6-4: Closed-loop simulation of uniform beam with $v_0(x)=\sin(2\pi x)$. 163

Fig. 6-5: Closed-loop simulation of uniform beam with unit impulse applied at center-span ($r/q_U=10^{-4}$ and $q_T=q_U$). 164

Fig. 6-6: Plots of gain matrices determined from LQR solution to discretized beam model. 165

Fig. 6-7: Normalized curvature feedback gain kernel for infinite beam. 172

Fig. 6-8: Normalized velocity feedback gain kernel for infinite beam. 172

Fig. 6-9: Normalized curvature feedback gain kernel for infinite plate. 181

Fig. 6-10: Normalized velocity feedback gain kernel for infinite plate. 181

Fig. 7-1: Schematic of the complete HAC/LAC control architecture. 185

LIST OF TABLES

Table 6-1: Comparison between optimal costs for distributed control and conventional lumped-parameter control. 166

NOMENCLATURE

ROMAN SYMBOLS

a	radius of rod of circular cross section
$\mathbf{a}$	vector of arbitrary coefficients for TEM interpolation functions
A	cross section area for general beam element
$\mathbf{B}_x$	matrix linear spatial differential operator for control input
c	stress wave propagation velocity
$\mathbf{c}$	vector of undetermined coefficients for open-loop control inputs
C	closed contour in the complex plane
$\mathbf{C}$	connectivity matrix for TEM assembly
D_{xy}	dual operator to L_{xy}
$\mathbf{D}$	finite difference matrix operator for second derivative
$\mathbf{D}_x$	matrix linear spatial differential operator for disturbance input
E	modulus of elasticity
E	internal energy of deformation of structural element
f	generalized distributed forcing input
$\mathbf{f}$	vector of basis functions for open-loop control inputs
$\tilde{f}$	net forcing due to initial conditions and distributed forces
f_1, f_2	normalized distributed feedback gain kernels for infinite beam or plate
F	internal force resultant for axial rod
$\mathbf{F}$	matrix of basis functions for open-loop control inputs
g	generic function of time
G	shear modulus
$\mathbf{G}$	dynamic flexibility matrix for TEM analysis
$\mathbf{G}_c$	compensator transfer function matrix
I	moment of inertia of cross section for general beam element
j	imaginary unit
J	cost functional
J_a	augmented cost functional
J_0	Bessel function of order zero
k	generalized stiffness or mass parameter
k_1, k_2	distributed feedback gain kernels for finite beam
$\mathbf{K}$	dynamic stiffness matrix for TEM analysis

L	structural element length
L_x	scalar linear differential operator
$\tilde{L}_x$	scalar linear differential operator
L_{xy}	linear spatial differential operator in two dimensions
$\mathbf{L}_x$	matrix linear spatial differential operator
L^{-1}	inverse Laplace transform operator
m	mass per unit length for general beam element
m	distributed curvature input
M	internal moment resultant for beam element
$\mathbf{n}$	distributed disturbance input vector
N	number of frequency samples used in inverse Laplace transform algorithm
N	mesh discretization grid size for distributed control solution
$\mathbf{p}$	distributed control costate vector
$\mathbf{P}_x$	distributed control Riccati operator matrix
$\mathbf{q}$	generalized TEM boundary force vector
$\mathbf{q}_d$	net effect of distributed forcing and initial conditions on $\mathbf{q}$
$\mathbf{q}_c$	control boundary forces
$\mathbf{Q}$	distributed control state penalty weighting matrix
r	distributed control effort penalty weighting
$\mathbf{R}$	weighting matrix for open-loop optimal control
s	complex frequency
S	internal shear resultant for beam element
$\mathbf{S}$	distributed control Riccati function matrix
t	time (independent variable)
t_f	open-loop optimal maneuver terminal time
T	simulation time for inverse Laplace transform algorithm
u_x, u_y	in-plane deformations for two-dimensional element
$\mathbf{u}$	structural state vector in TEM formulation
$\mathbf{u}$	distributed control input vector
$\mathbf{u}_p$	effect of distributed forcing and initial conditions on $\mathbf{u}$
v	generalized displacement
$\mathbf{v}_H$	homogeneous solution vector in TEM formulation
v_p	Green's function in TEM formulation

$\mathbf{w}$ generalized boundary displacement vector

$\mathbf{w}$ disturbance input vector

W primary N'th root of unity

$\mathbf{W}$ quadratic cost matrix for optimal open-loop maneuvers

x spatial coordinate (independent variable)

$\mathbf{x}$ distributed state vector

y dummy variable of integration

$\mathbf{y}$ vector of outputs of interest

$\mathbf{Y}$ response matrix to basis function inputs for optimal open-loop control problem

Y_0 Bessel function of order zero

z dummy variable of integration

$\mathbf{z}$ performance measure

Z primary 2N'th root of unity

GREEK SYMBOLS

α offset of integration contour from imaginary axis for inverse Laplace transform

β normalized inverse mass density

δ Dirac delta function

ε components of strain tensor

Φ dynamic stress function for TEM formulation

Γ interpolation matrix for TEM formulation

η normalized bending stiffness

Φ matrix relating $\mathbf{u}$ to $\mathbf{a}$ in TEM formulation

λ Lame constant

λ Lagrange multiplier vector

ν Poisson's ratio

θ bending rotation of cross section of beam element

Θ geometric matrix for TEM formulation

ρ mass density

σ components of normal stress

τ shear stress

ω radian frequency

$\Delta\omega$ frequency interval

Ξ internal energy matrix in TEM formulation

Ψ matrix relating **w** to **a** in TEM formulation

$\tilde{\Psi}$ matrix relating **q** to **a** in TEM formulation

ζ spatial frequency variable

∇^2 Laplacian operator

ANNOTATIONS

$(\dot{})$ differentiation with respect to time

$(\bar{})$ temporal Laplace transform

$(\hat{})$ spatial Fourier transform

$()^T$ transpose

$()^*$ complex conjugate

$()^*$ adjoint operator

$\delta()$ first variation

$()_i$ index for a vector quantity

$()_{ij}$ index for a matrix quantity

$()_u$ control component

$()_n$ disturbance component

$()_U$ potential energy component

$()_T$ kinetic energy component

$()_d$ dimensional form of variable

$()_0$ initial condition

$()^i$ element indentifier

${}^I()$ inertial reference frame

$()^{(i)}$ boundary point identifier

$()^G$ global coordinates

1 INTRODUCTION

This thesis examines the use of exact solutions of structural dynamics models for structural analysis and control design. The structural systems are modelled with sets of partial differential equations (PDE's), and their solutions are expressed in either the frequency or time domain, depending on the representation used. Each representation has motivated a structural control methodology in a natural way. The Transform Element Method (TEM) uses the Laplace transform to obtain exact, frequency-domain structural element models. An assembly procedure is then used to create a mathematically exact global model. Several open-loop control algorithms have been developed based on the TEM models generated. Alternatively, the direct PDE approach deals specifically with the underlying time-domain partial differential equations describing the structural behavior. For this approach, an extended state-space representation describes the dynamics. This methodology leads to a distributed control theory, which is analogous to traditional state-space control. These two representations are alternatives to conventional structural models used for control design. They are intended to alleviate the problems associated with control-structure interaction, which is described in the next section.

1.1 The Control-Structure Interaction (CSI) Problem

The requirements for many military and civilian structures applications both in space and on earth call for the use of large, high performance, lightweight structures. In most cases, the structural weight must be kept as small as possible to avoid excessive transport costs. However, the flexibility associated with large, lightweight structures increases the likelihood of troublesome structural behavior. The vibrational modes generally begin at low frequency, and are excited by exogenous disturbances. Potential sources of these disturbances include rotating machinery for terrestrial applications and attitude control, antenna retargeting and payload shifting for space applications. Often, the structure, disturbance and control bandwidths are close or overlapping, causing undesirable vibration to propagate through the structure. In systems with stringent

pointing requirements (such as space-based telescopes, interferometers, lasers, etc.), this can severely degrade performance. Similarly, for systems requiring pilot isolation or flutter control, performance degradation occurs if unwanted vibration is present. When these problems arise, some sort of vibration suppression, either active or passive, is required.

Passive damping techniques alone are usually insufficient to meet performance requirements. In order to achieve significant modal damping (on the order of 50%, say), an unacceptably large mass of damping material must be added to the structure. As a general rule, passive damping can only provide about 5% to 10% damping for a 5% increase in structural mass. (See, for example, Reference 1.) Consequently, these techniques provide low levels of vibration suppression and are well suited for addressing steady-state disturbances arising from on-board or environmental sources. Active control techniques are required for suppressing transient behavior and large, disturbance-induced structural responses.

Large, lightweight structures have three basic characteristics which make active control design difficult. First, the structures are difficult to model precisely. The structural dynamics solutions obtained from finite element techniques only approximately reproduce the high frequency behavior contained in the models. Typically, only the first few modes are known to any degree of accuracy. As a result, the active control design must be extremely robust. Unfortunately, robustness often leads to very conservative designs which sacrifice performance for stability. Second, these structures are modally dense and lightly damped. This makes the closed-loop system extremely sensitive to parameter variations, and often leads to instability. Third, the underlying dynamics are of infinite order. As a result, traditional full-order linear quadratic regulator (LQR) and linear quadratic gaussian (LQG) control designs are not directly applicable to these types of systems.

These structural characteristics lead to a phenomenon described by Balas [2] as "spillover," and can be explained as follows. In a typical control design procedure, the approximate finite element model is first truncated to include only those modes which are known to a good degree of accuracy. This becomes the evaluation model, against which various control designs are judged.

Typically, the evaluation model is of too high an order to achieve an equivalent order controller. As a result, a reduced order controller is designed, either directly from the evaluation model [3], or based on a further truncation of the evaluation model [4] [5]. In either case, the action of the controller excites all the modes of the evaluation model to some degree. This is referred to as control spillover. Likewise, the sensors associated with the controller also respond to the modes truncated from the evaluation model, leading to observation spillover. Additional control and observation spillover occurs when the reduced order controller is applied to the actual infinite order structure.

1.2 The Current Control Design Approach

Currently, the methodology generally employed in most structural control problems is the High-Authority Controller/Low-Authority Controller (HAC/LAC) approach [6]. This is a hierarchical control architecture that addresses many of the issues presented in the previous section. The design procedure usually involves three distinct procedures. In addition to developing the HAC and LAC active control systems, passive damping augmentation is usually designed. In many cases, prefiltering of command inputs is also required to minimize excitation of structural modes. The modal-based command shaping method developed by Singer [7] is an example of the prefiltering concept.

A passive damping treatment is almost always required in the active control design of infinite order, lightly damped systems. The closed-loop system is guaranteed to be unstable for undamped infinite order systems and any physically realizable controller (i.e., any controller with some amount of phase lag). This phenomenon is explained in Fig. 1-1. The figure on the left shows, qualitatively, the effect of ideal positional feedback on an undamped system. We see that the natural frequencies of the system can be altered, but the modes remain undamped. Any nonideality (phase lag) in the controller will cause some of the poles to move into the right half-plane. The lower modes can be damped by applying rate feedback to the structure, as shown in the figure on the right. However, any implementable controller will, above some frequency,

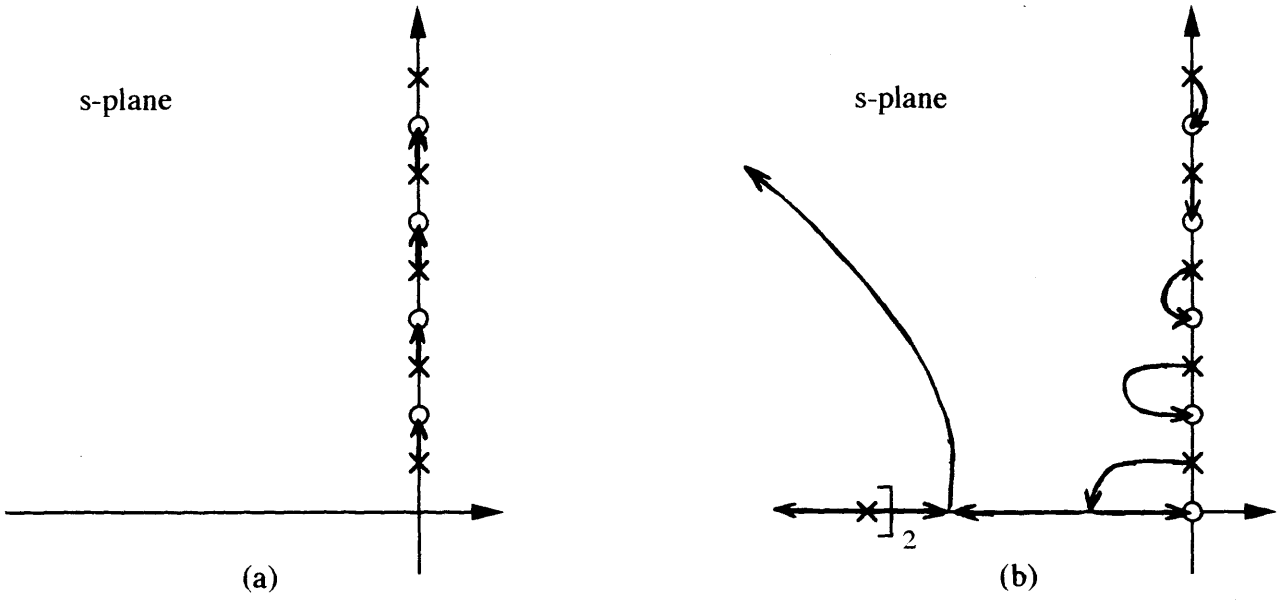

Fig. 1-1: Collocated feedback for an undamped system: (a) Position feedback alters the modal frequencies, but the system remains marginally stable. (b) Rate feedback, with controller dynamics modelled by a double pole on the real axis. Instability first occurs in the locus with approximate radius corresponding to the radius of the poles of the controller.

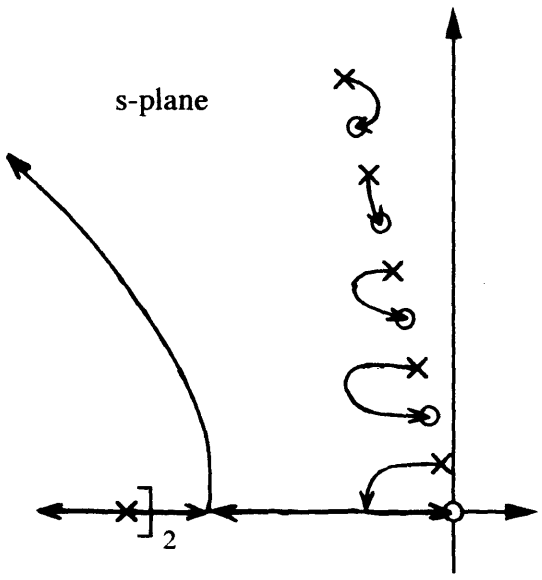

Fig. 1-2: Collocated feedback for a damped system. The passive damping, in this case, is sufficient to prevent instability, and the damping in the lower modes can be increased significantly. In an actual LAC design, many actuators and sensors are used, which enables greater damping of higher modes.

contribute sufficient phase lag to the system to cause instability. Furthermore, even slightly damped systems can be made unstable by increasing the gain of the controller sufficiently. As a result, passive damping is usually required for all high performance structures. For some applications, adequate passive damping may be inherently present in the structure, due to material friction, viscoelasticity, and/or joint hysteresis. High performance applications will likely require careful tailoring of the passive design in order to meet performance goals. By shifting the open-loop poles of the system into the left half-plane, passive damping has the added benefit of desensitizing the controller to modelling errors, thereby increasing robustness. Though attractive for practical and theoretical reasons, mass penalties place an upper limit to the amount of passive damping that can be implemented.

The LAC (also called active damping augmentation) is usually an *ad hoc* design, as the primary objective is to achieve robust control with a large number of simple controllers [8]. Typically, collocated rate feedback is employed. The effect of this form of feedback on the modes of the structural system is shown in Fig. 1-2. In this figure, we see that the damping of the higher modes is sufficient to prevent instability. The main objective of active damping augmentation is, as the name implies, to increase modal damping significantly, so that the HAC does not destabilize the system in the presence of modelling errors.

The primary design objectives are accomplished via the HAC. It is usually a dynamic compensator of high order, and utilizes information from sensors located throughout the structure. Multiple actuation is also commonplace. These actuators and sensors need not be distinct from those used in active damping augmentation. As the name implies, the HAC exerts high gain control on the structure, moving the closed-loop pole locations considerably.

Many factors determine the performance of the closed-loop system, but the accuracy of the underlying structural model is clearly critical. Typically, uncertainties in the dynamics of the structure lead to conservative control designs which have relatively low bandwidths. This ensures closed-loop stability in the presence of modelling errors, at the expense of reduced performance. For example, MacMartin [9] describes a method for minimizing the power imparted to the structure

at an interface using H∞ techniques. However, only the near field effects are considered. Reflections of the disturbances at other boundaries of the structure are not modelled. This represents a worst case design, with the assumption that nothing is known about the structure except in the immediate vicinity of the controller. Miller [10] uses a wave propagation approach to design controllers that absorb power at structural interfaces. Again, the lack of a far field model results in a conservative design. Clearly, then, a more accurate structural modelling approach would be beneficial. In particular, it is desirable to develop a representation that avoids the modal truncation and spatial discretization associated with finite element modelling while retaining the ability to model the dynamics at structural element interfaces. This is the basis for Partial Differential Equation (PDE) modelling approaches. The equations describing the structure are solved exactly, and remain mathematically exact at all frequencies. The issue of modelling error is then confined to knowledge of the physical parameters for the system and the actual choice of the mathematical equations describing the dynamics of the structural elements.

1.3 Summary of Related Research

Figure 1-3 displays some typical solution approaches to structural dynamics models and their relations to each other. Associated with each is a representative list of authors who have utilized these models in control design strategies. The most widely used modelling methodology is the finite element modelling (FEM) approach, which can be used to obtain either a modal model of the structure or a direct state-space model. A great deal of literature exists in the field of state-space control. For example, Stein and Athans [11] develop a formal algorithm for multivariable feedback control which essentially allows the designer to shape the singular values of the open-loop system, thereby ensuring certain robustness and performance characteristics. Likewise, Doyle [12] develops iterative design algorithms for H∞ controllers expressed in state-space form. Most of the literature on modal control has been generated by Meirovich. In Reference 13, for example, the sensitivity of modal-based controllers to the number of retained modes is studied. The method of asymptotic expansions has also found use as an approximate dynamics analysis tool [14] [15].

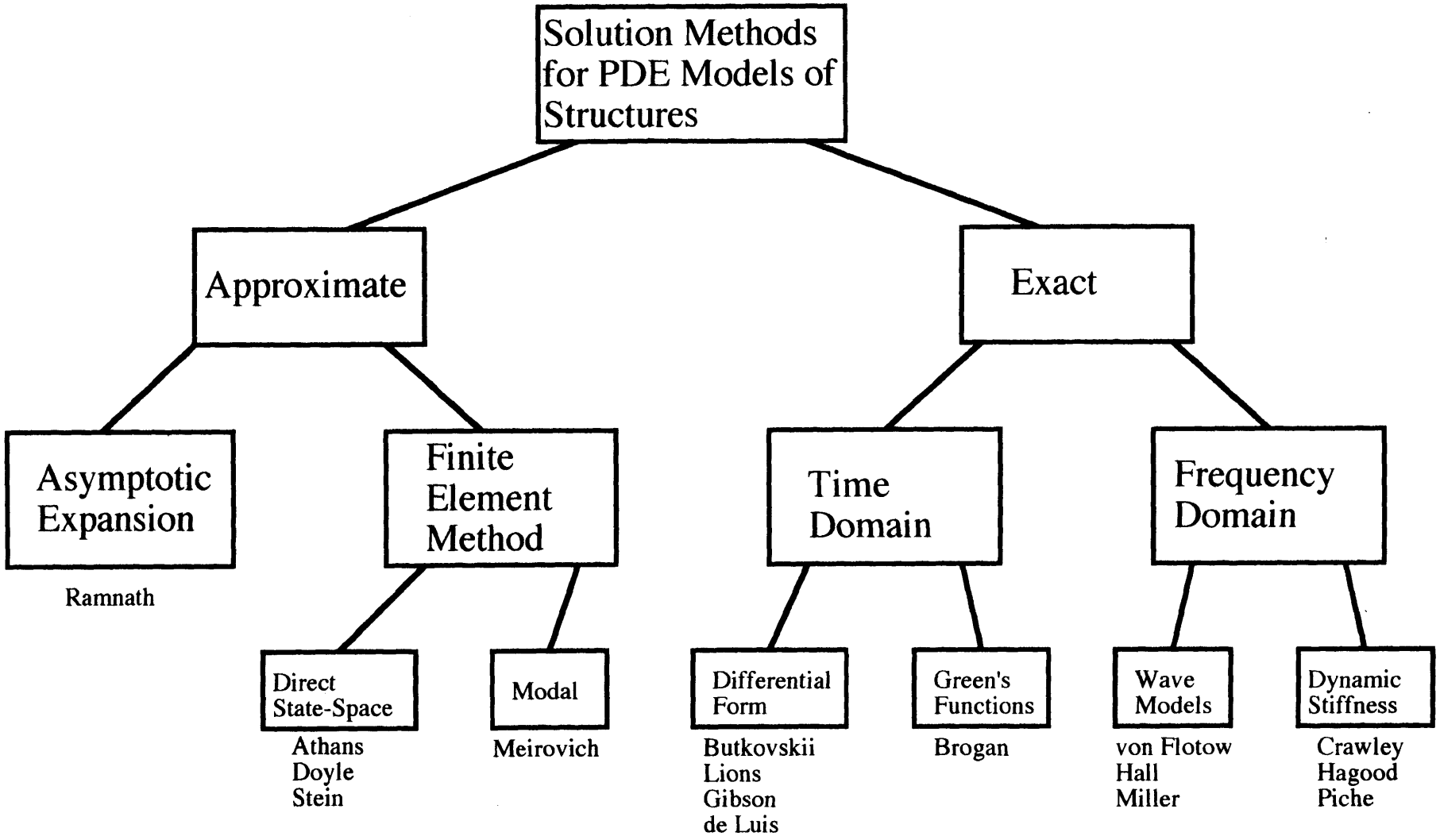

Fig. 1-3: Common types of structural dynamics solution techniques used for control design.

This method has been used, for example, to determine the stability of a deformable mirror structure [16] [17].

Control designs based on exact structural models have a more limited range of applicability than state-space designs, due primarily to the complexity of the mathematical description of the dynamics. Using the exact time-domain description of the system dynamics, two classes of control design have been developed. In the first, a Green's function approach is used to determine the system response to control and disturbance excitation. The works of Brogan [18] [19] [20] proceed along these lines. In the second, a differential description of the problem is used, resulting in partial differential equations of motion. The works of Butkovskii [21], Lions [22] and Gibson [23], among others, describe the design of distributed controllers for such systems. Using frequency-domain analysis techniques, two types of representation have also found use in structural control. The travelling wave approach has been used to develop wave-absorbing controllers for simple structures. The works of Mace [24] [25], von Flotow [26], Miller [27] [28], MacMartin [29], and Signorelli [30] apply travelling wave techniques to determine and/or control power flow through the structure. The dynamic stiffness (TEM) approach has also found limited use in closed-loop control. Piche [31] uses the dynamic stiffness matrix of a simple torsional structure to rigorously determine the stability of controllers acting at the boundaries of the structure.

1.4 Overview of the Thesis

The primary goal of this thesis is to examine the benefits and limitations of using mathematically exact solutions to structural dynamics models for control design. Ideally, we would like to develop new control algorithms which supplement those mentioned in the previous section. In this thesis, the use of both the TEM and the direct PDE representations for control design is demonstrated. The TEM representation is employed to obtain open-loop control solutions for arbitrary frame-like structures. Likewise, the direct PDE representation for simple structural systems is utilized to obtain closed-loop distributed controllers.

It should be mentioned here that the modelling errors associated with many structural systems are often larger in magnitude than the errors introduced by approximate solutions to such models (such as finite element analysis). These modelling errors arise from many sources. The physical dimensions and mass properties of the structure are often not known to great precision. Moreover, these properties may change with time due to thermal cycling and aging. In addition, nonlinear behavior is always present to some degree in an actual structure, while the structural models are often linear for mathematical simplicity. This is indeed the case for the models presented throughout this thesis. For example, a physical structural junction is never perfectly clamped nor pinned. Rather, joint compliance and free-play between members lead to complex nonlinear behavior. A linear dynamics model for such a system is therefore subject to errors. Also, nonlinear constitutive relations are often modelled with the linearized equations of elasticity. Finally, it must be stated that no physical system can be represented exactly by the partial differential equations of continuum mechanics, as the dynamics at the molecular level are ultimately governed by quantum mechanics.

Nevertheless, linear structural models continue to find use as control models, primarily because they capture the essential physical behavior of the structure, and because analysis and control design is simplified considerably by assuming a linear plant model. The use of exact solutions to these linear models can be useful in determining qualitative characteristics of the structural response as well as qualitative features of the structural control systems required to improve the performance of such structures. If, in addition, modelling errors are reasonably small (in comparison with the truncation errors arising from approximate solution techniques), quantitative predictions of structural behavior can also be extracted from the exact solutions. It is for these reasons that this thesis explores the use of exact solutions techniques for structural dynamics models.

The underlying philosophy regarding the formulations presented in this thesis is to delay numerical approximation and/or spatial discretization in the structural design until it is absolutely necessary. This is in contrast with existing approaches designed to handle a broad range of

systems where, in most cases, a finite order dynamics model is required. For these approaches, the designer carries the additional burden of determining the extent to which the discretization contributes to modelling error, in exchange for the ability to apply a generally accepted design algorithm. This thesis demonstrates that, for certain classes of problems, the mathematically exact representation can be retained when deriving the necessary conditions for optimality. Approximations are required only when solving the equations that arise from these necessary conditions. Thus, the necessary conditions correspond precisely with the exact mathematical model of the system, and reflect the underlying physical mechanisms from which such models are derived.

It is important to point out the difference between what is meant by a *model* and what is meant by a *representation* in this thesis. A *model* corresponds to the specific mathematical equations that describe (approximately) the dynamics of the structure. It is assumed throughout the following developments that the dynamics model for a particular structure has been determined *a priori*. While a model can never be considered exact, such a model may indeed have an exact *solution*. A *representation* is the form in which the dynamics equations are presented and/or manipulated. Thus, a given model can have more than one representation. In particular, a dynamics equation can be expressed in either the time domain (direct PDE representation) or in the frequency domain (TEM representation). Both representations convey the same information, as they both possess the differential equations dictated by the structural model. In light of this, we say that the finite element approach is a modelling methodology, while the TEM and direct PDE approaches are different representations of the same "exact" model. Nevertheless, the term *model* will sometimes be used in place of the word *representation* when describing the two exact approaches presented in this thesis.

The next three chapters address the TEM representation of structural models. Chapter 2 introduces the TEM methodology and its applications to structural analysis problems. The extension of the TEM approach to systems which experience large angular motions is addressed in Chapter 3. Open-loop control designs, based on TEM models, are presented in Chapter 4. The

extension to closed-loop control is also discussed. The subsequent chapters examine the use of direct structural model representation. Chapter 5 develops the direct PDE approach for one- and two-dimensional structural elements. The direct simulation of a simple one-dimensional system is also presented. The direct PDE approach leads naturally to a distributed control theory, which is developed in Chapter 6. The possibility of a hybrid approach for HAC/LAC control designs, which incorporates both TEM and direct PDE representations, is discussed in Chapter 7. Finally, conclusions and recommendations are presented in Chapter 8.

2 THE TRANSFORM ELEMENT MODELLING APPROACH

In this chapter, we introduce the Transform Element Modelling (TEM) method of structural analysis. This approach begins with the partial differential equations describing the dynamics of the individual elements that comprise the structure. The Laplace transform is then utilized to express these equations in the frequency-domain. Mathematically exact, frequency-dependent stiffness matrices, which relate a set of generalized forces to a set of generalized displacements at the element boundaries, are then derived. These stiffness matrices are then assembled to form a global model, in a manner similar to the traditional finite element assembly procedure. The advantages of this approach are described in Section 2.1. The procedure for converting frequency-domain data back into the time-domain is described in Section 2.2. The general theory for one-dimensional elements, and some simple representative examples, are presented in Section 2.3, while Section 2.4 applies the TEM methodology to two-dimensional structural element models. The assembly procedure is described in Section 2.5, and several applications of the TEM approach are presented in Section 2.6.

The TEM representation is not unique to this thesis. Earlier works by Wittrick [32], Piche [33], Langley [34] and Hagood [35], as well as many others, utilize the frequency-domain representation under such names as the dynamic stiffness method, the exact finite element method, and the continuum method. The developments presented in Sections 2.3 through 2.5 are intended to familiarize the reader with the notation presented herein, as well as introducing additional features of the TEM representation specific to this thesis. In particular, the nonhomogeneous terms arising from initial conditions and distributed forcing within structural elements are included in the framework, and require additional consideration. This is in contrast with most other frequency-domain research, where the analysis is confined to the imaginary axis and is usually restricted to steady-state sinusoidal motion. In some developments presented below, the nonhomogeneous

terms are ignored, primarily for clarity in presenting complicated expressions. It is nonetheless a simple matter to carry out the mathematics with these terms retained.

2.1 Advantages of the Transform Element Method

The TEM approach has several important advantages over the traditional Finite Element Method (FEM), as measured in terms of numerical accuracy and computational efficiency. The dynamics of the one-dimensional element models that comprise the global structural model to be analyzed are represented exactly in the TEM approach. This is made possible by the Laplace transform operation, which converts the time-domain partial differential equation of a structural element into a frequency-dependent ordinary differential equation. As a result, analytical general solutions to these equations are available for most common element models, such as Bernoulli-Euler and Timoshenko beams, and axial and torsional rods. More complicated elements can be handled by special numerical modelling approaches. This is in marked contrast to FEM modelling, where each element is typically divided into smaller subsections, each of which is constrained to deform with a finite number of degrees of freedom. For simple elements, the interpolation functions associated with the FEM deformational degrees of freedom satisfy the underlying differential equation exactly for the static case, but only approximate the exact solution in the dynamic case. Consequently, for dynamics problems, the FEM analysis can only yield approximate results. Conversely, the TEM approach, which utilizes frequency-dependent (generally transcendental) interpolation functions, is mathematically exact at all frequencies. Furthermore, since only one mathematical element is required for each physical structural element, the TEM approach is superior to the FEM methodology (in terms of computational speed) for certain applications.

For two-dimensional structural elements, general mathematically exact solutions are not available, but the TEM methodology makes it possible to approximate the solutions in terms of finite series of displacement functions. Each of these functions satisfies the underlying differential equation in the interior of the element exactly, and approximations are made only at the boundaries.

A comparison between the TEM and FEM methods in terms of speed and accuracy for two-dimensional elements has not yet been attempted.

Another important advantage of the TEM approach is its ability to incorporate general linear viscoelastic damping models in a straightforward manner. Using the correspondence principle, as described by Hughes [36], the physical parameter of interest is simply replaced with a frequency-dependent counterpart. For example, the Voigt damping mechanism is easily expressed by

$$E(s) = \left[1 + \bar{\sigma}_v \frac{s}{\omega_v}\right] E_0 \tag{2.1}$$

where E is the modulus of elasticity of the material, E_0 is its static value, s is the (generally complex) frequency, ω_v is a characteristic frequency, and $\bar{\sigma}_v$ is an empirically determined nondimensional parameter. A more general damping model, suggested by Hughes, is

$$E(s) = \left[1 + \sum_{i=1}^{N_\sigma} \sigma_i \frac{s^2+2\zeta_i\omega_i s}{s^2+2\zeta_i\omega_i s+\omega_i^2}\right] E_0 \tag{2.2}$$

where, for each value of i, σ_i is a characteristic scaling factor, ω_i is a characteristic frequency, and ζ_i is a characteristic damping ratio, all of which are empirically determined. However, the advantage of the TEM approach lies in its ability to model damping mechanisms of infinite order, such as the fractional derivative models discussed by Bagley [37]. Such models require the use of fractional calculus techniques when employed in the time domain, but are easily cast in the frequency-domain as fractional powers of the complex frequency. For example, the square root damping model is written as

$$E(s) = \left[1 + \bar{\sigma}_s \sqrt{\frac{s}{\omega_s}}\right] E_0 \tag{2.3}$$

where ω_s is a characteristic frequency and $\bar{\sigma}_s$ is empirically determined. Thus, since all linear viscoelastic damping models have frequency-domain representations, any such model can be used

in the TEM formulation. This capability has been exploited by many researches, the work of Hagood [35] being one example.

Yet another advantage of the TEM approach is the ability to take derivatives of time-domain functions. All that is required is multiplication of the function by the complex frequency variable. Similarly, additional multiplications by s yield higher order derivatives. Thus, given a set of frequency-domain data representing a time-domain response, it is a simple matter of multiplying the data by the complex frequency before invoking the inverse Laplace transform to obtain the derivative of the response.

2.2 Inverse Laplace transform algorithm

In any frequency-domain modelling approach, it is of paramount importance to have the ability to convert data back into the time-domain in a computationally efficient manner. This is the basis for many inverse Laplace transform algorithms. The first complete work on the subject was presented by Bellman [38]. Other specific approaches, such as the method of expansion by Laguerre functions described by Weeks [39] and Wing [40], have found limited application. A detailed comparison of several other approaches may be found in Davies [41]. These algorithms are primarily useful for determining the response at a single point in time with extreme accuracy, and are generally inefficient at generating an entire time-domain history. The reason is that these methods cannot be manipulated into a form amenable to fast Fourier transform (FFT) techniques. The most straightforward, stable and accurate method for general functions which does utilize the efficient FFT algorithm appears to be the numerical approach of Wilcox [42]. It is this method that has been used exclusively and extensively in this research, and it therefore deserves mention here.

The inverse Laplace algorithm is utilized in lieu of modal expansion of the frequency domain data primarily for convenience, as it can be applied directly to the frequency domain data and does not require any *a priori* knowledge of the modes of the system to be analyzed. This is important for the TEM representation, as modal frequencies and associated residues must be

computed iteratively (in contrast to finite element models, where the mode shapes are obtained via direct eigenvector decomposition).

The Laplace transform pair is expressed as

$$\begin{aligned} \bar{g}(s) &= \int_0^\infty g(t)\, e^{-st}\, dt \\ g(t) &= \frac{1}{2\pi j} \int_C \bar{g}(s)\, e^{st}\, ds \end{aligned} \tag{2.4a,b}$$

where the contour C is generally taken as a line parallel to the imaginary axis, lying to the right of all the singularities of $\bar{g}(s)$, as shown in Fig. 2-1. We will assume that $\bar{g}(s)$ has no poles with real parts greater than α, where α is a small positive number. The inverse transform then reduces to

$$g(t) = \frac{e^{\alpha t}}{2\pi} \int_{-\infty}^{\infty} \bar{g}(s)\, e^{j\omega t}\, d\omega\,, \quad s = \alpha + j\omega \tag{2.5}$$

Since the path of integration is displaced to the right of the imaginary axis, marginally stable and slightly unstable functions can be inverted. Because g(t) is assumed to be real-valued, it follows from Equation (2.4a) that $\bar{g}(s^*) = \bar{g}(s)^*$. As a result, Equation (2.5) reduces to

$$g(t) = e^{\alpha t}\, \mathrm{Re} \left\{ \frac{1}{\pi} \int_0^\infty \bar{g}(s)\, e^{j\omega t}\, d\omega \right\} \tag{2.6}$$

The numerical computation of g(t) involves calculating $\bar{g}(s)$ at N evenly-spaced complex frequencies along the integration contour, as shown in Fig. 2-2. These values are given by

$$\omega_k = (2k+1)\Delta\omega\,, \quad k = 0, \ldots, N-1 \tag{2.7}$$

The algorithm yields 2N values of g(t) at evenly-spaced time intervals, given by

$$t_m = \frac{2m+1}{4N} T\,, \quad m = 0, \ldots, 2N-1 \tag{2.8}$$

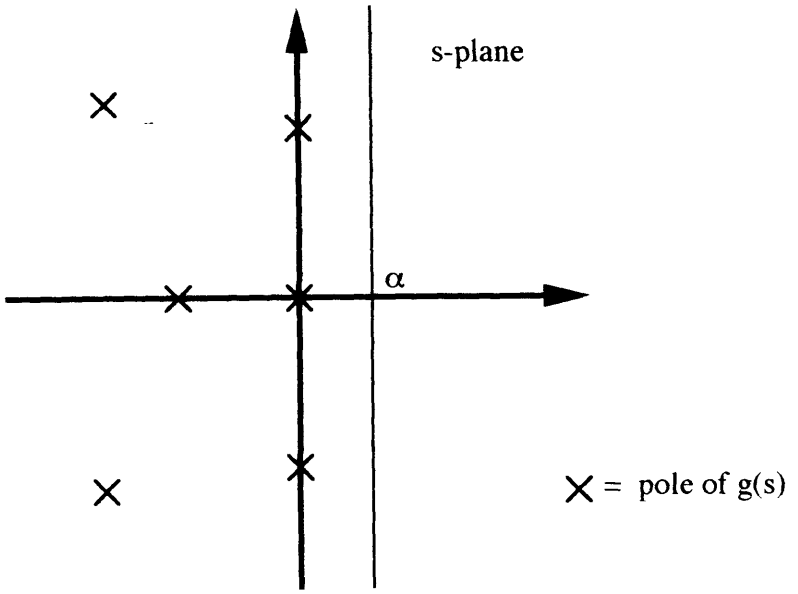

Fig. 2-1: The integration contour used in calculating the inverse Laplace transform.

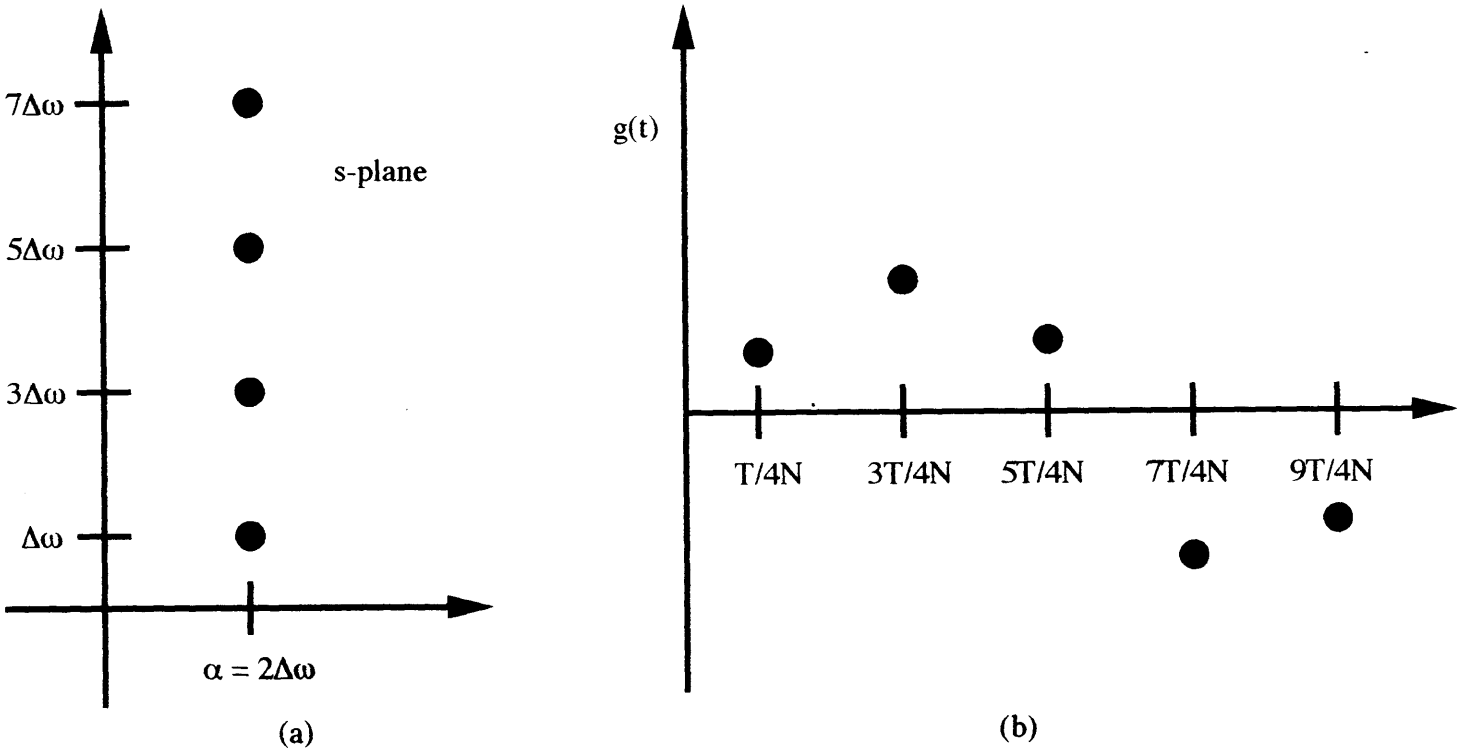

Fig. 2-2: (a) Frequency domain sampling used in the inverse Laplace transform algorithm, (b) Resulting time-domain samples.

where the time interval extends from t=0 to t=T. Wilcox [42] shows that, for reciprocity (i.e., in order that there exist a one-to-one relationship between the sampled functions and their transforms), the following relationship must hold:

$$\Delta\omega = \frac{\pi}{T} \tag{2.9}$$

Hence, Equation (2.6) can be approximated by the midpoint rule as follows:

$$g(t_m) \cong e^{\alpha t_m} \mathrm{Re} \left\{ \frac{2}{T} \sum_{k=0}^{N-1} \bar{g}(s_k)\, e^{j\pi(k+1/2)(m+1/2)/N} \right\} \tag{2.10}$$

Factoring out constant terms from within the summation and simplifying yields

$$g(t_m) \cong e^{\alpha t_m} \mathrm{Re} \left\{ \frac{2}{T} Z^{m/2} \sum_{k=0}^{N-1} \left[\bar{g}(s_k)\, Z^{(2k+1)/4} \right] Z^{km} \right\} \tag{2.11}$$

where

$$Z = e^{j\pi/N} \tag{2.12}$$

If we now define $\bar{g}_k$ and g_m by

$$\bar{g}_k = \bar{g}(s_k)\, Z^{(2k+1)/4}, \qquad g(t_m) = e^{\alpha t_m} \mathrm{Re} \left\{ \frac{2}{T} Z^{m/2}\, g_m \right\} \tag{2.13a,b}$$

Then Eq. (2.11) becomes

$$g_m = \sum_{k=0}^{N-1} \bar{g}_k\, Z^{km} \tag{2.14}$$

For computational efficiency, it is useful to write Eq. (2.14) in a form amenable to fast Fourier transform techniques. This is accomplished by separating the time-domain samples into even and odd sets. Thus,

$$\left.\begin{aligned} \tilde{g}_n &= g_{2n} \\ \tilde{g}_n &= g_{2n+1} \end{aligned}\right\} \quad n=0, \ldots, N-1 \tag{2.15}$$

and the inverse transform is applied twice, yielding

$$\tilde{g}_n = \sum_{k=0}^{N-1} \bar{g}_k W^{kn}, \qquad \tilde{g}'_n = \sum_{k=0}^{N-1} \bar{g}'_k W^{kn} \tag{2.16a,b}$$

where

$$\bar{g}'_k = \bar{g}_k Z^k, \qquad W = Z^2 = e^{2\pi j/N} \tag{2.17a,b}$$

Thus, given a series of samples, $\bar{g}(s_k)$, in the frequency-domain, the algorithm is as follows: Use Eq. 2.13a to obtain $\bar{g}_k$ and Eq. 2.17a to obtain $\bar{g}'_k$. Next, apply the fast Fourier transform, as described by Cooley [43], to obtain $\tilde{g}_n$ and $\tilde{g}'_n$. Upon reordering the data, which yields g_m, use Eq. 2.13b to obtain $g(t_m)$. Wilcox [42] shows that, as a general rule of thumb, it is best to take $\alpha=2\pi/T$. Using this rule, the author has determined the algorithm to be accurate to 0.1% for the first 75% of the simulation for all test functions, with some deterioration occuring after this time. This can be overcome by increasing the simulation time slightly and discarding the later data.

It should be noted that the inverse Laplace transform algorithm does not require zero-padding of the data to avoid aliasing, as is required by direct FFT methods. This is a consequence of the path along which the frequency domain data is sampled. Heuristically speaking, placing the integration path α units to the right of the imaginary axis has the equivalent effect of moving the poles of the system α units to the left, if the integration path is taken as the new imaginary axis. For example, if the frequency response has a pole at the origin, then the samples (g_m) given by Equation (2.14) would correspond to a pole at $s = -\alpha$. Consequently, the sequence g_m would contain a decaying exponential envelope, with time constant equal to $1/\alpha$. It is this envelope which suppresses the undesirable effects of aliasing. The exponential factor in Equation (2.13b) serves to remove this envelope from the final output sequence. Using the rule of thumb for determining α, we observe that the original sequence is attenuated by a factor of $e^{-2\pi} = 0.00187$ at $t = T$. Thus, aliasing contributes no more than 0.2% error to the output sequence, provided that the magnitude

of the frequency response decreases with increasing frequency or, in the worst case, remains more or less constant.

In cases where the time-domain response contains step discontinuities, it is useful to scale the frequency-domain data by a Gibbs' oscillation suppression factor, given by

$$f_k = \frac{\sin[(2k+1)\pi/2N]}{(2k+1)\pi/2N} \tag{2.18}$$

This has the equivalent effect in the time-domain of passing the signal through a finite-time integrator with time constant equal to the time between samples, as explained by Lanczos [44]. Consequently, this scaling does not affect the response where it is continuous in time, while it reduces Gibbs' oscillations considerably at discontinuities (at the expense of slightly increased rise time). Fig. 2-3 shows some time-domain responses generated by the inverse Laplace transform algorithm, both with and without the Gibbs suppression factor. The favorable effect of the scaling is obvious. Worthy of note in the figure are the rapid oscillations near the end of the time interval. These arise from the partitioning of the time-domain data into even and odd sets. The upper and lower envelopes of the oscillations represent the individual data sets if each were plotted individually. For the first 90% of the time interval, at least, the Gibbs suppression factor does a good job of ensuring that these data sets agree. Beyond this point, the data should be considered inaccurate.

2.3 One-dimensional element models

We now proceed to develop the TEM formulation for one-dimensional elements. The general equation of motion for a one-dimensional structural element can be written as

$$k_U L_x[v(x,t)] + k_T \ddot{v}(x,t) = f_d(x,t), \quad x \in [0,L], \quad t \in [0,\infty) \tag{2.19}$$

where $v(x,t)$ is a generalized displacement, $f_d(x,t)$ is a generalized distributed forcing function, L_x is a linear spatial differential operator of order n, and $\dot{(\,)}$ denotes differentiation with respect to time. The constants k_U and k_T are physical parameters related to the internal potential and kinetic

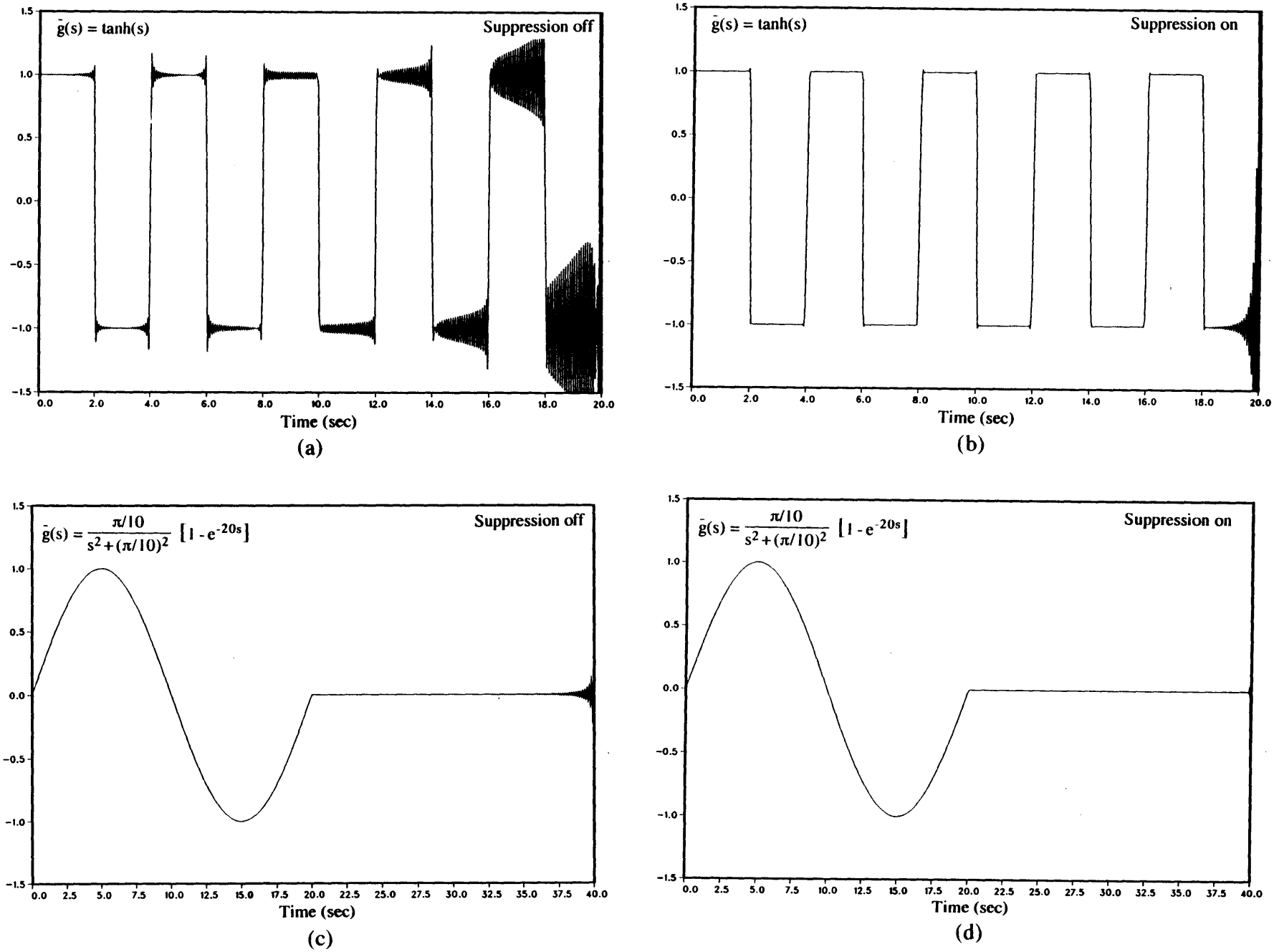

Fig. 2-3: Time domain responses generated by the inverse transform algorithm: (a) and (c): no Gibbs' suppression factor, (b) and (d): Gibbs' suppression factor used.

energy of deformation of the structural element, respectively. They can be thought of as generalized stiffness and mass parameters. The boundary conditions are as yet unspecified. The equation of motion is such that all relevant internal states (force resultants, moments, etc.) can be obtained via spatial differential operations on v(x,t).

2.3.1 Stiffness matrix formulation

For a one-dimensional element, it is possible to obtain an exact, frequency-dependent stiffness matrix relating generalized boundary forces and displacements. This is possible because the Laplace transform operation converts the partial differential equation into an ordinary differential equation, whose solution can be expressed analytically (usually in the form of transcendental functions of the complex frequency). Taking the Laplace transform of Eq. (2.19) leads to

$$L_x[\bar{v}(x,s)] + \frac{k_T}{k_U} s^2 \bar{v}(x,s) = \frac{1}{k_U}\left[\bar{f}_d(x,s) + k_T\, \dot{v}_0(x) + k_T\, s\, v_0(x)\right] \tag{2.20}$$

where s is the (generally complex-valued) Laplace variable, $\bar{(\,)}$ denotes the transform of a function, and $v_0(x)$ and $\dot{v}_0(x)$ represent the initial conditions. From this point on, the overbar on transformed functions will be assumed, so as to simplify the notation. Also, the right hand side of Eq. (2.20) will be lumped into a single function, $\tilde{f}_d(x,s)$, in the frequency-domain. This leads to

$$L_x[v(x,s)] + \frac{k_T}{k_U} s^2 v(x,s) = \tilde{f}_d(x,s) \tag{2.21}$$

We wish to express the solution to the preceeding equation in terms of generalized displacements and forces at the boundaries of the structural element. This facilitates the assembly of these structural elements into a general structural model, as will be discussed later. Thus, the general solution is expressed as

$$v(x,s) = \mathbf{v_H}(x,s)^T \mathbf{a}(s) + \int_0^L v_p(x,\xi,s)\, \tilde{f}_d(\xi,s)\, d\xi \tag{2.22}$$

where $v_H(x,s)$ is an n-vector of homogeneous solutions to Eq. (2.21) and $\mathbf{a}(s)$ is an n-vector of arbitrary constants. The Green's function, $v_p(x,\xi,s)$, corresponds to the operator $L_x + (k_T/k_U)\, s^2$ and satisfies the essential homogeneous boundary conditions at both boundaries.

We must now express the generalized boundary displacements, $\mathbf{w}(s)$, and generalized boundary forces, $\mathbf{q}(s)$, in terms of $\mathbf{a}(s)$. Since knowledge of $v(x,s)$ implies knowledge of the entire state throughout the element, these boundary conditions are obtained by simply evaluating $v(x,s)$ (and its derivatives) as given in Eq. (2.22) at the boundaries. This leads to linear relationships between the boundary states and the arbitrary constants, which can be expressed as

$$\mathbf{w}(s) = \Psi(s)\, \mathbf{a}(s) \tag{2.23}$$

and

$$\mathbf{q}(s) = \tilde{\Psi}(s)\, \mathbf{a}(s) + \mathbf{q}_d(s) \tag{2.24}$$

where $\Psi(s)$ and $\tilde{\Psi}(s)$ are n-by-n matrices, and $\mathbf{q}_d(s)$ is an n-vector arising from the integral term on the right hand side of Eq. (2.22). Because $v_p(x,\xi,s)$ satisfies (by construction) the homogeneous essential boundary conditions, there is no term in Eq. (2.23) corresponding to $\mathbf{q}_d(s)$. Combining Eqs. (2.23) and (2.24) leads to the desired relationship between the boundary forces and displacements, given by

$$\mathbf{q}(s) = \mathbf{K}(s)\, \mathbf{w}(s) + \mathbf{q}_d(s) \tag{2.25}$$

where $\mathbf{K}(s)$ is referred to as the dynamic stiffness matrix, and is given by

$$\mathbf{K}(s) = \tilde{\Psi}(s) \left[\Psi(s)\right]^{-1} \tag{2.26}$$

It should be noted that, at any complex frequency, Eq. (2.25) is mathematically exact. This is in contrast to traditional finite element stiffness matrices, which are usually derived from an approximate solution to the equation of motion describing the dynamics of the structural element.

2.3.2 Interpolation

The exact representation of the structural element model is not restricted to the boundary forces and displacements. In addition, the internal states of the element at an arbitrary location can be computed exactly. This is accomplished by first expressing the n-dimensional internal state vector, $\mathbf{u}(x,s)$, in terms of $v(x,s)$:

$$^{I}\mathbf{u}(x,s) = \tilde{L}_x[v(x,s)] \tag{2.27}$$

Here, $\tilde{L}_x$ is an n-dimensional spatial differential operator vector, and the superscript $(^{I})$ indicates that the elements of $\mathbf{u}(x,s)$ are expressed with respect to an inertial frame. Making use of Eq. (2.22), we obtain

$$^{I}\mathbf{u}(x,s) = \Phi(x,s)\,\mathbf{a}(s) + \mathbf{u}_p(x,s) \tag{2.28}$$

where the following definitions have been employed:

$$\Phi(x,s) = \tilde{L}_x\left[v_H(x,s)^T\right], \quad \mathbf{u}_p(x,s) = \int_0^L \tilde{L}_x\left[v_p(x,\xi,s)\right]\,\tilde{f}_d(\xi,s)\,d\xi \tag{2.29}$$

Using Eq. (2.23) to eliminate $\mathbf{a}(s)$ yields

$$^{I}\mathbf{u}(x,s) = \Phi(x,s)\left[\Psi(s)\right]^{-1}\mathbf{w}(s) + \mathbf{u}_p(x,s) \tag{2.30}$$

Thus, the internal states are easily expressed in terms of the boundary displacements.

It is usually more desirable to express the internal states in a frame fixed to one of the boundaries of the structural element. This is useful, for example, if the structure is undergoing a rigid motion in addition to experiencing internal deformation. Expressing the internal states with respect to such a frame would then indicate the amount of internal structural deformation only, rather than the absolute internal displacements and rotations. The internal generalized forces are invariant with respect to the coordinate frame used and are therefore not affected by this change of

reference. The general linearized relationship between the state vector expressed in the two frames is given by

$$\mathbf{u}(x,s) = {}^{I}\mathbf{u}(x,s) - \Theta(x)\,\mathbf{w}(s) \tag{2.31}$$

where $\mathbf{u}(x,s)$ is the state vector expressed in the moving frame and $\Theta(x)$ is an n-by-n matrix which is independent of frequency. Collecting the previous two equations yields

$$\mathbf{u}(x,s) = \Gamma(x,s)\,\mathbf{w}(s) + \mathbf{u}_p(x,s) \tag{2.32}$$

where

$$\Gamma(x,s) = \begin{bmatrix} \gamma_1(x,s)^T \\ \vdots \\ \gamma_n(x,s)^T \end{bmatrix} = \Phi(x,s)\left[\Psi(s)\right]^{-1} - \Theta(x) \tag{2.33}$$

A particular element of the internal state vector is then given by

$$u_i(x,s) = \gamma_i(x,s)^T\,\mathbf{w}(s) + u_{p_i}(x,s) \tag{2.34}$$

The interpolation matrix, Γ, is analogous to the set of interpolation functions used in finite element analysis. In either case, once the boundary displacements have been determined, the internal states are interpolated using these functions. For example, a Bernoulli-Euler beam finite element has as its interpolation functions the four cubic splines. In the static case, when loads are restricted to the boundary points, these cubics are mathematically exact. However, for dynamic analysis, they only approximately satisfy the beam equation. In contrast, Γ satisfies the underlying equation of motion at all frequencies, and indeed reduces to the cubic spline functions as the complex frequency approaches zero. Thus, once the generalized displacements at the boundaries are known, it is a simple matter to obtain the internal states. Once again, the formulation is mathematically exact, and no modal truncation or finite element approximations have been made.

2.3.3 Internal energy formulation

A useful scalar measure of the state of deformation of a flexible element is the total energy due to deformation. It is particularly useful in control applications, as it is a quadratic function of deformation amplitude and is therefore well suited for linear quadratic regulator problems. For finite element models, the internal energy for the system (or for an element) is obtained by pre- and post-multiplying the global (or local) stiffness matrix by the global (or local) displacement vector. Such a direct procedure is not available in the TEM representation. Consequently, the exact representation is sometimes replaced by an equivalent finite-order system for which parameters such as natural frequency and damping ratio may be determined. For steady-state sinusoidal motion, the approximate energy is then easily expressed in terms of these parameters. The work of Hagood and Crawley [45] takes this approach. However, in an effort to retain the mathematically exact representation of the dynamics of the individual structural elements, an alternative approach is presented here. The goal in this case, rather that to derive an approximate finite-order working model, is to obtain an expression for the internal energy at a prescribed time (in terms of a frequency-domain integral) which can be used for transient analysis.

The internal energy within a particular structural element is obtained by integrating the sum of the potential and kinetic energy densities over the length of the element. This leads to an expression of the form

$$E(t) = \frac{1}{2}\int_0^L \left[k_U u_U^2(x,t) + k_T \dot{u}_T^2(x,t) \right] dx \qquad (2.35)$$

where E(t) is the internal energy at time t, and $u_U(x,t)$ and $u_T(x,t)$ are components of the internal state vector related to the potential and kinetic energies, respectively. (For a Bernoulli-Euler beam, u_U would be the curvature, since it is directly related to internal bending energy, while u_T would be the transverse displacement.) Note that these components are now expressed in the time-domain. In order that the internal deformational energy be independent of rigid motion, it is imperative that $u_T(x,t)$ be expressed with respect to one of the boundaries of the element, as described in the

previous section. The second term in Eq. (2.35) then corresponds to the component of the kinetic energy associated with the relative deformation rate of the structural element, and excludes energy associated with rigid translational and rotational velocities.

The terms $u_U(x,t)$ and $u_T(x,t)$ are now expressed as the inverse Laplace transforms of the corresponding frequency-domain functions. This is accomplished via Eq. (2.5) and leads to

$$E(t) = \frac{k(t)}{2}\int_0^L \left\{ k_U \left(\int_{-\infty}^{\infty} \bar{u}_U(x,s)\, e^{j\omega t} d\omega \right)^2 + k_T \left(\int_{-\infty}^{\infty} s\ \bar{u}_T(x,s)\, e^{j\omega t} d\omega \right)^2 \right\} dx \qquad (2.36)$$

where

$$k(t) = \frac{e^{2\alpha t}}{4\pi^2} \qquad (2.37)$$

We seek an exact expression for the total energy of deformation. It is therefore necessary to replace the squared integrals with double integrals, so that the order of integration with respect to space and frequency may be reversed. This makes it possible to perform the spatial integration analytically. Thus, by writing each inverse transform integral next to itself, using different dummy variables of integration, and grouping the integrals together, we obtain

$$E(t) = \frac{k(t)}{2}\int_0^L \left\{ k_U \int_{-\infty}^{\infty}\int_{-\infty}^{\infty} u_U(x,s_1)\, u_U(x,s_2)\, e^{j(\omega_1+\omega_2)t} d\omega_1\, d\omega_2 \right.$$

$$\left. + k_T \int_{-\infty}^{\infty}\int_{-\infty}^{\infty} s_1\, s_2\, u_T(x,s_1)\, u_T(x,s_2)\, e^{j(\omega_1+\omega_2)t} d\omega_1\, d\omega_2 \right\} dx \qquad (2.38)$$

where

$$s_i = \alpha + j\omega_i \qquad (2.39)$$

For simplicity, we have assumed that the initial conditions are zero and that no distributed forcing occurs in the interior of the element. Interchanging the order of the spatial and frequency integrations in Eq. (2.38) yields

$$E(t) = \frac{k(t)}{2} \int_{-\infty}^{\infty}\int_{-\infty}^{\infty} \Big\{ k_U \int_0^L u_U(x,s_1)\, u_U(x,s_2)\, dx$$

$$+ k_T s_1 s_2 \int_0^L u_T(x,s_1)\, u_T(x,s_2)\, dx \Big\}\, e^{j(\omega_1+\omega_2)t}\, d\omega_1\, d\omega_2 \qquad (2.40)$$

We are now able to express the spatial integrals in terms of the boundary displacements. Making use of Eq. (2.34) leads to

$$\int_0^L u_i(x,s_1)\, u_i(x,s_2)\, dx = \mathbf{w}(s_1)^T \Xi_i(s_1,s_2)\, \mathbf{w}(s_2) \qquad (2.41)$$

where

$$\Xi_i(s_1,s_2) = \int_0^L \gamma_i(x,s_1)\, \gamma_i(x,s_2)^T\, dx \qquad (2.42)$$

Since $\gamma_U(x,s_1)$ and $\gamma_T(x,s_1)$ are expressed analytically, the matrices $\Xi_U(s_1,s_2)$ and $\Xi_T(s_1,s_2)$ can also be computed exactly at each frequency. Finally, substituting Eq. (2.41) into Eq. (2.40) yields

$$E(t) = \frac{k(t)}{2} \int_{-\infty}^{\infty}\int_{-\infty}^{\infty} \mathbf{w}(s_1)^T\, \Xi(s_1,s_2)\, \mathbf{w}(s_2)\, e^{j(\omega_1+\omega_2)t}\, d\omega_1\, d\omega_2 \qquad (2.43)$$

where

$$\Xi(s_1,s_2) = k_U \Xi_U(s_1,s_2) + k_T s_1 s_2 \Xi_T(s_1,s_2) \qquad (2.44)$$

Thus, given the boundary displacements in the frequency-domain, the energy of deformation is computable via a double integral. For general motions, an analytical solution does not exist, and E(t) must be computed numerically. The computation time is reduced by a factor of two by exploiting the following symmetry properties of Ξ:

$$\left.\begin{aligned} \Xi(s_2,s_1) &= \Xi(s_1,s_2)^T \\ \Xi(s_1^*,s_2) &= \Xi(s_1,s_2^*)^* \end{aligned}\right\} \qquad (2.45b,c)$$

Using these properties makes it possible to reduce the integral to

$$E(t) = k(t) \int_0^\infty \int_0^\infty \left[w(s_1)^T \Xi(s_1,s_2)\, w(s_2)\, e^{j(\omega_1+\omega_2)t} + w(s_1)^T \Xi(s_1,s_2^*)\, w(s_2)^*\, e^{j(\omega_1-\omega_2)t} \right] d\omega_1\, d\omega_2 \qquad (2.46)$$

In the actual implementation of this formula, the integrals are replaced with summations, the upper limits are replaced with finite frequencies, and a simple midpoint rule algorithm is invoked.

2.3.4 Axial rod example

We first consider a uniform rod constrained to deform axially, as shown in Fig. 2-4. For this element, the simplest model that describes its dynamic behavior is the wave equation, given by

$$-EA \frac{\partial^2}{\partial x^2} v(x,t) + \rho A \ddot{v}(x,t) = f_d(x,t) \qquad (2.47)$$

where v represents the axial deflection of the cross section, A is the cross sectional area, and ρ and E are the material density and modulus of elasticity, respectively. Implicit in this model is the assumption that the deformation of the element is uniform across the cross section. Also, Poisson's ratio effects are ignored. The internal state at any location, x, is therefore completely characterized by two components:

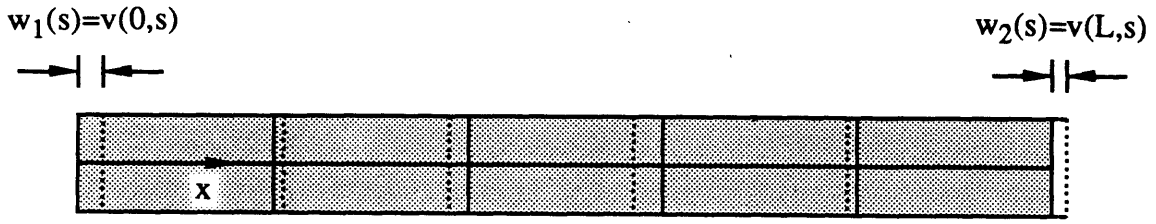

Fig. 2-4: Axial rod model. Deformation is uniform over cross-section.

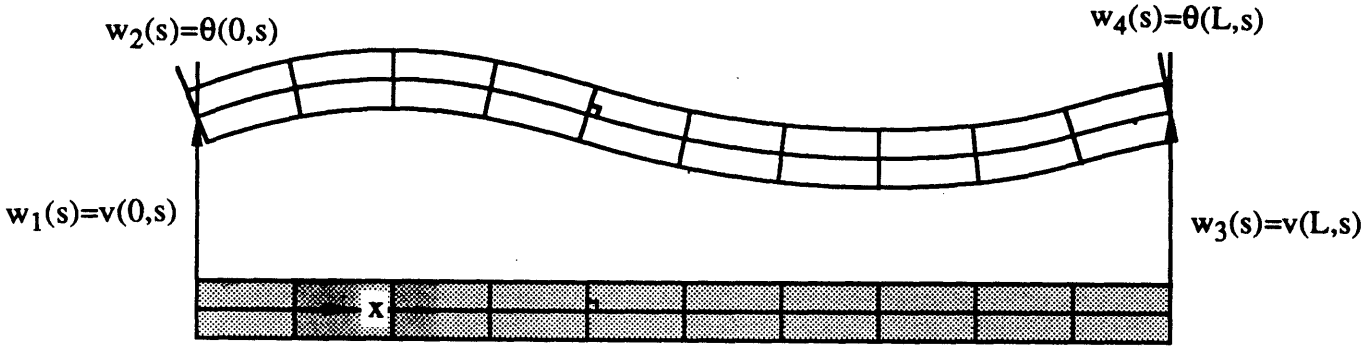

Fig. 2-5: Bernoulli-Euler beam model. Planar cross sections remain planar and perpendicular to deformed beam axis.

$$\mathbf{u}(x,s) = \begin{bmatrix} v(x,s) \\ F(x,s) \end{bmatrix} = \begin{bmatrix} 1 \\ EA\frac{\partial}{\partial x} \end{bmatrix} v(x,s) \tag{2.48}$$

Here, F represents the net force resultant within the rod. The generalized boundary forces and displacements are just these quantities evaluated at x=0 and x=L:

$$\mathbf{w}(s) = \begin{bmatrix} v(0,s) \\ v(L,s) \end{bmatrix}, \quad \mathbf{q}(s) = \begin{bmatrix} -F(0,s) \\ F(L,s) \end{bmatrix} = \begin{bmatrix} -EA\frac{\partial}{\partial x}v(0,s) \\ EA\frac{\partial}{\partial x}v(L,s) \end{bmatrix} \tag{2.49a,b}$$

The homogeneous solution vector is simply

$$\mathbf{v}_H(x,s)^T = \left[e^{\beta x}\ e^{-\beta x}\right], \quad \beta = \sqrt{\frac{\rho}{E}}\,s \tag{2.50}$$

and the Green's function kernel is

$$v_p(x,\xi,s) = \begin{cases} \dfrac{\sinh\beta(L-\xi)}{\beta\sinh\beta L}\sinh\beta x & x \le \xi \\ \dfrac{\sinh\beta\xi}{\beta\sinh\beta L}\sinh\beta(L-x) & x > \xi \end{cases} \tag{2.51}$$

Equations (2.49a,b) and (2.50) can be combined to determine the dynamic stiffness matrix, which is given by

$$\mathbf{K}(s) = \frac{EA\beta}{\sinh\beta L}\begin{bmatrix} \cosh\beta L & -1 \\ -1 & \cosh\beta L \end{bmatrix} \tag{2.52}$$

As expected, the elements of **K** are transcendental functions of the complex frequency. Also, this stiffness matrix reduces to the finite element static stiffness matrix for the axial rod in the limit as s approaches zero. The effects of initial conditions and distributed forcing are computed via

$$\mathbf{q}_d(s) = -\frac{EA}{\sinh\beta L}\int_0^L \begin{bmatrix} \sinh\beta(L-x) \\ \sinh\beta x \end{bmatrix} \tilde{f}_d(x,s)\,dx \tag{2.53}$$

and the interpolation matrix used to determine internal states is given by

$$\Gamma(s) = \frac{1}{\sinh\beta L}\begin{bmatrix} \sinh\beta(L-x) & \sinh\beta x \\ -\beta\cosh\beta(L-x) & \beta\cosh\beta x \end{bmatrix} - \begin{bmatrix} 1 & 0 \\ 0 & 0 \end{bmatrix} \tag{2.54}$$

The internal energy matrices are quite complex, but they are nonetheless expressible in an analytical form. The kinetic energy kernel can be expressed as the sum of the following four matrices:

$$\Xi_T(s_1,s_2) = \frac{1}{\Delta_1\Delta_2}\Lambda(\beta_1)^T\begin{bmatrix} F(\beta_1+\beta_2) & F(\beta_1-\beta_2) \\ F(-\beta_1+\beta_2) & F(-\beta_1-\beta_2)\end{bmatrix}\Lambda(\beta_2) + \begin{bmatrix} L & 0 \\ 0 & 0\end{bmatrix}$$

$$- \frac{1}{\Delta_1}\Lambda(\beta_1)^T\begin{bmatrix} F(\beta_1) & 0 \\ F(-\beta_1) & 0\end{bmatrix} - \frac{1}{\Delta_2}\begin{bmatrix} F(\beta_2) & F(-\beta_2) \\ 0 & 0\end{bmatrix}\Lambda(\beta_2) \qquad (2.55)$$

while the potential energy kernel is given by

$$\Xi_U(s_1,s_2) = \frac{\beta_1\beta_2}{\Delta_1\Delta_2}\Lambda(\beta_1)^T\begin{bmatrix} F(\beta_1+\beta_2) & -F(\beta_1-\beta_2) \\ -F(-\beta_1+\beta_2) & F(-\beta_1-\beta_2)\end{bmatrix}\Lambda(\beta_2) \qquad (2.56)$$

where the following definitions have been made:

$$\Lambda(\beta) = \begin{bmatrix} -e^{-\beta L} & 1 \\ e^{\beta L} & -1\end{bmatrix} \qquad (2.57a)$$

$$\Delta_i = 2\sinh\beta_i L \qquad (2.57b)$$

$$\beta_i = \sqrt{\frac{\rho}{E}}\, s_i \qquad (2.57c)$$

$$F(\beta) = \frac{1}{\beta}\left[e^{\beta L} - 1\right] \qquad (2.57d)$$

It is clear that, for even the simplest of structural element models, the internal energy expressions become quite complex. However, this is to be expected, as the energy is a quadratic function of deflection amplitude, and represents an integrated effect over the entire domain of the element.

The preceeding expressions for the stiffness and interpolation matrices are well suited for numerical computation, provided that the dimensionless complex frequency at which they are evaluated is neither too large nor too small in magnitude. For these extreme situations, numerical accuracy and overflow errors become issues. These problems are readily handled by using asymptotic approximations to the stiffness and interpolation matrices. A low frequencies, the

approximations are obtained by replacing the trigonometric and hyperbolic functions with appropriate series expansions, and truncating higher order terms. At high frequencies, the trigonometric functions are replaced by their (complex) exponential forms. A growing exponential is factored out of the numerator and denominator of each term, leaving an expression which involves only decaying exponentials. It should be noted that this asymptotic approximation cannot be made with all frequency-domain representations. Because the TEM approach involves interpolation between element boundaries, the interpolation functions are always bounded and well-behaved.

2.3.5 Bernoulli-Euler beam example

For bending elements, the simplest model is the Bernoulli-Euler beam, shown schematically in Fig. 2-5. The basic assumptions of the model are that planar cross sections of the beam remain planar and normal to the center-line after deformation, and that differential cross sections have negligible rotary inertia. Under these assumptions, the equation of motion becomes

$$EI\frac{\partial^4}{\partial x^4}v(x,t) + \rho A\ddot{v}(x,t) = f_d(x,t) \tag{2.58}$$

where v is the transverse deflection, E and ρ are the modulus of elasticity and density of the material, respectively, and A and I are the cross sectional area and moment of inertia, respectively. Taking the Laplace transform, we obtain

$$\frac{\partial^4}{\partial x^4}v(x,s) - \alpha^4 v(x,s) = \tilde{f}_d(x,s), \quad \alpha^4 = -\frac{\rho A s^2}{EI} \tag{2.59a,b}$$

For this element, the structural state vector has four elements, given by

$$^{I}\mathbf{u}(x,s) = \begin{bmatrix} v(x,s) \\ \theta(x,s) \\ M(x,s) \\ S(x,s) \end{bmatrix} = \begin{bmatrix} 1 \\ \frac{\partial}{\partial x} \\ EI\frac{\partial^2}{\partial x^2} \\ -EI\frac{\partial^3}{\partial x^3} \end{bmatrix} v(x,s) \tag{2.60}$$

where θ is the rotation of the cross section, and M and S are the internal moment and shear resultants, respectively. The generalized boundary displacements and forces are then

$$\mathbf{w}(s) = \begin{bmatrix} v(0,s) \\ \theta(0,s) \\ v(L,s) \\ \theta(L,s) \end{bmatrix} = \begin{bmatrix} v(0,s) \\ \frac{\partial}{\partial x} v(0,s) \\ v(L,s) \\ \frac{\partial}{\partial x} v(L,s) \end{bmatrix}, \quad \mathbf{q}(s) = \begin{bmatrix} -S(0,s) \\ -M(0,s) \\ S(L,s) \\ M(L,s) \end{bmatrix} = \begin{bmatrix} EI \frac{\partial^3}{\partial x^3} v(0,s) \\ -EI \frac{\partial^2}{\partial x^2} v(0,s) \\ -EI \frac{\partial^3}{\partial x^3} v(L,s) \\ EI \frac{\partial^2}{\partial x^2} v(L,s) \end{bmatrix} \tag{2.61a,b}$$

The homogeneous solution vector contains four elements as well, and is given by

$$\mathbf{v}_H(x,s)^T = \begin{bmatrix} e^{\alpha x} & e^{-\alpha x} & e^{j\alpha x} & e^{-j\alpha x} \end{bmatrix} \tag{2.62}$$

and the Green's function kernel follows as:

$$v_p(x,\xi,s) = \begin{cases} \dfrac{g_1(\xi,s)\, S^-(\alpha x) + g_2(\xi,s)\, C^-(\alpha x)}{4\alpha^3 (1 - ch\ ct)} & x \le \xi \\ \dfrac{g_3(\xi,s)\, S^-(\alpha(L-x)) + g_4(\xi,s)\, C^-(\alpha(L-x))}{4\alpha^3 (1 - ch\ ct)} & x > \xi \end{cases} \tag{2.63}$$

where

$$g_1(\xi,s) = -C^+(\alpha\xi) + ch\cos(\alpha(L-\xi)) - sh\sin(\alpha(L-\xi)) + ct\cosh(\alpha(L-\xi)) + st\sinh(\alpha(L-\xi)) \tag{2.64a}$$

$$g_2(\xi,s) = S^+(\alpha\xi) + ch\sin(\alpha(L-\xi)) - sh\cos(\alpha(L-\xi)) + ct\sinh(\alpha(L-\xi)) - st\cosh(\alpha(L-\xi)) \tag{2.64b}$$

$$g_3(\xi,s) = -C^+(\alpha(L-\xi)) + ch\cos(\alpha\xi) - sh\sin(\alpha\xi) + ct\cosh(\alpha\xi) + st\sinh(\alpha\xi) \tag{2.64c}$$

$$g_4(\xi,s) = S^+(\alpha(L-\xi)) + ch\sin(\alpha\xi) - sh\cos(\alpha\xi) + ct\sinh(\alpha\xi) - st\cosh(\alpha\xi) \tag{2.64d}$$

and the following trigonometric definitions have been made:

$$\begin{aligned} C^+(\alpha\xi) &= \cosh(\alpha\xi) + \cos(\alpha\xi) & C^-(\alpha\xi) &= \cosh(\alpha\xi) - \cos(\alpha\xi) \\ S^+(\alpha\xi) &= \sinh(\alpha\xi) + \sin(\alpha\xi) & S^-(\alpha\xi) &= \sinh(\alpha\xi) - \sin(\alpha\xi) \\ ch &= \cosh(\alpha L) & ct &= \cos(\alpha L) \\ sh &= \sinh(\alpha L) & st &= \sin(\alpha L) \end{aligned} \tag{2.65a-h}$$

For the beam element, the stiffness matrix is four-by-four, and is expressed as

$$\mathbf{K}(s) = \frac{EI}{\Delta(s)} \begin{bmatrix} K_6(s) & K_4(s) & -K_5(s) & K_3(s) \\ K_4(s) & K_2(s) & -K_3(s) & K_1(s) \\ -K_5(s) & -K_3(s) & K_6(s) & -K_4(s) \\ K_3(s) & K_1(s) & -K_4(s) & K_2(s) \end{bmatrix} \tag{2.66}$$

where

$$
\begin{aligned}
K_1(s) &= \frac{1}{\alpha^3}(sh - st) \\
K_2(s) &= \frac{1}{\alpha^3}(ch\ st - sh\ ct) \\
K_3(s) &= \frac{1}{\alpha^2}(ch - ct) \\
K_4(s) &= \frac{1}{\alpha^2} sh\ st \\
K_5(s) &= \frac{1}{\alpha}(sh + st) \\
K_6(s) &= \frac{1}{\alpha}(ch\ st + sh\ ct) \\
\Delta(s) &= \frac{1}{\alpha^4}(1 - ch\ ct)
\end{aligned}
\qquad (2.67a\text{-}g)
$$

This stiffness matrix also reduces to the static, finite element stiffness matrix as the complex frequency approaches zero. The effects of distributed forcing and initial conditions are determined via

$$
q_d(s) = \frac{EI}{2\alpha(1\text{-}chct)} \int_0^L \begin{bmatrix} \alpha\, g_1(x,s) \\ -\, g_2(x,s) \\ \alpha\, g_3(x,s) \\ g_4(x,s) \end{bmatrix} \tilde{f}_d(x,s)\, dx \qquad (2.68)
$$

and the interpolation matrix is most easily expressed by

$$
\Gamma(x,s) = \Phi(x,s)\left[\Psi(s)\right]^{-1} - \begin{bmatrix} 1 & x & 0 & 0 \\ 0 & 1 & 0 & 0 \\ 0 & 0 & 0 & 0 \\ 0 & 0 & 0 & 0 \end{bmatrix} \qquad (2.69)
$$

where

$$
\Phi(x,s) = \begin{bmatrix} e^{\alpha x} & e^{-\alpha x} & e^{j\alpha x} & e^{-j\alpha x} \\ \alpha e^{\alpha x} & -\alpha e^{-\alpha x} & j\alpha e^{j\alpha x} & -j\alpha e^{-j\alpha x} \\ EI\alpha^2 e^{\alpha x} & EI\alpha^2 e^{-\alpha x} & -EI\alpha^2 e^{j\alpha x} & -EI\alpha^2 e^{-j\alpha x} \\ -EI\alpha^3 e^{\alpha x} & EI\alpha^3 e^{-\alpha x} & jEI\alpha^3 e^{j\alpha x} & -jEI\alpha^3 e^{-j\alpha x} \end{bmatrix} \qquad (2.70)
$$

and

$$\left[\Psi(s)\right]^{-1} = \frac{1}{4\alpha(1 - \text{ch ct})}\begin{bmatrix} \alpha p_1 & p_2 & \alpha p_4 & p_3 \\ \alpha e^{\alpha L} p_4 & -e^{\alpha L} p_3 & \alpha e^{\alpha L} p_1 & -e^{\alpha L} p_2 \\ \alpha p_5 & -jp_6 & \alpha p_8 & -jp_7 \\ \alpha e^{j\alpha L} p_8 & j e^{j\alpha L} p_7 & \alpha e^{j\alpha L} p_5 & j e^{j\alpha L} p_6 \end{bmatrix} \tag{2.71}$$

In this last equation, the following definitions have been used:

$$\begin{aligned} p_1 &= 1 - e^{-\alpha L}(ct - st) & p_5 &= 1 - e^{-j\alpha L}(ch - jsh) \\ p_2 &= 1 - e^{-\alpha L}(ct + st) & p_6 &= 1 - e^{-j\alpha L}(ch + jsh) \\ p_3 &= e^{-\alpha L} - (ct - st) & p_7 &= e^{-j\alpha L} - (ch - jsh) \\ p_4 &= e^{-\alpha L} - (ct + st) & p_8 &= e^{-j\alpha L} - (ch + jsh) \end{aligned} \tag{2.72}$$

As was the case with the axial rod, the expressions for the internal energy of deformation are complex, but nonetheless expressible analytically. The potential energy matrix is

$$\Xi_U(s_1,s_2) = \alpha_1^2\alpha_2^2\,\Psi(s_1)^{-T}\begin{bmatrix} F(\beta_1) & F(\beta_2) & -F(\beta_3) & -F(\beta_4) \\ F(-\beta_2) & F(-\beta_1) & -F(-\beta_4) & -F(-\beta_3) \\ -F(j\beta_4) & -F(j\beta_3) & F(j\beta_1) & F(j\beta_2) \\ -F(-j\beta_3) & -F(-j\beta_4) & F(-j\beta_2) & F(-j\beta_1) \end{bmatrix}\Psi(s_2)^{-1} \tag{2.73}$$

while the kinetic energy matrix is

$$\begin{aligned} \Xi_T(s_1,s_2) = {} & \Psi(s_1)^{-T}\begin{bmatrix} F(\beta_1) & F(\beta_2) & F(\beta_3) & F(\beta_4) \\ F(-\beta_2) & F(-\beta_1) & F(-\beta_4) & F(-\beta_3) \\ F(j\beta_4) & F(j\beta_3) & F(j\beta_1) & F(j\beta_2) \\ F(-j\beta_3) & F(-j\beta_4) & F(-j\beta_2) & F(-j\beta_1) \end{bmatrix}\Psi(s_2)^{-1} + \begin{bmatrix} L & \frac{1}{2}L^2 & 0 & 0 \\ \frac{1}{2}L^2 & \frac{1}{6}L^3 & 0 & 0 \\ 0 & 0 & 0 & 0 \\ 0 & 0 & 0 & 0 \end{bmatrix} \\ & - \Psi(s_1)^{-T}\begin{bmatrix} F(\alpha_1) & G(\alpha_1) & 0 & 0 \\ F(-\alpha_1) & G(-\alpha_1) & 0 & 0 \\ F(j\alpha_1) & G(j\alpha_1) & 0 & 0 \\ F(-j\alpha_1) & G(-j\alpha_1) & 0 & 0 \end{bmatrix} - \begin{bmatrix} F(\alpha_2) & F(-\alpha_2) & F(j\alpha_2) & F(-j\alpha_2) \\ G(\alpha_2) & G(-\alpha_2) & G(j\alpha_2) & G(-j\alpha_2) \\ 0 & 0 & 0 & 0 \\ 0 & 0 & 0 & 0 \end{bmatrix}\Psi(s_2)^{-1} \end{aligned} \tag{2.74}$$

where

$$G(\beta) = \frac{L}{\beta}e^{\beta L} + \frac{1}{\beta^2}\left[1 - e^{\beta L}\right] \tag{2.75}$$

and

$$\begin{aligned} \beta_1 &= \alpha_1 + \alpha_2 \\ \beta_2 &= \alpha_1 - \alpha_2 \\ \beta_3 &= \alpha_1 + j\alpha_2 \\ \beta_4 &= \alpha_1 - j\alpha_2 \\ \alpha_i^4 &= -\frac{\rho A}{EI} s_i^2 \end{aligned} \tag{2.76}$$

As was the case for the axial rod, high and low frequency asymptotic approximations are required for the beam element as well. These approximations allow efficient numerical computation of the required quantities without sacrificing numerical accuracy.

2.3.6 Higher order elements

In many cases, the simple axial rod and Bernoulli-Euler beam models are insufficient to capture the high frequency characteristics of the structural system. This is particularly noticeable when analyzing the wave-like propagation of energy associated with impulsive disturbance sources. For these situations, more accurate structural models are required.

The simple axial rod model presented in Section 2.3.4 predicts dispersion-free propagation of elastic waves at all frequencies. We know from experience, however, that the propagation of axial stress waves through rods is always dispersive to some degree. For certain applications we may wish to introduce this phenomenon into the mathematical model in order that the simulated response be more realistic, in a manner that reflects the physics of the rod element to some degree. For rods of circular cross section, this can be achieved if a radial degree of freedom is introduced, as shown in Fig. 2-6. This is the basis for the Mindlin-Herrmann axial rod theory, which can be expressed mathematically by the following system:

$$-a^2(\lambda+2G)\frac{\partial^2}{\partial x^2} v_1(x,s) + \rho a^2 s^2 v_1(x,s) = 2a\lambda \frac{\partial}{\partial x} v_2(x,s) \tag{2.77a}$$

$$a^2\kappa^2 G \frac{\partial^2}{\partial x^2} v_2(x,s) - \left[8\kappa_1^2(\lambda+G) + \rho a^2 s^2\right] v_2(x,s) = 4a\kappa_1^2\lambda \frac{\partial}{\partial x} v_1(x,s) \tag{2.77b}$$

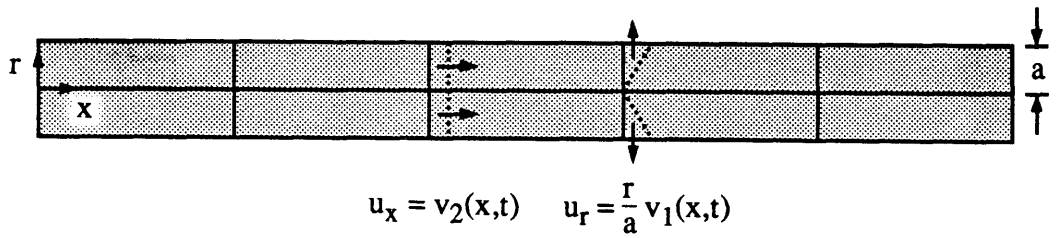

Fig. 2-6: Mindlin-Herrmann rod model. Two deformational degrees of freedom are allowed. Poisson's ratio couples axial and radial deformation modes.

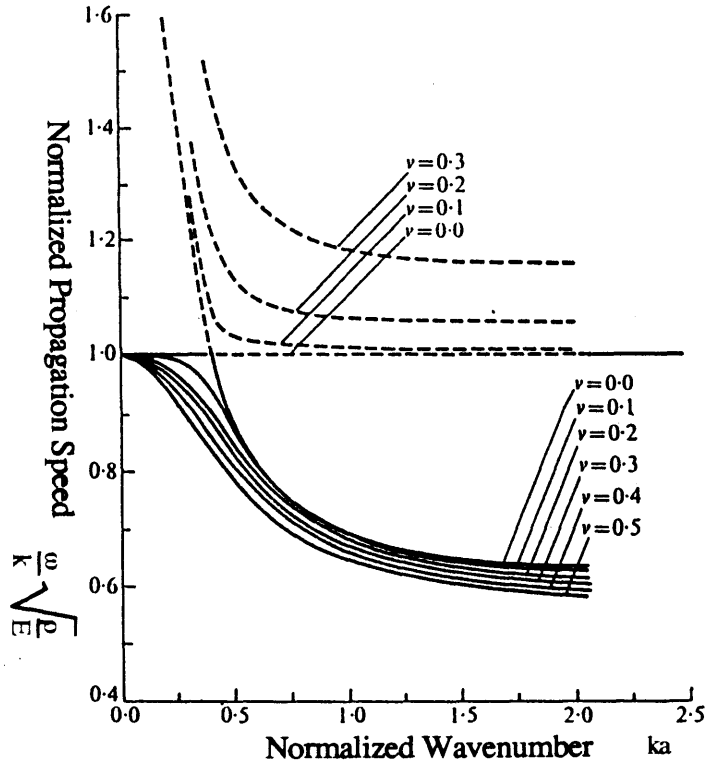

Fig. 2-7: Dispersion curves associated with the Mindlin-Herrmann model.

In these equations, v_1 and v_2 are the axial and radial displacements, respectively, a represents the radius of the rod, λ and G are the Lame constants of the material, and κ and κ_1 are empirically determined parameters. This model yields the dispersion curves shown in Fig. 2-7, and reproduces the dispersion characteristics of the rod more accurately than the simple rod model. The modified stiffness matrix for the Mindlin-Herrmann model is given in Appendix A.

A more realistic beam model is the Timoshenko beam, shown in Fig. 2-8. This model allows for shearing of the cross sections with respect to the center-line of the beam, and accounts for rotary inertia. The equation of motion is given by

$$EI\frac{\partial^4}{\partial x^4}v(x,t) + \rho A\ddot{v}(x,t) - \rho I\left[1+\frac{Ek}{G}\right]\frac{\partial^2}{\partial x^2}\ddot{v}(x,t) + \frac{\rho^2 Ik}{G}\ddot{\ddot{v}}(x,t) = f_d(x,t) \qquad (2.78)$$

where G is the shear modulus of the material and k is an empirically determined correction factor. The Timoshenko model is capable of supporting both a shear and a bending mode of propagation, as shown in the dispersion curves in Fig. 2-9. This model also places a finite upper limit on the flexural propagation speed, which is unrealistically unbounded in the Bernoulli-Euler model. While the enhanced equation of motion may not significantly reduce modelling error, it does introduce these physically realistic characteristics into the model in a manner motivated by physical arguments. Details on the stiffness matrix for the Timoshenko model are presented in Appendix A.

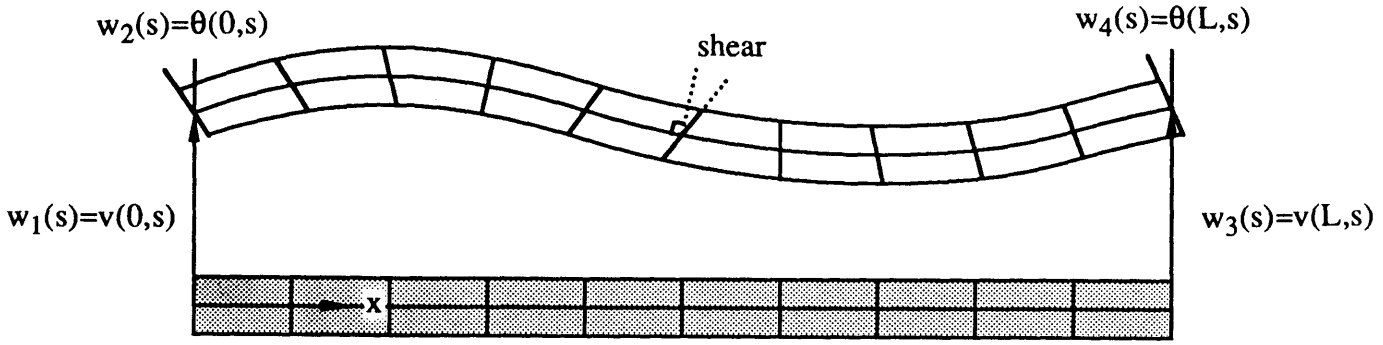

Fig. 2-8: Timoshenko beam model. Shearing of cross-sections is allowed, and cross-section rotary inertia is modelled.

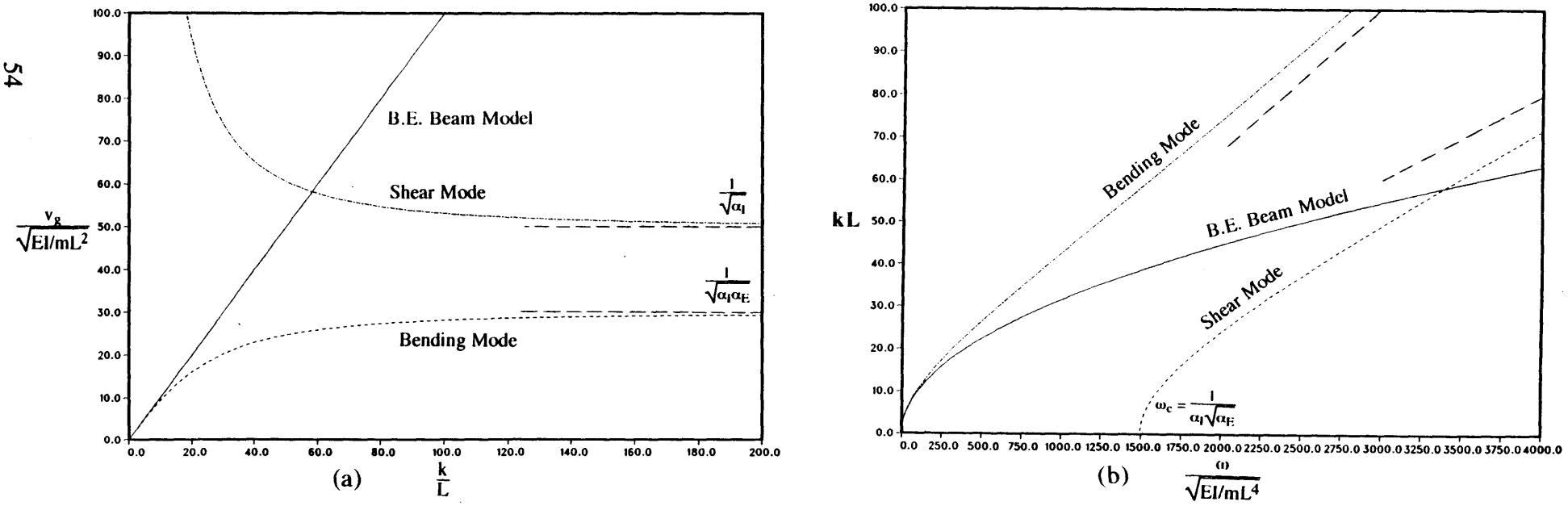

Fig. 2-9: Timoshenko beam dispersion characteristics (α_I=4x10^{-4}, α_E=2.8): (a) Dispersion curves, (b) Frequency spectrum.

2.4 Two-dimensional elements

Two dimensional elements are modelled using partial differential equations with three independent variables (two spatial dimensions and time). Therefore, the modelling of two-dimensional elements using the TEM methodology cannot produce mathematically exact results, as was the case for one-dimensional models. The reason is that the dynamics equation remains a partial differential equation in two spatial variables after the Laplace transform operation. As a result, there exist an infinity of homogeneous solutions for any particular element model. To this infinite set, there corresponds an infinity of points along the boundary (which spans a one-dimensional domain) on which boundary conditions must be satisfied. Nevertheless, by using a sufficiently large number of homogeneous solutions and considering only a sufficiently large, but finite, set of boundary points, an accurate TEM solution is possible. An example of boundary discretization, for the case of in-plane deformation, is shown in Fig. 2-10. It is conjectured that, for a given amount of computational capability, this approach yields results superior in accuracy to the traditional FEM methodology. In the following sections, we consider two two-dimensional elements: a plate bending element and a plane stress element. However, we first study a special case of a two-dimensional element, where application of the TEM approach does indeed yield an ordinary differential equation.

2.4.1 Axisymmetric Elements

When both the geometry of and the forcing on a two-dimensional element are axisymmetric, it is possible to reduce the spatial dependence of the problem to one dimension. This is accomplished by using polar coordinates. As an example, consider a flexible membrane of uniform thickness under a uniform tension, T. Its equation of motion is

$$T \nabla^2 v(r,\theta,t) = m \ddot{v}(r,\theta,t) - f(r,\theta,t) \tag{2.79}$$

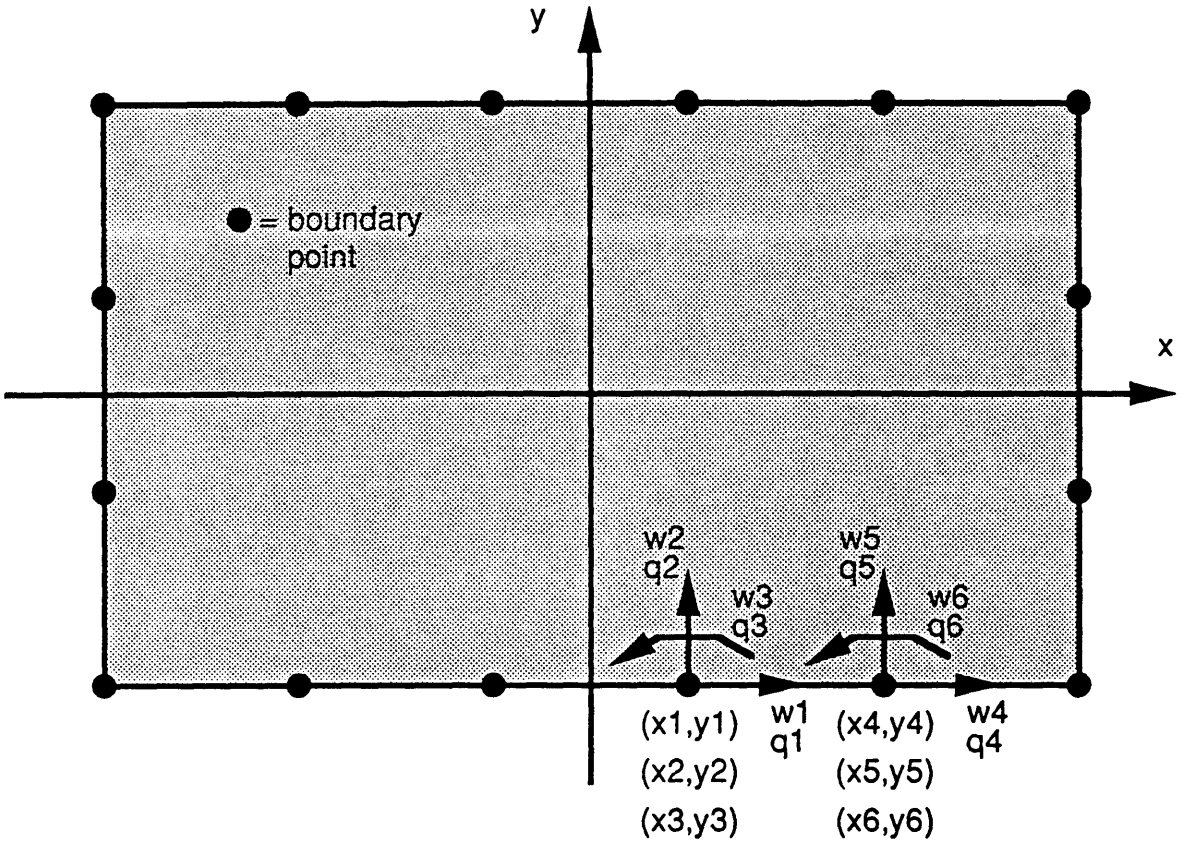

Fig. 2-10: Typical two-dimensional element with three generalized displacements and forces at each boundary point. In-plane deformation is assumed. The numbering scheme shown continues along the entire boundary of the element.

where m is the density per unit area of the membrane and f is the distributed applied transverse force. Assuming axial symmetry and taking the Laplace transform of both sides of the equation, we obtain

$$r^2 \frac{\partial^2}{\partial r^2} \bar{v}(r,s) + r \frac{\partial}{\partial r} \bar{v}(r,s) + (\alpha r)^2 \bar{v}(r,s) = -\frac{r^2}{T} \bar{f}(r,s) \tag{2.80}$$

where

$$\alpha^2 = -\frac{ms^2}{T} \tag{2.81}$$

As observed earlier, the initial conditions can be lumped in with the forcing function if they are nonzero. This ODE has the homogeneous solution

$$\bar{v}_h(r,s) = A(s)\, J_0(\alpha r) + B(s)\, Y_0(\alpha r) \tag{2.82}$$

where J_0 and Y_0 are Bessel functions of order zero, and A and B are arbitrary constants. To obtain the complete solution, which includes the effects of forcing, we utilize the method of variation of parameters, letting both A and B vary as functions of r. We then substitute the modified homogeneous solution into the equation of motion, differentiating as needed. By construction, many terms cancel, and we are left with

$$\alpha r^2 \left[\frac{\partial}{\partial r} A(r,s) \frac{\partial}{\partial r} J_0(\alpha r) + \frac{\partial}{\partial r} B(r,s) \frac{\partial}{\partial r} Y_0(\alpha r) \right] = -\frac{r^2}{T} \bar{f}(r,s) \tag{2.83}$$

subject to the imposed constraint

$$\frac{\partial}{\partial r} A(r,s)\, J_0(\alpha r) + \frac{\partial}{\partial r} B(r,s)\, Y_0(\alpha r) = 0 \tag{2.84}$$

These last two equations suffice to solve for the derivatives of A and B, as we have two equations in two unknowns. Expressing the solution in matrix form, we have

$$\begin{bmatrix} A'(r,s) \\ B'(r,s) \end{bmatrix} = \begin{bmatrix} J_0(\alpha r) & Y_0(\alpha r) \\ \alpha r^2 J_0'(\alpha r) & \alpha r^2 Y_0'(\alpha r) \end{bmatrix}^{-1} \begin{bmatrix} 0 \\ -\frac{r^2}{T}\bar{f}(r,s) \end{bmatrix}$$

$$= \frac{\bar{f}(r,s)}{\alpha T\left[J_0(\alpha r)Y_0'(\alpha r) - J_0'(\alpha r)Y_0(\alpha r)\right]} \begin{bmatrix} Y_0(\alpha r) \\ -J_0(\alpha r) \end{bmatrix}$$

$$= \frac{\pi r \bar{f}(r,s)}{2T} \begin{bmatrix} Y_0(\alpha r) \\ -J_0(\alpha r) \end{bmatrix} \qquad (2.85)$$

The last expression is a consequence of the fact that the Wronskian appearing in the denominator of the second expression has the value $2/(\pi\alpha r)$. This can be verified in any reference on mathematical functions [46]. The general solution for the membrane problem then follows as

$$\bar{v}_g(r,s) = \left[J_0(\alpha r)\ Y_0(\alpha r)\right]\begin{bmatrix} A(0,s) \\ B(0,s) \end{bmatrix} + \frac{\pi}{2T}\left[J_0(\alpha r)\ Y_0(\alpha r)\right]\int_0^r \begin{bmatrix} \rho Y_0(\alpha\rho) \\ -\rho J_0(\alpha\rho) \end{bmatrix} \bar{f}(\rho,s)\, d\rho \qquad (2.86)$$

In order that the solution be well-behaved at the origin, we must have $B(0) = 0$. The other constant is determined from the boundary conditions for the problem. Let us assume that the membrane is supported along a circle of radius R, so that $\bar{v}(R,s) = 0$ for all s. We can then use this information to solve for A(0) and substitute the result back into Equation (2.86). The complete solution then becomes, after much algebraic manipulation,

$$\bar{v}(r,s) = \frac{\pi}{2TJ_0(\alpha R)}\left[\left[J_0(\alpha r)Y_0(\alpha R) - Y_0(\alpha r)J_0(\alpha R)\right]\int_0^r J_0(\alpha\rho)\,\bar{f}(\rho,s)\,\rho\, d\rho \right.$$

$$\left. + J_0(\alpha r)\int_r^R \left[J_0(\alpha\rho)Y_0(\alpha R) - Y_0(\alpha\rho)J_0(\alpha R)\right]\bar{f}(\rho,s)\,\rho\, d\rho \right] \qquad (2.87)$$

Figure 2-11 displays the deflection of a membrane as a function of radial distance at consecutive time frames. The forcing input in this case is impulsive in time, and is distributed uniformly over the area $r < 0.1$ R. From the plots, we can identify the wavelike propagation of the disturbance, which diminishes with distance from the origin. Also evident is the reflection of the

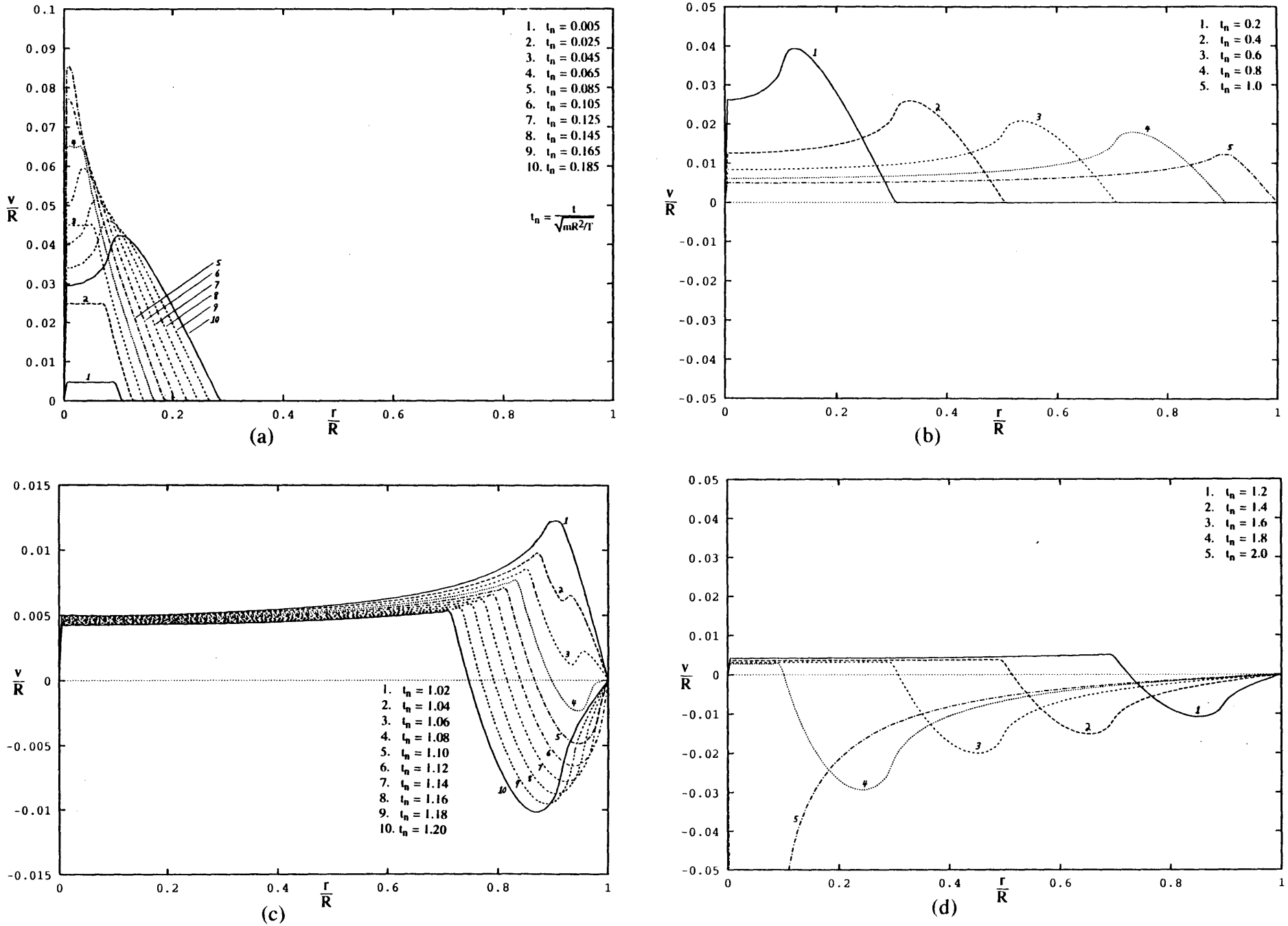

Fig. 2-11: Response of a membrane impacted at center (r=0): (a) Development of disturbance pulse, (b) Propagation of pulse to fixed boundary at r=R, (c) Reflection of disturbance at boundary, (d) Return pulse.

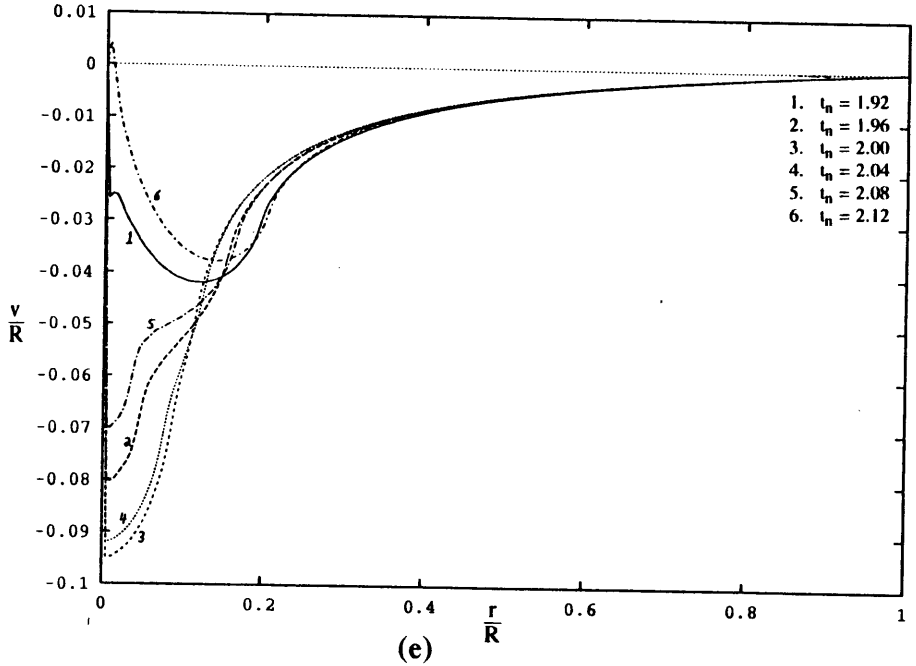

(e)

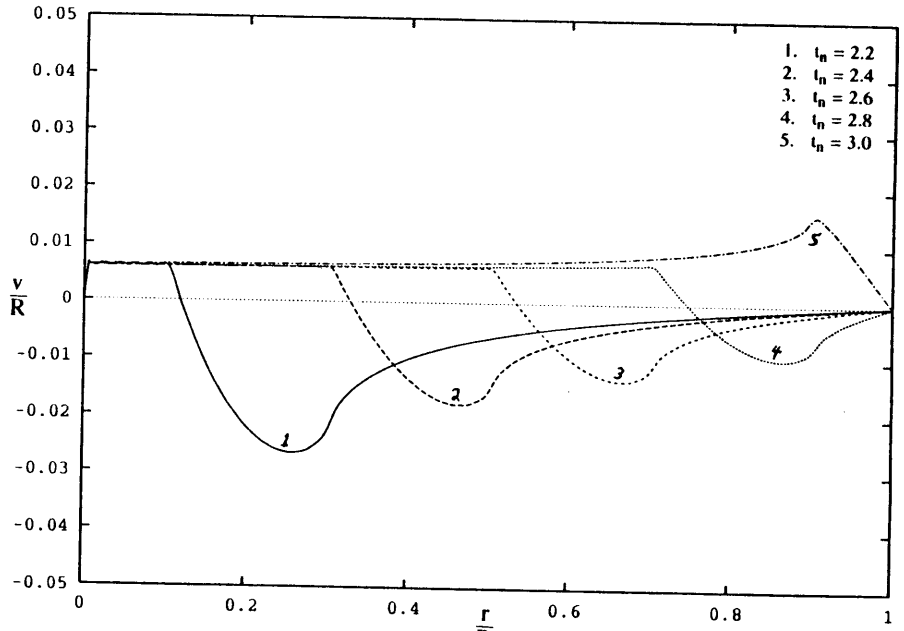

(f)

Fig. 2-11: (Continued) (e) Reflection of disturbance at center of membrane, (f) Second out-going pulse

disturbance at the support location r = R (where the pulse is inverted) and the "reflection" as the pulse returns to the center of the membrane (where it is not inverted).

Unfortunately, this type of structural element model cannot be utilized in the analysis of a more complex structure due to the assumption of axial symmetry. Additional elements attached at arbitrary points along the boundary destroy the symmetry. The resulting solution depends on azimuthal as well as radial position, and the transformed equation of motion remains a PDE. As a result, an exact analytical solution is not available. To handle such cases in an approximate sense, we now turn to general two-dimensional element models.

2.4.2 Plate bending element

The TEM formulation for plate elements bears some resemblance to previous work by Kulla [47]. The transformed equation of motion for a plate in bending is

$$D\nabla^4 v(x,y,s) + ms^2 v(x,y,s) = 0 \tag{2.88}$$

where v is the deflection normal to the plane of the element, m is the mass per unit area, and ∇^4 is the biharmonic operator. Also, D is the bending rigidity, given by

$$D = \frac{Eh^3}{12(1-\nu^2)} \tag{2.89}$$

where h is the thickness of the plate and ν is the Poisson's ratio of the material. Note that we have assumed no distributed forcing and zero initial conditions. The homogeneous solution vector is of infinite dimension, with each entry having the form

$$v_{H_i}(x,y,s) = e^{\alpha_i x + \beta_i y} \tag{2.90}$$

Substituting this equation into Eq. (2.88) yields the characteristic equation

$$\left[\alpha_i^2 + \beta_i^2\right]^2 + \frac{ms^2}{D} = 0 \tag{2.91}$$

Thus, for each complex-valued α (or β), there exist four independent homogeneous solutions corresponding to the four complex-valued β's (or α's) obtained from the characteristic equation.

To obtain an approximate plate solution, we must select a finite set of values for α (or β). A general method of selecting this set has not been developed in this research. From this set, we obtain a truncated solution vector, and the approximate expression for the deflection field becomes

$$v(x,y,s) = \mathbf{v}_H(x,y,s)^T \mathbf{a}(s) \tag{2.92}$$

The problem has now been reduced to determining the coefficient vector, $\mathbf{a}(s)$, in terms of the boundary conditions. A finite set of boundary points on the element is therefore selected. The total number of boundary conditions specified at these points, n, must equal the dimension of the homogeneous solution vector, so that the problem is not underspecified. (Typically, three boundary conditions are imposed at each point.) The boundary condition constraints can be written in the form

$$w_i(s) = L_{xy}^{(i)}\left[v(x_i,y_i,s)\right] = L_{xy}^{(i)}\left[\mathbf{v}_H(x_i,y_i,s)\right]^T \mathbf{a}(s)\,, \quad i=1,...,n \tag{2.93a}$$

$$q_i(s) = D_{xy}^{(i)}\left[v(x_i,y_i,s)\right] = D_{xy}^{(i)}\left[\mathbf{v}_H(x_i,y_i,s)\right]^T \mathbf{a}(s)\,, \quad i=1,...,n \tag{2.93b}$$

where $L_{xy}^{(i)}$ is a linear spatial differential operator (independent of s) relating the approximate solution, v, to the i'th generalized displacement on the boundary, w_i. Similarly, $D_{xy}^{(i)}$ relates v to the corresponding dual generalized force, q_i. Grouping Eqs. (2.93a) and (2.93b) into matrix form yields

$$\mathbf{w}(s) = \Psi(s)\,\mathbf{a}(s)\,, \quad \mathbf{q}(s) = \tilde{\Psi}(s)\,\mathbf{a}(s) \tag{2.94a,b}$$

where

$$\Psi(s) \triangleq \begin{bmatrix} L_{xy}^{(1)}\left[\mathbf{v}_H(x_1,y_1,s)\right]^T \\ \vdots \\ L_{xy}^{(n)}\left[\mathbf{v}_H(x_n,y_n,s)\right]^T \end{bmatrix}, \quad \tilde{\Psi}(s) \triangleq \begin{bmatrix} D_{xy}^{(1)}\left[\mathbf{v}_H(x_1,y_1,s)\right]^T \\ \vdots \\ D_{xy}^{(n)}\left[\mathbf{v}_H(x_n,y_n,s)\right]^T \end{bmatrix} \tag{2.95a,b}$$

Finally, the dynamic stiffness matrix follows from eliminating **a** from Eqs. (2.94a) and (2.94b):

$$\mathbf{K}(s) = \tilde{\Psi}(s)\left[\Psi(s)\right]^{-1} \tag{2.96}$$

Obviously, the choice of boundary points affects the accuracy of the solution, and should depend on the geometry of the element. A quantitative relationship between the boundary point locations and the solution accuracy has not yet been developed for the TEM approach, but would probably follow the same general guidelines used in finite element and boundary element techniques. A general rule of thumb is to space the boundary points more closely together near corners of the element, where internal stress gradients are large.

The distinguishing feature of this approach (as compared with finite element modelling methods) is that the finite dimensional solution vector has frequency dependence. Furthermore, these basis solutions satisfy the underlying PDE exactly, and a linear combination of these functions is chosen to minimize (in some sense) the error along the boundary. In the above development, point collocation is used, and we require that there exist as many boundary conditions as basis solutions. Should there exist more boundary points than basis solutions, a least-squares approach could be utilized. Similarly, if fewer boundary points exist, there exist an infinity of linear combinations that satisfy the boundary conditions, and the optimal combination could be determined based on some other criterion. The TEM methodology is therefore a Galerkin approach, and requires solving a family of PDE's parametrized by the complex frequency. On the other hand, finite element shape functions almost never satisfy the dynamics equations, particularly in the case of two-dimensional elements. Hence, at higher frequencies, a finer discretization is required to reproduce the detail of the structural deformation arising from shorter characteristic wavelengths. By relaxing the requirement that the dynamics equations be satisfied exactly, very simple functions can be chosen, and the entire modelling procedure can be computerized. Thus, in contrast with the TEM methodolgy, finite element modelling is a Rayleigh-Ritz approach.

2.4.3 Plane stress element

For plane stress problems, the difficulty lies in expressing the state of deformation in terms of a single scalar function, as there are two in-plane deformational degrees of freedom. To remedy this situation, it becomes necessary to derive a frequency-dependent stress function, from which all internal stresses and both in-plane displacements can be determined. This is accomplished by working directly with the basic plane stress relations, expressed in the frequency-domain. For linear, isotropic, plane stress problems, the stress-strain relations are

$$\varepsilon_x = \frac{1}{E}(\sigma_x - \nu\,\sigma_y) \tag{2.97a}$$

$$\varepsilon_y = \frac{1}{E}(\sigma_y - \nu\,\sigma_x) \tag{2.97b}$$

$$\varepsilon_{xy} = \frac{1}{2G}\tau_{xy} = \frac{1+\nu}{E}\tau_{xy} \tag{2.97c}$$

where E,G, and ν are the extensional modulus, shear modulus and Poisson's ratio of the material, respectively. The equations of force equilibrium, expressed in the frequency-domain, are

$$\frac{\partial\sigma_x}{\partial x} + \frac{\partial\tau_{xy}}{\partial y} = \rho s^2 u_x\,, \qquad \frac{\partial\tau_{xy}}{\partial x} + \frac{\partial\sigma_y}{\partial y} = \rho s^2 u_y \tag{2.98a,b}$$

where ρ is the density of the material and s is the (generally complex) Laplace variable. To these, we must add the geometric relations

$$\varepsilon_x = \frac{\partial u_x}{\partial x}, \qquad \varepsilon_y = \frac{\partial u_y}{\partial y}, \qquad \varepsilon_{xy} = \frac{1}{2}\left(\frac{\partial u_x}{\partial y} + \frac{\partial u_y}{\partial x}\right) \tag{2.99a,b,c}$$

and the compatibility constraint

$$\frac{\partial^2\varepsilon_x}{\partial y^2} + \frac{\partial^2\varepsilon_y}{\partial x^2} = 2\frac{\partial^2\varepsilon_{xy}}{\partial x\partial y} \tag{2.100}$$

Substituting Eqs. (2.97a) and (2.97b) into equation (2.100) yields

$$\frac{\partial^2\sigma_x}{\partial y^2} + \frac{\partial^2\sigma_y}{\partial x^2} - \nu\left(\frac{\partial^2\sigma_x}{\partial x^2} + \frac{\partial^2\sigma_y}{\partial y^2}\right) = 2(1+\nu)\frac{\partial^2\tau_{xy}}{\partial x\partial y} \tag{2.101}$$

while adding the derivative of Eq. (2.98a) with respect to x to the derivative of equation (2.98b) with respect to y produces

$$2\frac{\partial^2\tau_{xy}}{\partial x\partial y}+\left(\frac{\partial^2\sigma_x}{\partial x^2}+\frac{\partial^2\sigma_y}{\partial y^2}\right)=\rho s^2\left(\frac{\partial u_x}{\partial x}+\frac{\partial u_y}{\partial y}\right) \tag{2.102}$$

Eliminating τ_{xy} between the previous two relations results in

$$\frac{\partial^2\sigma_x}{\partial y^2}+\frac{\partial^2\sigma_y}{\partial x^2}+\frac{\partial^2\sigma_x}{\partial x^2}+\frac{\partial^2\sigma_y}{\partial y^2}=(1+\nu)\rho s^2\left(\frac{\partial u_x}{\partial x}+\frac{\partial u_y}{\partial y}\right) \tag{2.103}$$

Substituting Eqs. (2.97a), (2.97b), (2.99a) and (2.99b) into equation (2.103) yields

$$\frac{\partial^2\sigma_x}{\partial y^2}+\frac{\partial^2\sigma_y}{\partial x^2}+\frac{\partial^2\sigma_x}{\partial x^2}+\frac{\partial^2\sigma_y}{\partial y^2}=(1+\nu)(1-\nu)\frac{\rho s^2}{E}\left(\sigma_x+\sigma_y\right) \tag{2.104}$$

which reduces to

$$\left[\nabla^2-(1-\nu^2)\frac{\rho s^2}{E}\right]\left(\sigma_x+\sigma_y\right)=0 \tag{2.105}$$

where ∇^2 is the two dimensional spatial Laplacian operator. Because σ_x and σ_y are independent variables, we still need one additional equation, so as to uniquely identify σ_x and σ_y. The second equation is obtained by subtracting the derivative of Eq. (2.98b) with respect to y from the derivative of Eq. (2.98a) with respect to x, yielding

$$(1+\nu)\frac{\rho s^2}{E}\left(\sigma_x-\sigma_y\right)=\frac{\partial^2\sigma_x}{\partial x^2}-\frac{\partial^2\sigma_y}{\partial y^2} \tag{2.106}$$

This relation is equivalent to

$$2(1+\nu)\frac{\rho s^2}{E}\left(\sigma_x-\sigma_y\right)=\nabla^2\left(\sigma_x-\sigma_y\right)+\frac{\partial^2\sigma_x}{\partial x^2}-\frac{\partial^2\sigma_x}{\partial y^2}+\frac{\partial^2\sigma_y}{\partial x^2}-\frac{\partial^2\sigma_y}{\partial y^2} \tag{2.107}$$

from which we obtain

$$\left[\nabla^2-2(1+\nu)\frac{\rho s^2}{E}\right]\left(\sigma_x-\sigma_y\right)=\left[-\frac{\partial^2}{\partial x^2}+\frac{\partial^2}{\partial y^2}\right]\left(\sigma_x+\sigma_y\right) \tag{2.108}$$

Equations (2.105) and (2.108) represent two linear partial differential equations in two variables (the sum and difference of the normal stresses). This system can be reduced to a single equation by defining a frequency dependent stress function, Φ, so that the following relations hold:

$$(\sigma_x + \sigma_y) = \left[\nabla^2 - 2(1+\nu)\frac{\rho s^2}{E}\right]\Phi \tag{2.109a}$$

$$(\sigma_x - \sigma_y) = \left[-\frac{\partial^2}{\partial x^2} + \frac{\partial^2}{\partial y^2}\right]\Phi \tag{2.109b}$$

Then, in terms of Φ, Eq. (2.108) is identically satisfied, while Eq. (2.105) becomes

$$\left[\nabla^2 - \frac{s^2}{c_c^2}\right]\left[\nabla^2 - \frac{s^2}{c_s^2}\right]\Phi = 0 \tag{2.110}$$

where

$$c_c = \sqrt{\frac{E}{\rho(1-\nu^2)}}, \quad c_s = \sqrt{\frac{G}{\rho}}, \quad c_0 = \sqrt{\frac{E}{\rho}} \tag{2.111a,b,c}$$

The constants c_c, c_s and c_0 are readily identified as the propagation velocities of compression and shear waves in a plane and compression waves in a three dimensional medium, respectively. It is interesting to note that, under static conditions (s=0), equation (2.110) reduces to the familiar biharmonic equation associated with the Airy stress function.

It remains to determine the physical entities of interest in terms of Φ. In the traditional stress function formulation, the stresses are expressed as derivative operators on Φ. In order to obtain similar differential operator expressions in this development, it is necessary to define a related function, v, such that the following relationship holds:

$$\Phi = \frac{\partial^2 v}{\partial x \partial y} \tag{2.112}$$

The final form of Eq. (2.110) then becomes

$$\frac{\partial^2}{\partial x \partial y}\left[\nabla^2 - \frac{s^2}{c_c^2}\right]\left[\nabla^2 - \frac{s^2}{c_s^2}\right]v = 0 \tag{2.113}$$

Equations (2.109) and (2.112) can then be used to determine the normal stresses in terms of v:

$$\sigma_x = \frac{\partial^2}{\partial x \partial y}\left[\frac{\partial^2}{\partial y^2} - \frac{s^2}{2c_s^2}\right]v, \quad \sigma_y = \frac{\partial^2}{\partial x \partial y}\left[\frac{\partial^2}{\partial x^2} - \frac{s^2}{2c_s^2}\right]v \tag{2.114a,b}$$

Now, combining Eqs. (2.97a), (2.99a) and the derivative of Eq. (2.98a) with respect to x leads to

$$\frac{\partial^2 \tau_{xy}}{\partial x \partial y} = \frac{\rho s^2}{E}(\sigma_x - \nu\,\sigma_y) - \frac{\partial^2 \sigma_x}{\partial x^2} \tag{2.115}$$

Substituting Eqs. (2.114a) and (2.114b) into equation (2.115) and integrating with respect to both x and y yields

$$\tau_{xy} = \left[- \frac{\partial^4}{\partial x^2 \partial y^2} + \frac{s^2}{c_0^2} \nabla^2 - \frac{s^4}{c_0^2 c_c^2} \right] v \tag{2.116}$$

Thus, Eqs. (2.114) and (2.116) are the desired relations between the stresses and v. Furthermore, making use of Eqs. (2.97) and (2.99) leads to

$$u_x = \frac{1}{E} \frac{\partial}{\partial y} \left[\frac{\partial^2}{\partial y^2} - \nu \frac{\partial^2}{\partial x^2} - \frac{s^2}{c_c^2} \right] v \tag{2.117a}$$

$$u_y = \frac{1}{E} \frac{\partial}{\partial x} \left[\frac{\partial^2}{\partial x^2} - \nu \frac{\partial^2}{\partial y^2} - \frac{s^2}{c_c^2} \right] v \tag{2.117b}$$

Thus, unlike the traditional stress function formulation, this development also expresses the displacements in terms of the frequency dependent function, v.

We are now in a position to apply the same methodology as was used for the plate bending element. Once again, the assumed form of the homogeneous solution is

$$v_{H_i}(x,y,s) = e^{\alpha_i x + \beta_i y}, \quad i=1,...,n \tag{2.118}$$

where α and β are functions of s. This leads to the characteristic equation:

$$\alpha_i \beta_i \left[(\alpha_i^2 + \beta_i^2) - \frac{s^2}{c_c^2} \right] \left[(\alpha_i^2 + \beta_i^2) - \frac{s^2}{c_s^2} \right] = 0, \quad i=1,...,n \tag{2.119}$$

Of the four solutions to this equation, two (α=0 and β=0) are spurious. The other two determine the relationship that must hold between α and β for each basis solution. The rigid body modes are accounted for by setting s equal to zero. As is the case for the plate bending element, the actual choices for α_i and β_i vary depending on the geometry of the element and are not discussed here.

2.5 Assembly Procedure

The assembly of individual elements to form a global structural model is performed in a manner similar to traditional FEM techniques. The element equations are first collected into a large, unreduced matrix equation, given by

$$\begin{bmatrix} \mathbf{q}^1(s) \\ \cdot \\ \cdot \\ \mathbf{q}^N(s) \end{bmatrix} = \begin{bmatrix} \mathbf{K}^1(s) & & & \mathbf{0} \\ & \mathbf{K}^2(s) & & \\ & & \cdot & \\ \mathbf{0} & & & \mathbf{K}^N(s) \end{bmatrix} \begin{bmatrix} \mathbf{w}^1(s) \\ \cdot \\ \cdot \\ \mathbf{w}^N(s) \end{bmatrix} + \begin{bmatrix} \mathbf{q}_d^1(s) \\ \cdot \\ \cdot \\ \mathbf{q}_d^N(s) \end{bmatrix} \tag{2.120}$$

where the superscripts identify the individual elements. The geometry of the interconnections between elements is specified by a connectivity matrix, **C**, which relates the local boundary displacements of the elements to a set of global displacements, $\mathbf{w}_0^G(s)$, that define the global model:

$$\begin{bmatrix} \mathbf{w}^1(s) \\ \cdot \\ \cdot \\ \mathbf{w}^N(s) \end{bmatrix} = \mathbf{C}\, \mathbf{w}_0^G(s) \tag{2.121}$$

Figure 2-12 presents a simple planar structural system and the associated connectivity matrix. The system consists of two physical elements, each of which is modelled by an axial element and a bending element. Each physical element has three degrees of freedom at each boundary. (If out-of-plane motion is to be included, each physical element would require an additional bending element as well as a torsional element. Six degrees of freedom would then exist at each physical element boundary.) Piche [33] and Hagood [35] (among others) show that, for small, linear displacements, the following dual relationship holds:

$$\mathbf{q}_0^G(s) = \mathbf{C}^T \begin{bmatrix} \mathbf{q}^1(s) \\ \cdot \\ \cdot \\ \mathbf{q}^N(s) \end{bmatrix} \tag{2.122}$$

Using these connectivity relations in Eq. (2.120) yields the unreduced system model

$$\mathbf{q}_0^G(s) = \mathbf{K}_0^G(s)\, \mathbf{w}_0^G(s) + \mathbf{q}_{d0}^G(s) \tag{2.123}$$

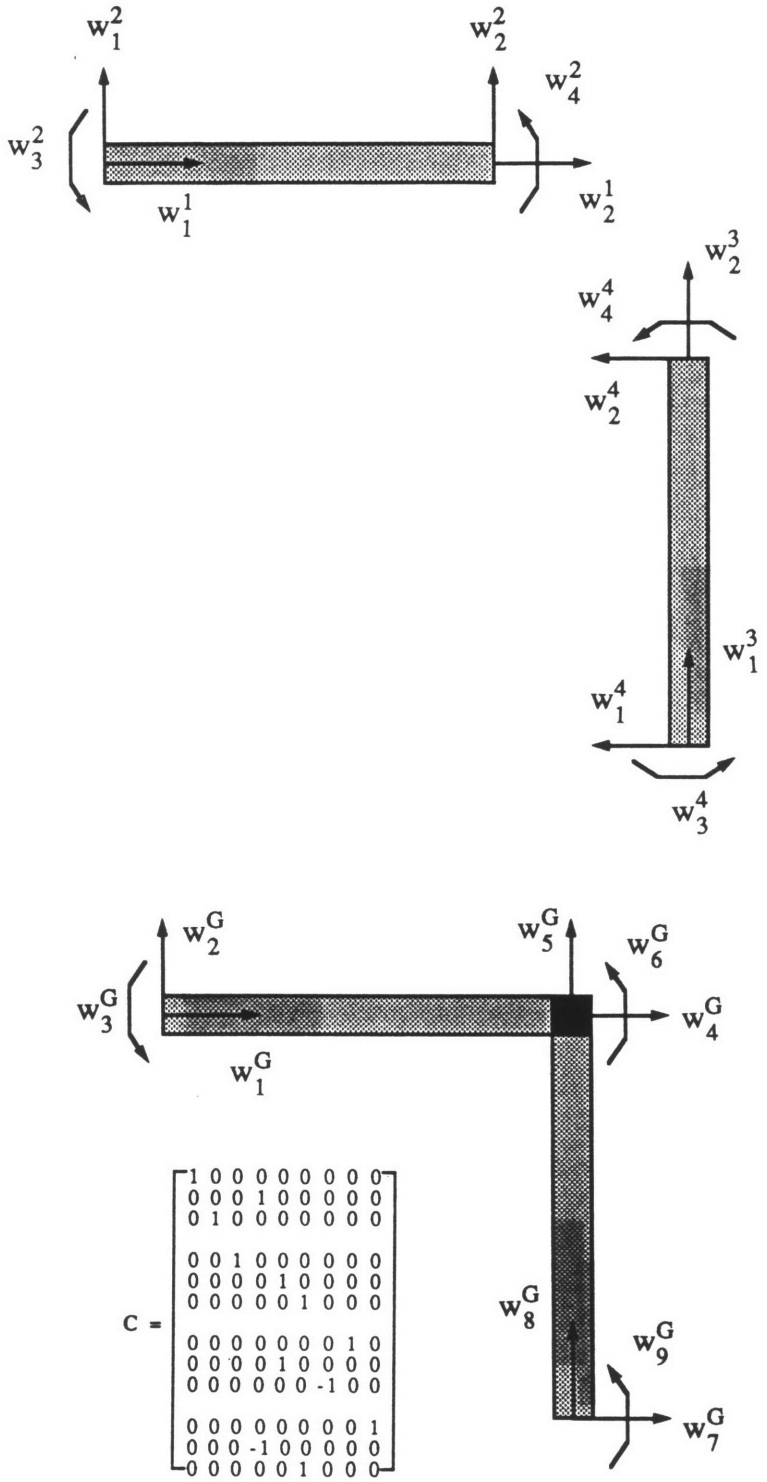

Fig. 2-12: Assembly of simple structure consisting of two physical elements. For in-plane motion, each physical elements contains two mathematical elements. Mathematical elements 1 and 3 are axial models, and elements 2 and 4 are beam models. The joint is assumed to be massless.

where

$$\mathbf{K}_0^G(s) = \mathbf{C}^T \begin{bmatrix} \mathbf{K}^1(s) & & \mathbf{0} \\ & \mathbf{K}^2(s) & \\ \mathbf{0} & & \mathbf{K}^N(s) \end{bmatrix} \mathbf{C}, \quad \mathbf{q}_{d0}^G(s) = \mathbf{C}^T \begin{bmatrix} \mathbf{q}_d^1(s) \\ \vdots \\ \mathbf{q}_d^N(s) \end{bmatrix} \tag{2.124a,b}$$

At this point, if there are any global displacements that are constrained, they are removed from the unreduced model. This produces the desired global model, given by

$$\mathbf{q}^G(s) = \mathbf{K}^G(s)\,\mathbf{w}^G(s) + \mathbf{q}_d^G(s) \tag{2.125}$$

Equation (2.125) represents the global dynamic stiffness matrix for the structural model. It is mathematically exact, and must be calculated at each frequency of interest. To compute the response of the model to various excitations, we must solve for the global displacements. Thus,

$$\mathbf{w}^G(s) = \mathbf{G}(s)\left[\mathbf{q}^G(s) - \mathbf{q}_d^G(s)\right], \quad \mathbf{G}(s) = \left[\mathbf{K}^G(s)\right]^{-1} \tag{2.126a,b}$$

Here, G(s) represents the global transfer function matrix for the model. If, in addition, the local boundary displacements for a particular element are desired, a partition of the connectivity matrix must be used:

$$\mathbf{w}^i(s) = \mathbf{C}_w^i\,\mathbf{G}(s)\left[\mathbf{q}^G(s) - \mathbf{q}_d^G(s)\right] \tag{2.127}$$

Finally, the internal states of a particular element are available via

$$\mathbf{u}^i(x,s) = \Gamma^i(x,s)\,\mathbf{C}_w^i\,\mathbf{G}(s)\left[\mathbf{q}^G(s) - \mathbf{q}_d^G(s)\right] + \mathbf{u}_p^i(x,s) \tag{2.128}$$

In practice, the matrix multiplications are never performed literally. The connectivity and unreduced stiffness matrices are highly structured, making it possible to write specialized algorithms for each equation given above. This dramatically increases the overall computation speed of the assembly process.

2.6 Applications

This section discusses some of the applications of the TEM modelling approach. All applications require global model assembly, and, consequently, a general TEM structural modelling code has been developed. Currently available TEM software, such as the DISTEL code written by Poelaert [48], could not be used, as the transform variable is typically restricted to the imaginary-axis.

2.6.1 Modal frequencies

In many cases, all that is required from a structural model is a set of modal frequencies. While the TEM methodology provides significantly more information, it is nonetheless possible to obtain modal frequencies using an algorithm developed by Wittrick [32]. This robust algorithm uses information about the stiffness matrix, evaluated at a trial frequency, to determine the number of modes whose frequencies are below the trial frequency. Also required by the algorithm are the modal frequencies of the individual elements with all boundary displacements constrained to zero. The algorithm is designed for undamped structures only, and additional root searching techniques are required in the analysis of damped structures. Even in damped cases, however, the algorithm provides a reasonable initial estimate of the location of the damped modal frequencies. This algorithm was not implemented in this research, as adequately accurate modal information was available from plots of appropriate transfer functions, as described below.

2.6.2 Frequency response and transfer functions

The primary advantage of the TEM approach is its ability to provide the exact transfer function matrix at any frequency of interest. This is obtained by numerically inverting the dynamic stiffness matrix. The stiffness matrix, $\mathbf{K}(s)$, represents a matrix of complex impedances relating generalized boundary forces to boundary displacements. Consequently, $\mathbf{G}(s)$ is a matrix of complex admittances, and is often called the dynamic flexibility matrix.

The transfer functions of cantilevered axial rods and Bernoulli-Euler beams with various damping models are shown in Fig. 2-13. For the rod, the input is an applied force on the free end and the output is the axial deflection at that end. Similarly, for the beam, the input is an applied transverse force on the free end and the output is the transverse deflection at that end. It should be noted that the accuracy of these transfer functions extends arbitrarily high in frequency, insofar as the mathematical models represent the actual physical system.

In order to demonstrate the capabilities and advantages of the TEM methodology, a reasonably complex structure was analyzed. The Spacecraft COntrol Laboratory Experiment (SCOLE) model is a three dimensional asymmmetric structure proposed by NASA as a design challenge [49]. It consists of a rigid shuttle and hexagonal truss antenna connected by a flexible mast, as shown in Fig. 2-14. Previous authors have treated the antenna as being rigid. In this effort, however, the flexibility of the antenna is considered. The TEM model thus contains thirteen beam elements (the mast and twelve antenna elements) and a six degree of freedom rigid mass representing the shuttle. In addition to the six rigid degrees of freedom, a total of 52 partial differential equations, incorporating axial, bending and torsional modes, are modeled. For comparison, the SCOLE model was also analysed using ASTROS, which incorporates a finite element algorithm similar to that found in NASTRAN. For the finite element model, the mast was divided into 32 equal elements, and each of the antenna beams was divided into four lumped elements, leading to 480 degrees of freedom.

Figure 2-15 compares the transfer functions from a torque applied to the shuttle about the axis of the mast to various points along the mast and antenna. The TEM and FEM models agree rather well at low frequencies. However, it is clear that the finite element model becomes inaccurate beyond the first few modes. Part of the discrepency is due to the small amount of damping present in the TEM model, which could not be modelled in ASTROS, but the spurious modes predicted by the FEM model are clearly a consequence of spatial discretization. What is considerably more striking is the relative computation time requred to generate the transfer

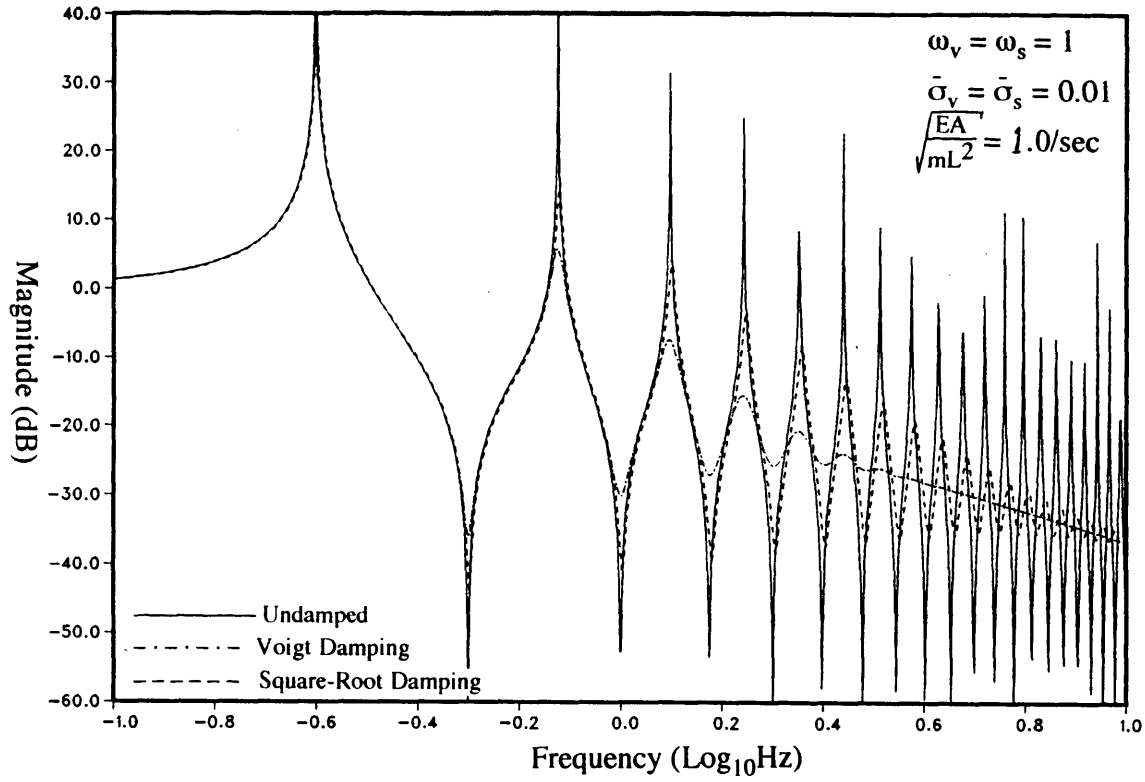

(a)

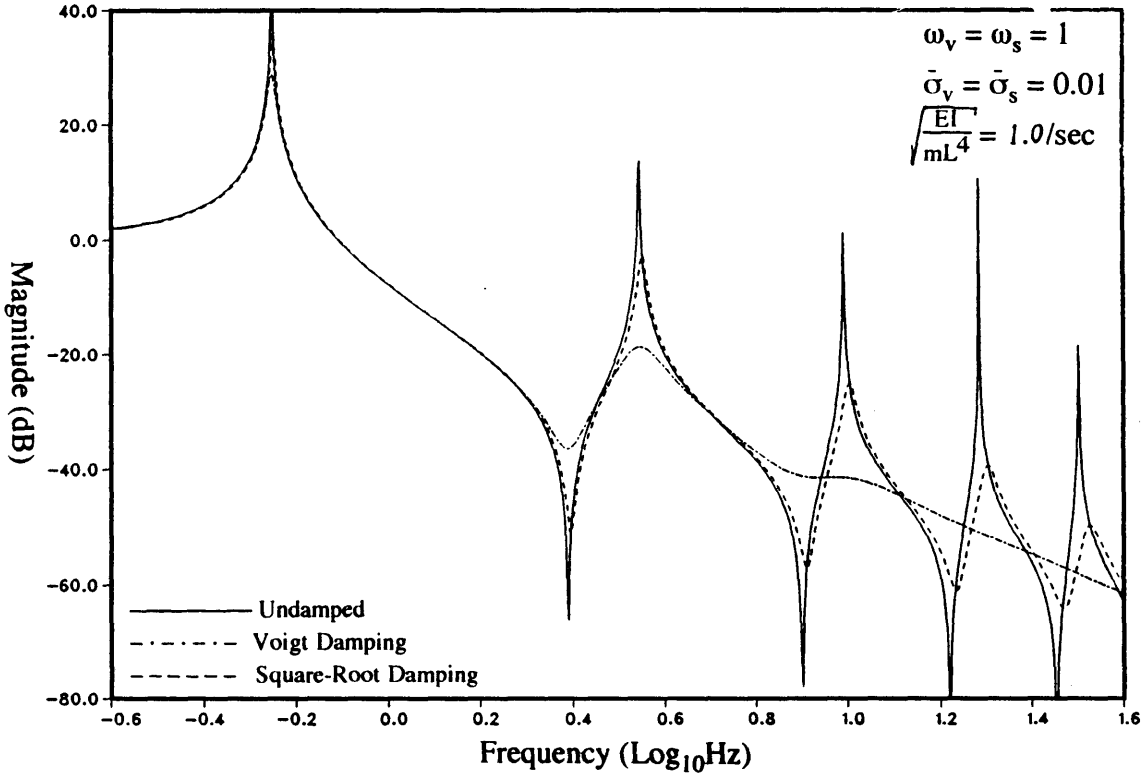

(b)

Fig. 2-13: Transfer functions of simple cantilevered element with various frequency-domain damping models: (a) Axial tip force to axial tip displacement, (b) Transverse tip force to transverse tip displacement.

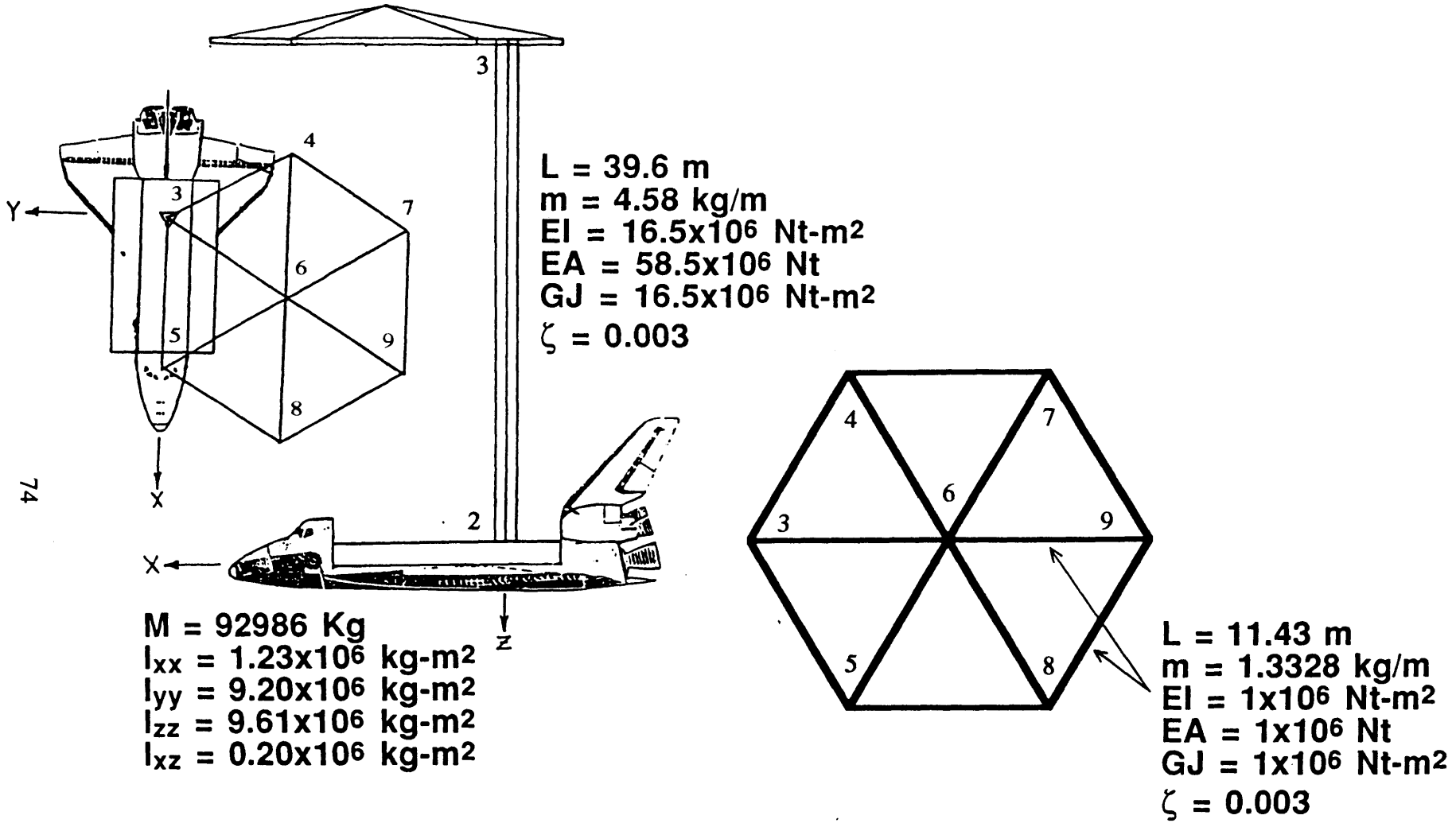

Fig. 2-14: Schematic of the SCOLE structural system with flexible antenna model. Node numbers are indicated.

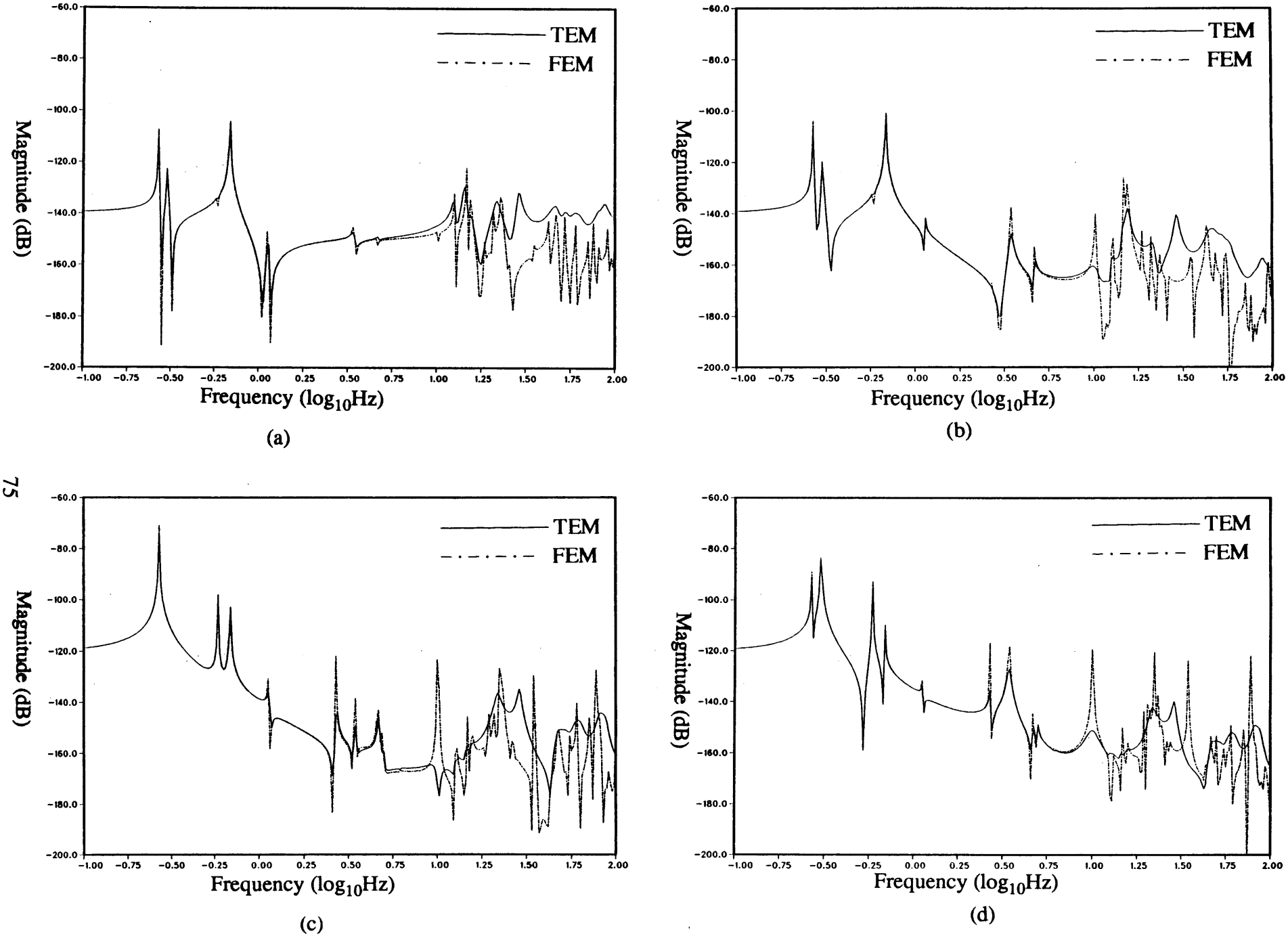

Fig. 2-15: Transfer functions from yaw torque on shuttle to various points on SCOLE model as determined by TEM and FEM models: (a) rotation of node 3 about z-axis, (b) rotation of node 6 about z-axis, (c) translation of node 6 in x-direction, (d) translation of node 6 in y-direction.

functions shown. On a micro-VAX machine, the TEM analysis required approximately one hour of CPU time, in contrast with several *days* of CPU time for the FEM approach. This acceleration is due primarily to the reduction of the total degrees of freedom in the model, which is associated with the lack of spatial discretization of the beam elements. Since the computation time associated with matrix inversion is roughly proportional to the cube of the dimension of the matrix, the reduction in total degrees of freedom has a profound effect on computaion time. In practice, however, FEM codes generate frequency response data using modal analysis rather than stiffness matrix inversion at each frequency. In such an analysis, an eigenvector decomposition of the FEM model is performed only once. Nevertheless, this single operation may require more CPU time than the many TEM inversions required to obtain the required frequency-domain data, due to the larger number of degrees of freedom in the FEM model.

As an example, let us assume that the ratio between the number of FEM and TEM degrees of freedom is six. The approximate speedup factor for a single matrix inversion will then be 216 (assuming that matrix inversion and eigenvector decomposition require approximately the same amount of computation). This is, of course, an extremely rough estimate, as the actual speedup will depend upon additional efficiency considerations, such as the effects of sparse matrix inversion routines and parallel processing, and the relative computational costs of real versus complex arithmetic operations. In addition, the FEM approach may not require all the eigenvalues and eigenvectors, given the frequency range of interest. For a given amount of computational capability, the analyst must therefore decide whether it is more useful to obtain the mathematically exact response (obtained via TEM inversion) at a finite set of frequencies or the approximate response (given by the sum of modal contributions) at all frequencies. Clearly, if the fidelity of the mathematical model at high frequencies is of great importance, the TEM approach would probably be favorable.

2.6.3 Time-domain simulation

A final application of the TEM approach for structural analysis is in the time-domain simulation of structural responses. This is accomplished via the inverse Laplace transform algorithm presented in Sec. 2.2. The flexibility matrix is evaluated at a finite set of N frequencies, and is multiplied by the global force vector, which contains the Laplace transforms of the forcing functions evaluated at those same frequencies. The resulting displacement vectors are then collected, and the algorithm generates the time-domain responses evaluated at a set of 2N points in time.

Fig. 2-16 compares the responses of a simple axial rod and a Mindlin-Herrmann rod. The rods are clamped at one end, with forcing input and displacement output at the free end. The top figure shows the force-to-displacement frequency responses at frequencies above the third resonance of the simple beam model. As expected, the introduction of an additional degree of freedom in the Mindlin-Herrmann model results in slightly lower resonant frequencies. The bottom figure compares the time-domain impulse responses of the two beam models. The dispersive effects of the higher order model are apparent.

Figure 2-17 compares the Bernoulli-Euler and Timoshenko beam models. Both beams are free at both ends, and are impacted with a unit transverse impulse at the left boundary. Shown are the translations and cross-sectional rotations of the beams at either boundary. Here, the effect of finite disturbance propagation velocity is the primary distinction between the models. The Timoshenko beam shows no response at the right boundary during the finite amount of time required for the disturbance to travel across the beam, while the Bernoulli-Euler beam response is almost instantaneous. Also, the lack of rotary inertia associated with the Bernoulli-Euler model causes instant rotation of the beam cross-section at the right boundary. This rotation is more gradual in the Timoshenko simulation, due to finite rotary inertia.

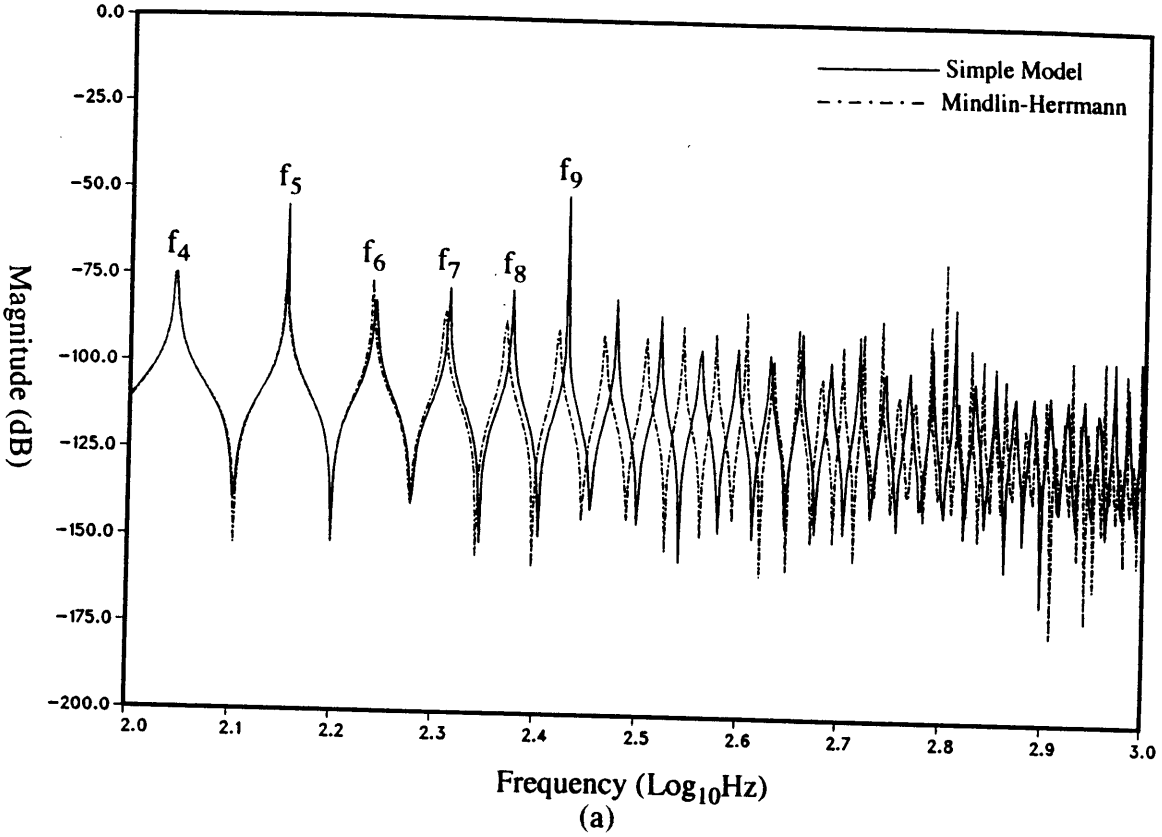

(a)

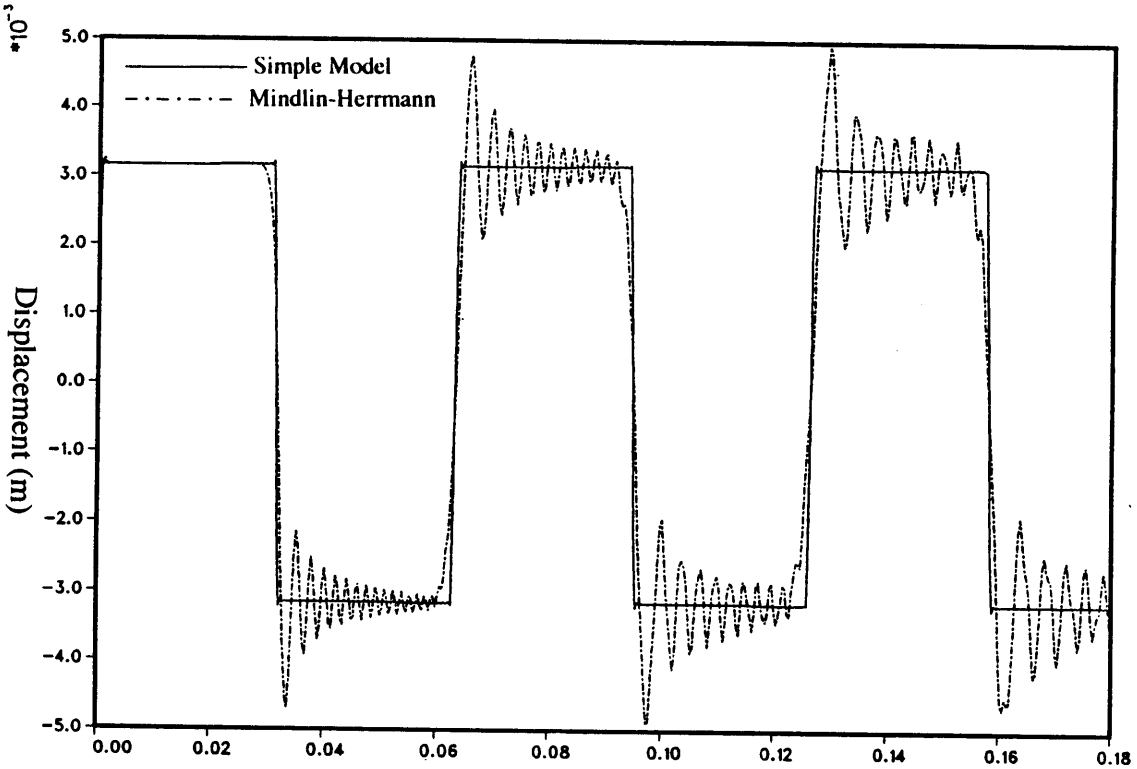

(b)

Fig. 2-16: Comparison between simple axial rod and Mindlin-Herrmann rod models: (a) Frequency response of cantilevered rod from tip force to tip displacement, (b) Time-domain response of rod impacted with unit tip impulse.

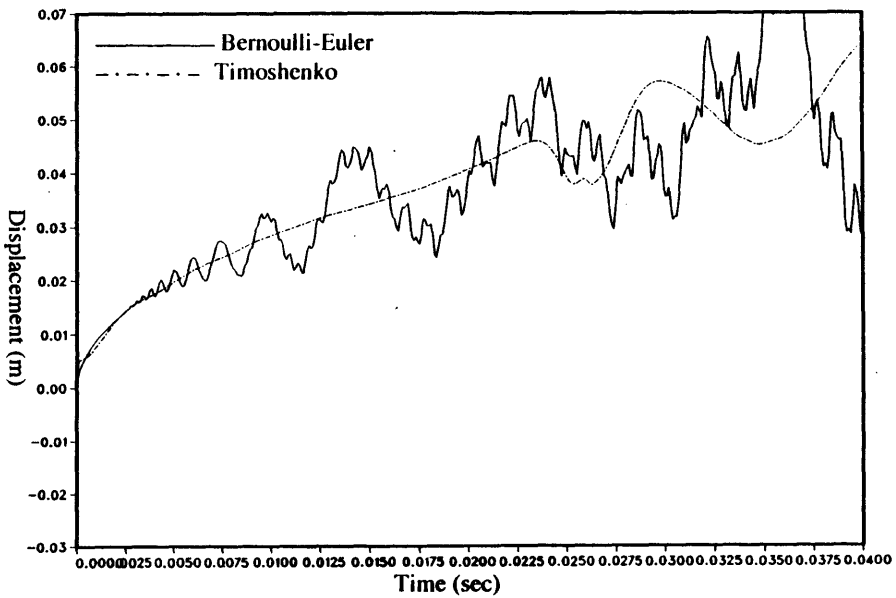

(a)

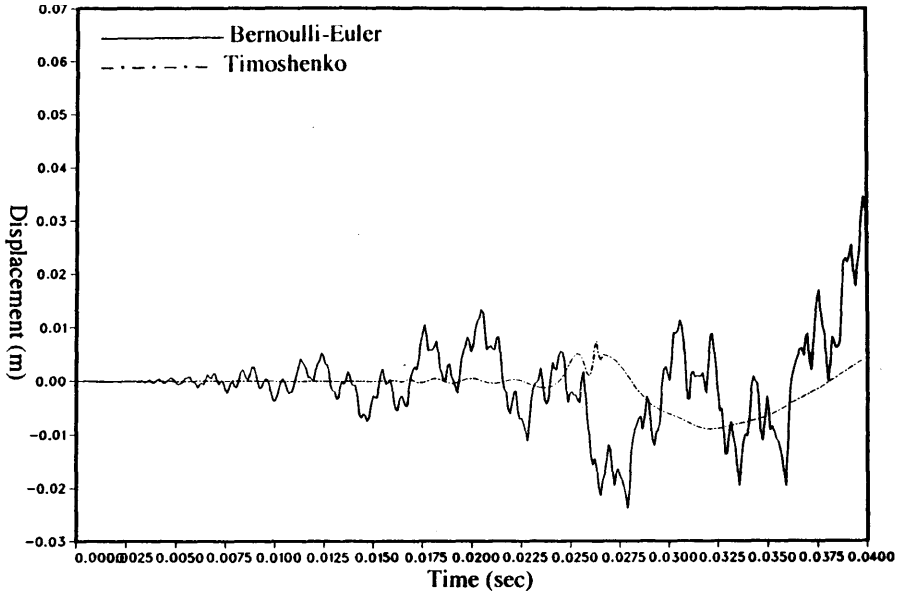

(b)

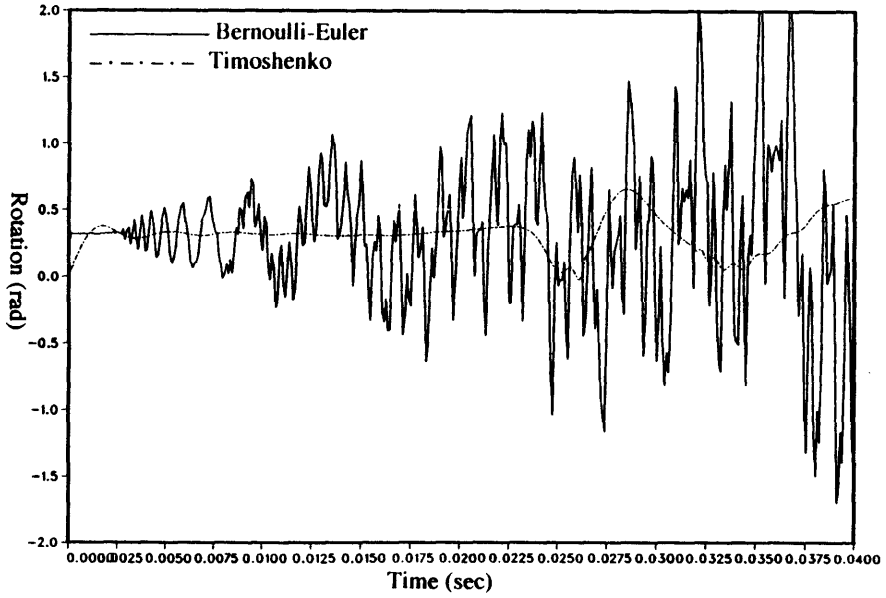

(c)

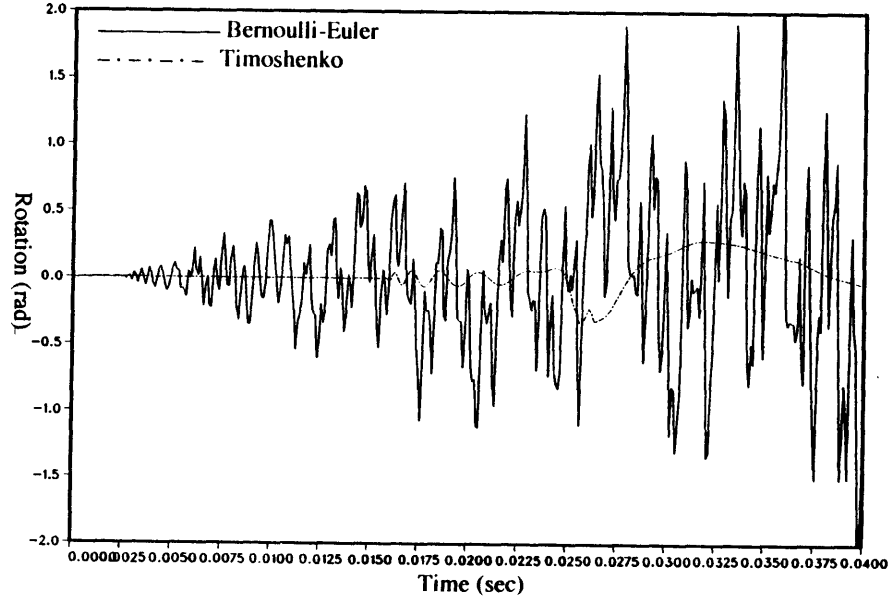

(d)

Fig. 2-17: Time-domain impulse responses of free-free beam element impacted with unit transverse force on left boundary (α_I=4x10^{-4}, α_E=2.8): (a) Transverse deflection of left boundary, (b) Transverse deflection of right boundary, (c) Rotation of left boundary, (d) Rotation of right boundary.

3 TRANSFORM ELEMENT FORMULATION FOR ARBITRARY MOTIONS

The TEM formulation described in Chapter 2 provides an exact PDE model of complex structures with small motions. Because the nodal displacements are all referenced to the inertial frame, the small deformation assumption for the elastic deformation also implies small rigid body motion of the total structure. To allow larger ranges of motion at articulated joints, one can embed the element reference frames at the undeformed element location, which may have both rigid body rotational and translational motion. This type of approach has been used in multibody tools such as DISCOS, TREETOPS, DADS and ADAMS. As shown in the following sections, the coupling of the rigid and elastic degrees of freedom results in a set of integro-partial differential equations. The formulation will be derived using a planar example. The extension to three dimensions should be straightforward.

3.1 Mathematical Model

In this subsection, we derive the equations of motion of a simple mass/appendage system subject to large rigid motions. We then proceed to use the TEM approach to obtain a solution that gives the accelerations and velocities of the system as functions of the applied forces. An inverse Laplace transform is required if the time-domain response is needed. Although the rigid motions can be quite large, the elastic deformations are still assumed small, so that the simple rod and beam equations, which arise from linear elasticity assumptions, are still valid.

3.1.1 Equations of Motion

Consider a single uniform beam, cantilevered to a rigid mass, as shown in Fig. 3-1. The beam's coordinate frame is fixed to the rigid mass, which can undergo rigid body motion. In order to simplify the development considerably, the motion of the system is assumed to be planar.

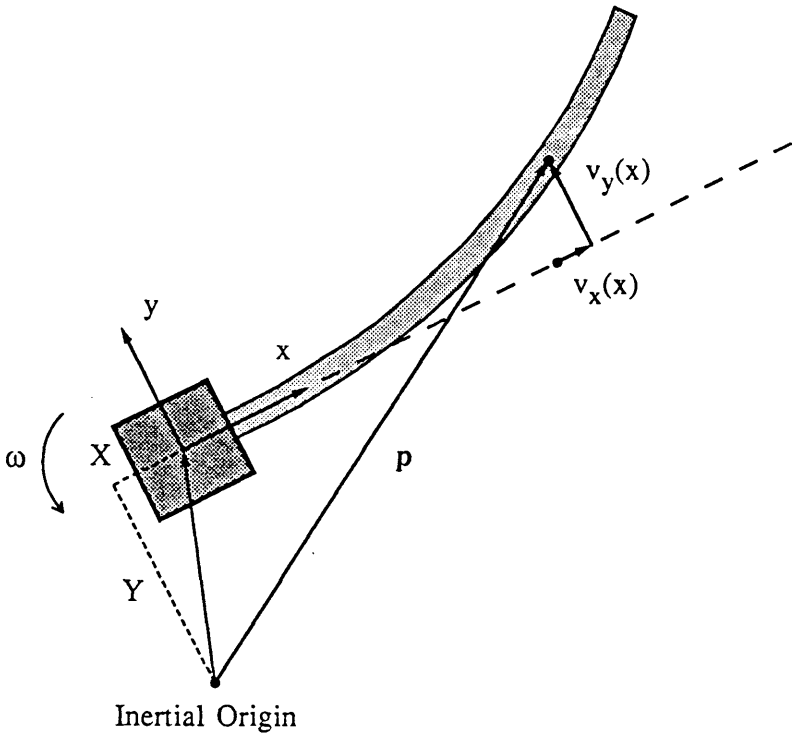

(a)

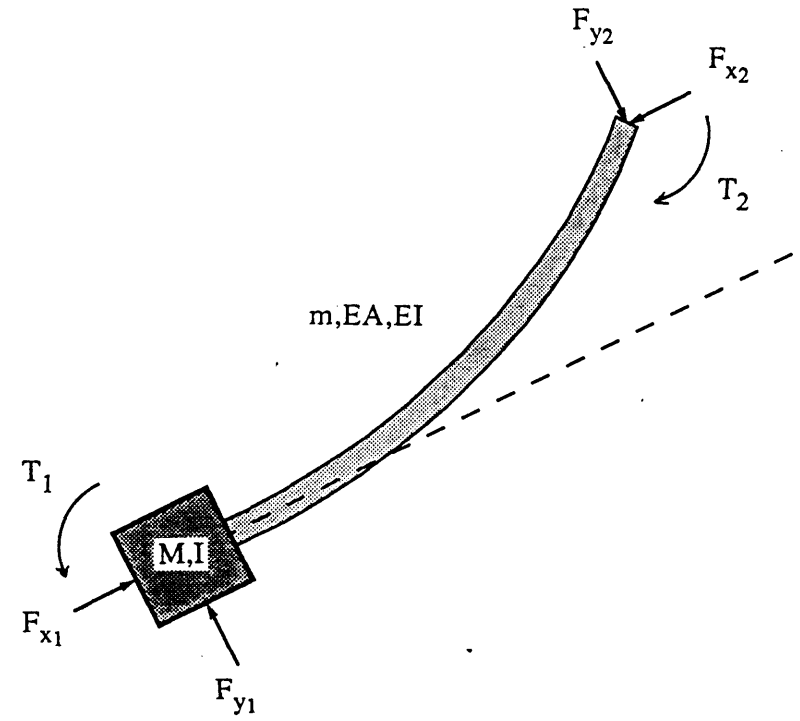

(b)

Fig. 3-1: Beam cantilevered to arbitrarily moving rigid mass: (a) Deformation geometry, (b) Physical properties and applied forces and torques.

Torques and forces can be applied to either end of the beam/mass system. The equations of motion will be derived using Hamilton's principle.

The vector from the inertial origin to an arbitrary point on the beam is given by

$$\mathbf{p} = \begin{bmatrix} X \\ Y \end{bmatrix} + \begin{bmatrix} x+v_x \\ v_y \end{bmatrix} \tag{3.1}$$

where all the vectors are expressed in body coordinates. Note that we have considered axial and transverse deformation in terms of independent variables. In fact, finite transverse deformation has a second order effect on axial displacement. While this effect can be neglected for small angular rates, it must be considered for large rates, as described in a later section. The velocity of the point, $\dot{\mathbf{p}}$, is given by

$$\dot{\mathbf{p}} = \begin{bmatrix} V_x \\ V_y \end{bmatrix} + \begin{bmatrix} \dot{v}_x - \omega v_y \\ \dot{v}_y + \omega(x+v_x) \end{bmatrix} \tag{3.2}$$

where

$$\begin{bmatrix} V_x \\ V_y \end{bmatrix} = \begin{bmatrix} \dot{X} - \omega Y \\ \dot{Y} + \omega X \end{bmatrix} \tag{3.3}$$

The kinetic energy for both the rigid mass and the beam can then be written

$$T = \tfrac{1}{2}M\left[V_x^2 + V_y^2\right] + \tfrac{1}{2}I\omega^2 + \tfrac{1}{2}m\int_0^L \left[V_x^2 + \dot{v}_x^2 + \omega^2\dot{v}_y^2 + 2\dot{v}_x V_x - 2\omega v_y V_x - 2\dot{v}_x\omega v_y \right.$$
$$\left. + V_y^2 + \dot{v}_y^2 + \omega^2(x+v_x)^2 + 2\dot{v}_y V_y + 2\omega(x+v_x)V_y + 2\dot{v}_y\omega(x+v_x)\right] dx \tag{3.4}$$

where M and I are the mass and inertia, respectively, of the lumped mass, m is the mass per unit length of the beam, and L is its total length. The potential energy due to bending and axial

extension is given by

$$U = \frac{1}{2}EI\int_0^L \left[\frac{\partial^2}{\partial x^2}v_y(x)\right]^2 dx + \frac{1}{2}EA\int_0^L \left[\frac{\partial}{\partial x}v_x(x)\right]^2 dx \tag{3.5}$$

Virtual work due to the external loads is given by

$$\begin{aligned}\delta W = {} & (F_{x_1}-F_{x_2})\delta X + (F_{y_1}-F_{y_2})\delta Y + \left[T_1 - T_2 + XF_{y_1} - Y(F_{x_1}-F_{x_2}) - (X+L)F_{y_2}\right]\delta\theta \\ & - F_{x_2}\delta v_x(L) - F_{y_2}\delta v_y(L) + \left[YF_{x_2} - (X+L)F_{y_2} - T_2\right]\delta v_y'(L)\end{aligned} \tag{3.6}$$

We now seek an expression for the variation in kinetic and potential energy due to all virtual displacements. Thus,

$$\begin{aligned}\int_{t_1}^{t_2}\delta(T-U)\,dt = {} & \int_{t_1}^{t_2}\Big\{ \left[(M+mL)V_x + m\int_0^L(\dot{v}_x - \omega v_y)\,dx\right]\delta V_x \\ & + \left[(M+mL)V_y + \frac{1}{2}mL^2\omega + m\int_0^L(\dot{v}_y + \omega v_x)\,dx\right]\delta V_y \\ & + \left[(I+\frac{1}{3}mL^3)\omega + \frac{1}{2}mL^2V_y + m\int_0^L(\omega\dot{v}_y^2 - \dot{v}_x v_y - v_y V_x + 2x\omega v_x + \omega v_x^2 + V_y v_x + x\dot{v}_y + v_x\dot{v}_y)\,dx\right]\delta\omega \\ & - m\int_0^L\left[(\omega V_x + \dot{v}_x\omega)\,\delta v_y - (\omega^2\dot{v}_y + \dot{v}_y + V_y + x\omega + \omega v_x)\,\delta\dot{v}_y\right]dx \\ & + m\int_0^L\left[(\omega V_y + x\omega^2 + \omega^2 v_x + \omega\dot{v}_y)\,\delta v_x + (V_x + \dot{v}_x - \omega v_y)\,\delta\dot{v}_x\right]dx \\ & - \int_0^L EA\left[\frac{\partial}{\partial x}v_x(x)\right]\delta\left[\frac{\partial}{\partial x}v_x(x)\right]dx - \int_0^L EI\left[\frac{\partial^2}{\partial x^2}v_y(x)\right]\delta\left[\frac{\partial^2}{\partial x^2}v_y(x)\right]dx \Big\}\,dt\end{aligned} \tag{3.7}$$

The terms involving spatial derivatives of v_x and v_y must now be integrated by parts, in order that there be no derivatives operating on δv_x or δv_y. The associated integrated terms determine the

boundary conditions for the system. We also have, from Eq. (3.3),

$$\delta V_x = \delta\dot{X} - \omega\delta Y - Y\delta\dot{\theta} \tag{3.8a}$$

$$\delta V_y = \delta\dot{Y} + \omega\delta X + X\delta\dot{\theta} \tag{3.8b}$$

$$\delta\omega = \delta\dot{\theta} \tag{3.8c}$$

Substituting these relations into the above expression and integrating by parts with respect to time leads to an expression that depends upon the variations δX, δY, $\delta\theta$, δv_x, and δv_y only. The integrated terms arising from these manipulations vanish at t_1 and t_2. We can then invoke Hamilton's principle:

$$\int_{t_1}^{t_2}\left[\delta(T-U)+\delta W\right] dt = 0, \qquad \left.\begin{matrix}\delta v_x=\delta v_y=0 \;\; 0\le x\le L \\ \delta X=\delta Y=\delta\theta=0\end{matrix}\right\} \; t=t_1,t_2 \tag{3.9}$$

Collecting the coefficients of δX, δY, $\delta\theta$, δv_x, and δv_y, and setting each to zero independently, leads to the five equations of motion for the system:

$$I_0\dot{\omega} + \tfrac{1}{2}mL^2(\dot{V}_y + \omega V_x) + m\int_0^L\left[x\ddot{v}_y - (\dot{V}_x - \omega V_y)v_y + (\dot{V}_y + \omega V_x)v_x + 2x(\dot{\omega}v_x + \omega\dot{v}_x)\right] dx = T_1 - T_2 - LF_{y_2} \tag{3.10a}$$

$$M_0(\dot{V}_y + \omega V_x) + \tfrac{1}{2}mL^2\dot{\omega} + m\int_0^L\left[\ddot{v}_y - \omega^2 v_y + \dot{\omega}v_x + 2\omega\dot{v}_x\right] dx = F_{y_1} - F_{y_2} \tag{3.10b}$$

$$M_0(\dot{V}_x - \omega V_y) - \tfrac{1}{2}mL^2\omega^2 + m\int_0^L\left[\ddot{v}_x - \omega^2 v_x - \dot{\omega}v_y - 2\omega\dot{v}_y\right] dx = F_{x_1} - F_{x_2} \tag{3.10c}$$

$$\ddot{v}_y + \frac{EI}{m}\frac{\partial^4}{\partial x^4}v_y - \omega^2 v_y = -\dot{\omega}x - (\dot{V}_y + \omega V_x) - \dot{\omega}v_x - 2\omega\dot{v}_x \tag{3.10d}$$

$$\ddot{v}_x - \frac{EA}{m}\frac{\partial^2}{\partial x^2}v_x - \omega^2 v_x = \omega^2 x - (\dot{V}_x - \omega V_y) + \dot{\omega}v_y + 2\omega\dot{v}_y \tag{3.10e}$$

where

$$M_0 = M+mL\,, \quad I_0 = I+\tfrac{1}{3}mL^3 \tag{3.11a,b}$$

These equations are quite complex, involving many nonlinear terms. For simplicity, we will assume that the rotation rate, ω, of the mass can be linearized about a constant value, Ω. This situation typically arises when analyzing the motion of rotating spacecraft with flexible appendages. The initial rotation rate remains more-or-less constant, with small perturbations from interaction with the appendages. Thus, substituting $\Omega+\omega$ for ω, and neglecting all remaining nonlinear terms, we are left with

$$I_0\dot{\omega} + \tfrac{1}{2}mL^2A_y + m\int_0^L \left[x\ddot{v}_y + 2x\Omega\dot{v}_x^p\right] dx = T_1 - T_2 - LF_{y_2} \tag{3.12a}$$

$$M_0 A_y + \tfrac{1}{2}mL^2\dot{\omega} + m\int_0^L \left[\ddot{v}_y - \Omega^2 v_y + 2\Omega\dot{v}_x^p\right] dx = F_{y_1} - F_{y_2} \tag{3.12b}$$

$$M_0 A_x - mL^2\Omega\omega + m\int_0^L \left[\ddot{v}_x^p - \Omega^2 v_x^p - 2\Omega\dot{v}_y\right] dx = F_{x_1} - F_{x_2} \tag{3.12c}$$

$$\ddot{v}_y + \frac{EI}{m}\frac{\partial^4}{\partial x^4}v_y - \Omega^2 v_y = -\dot{\omega}x - A_y - 2\Omega\dot{v}_x^p \tag{3.12d}$$

$$\ddot{v}_x^p - \frac{EA}{m}\frac{\partial^2}{\partial x^2}v_x^p - \Omega^2 v_x^p = \Omega^2 x + 2x\Omega\omega - A_x + 2\Omega\dot{v}_y \tag{3.12e}$$

where

$$A_x(t) = \dot{V}_x(t) - \Omega V_y(t) - A_x^{nom} \tag{3.13a}$$

$$A_y(t) = \dot{V}_y(t) + \Omega V_x(t) \tag{3.13b}$$

$$v_x^p(x,t) = v_x(x,t) - v_x^{nom}(x) \tag{3.13c}$$

This set of equations is referenced to the nominal deformed state of the system. In this reference state, the beam is under axial tension due to the rotation of the system, which results in a steady-

state axial displacement field, $v_x^{nom}(x)$. The rotation is about a center of mass which may not coincide with the zero-rotation center of mass, due to the axial stretching. Also, the variable A_x represents a perturbation from the nominal value of $-\Omega^2 d$, where d is the distance from the rigid mass to the center of mass of the structure in the deformed configuration. The remaining variables (V_x and v_y) are linearized about zero. A derivation of the exact nominal configuration under constant rotation can be found in Appendix B. To this set of equations we must add the boundary conditions

$$EI\frac{\partial^2}{\partial x^2}v_y(0) = I\dot{\omega} - T_1 \tag{3.14a}$$

$$EI\frac{\partial^3}{\partial x^3}v_y(0) = -MA_y + F_{y1} \tag{3.14b}$$

$$EA\frac{\partial}{\partial x}v_x(0) = MA_x - F_{x1} \tag{3.14c}$$

$$EI\frac{\partial^2}{\partial x^2}v_y(L) = -T_2 \tag{3.14d}$$

$$EI\frac{\partial^3}{\partial x^3}v_y(L) = F_{y2} \tag{3.14e}$$

$$EA\frac{\partial}{\partial x}v_x(L) = -F_{x2} \tag{3.14f}$$

These conditions can be derived either from force equilibrium considerations or directly from the integrated terms arising from the spatial integration by parts of Equation (3.7).

It should be noted that even small elastic deformations, when integrated over the length of the flexible appendage, may give rise to large angular rotations of cross sections of the appendage. As a result, a large bending deformation gives rise to a small amount of axial displacement towards the root of the appendage. This effect is called foreshortening, and is described in Fig. 3-2. While this phenomenon is of second order for small rigid angular rates, it becomes first order if the initial rotation rate is large. For sufficiently large rates, its effect is so pronounced that a mathematical model which excludes the required correction terms will incorrectly predict instability above a critical initial angular rate. (This inaccurate prediction is sometimes sarcastically referred to as "buckling under tension.") The treatment of foreshortening is deferred to Section 3.2.

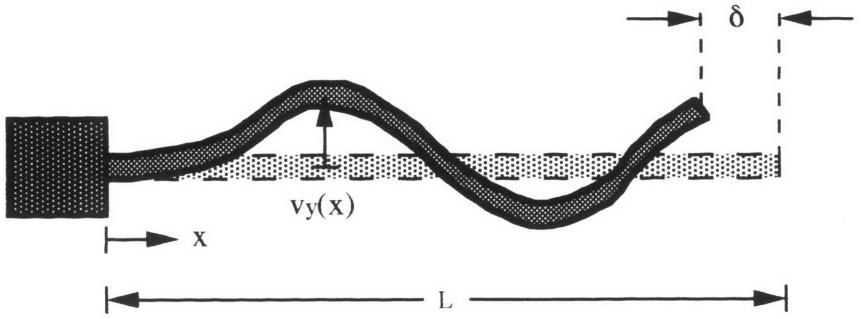

$$\delta \approx \frac{1}{2}\int_0^L \left[v_y(x) \right]^2 dx$$

Fig. 3-2: The foreshortening phenomenon arising from finite transverse deformation.

3.1.2 Solution of the Integral-Partial Differential Equations

Equations (3.12a-e) represent a linear system of integro-partial differential equations. In order to obtain an analytic solution, it is neccessary to transform the partial differential equations (3.12d) and (3.12e) into the frequency-domain, using the Laplace transform. In doing so, it will be possible to express the integrals arising on Equations (3.12a), (3.12b) and (3.12c) in terms of the boundary variables alone. The boundary conditions can then be used to relate these quantities to the applied forces. The result is a dynamic stiffness matrix, similar to the type discussed in the previous chapter. The inverse Laplace transform can then be used to convert the response of the system back into the time-domain.

It is convenient to normalize the equations of motion for the following development. By making the following definitions:

$$\hat{A}_x = \frac{1}{Ls^2}\bar{A}_x\,, \qquad \hat{A}_y = \frac{1}{Ls^2}\bar{A}_y\,, \qquad \hat{\omega} = \frac{1}{s}\bar{\omega} \tag{3.15a-c}$$

$$\hat{v}_x = \frac{1}{L}\bar{v}_x^p\,, \qquad \hat{v}_y = \frac{1}{L}\bar{v}_y \qquad \hat{\Omega} = \frac{1}{s}\Omega \tag{3.15d-f}$$

$$\hat{T} = \frac{1}{I_0 s^2}(\bar{T}_1 - \bar{T}_2 - L\bar{F}_{y2})\,, \quad \hat{F}_x = \frac{1}{M_0 L s^2}(\bar{F}_{x1} - \bar{F}_{x2})\,, \quad \hat{F}_y = \frac{1}{M_0 L s^2}(\bar{F}_{y1} - \bar{F}_{y2}) \tag{3.15g-i}$$

$$\alpha^4 = -\frac{mL^4 s^2}{EI}\,, \qquad \beta^2 = -\frac{mL^2 s^2}{EA} \tag{3.15j,k}$$

$$\gamma_M = -\frac{mL}{M_0}\,, \qquad \gamma_I = -\frac{mL^3}{I_0} \tag{3.15l,m}$$

the equations of motion become

$$\hat{\omega} + \frac{1}{2}\gamma_I\hat{A}_y + \gamma_I\left[\frac{1}{L^2}\int_0^L x\,\hat{v}_y\,dx\right] + 2\gamma_I\hat{\Omega}\left[\frac{1}{L^2}\int_0^L x\,\hat{v}_x\,dx\right] = \hat{T} \tag{3.16a}$$

$$\hat{A}_y + \frac{1}{2}\gamma_M\hat{\omega} + \gamma_M(1-\hat{\Omega}^2)\left[\frac{1}{L}\int_0^L \hat{v}_y\,dx\right] + 2\gamma_M\hat{\Omega}\left[\frac{1}{L}\int_0^L \hat{v}_x\,dx\right] = \hat{F}_y \tag{3.16b}$$

$$\hat{A}_x - \gamma_M\hat{\Omega}\hat{\omega} + \gamma_M(1-\hat{\Omega}^2)\left[\frac{1}{L}\int_0^L \hat{v}_x\,dx\right] - 2\gamma_M\hat{\Omega}\left[\frac{1}{L}\int_0^L \hat{v}_y\,dx\right] = \hat{F}_x \tag{3.16c}$$

$$L^4\frac{\partial^4}{\partial x^4}\hat{v}_y - \alpha^4(1-\hat{\Omega}^2)\hat{v}_y = 2\alpha^4\hat{\Omega}\hat{v}_x + \alpha^4\hat{A}_y + \alpha^4\frac{x}{L}\hat{\omega} \tag{3.16d}$$

$$L^2\frac{\partial^2}{\partial x^2}\hat{v}_x + \beta^2(1-\hat{\Omega}^2)\hat{v}_x = 2\beta^2\hat{\Omega}\hat{v}_y - \beta^2\hat{A}_x + 2\beta^2\hat{\Omega}\frac{x}{L}\hat{\omega} \tag{3.16e}$$

The two coupled partial differential equations are solved by defining the state and rigid motion vectors

$$\mathbf{x}(x) = \left[\hat{v}_y \quad L\frac{\partial}{\partial x}\hat{v}_y \quad L^2\frac{\partial^2}{\partial x^2}\hat{v}_y \quad L^3\frac{\partial^3}{\partial x^3}\hat{v}_y \quad \hat{v}_x \quad L\frac{\partial}{\partial x}\hat{v}_x\right]^T \tag{3.17a}$$

$$\mathbf{y} = \left[\hat{\omega} \quad \hat{A}_y \quad \hat{A}_x\right]^T \tag{3.17b}$$

and then solving the equivalent system

$$\frac{\partial}{\partial x}\mathbf{x}(x) = \frac{1}{L}\mathbf{A}\,\mathbf{x}(x) + \frac{1}{L}\mathbf{B}_0\mathbf{u} + \frac{x}{L^2}\mathbf{B}_1\mathbf{y} \tag{3.18}$$

where

$$\mathbf{A} = \begin{bmatrix} 0 & 1 & 0 & 0 & 0 & 0 \\ 0 & 0 & 1 & 0 & 0 & 0 \\ 0 & 0 & 0 & 1 & 0 & 0 \\ \alpha^4(1-\hat{\Omega}^2) & 0 & 0 & 0 & 2\alpha^4\hat{\Omega} & 0 \\ 0 & 0 & 0 & 0 & 0 & 1 \\ 2\beta^2\hat{\Omega} & 0 & 0 & 0 & -\beta^2(1-\hat{\Omega}^2) & 0 \end{bmatrix}, \quad \mathbf{B}_0 = \begin{bmatrix} 0 & 0 & 0 \\ 0 & 0 & 0 \\ 0 & 0 & 0 \\ 0 & \alpha^4 & 0 \\ 0 & 0 & 0 \\ 0 & 0 & -\beta^2 \end{bmatrix}, \quad \mathbf{B}_1 = \begin{bmatrix} 0 & 0 & 0 \\ 0 & 0 & 0 \\ 0 & 0 & 0 \\ \alpha^4 & 0 & 0 \\ 0 & 0 & 0 \\ 2\beta^2\hat{\Omega} & 0 & 0 \end{bmatrix} \tag{3.19a-c}$$

It is easy to show that this system has the solution

$$\mathbf{x}(x) = e^{\mathbf{A}(x/L)}\mathbf{x}(0) + \mathbf{A}^{-1}\left[e^{\mathbf{A}(x/L)} - \mathbf{I}\right]\mathbf{B}_0\mathbf{u} + \left[\mathbf{A}^{-2}\left[e^{\mathbf{A}(x/L)} - \mathbf{I}\right] - \frac{1}{2}\mathbf{A}^{-1}\right]\mathbf{B}_1\mathbf{y} \tag{3.20}$$

This solution can be determined by any of a number of methods and is verified by direct substitution. The state vector integrals then follow as

$$\frac{1}{L}\int_0^L \mathbf{x}(x)\,dx = \mathbf{F}\mathbf{x}(0) + \tilde{\mathbf{F}}\mathbf{y} \tag{3.21a}$$

$$\frac{1}{L^2}\int_0^L x\,\mathbf{x}(x)\,dx = \mathbf{G}\mathbf{x}(0) + \tilde{\mathbf{G}}\mathbf{y} \tag{3.21b}$$

with

$$\mathbf{F} = \mathbf{A}^{-1}\left[e^{\mathbf{A}} - \mathbf{I}\right], \quad \tilde{\mathbf{F}} = \mathbf{A}^{-1}\left[\mathbf{F} - \mathbf{I}\right]\mathbf{B}_0 + \left[\mathbf{A}^{-2}\left[\mathbf{F} - \mathbf{I}\right] - \frac{1}{2}\mathbf{A}^{-1}\right]\mathbf{B}_1 \tag{3.22a,b}$$

$$\mathbf{G} = \mathbf{A}^{-1}\left[e^{\mathbf{A}} - \mathbf{F}\right], \quad \tilde{\mathbf{G}} = \mathbf{A}^{-1}\left[\mathbf{G} - \frac{1}{2}\mathbf{I}\right]\mathbf{B}_0 + \left[\mathbf{A}^{-2}\left[\mathbf{G} - \frac{1}{2}\mathbf{I}\right] - \frac{1}{3}\mathbf{A}^{-1}\right]\mathbf{B}_1 \tag{3.22c,d}$$

Of the six natural boundary conditions given in Equations (3.14a-f), only three are used. The remaining three are replaced with the three essential conditions at x=0. The new set of normalized boundary conditions are then

$$\hat{v}_y(0) = 0 \tag{3.23a}$$

$$L\frac{\partial}{\partial x}\hat{v}_y(0) = 0 \tag{3.23b}$$

$$L^2\frac{\partial^2}{\partial x^2}\hat{v}_y(0) = -\frac{I}{mL^3}\alpha^4\hat{\omega} + \frac{I_0}{mL^3}\alpha^4\hat{T}_1 \tag{3.23c}$$

$$L^3\frac{\partial^3}{\partial x^3}\hat{v}_y(0) = \frac{M}{mL}\alpha^4\hat{A}_y - \frac{M_0}{mL}\alpha^4\hat{F}_{y1} \tag{3.23d}$$

$$\hat{v}_x(0) = 0 \tag{3.23e}$$

$$L\frac{\partial}{\partial x}\hat{v}_x(0) = -\frac{M}{mL}\beta^2\hat{A}_x + \frac{M_0}{mL}\beta^2\hat{F}_{x1} \tag{3.23f}$$

At this point, we have succeeded in expressing the transformed system as a set of thirteen linear equations in thirteen unknowns. The unknown variables are the four integrals found in Equations (3.12a-c), the six elements of the state vector **x** evaluated at x = 0, and the angular and linear accelerations of the rigid mass, represented by **y**. We can eliminate the integrals by substituting the appropriate partitions of Equations (3.21a,b) into Equations (3.12a-c). We can then eliminate the state vector unknowns by means of the above boundary conditions. We are therefore left with three equations in three unknowns, which can be represented symbolically as

$$\left[\mathbf{M} + \mathbf{C}(\mathbf{DE} + \tilde{\mathbf{D}})\right]\mathbf{y} = \left[\mathbf{I} + \mathbf{CDK} \mid -\mathbf{H}\right]\mathbf{f} \tag{3.24}$$

where

$$\mathbf{f} = \left[\hat{T}_1\ \hat{F}_{y1}\ \hat{F}_{x1}\ \hat{T}_2\ \hat{F}_{y2}\ \hat{F}_{x2}\right]^T \tag{3.25}$$

and

$$\mathbf{E} = \begin{bmatrix} -\frac{I}{mL^3}\alpha^4 & 0 & 0 \\ 0 & \frac{M}{mL}\alpha^4 & 0 \\ 0 & 0 & -\frac{M}{mL}\beta^2 \end{bmatrix}, \quad \mathbf{M} = \begin{bmatrix} 1 & \frac{1}{2}\gamma_I & 0 \\ \frac{1}{2}\gamma_M & 1 & 0 \\ -\gamma_M\hat{\Omega} & 0 & 1 \end{bmatrix}, \quad \mathbf{H} = \begin{bmatrix} 1 & L & 0 \\ 0 & 1 & 0 \\ 0 & 0 & 1 \end{bmatrix} \tag{3.26a-c}$$

$$\mathbf{K} = \begin{bmatrix} -\frac{I_0}{mL^3}\alpha^4 & 0 & 0 \\ 0 & \frac{M_0}{mL}\alpha^4 & 0 \\ 0 & 0 & -\frac{M_0}{mL}\beta^2 \end{bmatrix}, \quad \mathbf{C} = \begin{bmatrix} \gamma_I & 2\gamma_I\hat{\Omega} & 0 & 0 \\ 0 & 0 & \gamma_M(1-\hat{\Omega}^2) & 2\gamma_M\hat{\Omega} \\ 0 & 0 & -2\gamma_M\hat{\Omega} & \gamma_M(1-\hat{\Omega}^2) \end{bmatrix} \tag{3.26d,e}$$

$$\mathbf{D} = \begin{bmatrix} g_{13} & g_{14} & g_{16} \\ g_{53} & g_{54} & g_{56} \\ f_{13} & f_{14} & f_{16} \\ f_{53} & f_{54} & f_{56} \end{bmatrix}, \quad \tilde{\mathbf{D}} = \begin{bmatrix} \tilde{g}_{13} & \tilde{g}_{14} & \tilde{g}_{16} \\ \tilde{g}_{53} & \tilde{g}_{54} & \tilde{g}_{56} \\ \tilde{f}_{13} & \tilde{f}_{14} & \tilde{f}_{16} \\ \tilde{f}_{53} & \tilde{f}_{54} & \tilde{f}_{56} \end{bmatrix} \tag{3.26f,g}$$

Equation (3.24) has the general form of a dynamic stiffness equation, except that only the generalized displacements at x=0 are considered. It is a simple matter to augment these equations with three additional relations which involve the three generalized displacements at x=L. The stiffness matrix for this planar example is then 6-by-6, and relates the generalized boundary forces and displacements in the manner described in the previous chapter.

Observing Equations (3.18) and (3.19a), we see that, for this system, the axial and bending solutions are coupled. Consequently, the matrix exponential in Equation (3.20) has no analytical expression. The matrix exponential is therefore computed by first decomposing **A** into its eigenvectors and eigenvalues, taking the exponentials of the individual eigenvalues, and then reconstructing the matrix exponential using the same eigenvectors. Beyond this operation all calculations are performed numerically. An exception to this is when Ω is zero. In that case, an analytical solution to the dynamics of the system can be carried to completion. Without going into excessive detail, we present only the result here:

$$\begin{bmatrix} \gamma_M(\text{cdif-sdif}) + \frac{I}{M_0L^2}(\text{csum-sdif}) & \gamma_M(\text{ssum-cdif}) + (1-\gamma_M)(\text{csum-ssum}) \\ \gamma_M(\text{cdif}) - \frac{I}{M_0L^2}(\text{sdif}) & \gamma_M(\text{ssum}) + (1-\gamma_M)(\text{csum}) \end{bmatrix} \begin{bmatrix} \hat{\omega} \\ \hat{A}_y \end{bmatrix}$$

$$= \begin{bmatrix} \frac{I_0}{M_0L^2}(\text{csum-sdif}) & (\text{csum-ssum}) & -\frac{I_0}{M_0L^2} & -1 \\ -\frac{I_0}{M_0L^2}(\text{sdif}) & (\text{csum}) & 0 & -1 \end{bmatrix} \begin{bmatrix} \hat{T}_1 \\ \hat{F}_{y1} \\ \hat{T}_2 \\ \hat{F}_{y2} \end{bmatrix} \tag{3.27a}$$

$$\left[\gamma_M \frac{\sin\beta}{\beta} + (1-\gamma_M)\right] \hat{A}_x = \begin{bmatrix} \cos\beta & -1 \end{bmatrix} \begin{bmatrix} \hat{F}_{x1} \\ \hat{F}_{x2} \end{bmatrix} \tag{3.27b}$$

where

$$\text{csum} = \frac{1}{2}\left[\cosh\alpha+\cos\alpha\right], \qquad \text{ssum} = \frac{1}{2\alpha}\left[\sinh\alpha+\sin\alpha\right] \tag{3.28a,b}$$

$$\text{cdif} = \frac{1}{2\alpha^2}\left[\cosh\alpha-\cos\alpha\right], \qquad \text{sdif} = \frac{1}{2\alpha^3}\left[\sinh\alpha-\sin\alpha\right] \tag{3.28c,d}$$

Figures 3-3 through 3-6 compare several simulation runs using the TEM approach with results from simulations using the DISCOS multibody program. In the first two runs, there is no mass at the root of the beam, while in the remaining runs, the mass is set to 1.0 kg and the inertia is zero. The beam has a length of 1 m, and a mass distribution of 1.0 kg/m. The bending stiffness is set to 1.0 Nt-m^2 for the first and third runs, and is modified to 0.04 Nt-m^2 for the second and fourth runs. The beam model used in DISCOS consists of fourteen lumped masses, equally spaced along the length of the beam, with the first four free-free modes retained. The only forcing input is a torque pulse of constant amplitude of 1.0 Nt-m, lasting 0.1 second, applied to the rigid mass. Shown in the graphs are the linear and angular rates of the rigid mass, and the inertial position and angular orientation of the rigid mass. In all four runs, the value of Ω is set to zero. Consequently, the TEM formulation predicts no axial deformation.

The TEM and DISCOS runs agree reasonably well for the first and third cases, where the beam is relatively stiff. Because the Gibb's suppression factor used in the inverse Laplace transform tends to filter out that portion of the response higher in frequency than the sampling

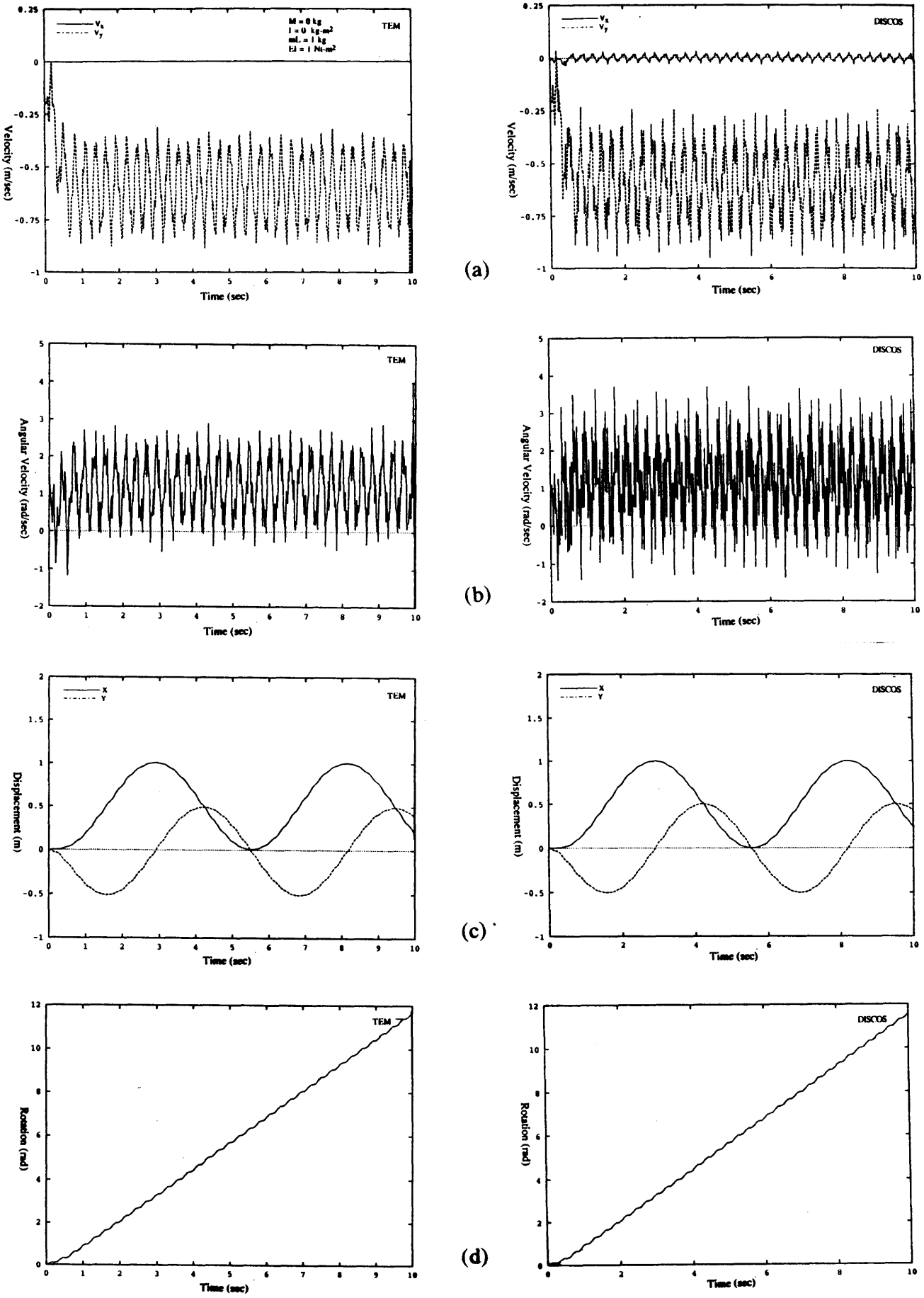

Fig. 3-3: Comparison of TEM and DISCOS simulations of mass/appendage system (first run): (a) Translational velocity of mass in body-fixed frame, (b) Angular velocity of mass, (c) Inertial position of rigid mass, (d) Rotation angle of rigid mass.

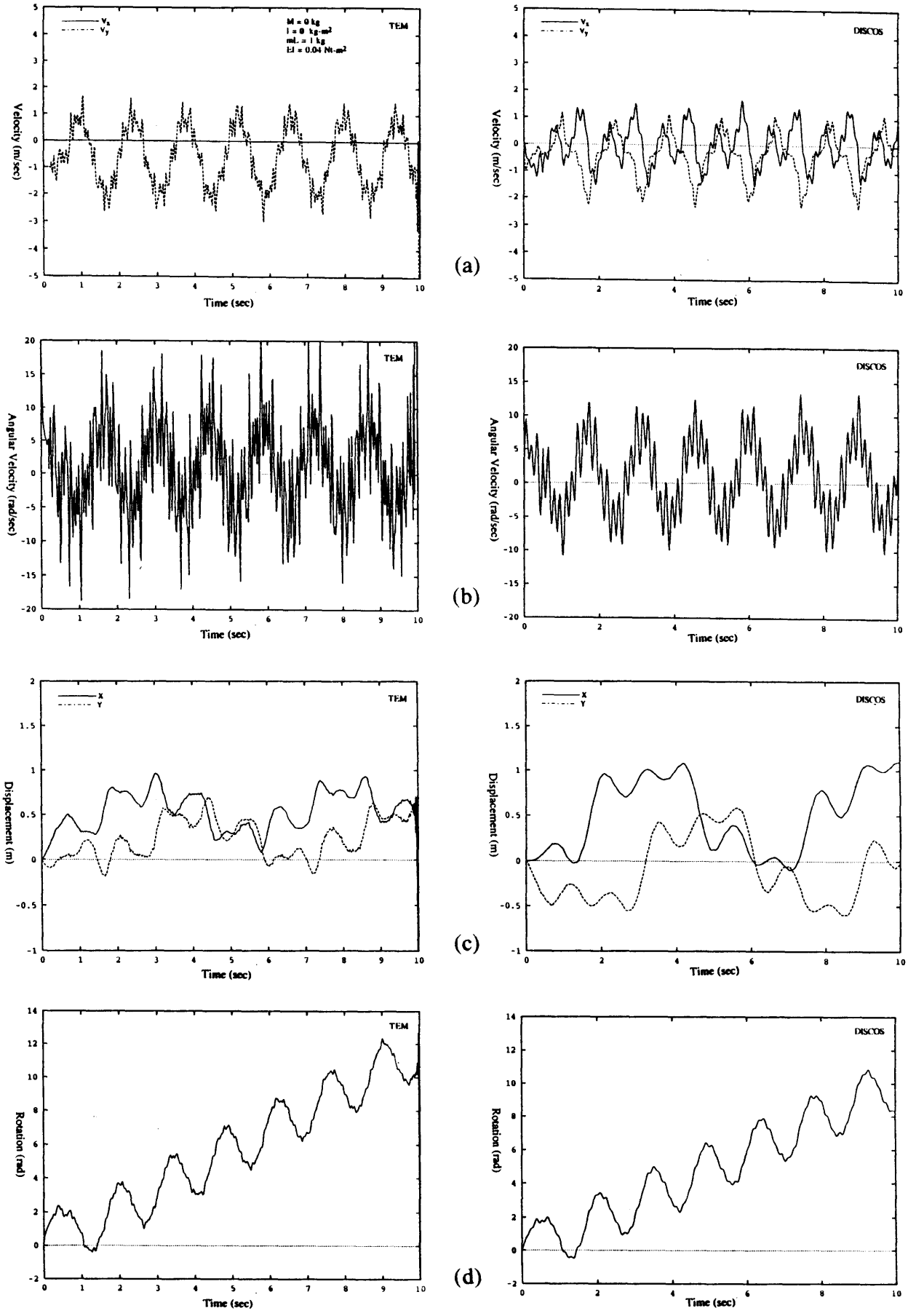

Fig. 3-4: Comparison of TEM and DISCOS simulations of mass/appendage system (second run): (a) Translational velocity of mass in body-fixed frame, (b) Angular velocity of mass, (c) Inertial position of rigid mass, (d) Rotation angle of rigid mass.

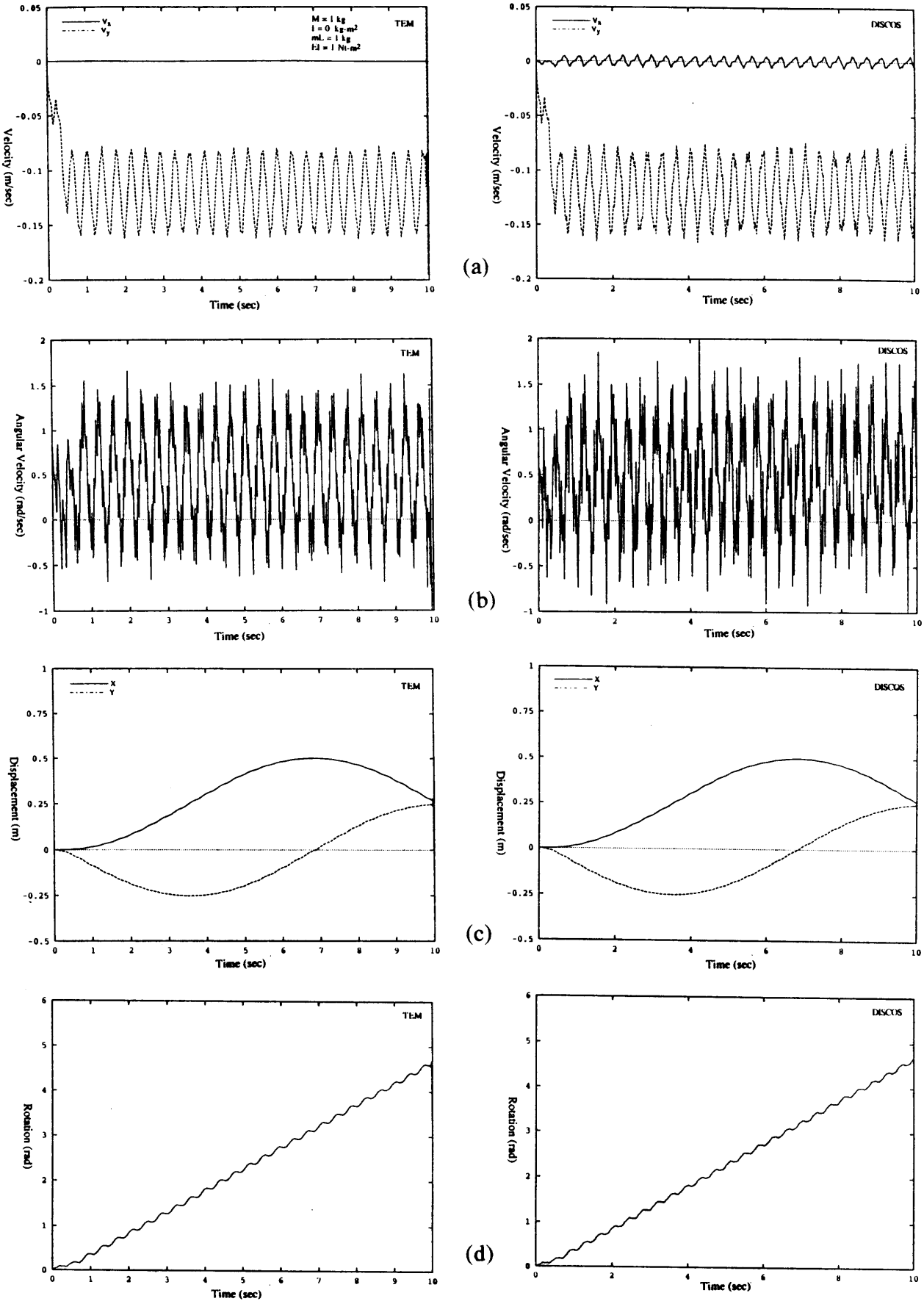

Fig. 3-5: Comparison of TEM and DISCOS simulations of mass/appendage system (third run): (a) Translational velocity of mass in body-fixed frame, (b) Angular velocity of mass, (c) Inertial position of rigid mass, (d) Rotation angle of rigid mass.

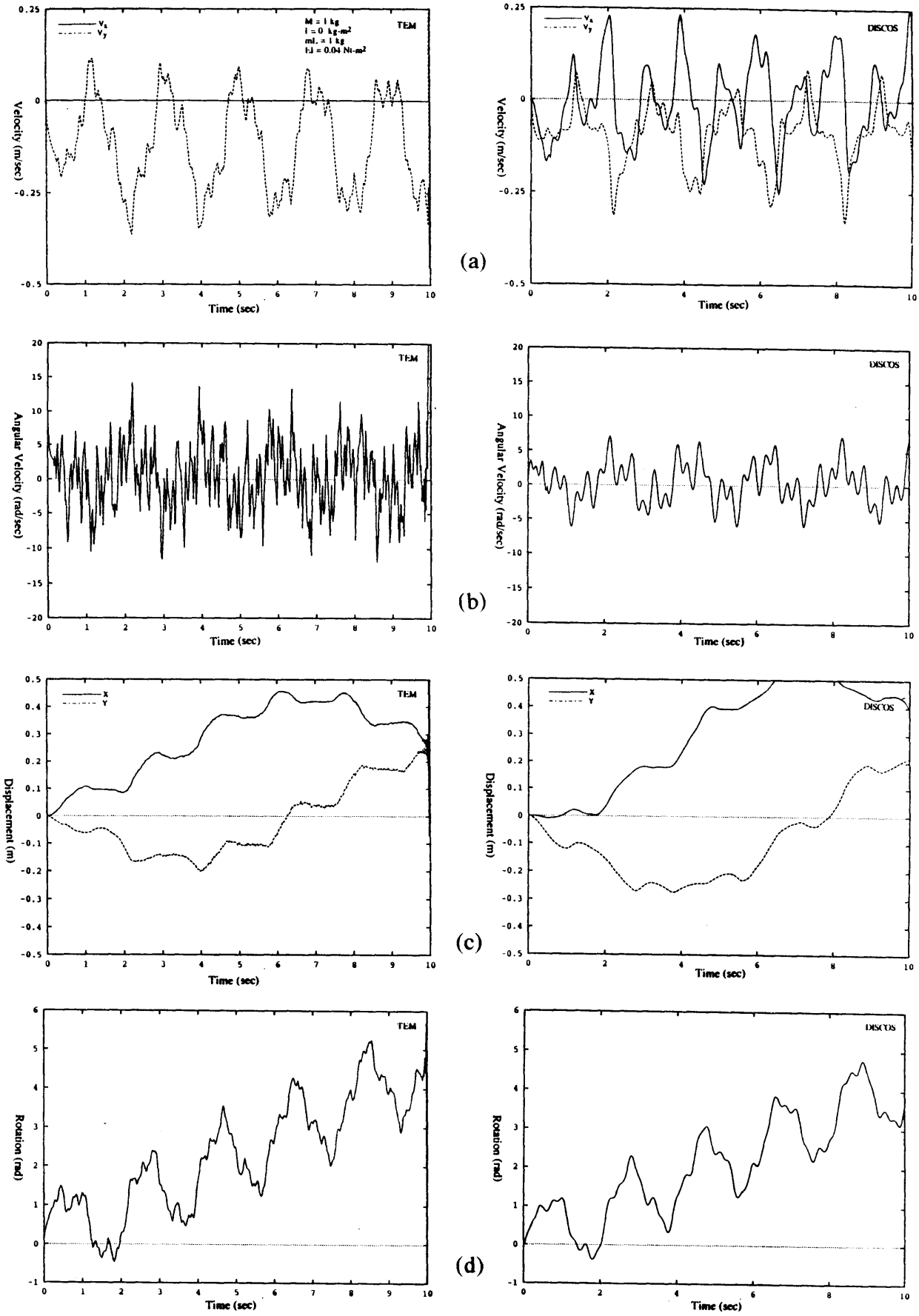

Fig. 3-6: Comparison of TEM and DISCOS simulations of mass/appendage system (fourth run): (a) Translational velocity of mass in body-fixed frame, (b) Angular velocity of mass, (c) Inertial position of rigid mass, (d) Rotation angle of rigid mass.

frequency, the TEM plots actually show less motion than the DISCOS plots. This occurs because the fourth mode of the beam (which is the highest mode included in the DISCOS model) is actually higher in frequency than the sampling frequency. In the second and fourth runs, where the stiffness is reduced, the TEM simulations do indeed display higher frequency motions. However, for these runs, the DISCOS model is capable of recovering the dynamics associated with the large deformational motion of the beam better than the TEM model. This is consistent with the TEM assumption that the angular velocity is small. The DISCOS methodology makes no such assumption. The reduced bending stiffness leads to large local angular rates at the point of torque application which are not captured in the TEM model. It is interesting to note, however, that the TEM and DISCOS simulations do agree reasonably well for the inertial positions and rotation angles, even in the runs with reduced bending stiffness.

3.2 Foreshortening Effects

As discussed above, the incorporation of foreshortening effects into the mathematical model is important when large initial angular rates are considered. In this section, we provide a simple second order correction term to the deformation kinematics. This term acts in the axial direction, adding to the deformation due to axial extension or compression.

When bending alone is considered, we can assume that the length of the flexible appendage remains constant. Denoting s as the distance travelled along the axis of the beam in the deformed configuration, we have the relationship

$$ds^2 = dx^2 + dy^2 \tag{3.29}$$

This equation can be solved for dx, yielding

$$dx = \sqrt{ds^2 - dy^2} = \sqrt{1 - (dy/ds)^2}\, ds \cong 1 - \frac{1}{2}\left[\frac{dy}{ds}\right]^2 \tag{3.30}$$

The last expression is correct to second order. To determine the deformed location, p(x), of a particular cross section of the beam in the deformed configuration, we would like to integrate this

second order expression with respect to s. However, the bending deformation is assumed to be a function of x. Fortunately, this does not present a problem, as the error introduced by replacing s with x is fourth order. Thus, we obtain

$$p(x) \cong x - \frac{1}{2}\int_0^x \left[\frac{dy}{dx}\right]^2 dx = x - \frac{1}{2}\int_0^x \left[\frac{d}{dx}v_y\right]^2 dx \tag{3.31}$$

The entire position vector, including axial effects, is then

$$\mathbf{p} = \begin{bmatrix} X + x + v_x - \frac{1}{2}\int_0^x \left[\frac{d}{dx}v_y\right]^2 dx \\ Y + v_y \end{bmatrix} \tag{3.32}$$

The equations of motion can be rederived using this modified kinematic relationship. In doing so, only one term contributes to the linearized equations of motion. Without digressing into a full derivation, we present only the results here. The variation in kinetic energy is modified to

$$\delta T' = \delta T - m\Omega^2 \int_0^L x \int_0^x \left[\frac{\partial}{\partial \xi}v_y(\xi)\right] \delta\left[\frac{\partial}{\partial \xi}v_y(\xi)\right] d\xi\, dx \tag{3.33}$$

This additional term is then integrated by parts twice, yielding

$$\begin{aligned} \delta T' &= \delta T + \frac{1}{2}m\Omega^2 \int_0^L x^2 \left[\frac{\partial}{\partial x}v_y(x)\right] \delta\left[\frac{\partial}{\partial x}v_y(x)\right] dx \\ &\quad - \left[\frac{1}{2}m\Omega^2 x^2 \int_0^x \left[\frac{\partial}{\partial \xi}v_y(\xi)\right] \delta\left[\frac{\partial}{\partial \xi}v_y(\xi)\right] d\xi\right]_0^L \\ &= \delta T - \frac{1}{2}m\Omega^2 \int_0^L (L^2 - x^2)\left[\frac{\partial}{\partial x}v_y(x)\right] \delta\left[\frac{\partial}{\partial x}v_y(x)\right] dx \\ &= \delta T - \frac{1}{2}m\Omega^2 \int_0^L \left[(L^2 - x^2)\left[\frac{\partial^2}{\partial x^2}v_y(x)\right] - 2x\left[\frac{\partial}{\partial x}v_y(x)\right]\right] \delta v_y(x)\, dx \end{aligned} \tag{3.34}$$

Upon application of Lagrange's equation, the modified bending equation becomes

$$\frac{EI}{m}\frac{\partial^4}{\partial x^4}v_y + \frac{1}{2}\Omega^2(L^2 - x^2)\frac{\partial^2}{\partial x^2}v_y - \Omega^2 x\frac{\partial}{\partial x}v_y - \Omega^2 v_y + \ddot{v}_y = -\dot{\omega}x - A_y - 2\Omega\dot{v}_x \qquad (3.35)$$

while the linearized equation for axial deformation remains unchanged. Note that the foreshortening terms vanish when Ω is zero, as expected.

Unfortunately, the presence of these terms makes it impossible to express the general solution to the system dynamics in the form of a matrix exponential. The reason is that the coefficients of the first and second spatial derivatives of v_y have spatial dependence. It may be possible to find an approximate solution, or express the exact solution in terms of special functions. Such an endeavor is considered beyond the scope of this thesis.

3.3 Discussion

By expressing the deformation of the flexible structure with respect to a moving reference frame, it is possible to apply the TEM methodology to structures undergoing arbitrarily large motions. Unfortunately, arbitrarily large angular motion of the total structure, which may include articulated joints, requires a nonlinear model for the correct description of both the dynamics of the motion and the kinematics at the joints. The nonlinearity arises because the individual reference frames with respect to which each flexible element is referenced may undergo large angular rotations and/or displacements with respect to one another. Future efforts should explore the use of perturbation techniques that allow the Laplace transform to be used while still including the effects of the nonlinear terms.

4 CONTROL DESIGN BASED ON TRANSFORM ELEMENT MODELS

Because the TEM formulation utilizes exact solutions to the mathematical models that describe structural dynamics behavior, it is possible to achieve remarkable nominal performance in open-loop slewing maneuvers of flexible structures. This is the subject of Section 4.1 of this chapter. By nominal, we mean that the response of the structure is assumed to be described exactly by the governing partial differential equations. Of course, the response of the actual structure will deviate from nominal due to modelling errors. Generally speaking, greater modelling errors lead to poorer performance. This is one of the fundamental motivating factors in the development of closed-loop control. Unfortunately, because the TEM methodology does not immediately yield a finite dimensional state-space representation of the structual model, traditional state-space control methods are not directly applicable in the closed-loop case. (In actuality, no finite representation can exist, as the mathematical model is of infinite order.) Methods for achieving closed-loop control solutions without state-space models are discussed in Section 4.2.

4.1 Open-Loop Control

In this section, we develop an open-loop control algorithm that takes advantage of the quality of the structural model available via the TEM methodology. We restrict attention to finite-time, linear maneuvers with a quadratic cost functional. We also assume that the structure is initially at rest. The desired terminal condition is expressed by

$$\mathbf{y}(t_f) = \mathbf{y}_d \tag{4.1}$$

where t_f is the maneuver time, $\mathbf{y}(t)$ is a vector of variables of interest, and $\mathbf{y}_d$ contains the desired terminal values of these variables. The elements of $\mathbf{y}$ could include, for example, the displacement and rotation of a rigid mass on the structure, or the relative transverse deflection of a point on a flexible member. The available control forces are also collected into a single vector, $\mathbf{q}_c(t)$, of

dimension N_c. These control forces are then a subset of the global generalized forces defined by the system model. In order that these forces be continuous in time, we must impose the additional constraint

$$\mathbf{q}_c(0) = \mathbf{q}_c(t_f) = \mathbf{0} \tag{4.2}$$

Also, the quadratic cost functional is given by

$$J = \frac{1}{2}\left[\mathbf{y}(t_f) - \mathbf{y}_d\right]^T \mathbf{R}_{yy}\left[\mathbf{y}(t_f) - \mathbf{y}_d\right] + \frac{1}{2}\int_0^{t_f}\left[\mathbf{q}_c(t)^T \mathbf{R}_{qq}\,\mathbf{q}_c(t) + \dot{\mathbf{q}}_c(t)^T \tilde{\mathbf{R}}_{qq}\,\dot{\mathbf{q}}_c(t)\right] dt \tag{4.3}$$

where $\mathbf{R}_{yy}$, $\mathbf{R}_{qq}$, and $\tilde{\mathbf{R}}_{qq}$ are symmetric, positive definite weighting matrices.

We must now express the output vector in terms of the control vector via the system dynamics. This is accomplished using the convolution integral

$$\mathbf{y}(t) = \int_0^t \mathbf{G}_y(t-\tau)\,\mathbf{q}_c(\tau)\,d\tau \tag{4.4}$$

where $\mathbf{G}_y(t)$ represents the impulse response matrix relating $\mathbf{y}(t)$ to $\mathbf{q}_c(t)$. The convolution integral is calculated efficiently using the inverse Laplace transform algorithm of Sec. 2.2:

$$\mathbf{y}(t) = L^{-1}\left[\mathbf{G}_y(s)\,\mathbf{q}_c(s)\right] \tag{4.5}$$

4.1.1 Finite-basis control approximation

By substituting Eq. (4.4) in Eq. (4.3), we observe that the cost functional depends on $\mathbf{q}_c(t)$ only. Setting the first variation in cost to zero therefore yields

$$\delta J = \left[\int_0^{t_f} \mathbf{G}_y(t_f-t)\,\mathbf{q}_c(t)\,dt - \mathbf{y}_d\right]^T \mathbf{R}_{yy}\left[\int_0^{t_f} \mathbf{G}_y(t_f-t)\,\delta\mathbf{q}_c(t)\,dt\right]$$
$$+ \int_0^{t_f}\left[\mathbf{q}_c(t)^T \mathbf{R}_{qq}\,\delta\mathbf{q}_c(t) + \dot{\mathbf{q}}_c(t)^T \tilde{\mathbf{R}}_{qq}\,\delta\dot{\mathbf{q}}_c(t)\right] dt = 0 \tag{4.6}$$

The problem then lies in solving this equation for $\mathbf{q}_c(t)$. Unfortunately, this is not a simple matter, as both the control vector and its variation appear within the integrals. However, if the control inputs are restricted to a subspace spanned by a finite set of basis functions defined over the interval $[0,t_f]$, a numerical solution is easily obtained. Each control input is first approximated by

$$\mathbf{q}_{c_i}(t) = \mathbf{f}_q(t)^T \mathbf{c}_i, \quad i = 1,...,N_c \tag{4.7}$$

where $\mathbf{f}_q(t)$ is a vector of known basis functions of time (usually sine and cosine functions), and $\mathbf{c}_i$ is a vector of undetermined coefficients corresponding to the i'th control input. The entire control vector can then be conveniently expressed as

$$\mathbf{q}_c(t) = \mathbf{F}_q(t)\,\mathbf{c} \tag{4.8}$$

where the following definitions have been used:

$$\mathbf{F}_q(t) = \begin{bmatrix} \mathbf{f}_q(t)^T & & \mathbf{0} \\ & \mathbf{f}_q(t)^T & \\ \mathbf{0} & & \mathbf{f}_q(t)^T \end{bmatrix}, \quad \mathbf{c} = \begin{bmatrix} \mathbf{c}_1 \\ \vdots \\ \mathbf{c}_{N_c} \end{bmatrix} \tag{4.9a,b}$$

Using this finite-basis approximation, the optimal control problem is reduced to determining the coefficient vector, $\mathbf{c}$. The variations in the control vector are then

$$\delta\mathbf{q}_c(t) = \mathbf{F}_q(t)\,\delta\mathbf{c}, \quad \delta\dot{\mathbf{q}}_c(t) = \dot{\mathbf{F}}_q(t)\,\delta\mathbf{c} \tag{4.10a,b}$$

and the constraints given by Eq. (4.2) reduce to

$$\mathbf{F}_q(0)\,\mathbf{c} = \mathbf{F}_q(t_f)\,\mathbf{c} = \mathbf{0} \tag{4.11}$$

Furthermore, the vector of desired outputs is expressed by

$$\mathbf{y}(t_f) = \mathbf{Y}(t_f)\,\mathbf{c} \tag{4.12}$$

where $\mathbf{Y}(t)$ is the basis function response matrix, and is given by

$$\mathbf{Y}(t) = \int_0^t \mathbf{G}_y(t-\tau)\,\mathbf{F}_q(\tau)\,d\tau = L^{-1}\left[\mathbf{G}_y(s)\,\mathbf{F}_q(s)\right] \tag{4.13}$$

4.1.2 Solution without minimization

Grouping Eqs. (4.11) and (4.12) yields the matrix equation

$$\begin{bmatrix} \mathbf{Y}(t_f) \\ \mathbf{F}_q(0) \\ \mathbf{F}_q(t_f) \end{bmatrix} \mathbf{c} = \begin{bmatrix} \mathbf{y}_d \\ \mathbf{0} \\ \mathbf{0} \end{bmatrix} \tag{4.14}$$

If the number of desired outputs and the number of unknown coefficients are such that the matrix in this equation is square, then $\mathbf{c}$ is uniquely determined. Typically, however, there are many elements in $\mathbf{c}$, so that Eq. (4.14) is underdetermined. Consequently, many choices for $\mathbf{c}$ will meet the terminal constraints. We therefore have some freedom in choosing which particular $\mathbf{c}$ to use. For a given problem, the particular choice minimizes some predefined cost functional, which provides a measure of nominal performance. The next two subsections describe two such cost functionals.

4.1.3 Minimization with point constraints

We first use the cost functional given by Eq. (4.3) and adjoin the constraints given by Eq. (4.11) via two Lagrange multipliers, λ_0 and λ_f. Taking variations in $\mathbf{c}$ yields

$$\begin{aligned} \delta J = & \left[\mathbf{Y}(t_f)\mathbf{c} - \mathbf{y}_d\right]^T \mathbf{R}_{yy} \mathbf{Y}(t_f)\, \delta\mathbf{c} \\ & + \mathbf{c}^T \left\{ \int_0^{t_f} \left[\mathbf{F}_q(t)^T \mathbf{R}_{qq} \mathbf{F}_q(t) + \dot{\mathbf{F}}_q(t)^T \tilde{\mathbf{R}}_{qq} \dot{\mathbf{F}}_q(t) \right] dt \right\} \delta\mathbf{c} \\ & + \lambda_0^T \mathbf{F}_q(0)\, \delta\mathbf{c} + \lambda_f^T \mathbf{F}_q(t_f)\, \delta\mathbf{c} + \delta\lambda_0^T \mathbf{F}_q(0)\, \mathbf{c} + \delta\lambda_f^T \mathbf{F}_q(t_f)\, \mathbf{c} = 0 \end{aligned} \tag{4.15}$$

leading to the following matrix equation:

$$\begin{bmatrix} \mathbf{W} & \mathbf{F}_q(0)^T & \mathbf{F}_q(t_f)^T \\ \mathbf{F}_q(0) & \mathbf{0} & \mathbf{0} \\ \mathbf{F}_q(t_f) & \mathbf{0} & \mathbf{0} \end{bmatrix} \begin{bmatrix} \mathbf{c} \\ \lambda_0 \\ \lambda_f \end{bmatrix} = \begin{bmatrix} \mathbf{Y}(t_f)^T \mathbf{R}_{yy} \mathbf{y}_d \\ \mathbf{0} \\ \mathbf{0} \end{bmatrix} \tag{4.16}$$

where

$$W = Y(t_f)^T R_{yy} Y(t_f) + \int_0^{t_f} \left[F_q(t)^T R_{qq} F_q(t) + \dot{F}_q(t)^T \tilde{R}_{qq} \dot{F}_q(t) \right] dt \qquad (4.17)$$

This is a symmetric system, and can be solved using standard linear algebra routines.

A unique advantage of this approach is that it readily accommodates penalties in higher derivatives of both control effort and structural deformation. In the frequency-domain, differentiation merely requires multiplication of the data by the Laplace transform variable. The inverse transformation then produces the derivative of the original signal. Higher order derivatives are obtained by multiplying by higher powers of the complex frequency. Incorporating higher derivative penalties in the traditional optimal control formulation is considerably more difficult.

It should be noted that the only approximation in the entire development involves expressing the control inputs in terms of the basis functions. The dynamics of the entire structure are accounted for, since the impulse responses are exact (insofar as the original equations represent physical reality). Also, the structural deformations are assumed to be small, so that linearization does not introduce significant errors. As a result, large angle slew maneuvers are not included in this class of problems. It is possible, however, to express structural deformations with respect to a nominal condition during a large angle slew, and then linearize about that reference, as discussed in the previous chapter.

In an earlier analytical study by Skaar [50], the open-loop control of a rigid mass with a flexible appendage, shown in Fig. 4-1, was studied. The appendage can undergo both axial and bending deformation. In his work, structural deformation penalties were not incorporated into the cost function; rather, the terminal conditions were adjoined to the cost functional as constraints. Skaar derived analytical expressions for impulse responses of the simple mass/appendage structure and thus obtained closed form optimal control solutions for the structure. Though successful for this application, his approach does not readily generalize for more complex structures. In contrast, the formulation presented here readily generalizes for realistic complex structures. Skaar's example, however, is used as a first example to validate the optimal control formulation.

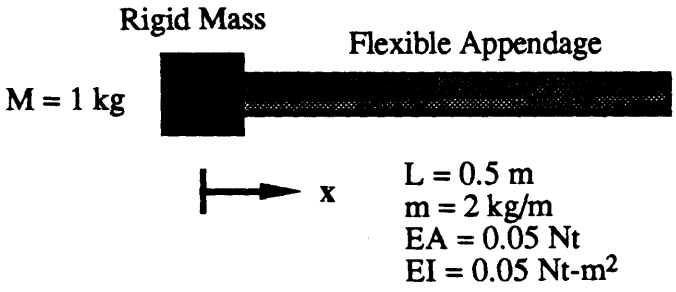

Fig. 4-1: Simple mass/flexible appendage structural model used in the open-loop optimal control demonstrations.

The maneuver involves translating the mass a distance of 10 meters along the axis of the flexible appendage, bringing it to rest with minimal residual energy and post-maneuver drift after 20 seconds. Thus, the axial deformation of the appendage is to be suppressed. The first case places terminal penalties on the final position and velocity of the rigid mass and on a point 0.8 of the length along the flexible appendage. A small penalty is also placed on control rate (to keep it bounded), and 17 basis functions are used to approximate the control input. By keeping the control penalty small, the penalties on defomation at the final time essentially become terminal constraints. The results, shown in Fig. 4-2, indicate that the terminal conditions are matched, and residual energy is negligible. In the second case, the member stiffness is reduced by a factor of four, so that the primary modal frequency of the structure corresponds, approximately, to the frequency of the first basis function of the control input. The results of this case, presented in Fig. 4-3, indicate that the control input has been adjusted so that excitation of the primary mode of the structure is suppressed. Again, the terminal conditions are matched, and residual internal energy is negligible.

The second example is the SCOLE structure analysed in Sec. 2.6.2. The maneuver presented here consists of a ten second, 0.1 radian rotation about the z-axis of the shuttle. This maneuver is a purely academic exercise, and is unrelated to the maneuver specified in the original design challenge. For the first case, torque controls directed along the z-axis are placed at either end of the mast (nodes 2 and 3). Due to the asymmetry of the structure, gyroscopic coupling is expected. Consequently, roll and pitch torque controls are also located on the shuttle (node 2). The cost of control effort is equally weighted among the control inputs, and is kept small to ensure that the terminal conditions are satisfied. Equal terminal magnitude and rate penalties are applied to the roll, pitch and yaw angles of the shuttle, as well as the torsional deformation of the mast at its midpoint and at the mast/antenna junction.

The results of the first SCOLE slew are shown in Fig. 4-4. It is clear that, although the shuttle has rotated the prescribed amount, there is a small amount of residual torsional energy in the structure. This energy is due primarily to the deformation of the antenna and mast at the terminal

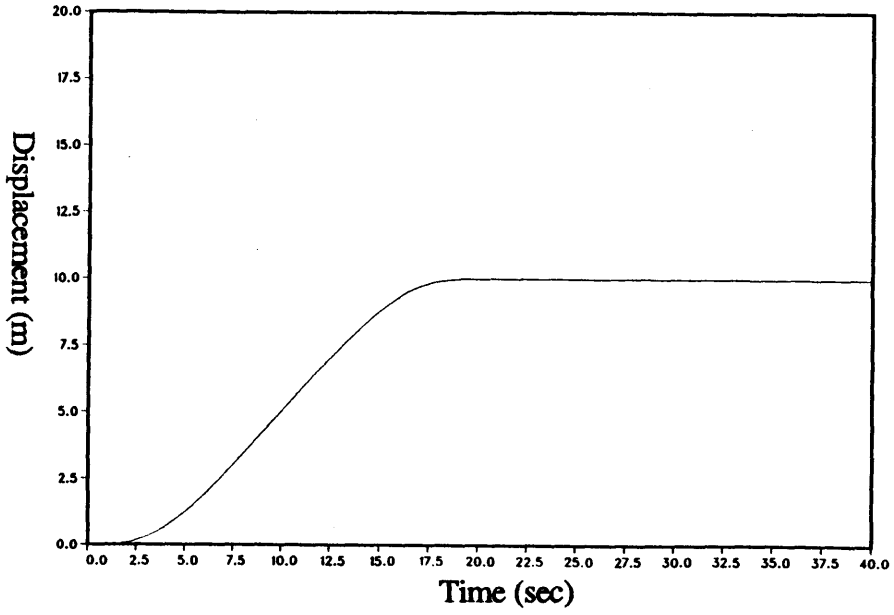

(a)

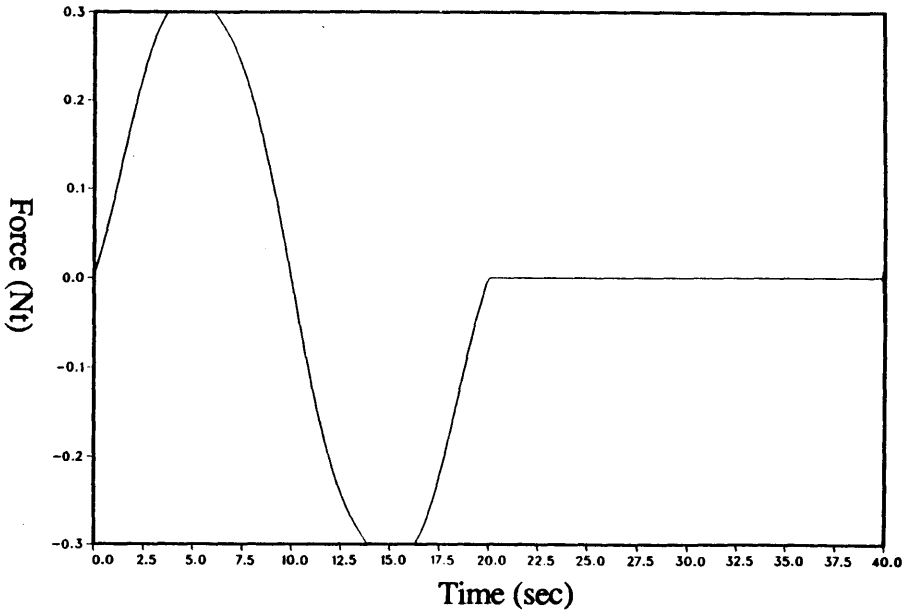

(b)

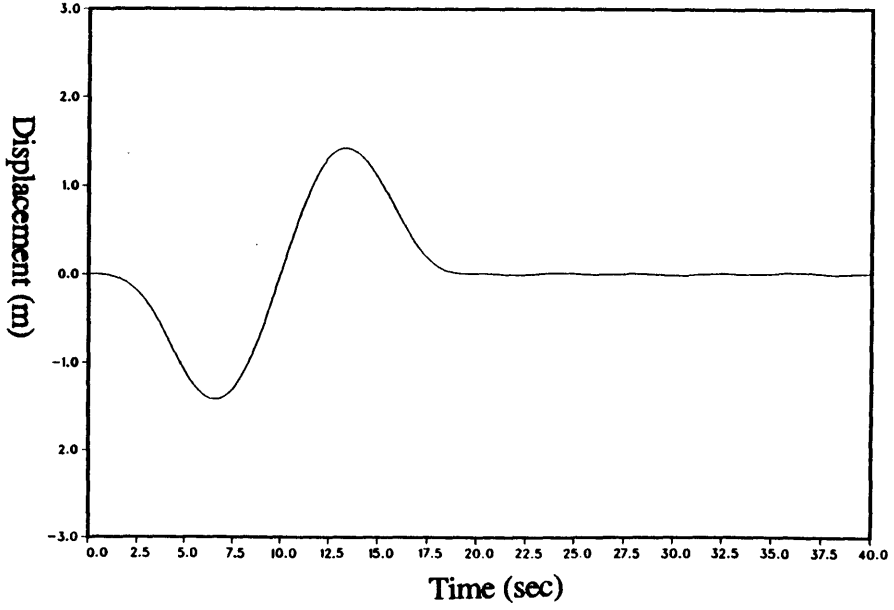

(c)

Fig. 4-2: Results of optimal maneuver of mass/flexible appendage system: (a) position of rigid mass, (b) control force applied to rigid mass, (c) deformation of tip of flexible appendage with respect to position of rigid mass.

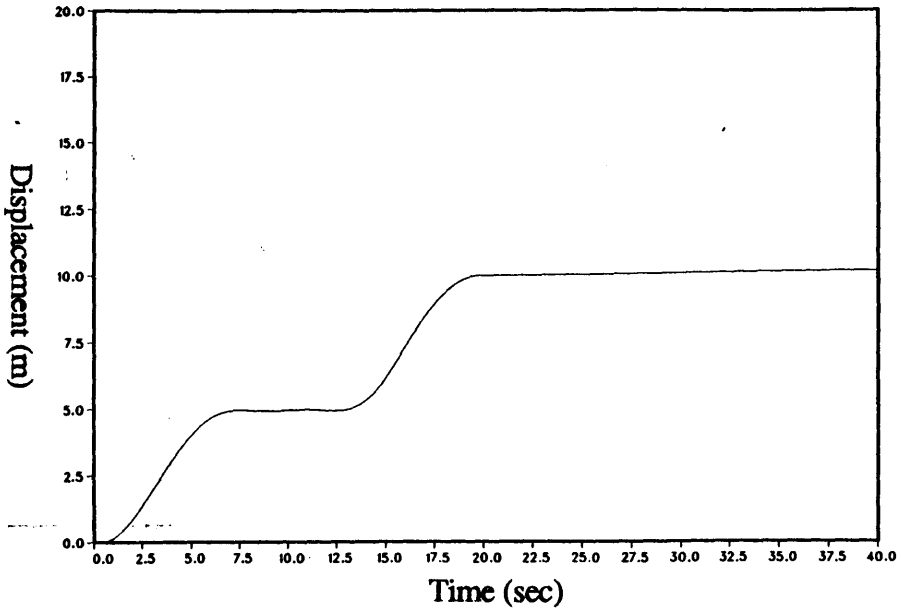

(a)

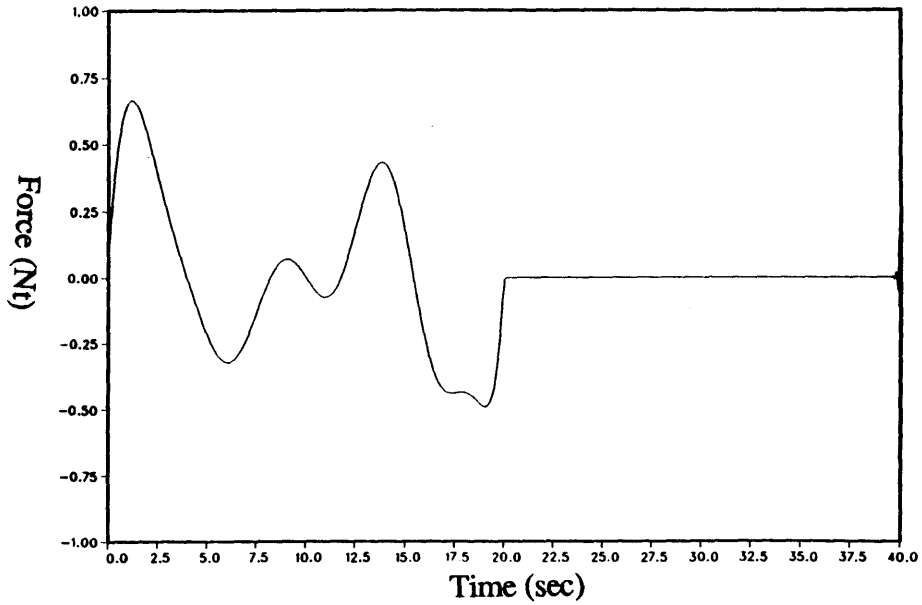

(b)

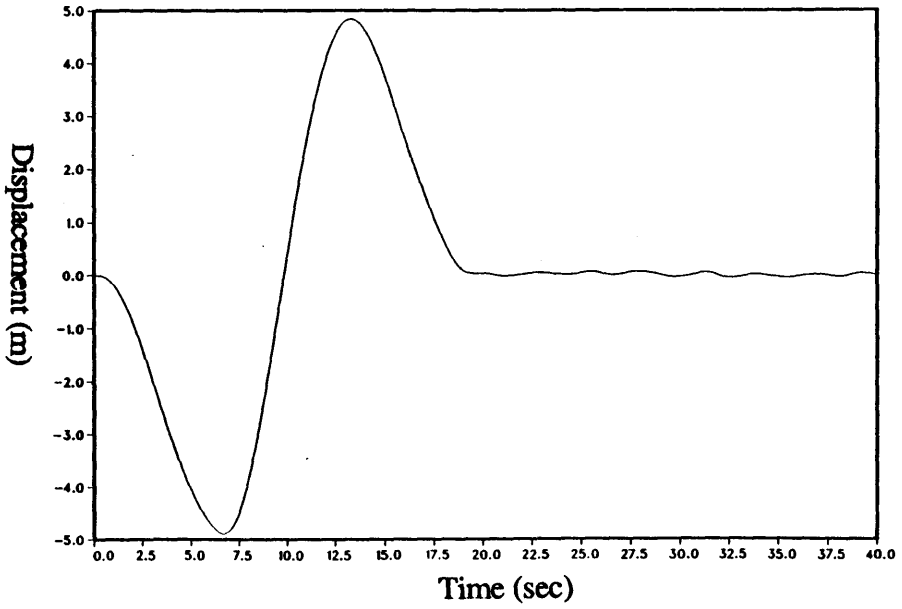

(c)

Fig. 4-3: Results of optimal maneuver of mass/flexible appendage system with reduced axial stiffness: (a) position of rigid mass, (b) control force applied to rigid mass, (c) deformation of tip of flexible appendage with respect to position of rigid mass.

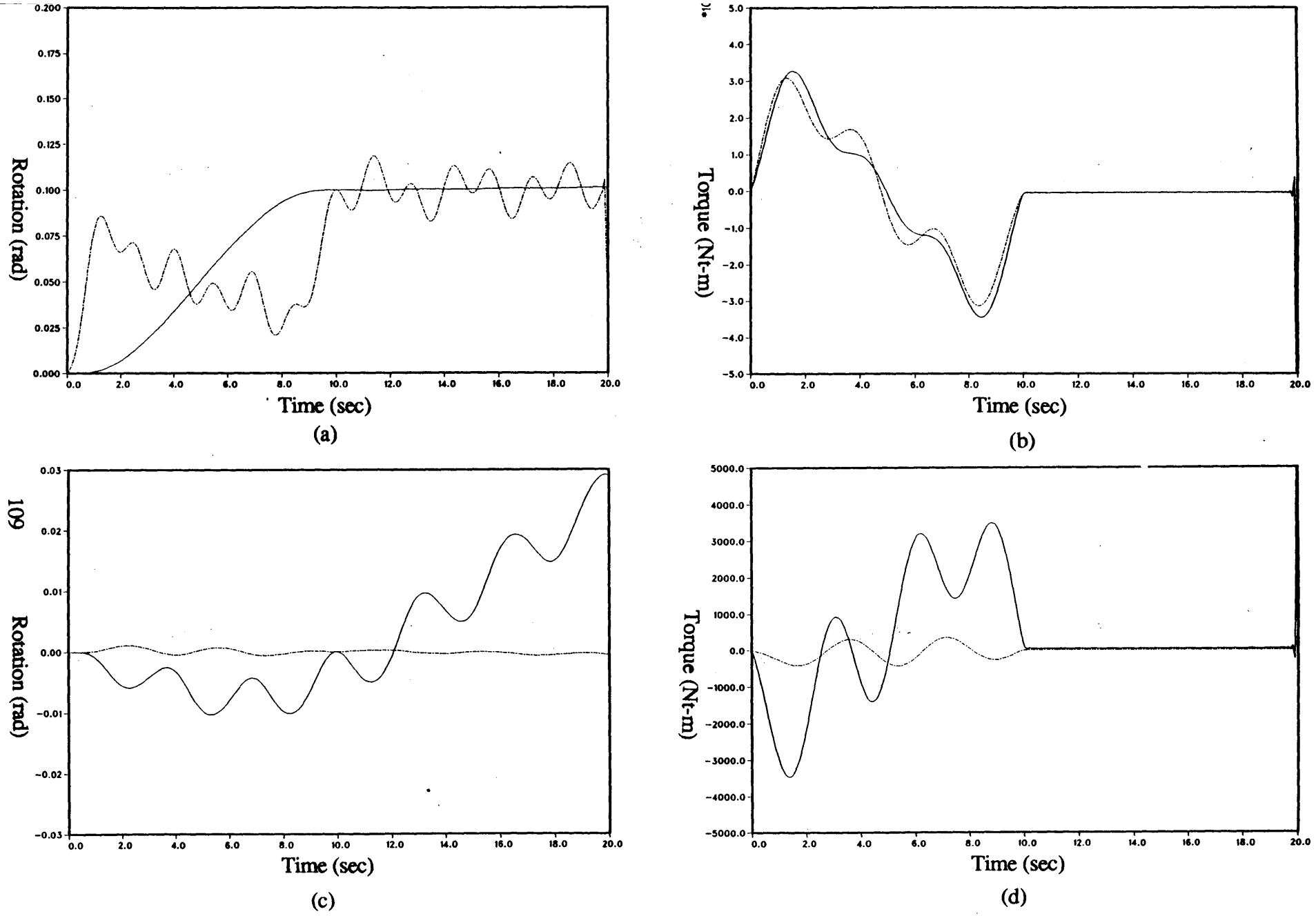

Fig. 4-4: Optimal rotational slew of SCOLE structure with four control inputs (see text): (a) yaw angle of shuttle (———) and rotation of node 3 about z-axis (- · -), (b) yaw torque applied to shuttle (———) and node 3 about z-axis (- · -), (c) roll angle (———) and pitch angle (- · -) of shuttle, (d) roll torque (———) and pitch torque (- · -) applied to shuttle.

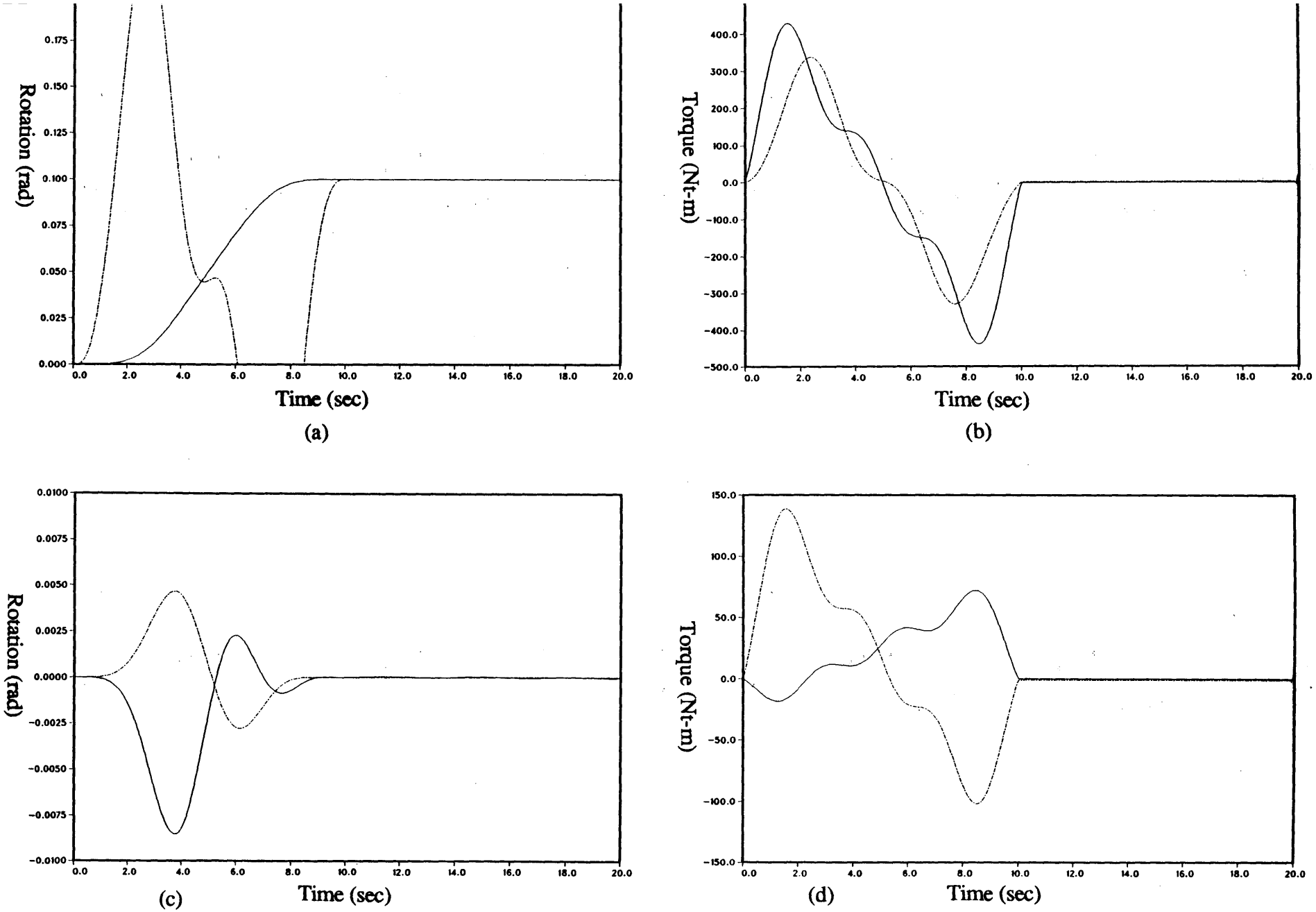

Fig. 4-5: Optimal rotational slew of SCOLE structure with nine control inputs (see text): (a) yaw angle of shuttle (———) and rotation of node 3 about z-axis (- · -), (b) yaw torque applied to shuttle (———) and node 3 about z-axis (- · -), (c) roll angle (———) and pitch angle (- · -) of shuttle, (d) roll torque (———) and pitch torque (- · -) applied to shuttle,

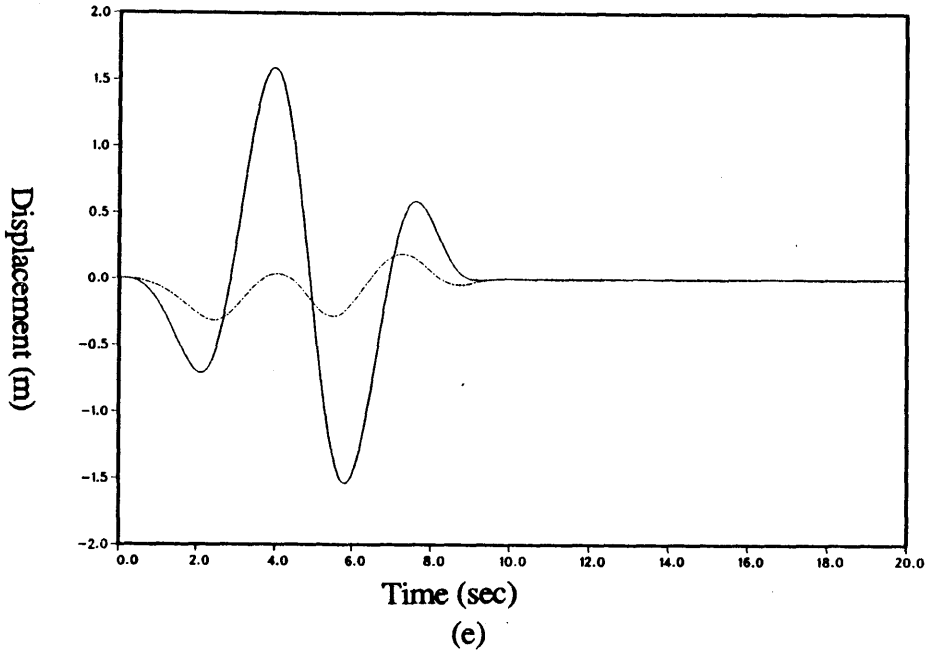

(e)

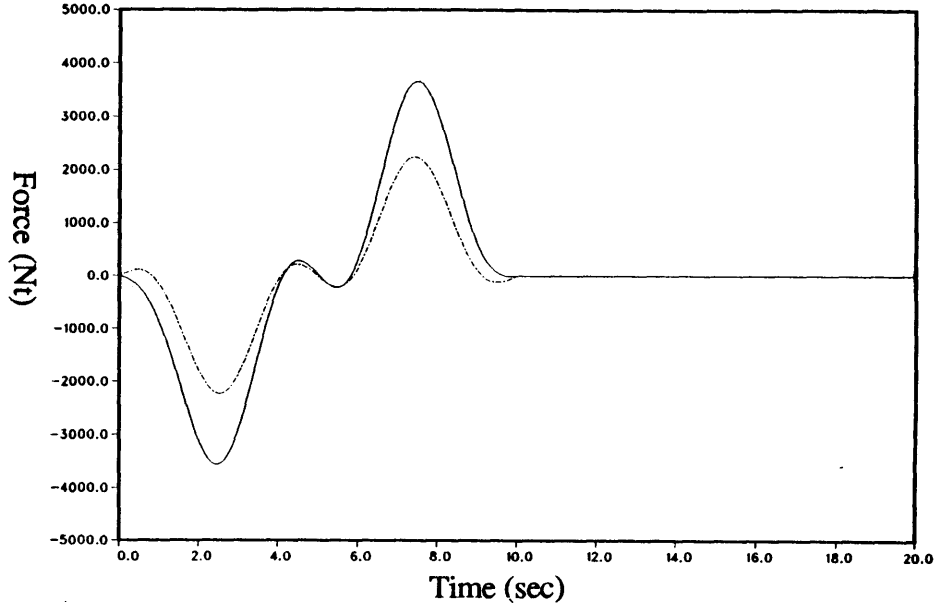

(f)

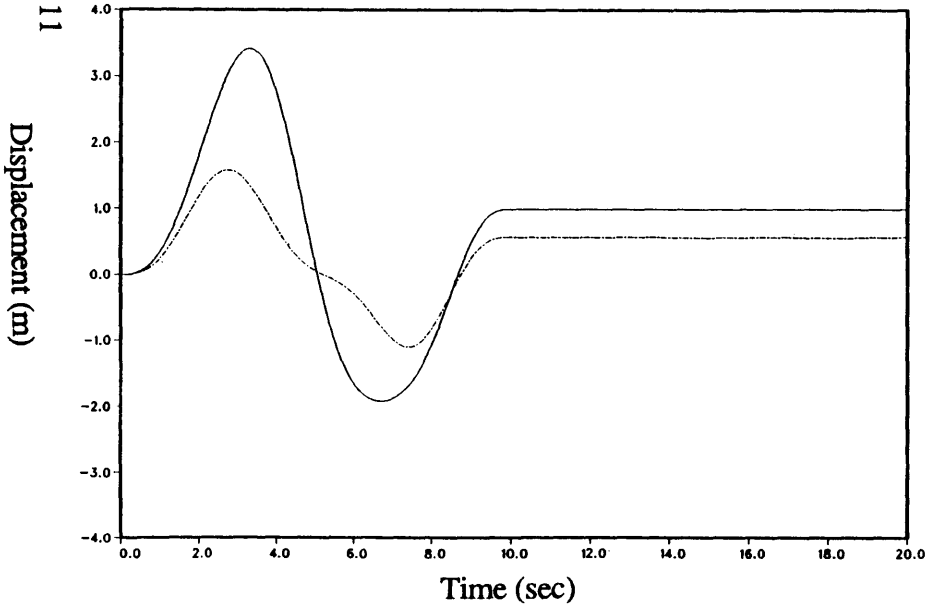

(g)

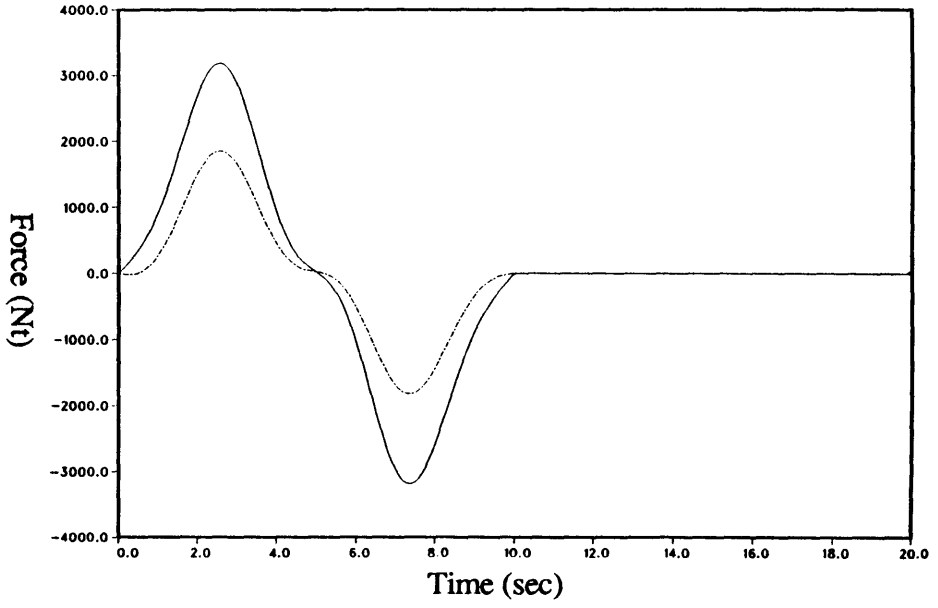

(h)

Fig. 4-5: (Continued) (e) deflection of node 3 in x-direction (———) and y-direction (- · -), (f) control force applied to node 3 in x-direction (———) and y-direction (- · -), (g) deflection of node 6 in x-direction (———) and y-direction (- · -), (h) control force applied to node 9 in x-direction (———) and y-direction (- · -).

time. Also, the set of controls utilized are incapable of suppressing out-of-plane deflection of the antenna, which is caused by the asymmetry of the structure.

In order to suppress this residual energy, additional controls are placed on the antenna. Forces in the plane of the antenna are available at the mast/antenna junction and directly across the antenna (nodes 3 and 9). In addition, an out-of-plane thruster is placed at the latter location. Thus, a total of nine control inputs are used. Furthermore, additional penalties are placed on transverse antenna deformation at nodes 4 and 8. The improvement in the slew response can be seen in Fig. 4-5, which indicates that most of the residual vibration has been eliminated. For this maneuver, most of the torque is generated by the antenna thrusters across from the mast. In reality, this distribution of control effort would be unwise, as it would lead to excessive stress in the mast/antenna junction. Also, as shown in the figure, this trajectory causes a large amount of torsional deformation of the mast. By adjusting the relative weights on the controls and structural deformation outputs, it would be possible to converge upon a more realistic trajectory. However, this control solution provides an adequate demonstration of the formulation presented here.

4.1.4 Minimization of flexible energy

Another method of obtaining an optimal solution consists of minimizing the residual flexural energy within the structural elements at the terminal time. This is achieved by expressing the generalized boundary displacements of the i'th element in terms of the undermined coefficients:

$$\mathbf{w}^i(s) = \mathbf{C}_w^i \, \mathbf{G}_q(s) \, \mathbf{F}_q(s) \, \mathbf{c} = \mathbf{H}^i(s) \, \mathbf{c} \tag{4.18}$$

Making use of Eq. (2.43) then yields

$$E^i(t) = \frac{1}{2} \mathbf{c}^T \mathbf{E}_0^i(t) \, \mathbf{c} \tag{4.19}$$

where

$$\mathbf{E}_0^i(t) = k(t) \int_{-\infty}^{\infty} \int_{-\infty}^{\infty} \mathbf{H}^i(s_1)^T \, \Xi^i(s_1, s_2) \, \mathbf{H}^i(s_2) \, e^{j(\omega_1+\omega_2)t} d\omega_1 d\omega_2 \tag{4.20}$$

Included in the cost functional are the weighted penalties on residual energy for a set of N_f flexible elements and weighted penalties on control effort and control rate. To this we adjoin the desired terminal conditions and the constraints on the controls at the beginning and end of the maneuver. The cost functional is thus

$$J = \sum_{i=1}^{N_f} r_i E^i(t_f) + \frac{1}{2} \int_0^{t_f} \left[\mathbf{q}_c(t)^T \mathbf{R}_{qq} \mathbf{q}_c(t) + \dot{\mathbf{q}}_c(t)^T \tilde{\mathbf{R}}_{qq} \dot{\mathbf{q}}_c(t) \right] dt$$
$$+ \lambda^T \left[\mathbf{y}(t_f) - \mathbf{y}_d \right] + \lambda_0^T \mathbf{q}_c(0) + \lambda_f^T \mathbf{q}_c(t_f) \tag{4.21}$$

Setting variations in J due to $\mathbf{c}$ to zero yields

$$\begin{bmatrix} \mathbf{W} & \mathbf{Y}(t_f)^T & \mathbf{F}_q(0)^T & \mathbf{F}_q(t_f)^T \\ \mathbf{Y}(t_f) & \mathbf{0} & \mathbf{0} & \mathbf{0} \\ \mathbf{F}_q(0) & \mathbf{0} & \mathbf{0} & \mathbf{0} \\ \mathbf{F}_q(t_f) & \mathbf{0} & \mathbf{0} & \mathbf{0} \end{bmatrix} \begin{bmatrix} \mathbf{c} \\ \lambda \\ \lambda_0 \\ \lambda_f \end{bmatrix} = \begin{bmatrix} \mathbf{0} \\ \mathbf{y}_d \\ \mathbf{0} \\ \mathbf{0} \end{bmatrix} \tag{4.22}$$

where

$$\mathbf{W} = \sum_{i=1}^{N_f} r_i \, \mathbf{E}_0^i(t_f) + \int_0^{t_f} \left[\mathbf{F}_q(t)^T \mathbf{R}_{qq} \mathbf{F}_q(t) + \dot{\mathbf{F}}_q(t)^T \tilde{\mathbf{R}}_{qq} \dot{\mathbf{F}}_q(t) \right] dt \tag{4.23}$$

Again, this system is symmetric, and can be solved with standard linear algebra software packages.

The minimum residual energy approach was applied to the simple mass/appendage system studied in the previous section. Two maneuvers were performed, both with a prescribed final displacement of 10 meters after 20 seconds. In the first maneuver, the desired final velocity of the rigid mass was zero, while in the second, the final velocity was 1 meter/second. The control penalties were kept small, as in the previous section, and eighteen basis functions (sines and

cosines) were used. The results of these maneuvers are shown in Fig.'s 4-6 and 4-7. In each case, the residual energy is seen to be negligible. For the second case, it is interesting to note that, because the internal energy formulation does not include kinetic energy due to rigid motion, it is possible to achieve a terminal condition where the total energy is large (due to translational velocity), while the deformational energy remains negligible.

The same structure can be used to perform rotational maneuvers. In this case, the bending of the flexible appendage must be considered, and the control input is now a torque applied to the rigid mass. Slews of 0.1 radians with terminal angular velocities of both zero and 1 radian/second were demonstrated. The results, shown in Fig.'s 4-8 and 4-9, indicate that performance comparable to the axial cases was achieved. In both cases, the control torque begins in the negative direction (anticipating the deformation of the structure), then gradually rotates the structure to the desired terminal configuration.

The minimum energy cost functional leads to system trajectories with far less residual energy than those obtained via point constraints. Furthermore, minimization of total deformational energy also avoids the problem of selecting which points to constrain, which is usually carried out in an *ad hoc* manner.. All that is required is a relative cost weighting for each flexible element of interest. However, because the calculation of internal energy involves a double integral, the minimum energy approach requires more computational effort. The minimum energy cost functional was not applied to the SCOLE maneuver problem.

4.2 Closed-loop control

The closed-loop control of infinite order systems expressed in the transformed domain is a considerably more difficult problem. The exact dynamics of the mathematical model are available in the frequency-domain only, and no finite dimensional state space realization is possible. As a result, state space techniques, such as LQR and LQG methodologies, are not applicable. However, the control problem can be posed in a form amenable to frequency-domain design techniques. It is assumed that, for a given structural model, a set of disturbance forces act at global

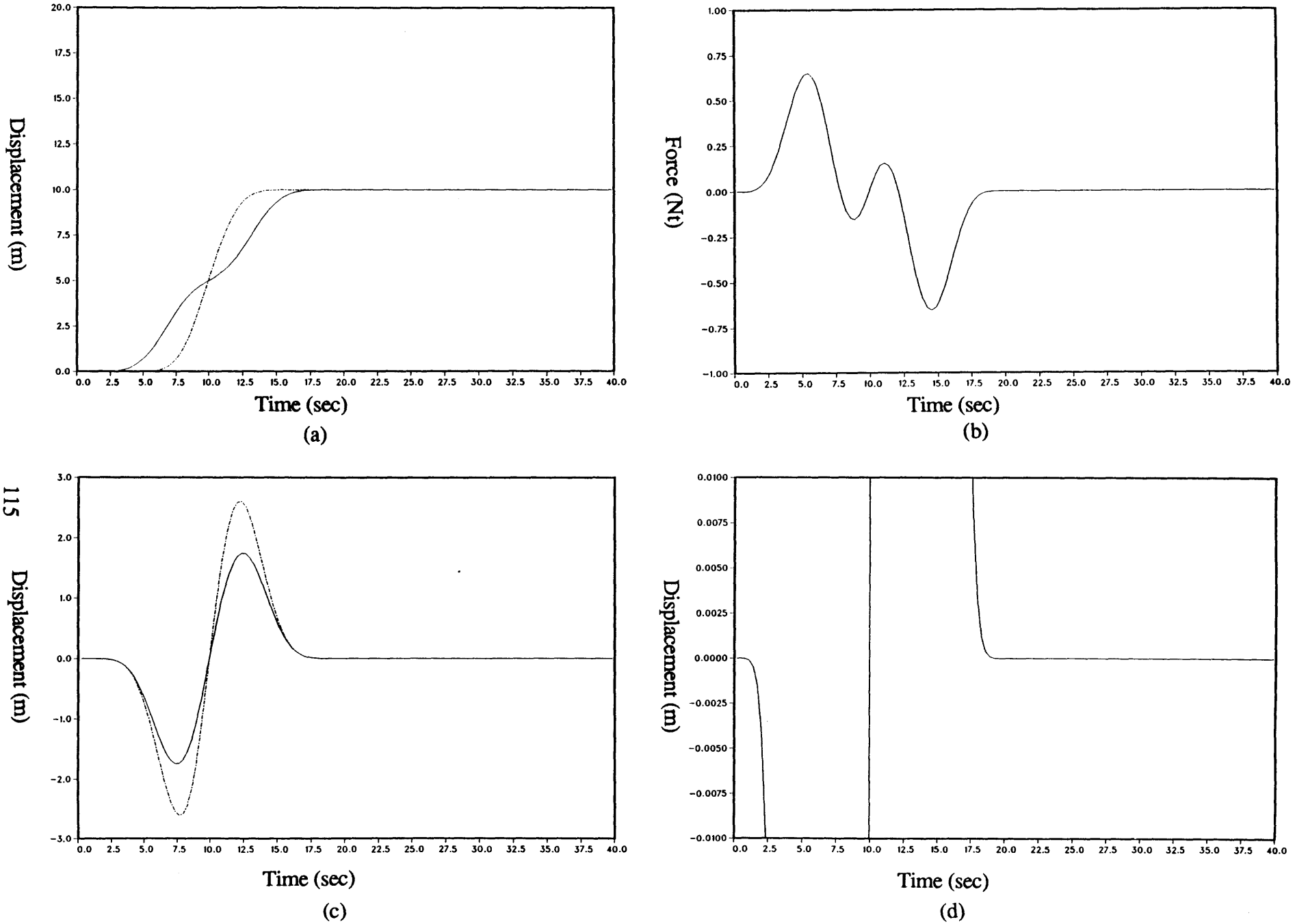

Fig. 4-6: Linear slew maneuver with residual energy cost functional and terminal velocity of 0 m/sec: (a) Position of rigid mass (———) and tip of flexible appendage (- · -), (b) control force applied to rigid mass, (c) axial deformation of flexible appendage at center-span (———) and tip (- · -) with respect to position of rigid mass, (d) same plot as (c) with expanded vertical scale.

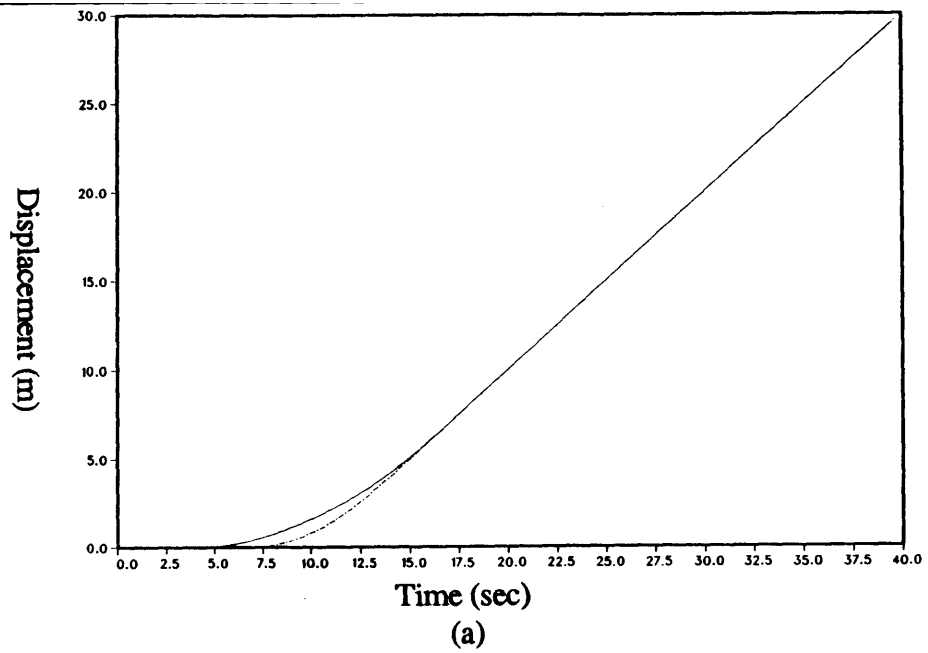

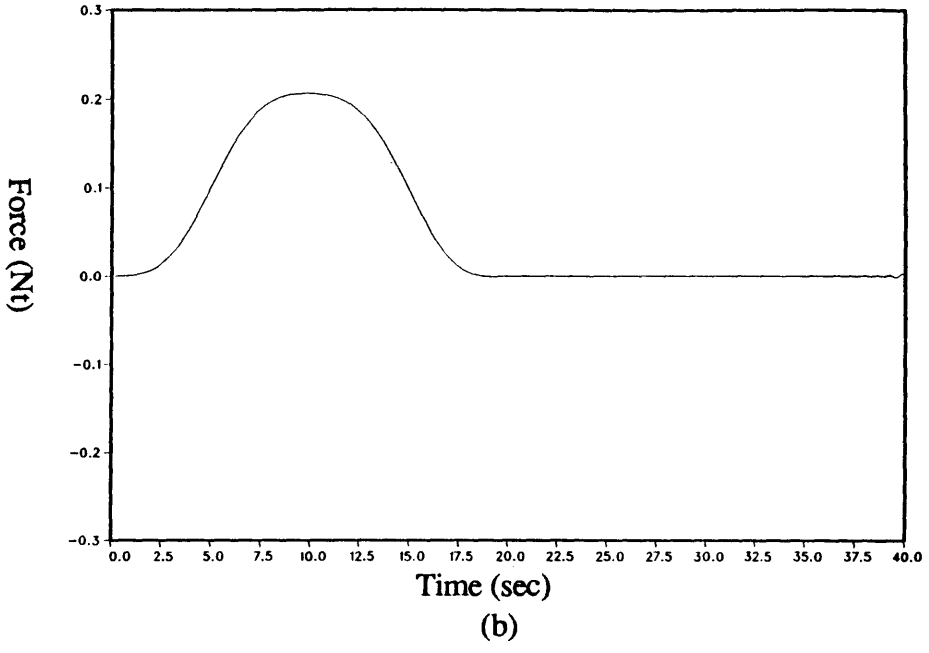

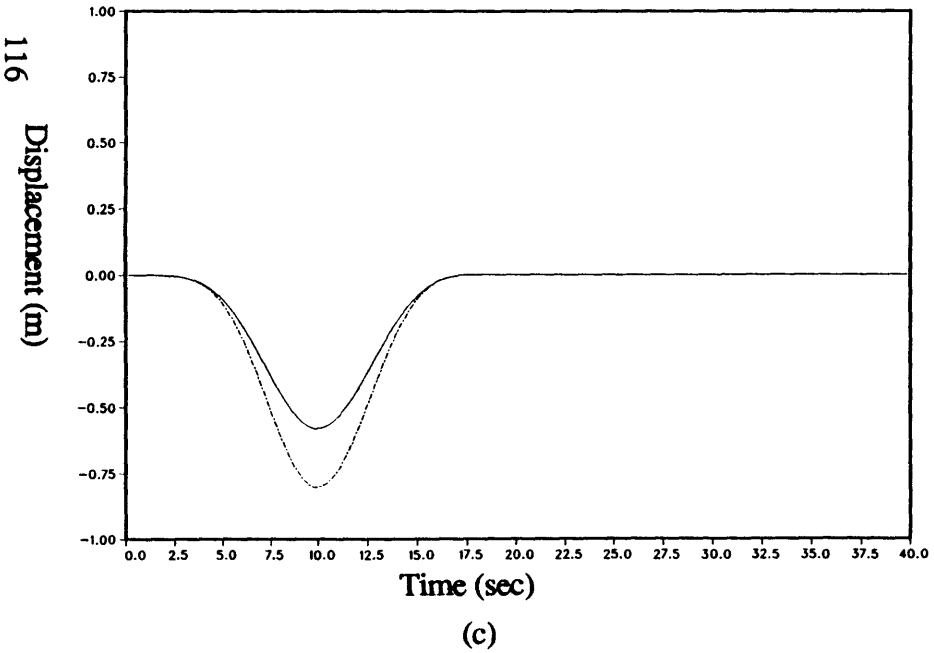

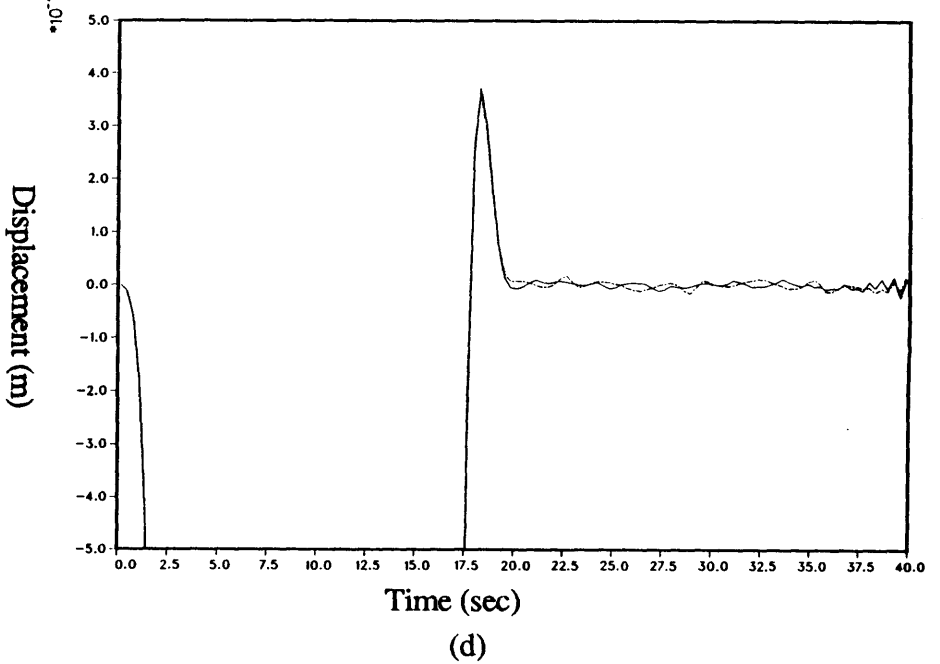

Fig. 4-7: Linear slew maneuver with residual energy cost functional and terminal velocity of 1 m/sec: (a) Position of rigid mass (———) and tip of flexible appendage (- · -), (b) control force applied to rigid mass, (c) axial deformation of flexible appendage at center-span (———) and tip (- · -) with respect to position of rigid mass, (d) same plot as (c) with expanded vertical scale.

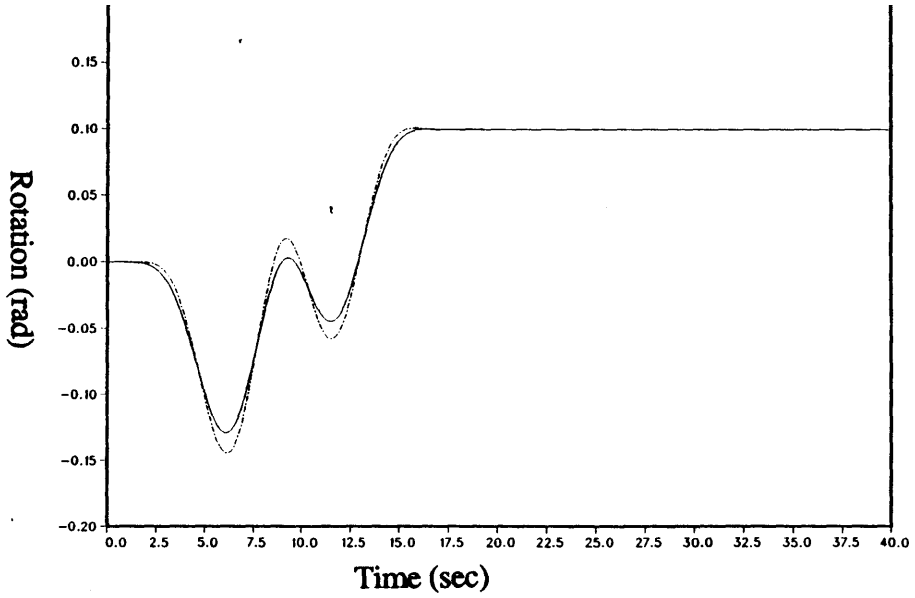

(a)

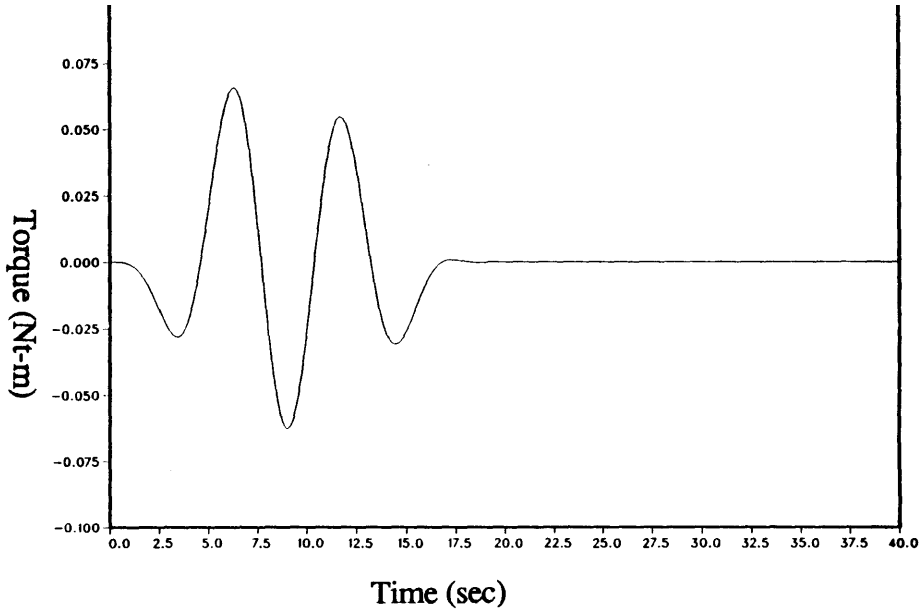

(b)

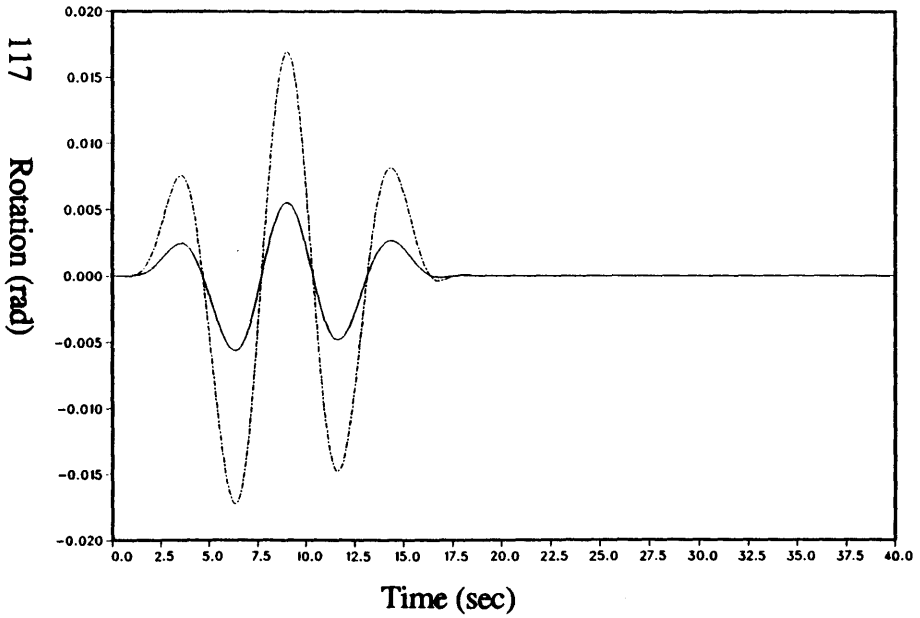

(c)

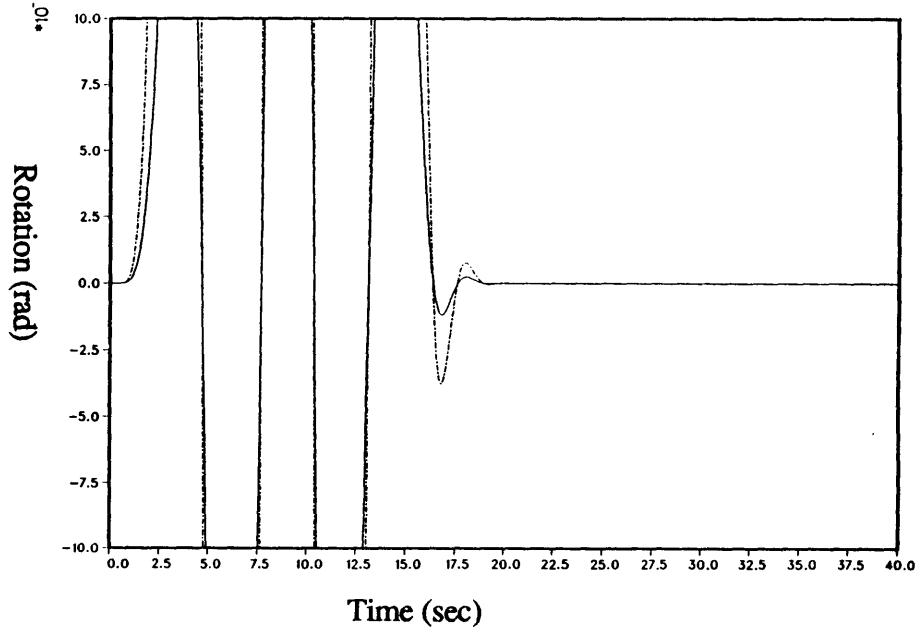

(d)

Fig. 4-8: Rotational slew maneuver with residual energy cost functional and terminal angular velocity of 0 rad/sec: (a) Rotation of rigid mass (———) and tip of flexible appendage (- · -), (b) control torque applied to rigid mass, (c) transverse deformation of flexible appendage at center-span (———) and tip (- · -) with respect to position of rigid mass, (d) same plot as (c) with expanded scale.

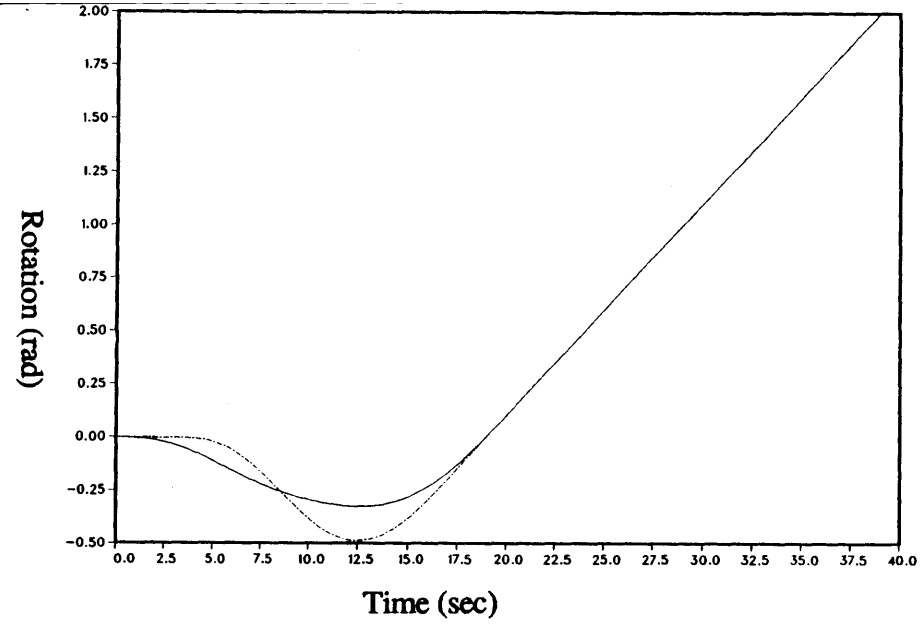

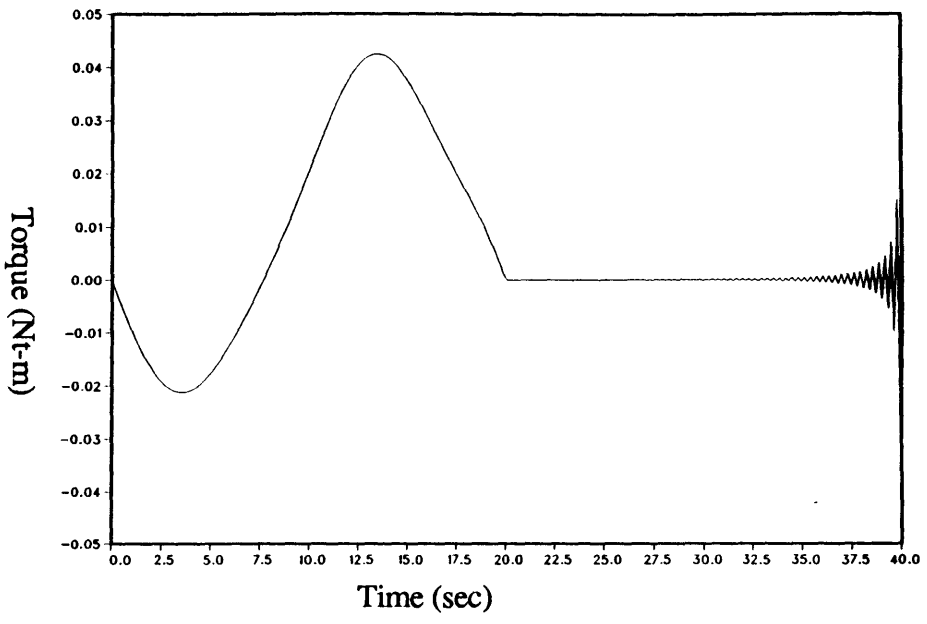

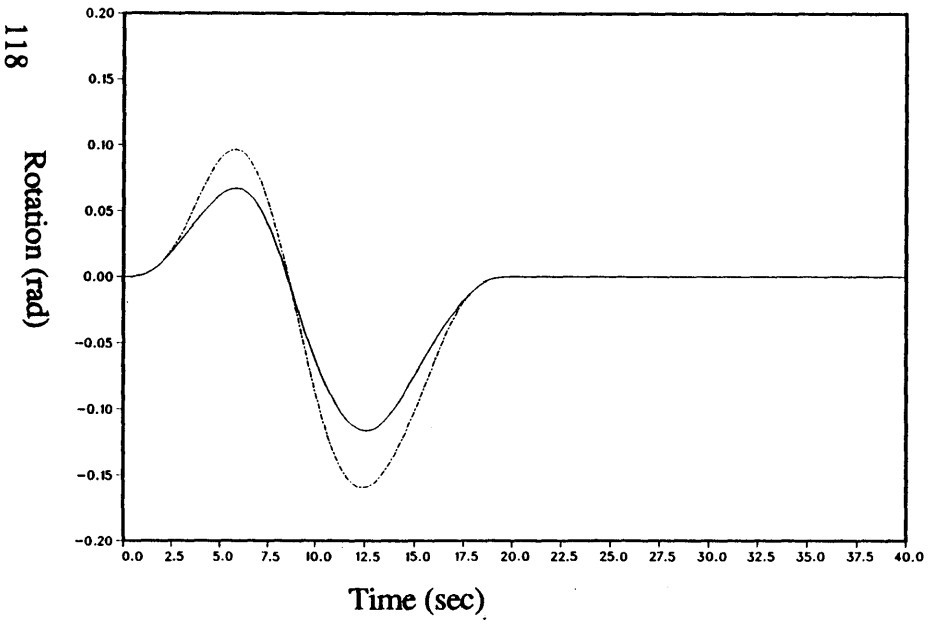

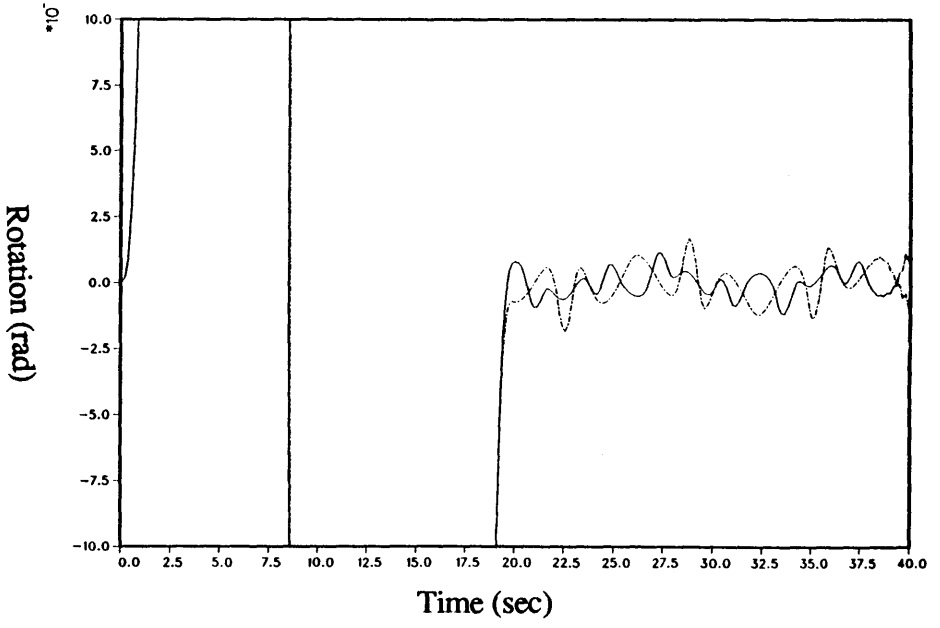

Fig. 4-9: Rotational slew maneuver with residual energy cost functional and terminal angular velocity of 0.1 rad/sec: (a) Rotation of rigid mass (———) and tip of flexible appendage (- · -), (b) control torque applied to rigid mass, (c) transverse deformation of flexible appendage at center-span (——) and tip (- · -) with respect to position of rigid mass, (d) same plot as (c) with expanded scale.

element junctions, and performance is measured in terms of some set of global generalized displacements. The control objective is then to minimize, in some sense, the transfer function from the set of disturbances, $\mathbf{w}(t)$, to the performance measure, $\mathbf{z}(t)$. This is to be accomplished by a finite order controller which has available as inputs a finite set of measured generalized displacements, $\mathbf{y}(t)$, and acts on a finite set of actuators, $\mathbf{u}(t)$, located on the structure. The situation is depicted in Fig. 4-10. The transfer functions from disturbances and control inputs to the performance metric and measured outputs are easily obtained as partitions of the dynamic flexibility matrix. Note that this control problem is in the "standard form," which has been studied extensively by Francis [51] and Doyle [12] for finite dimensional plants.

For this problem, the transfer functions are partitioned as

$$\begin{bmatrix} \mathbf{z}(s) \\ \mathbf{y}(s) \end{bmatrix} = \begin{bmatrix} \mathbf{G}_{zw}(s) & \mathbf{G}_{zu}(s) \\ \mathbf{G}_{yw}(s) & \mathbf{G}_{yu}(s) \end{bmatrix} \begin{bmatrix} \mathbf{w}(s) \\ \mathbf{u}(s) \end{bmatrix} \tag{4.24}$$

and the controller is expressed as

$$\mathbf{u}(s) = \mathbf{G}_c(s)\mathbf{y}(s) \tag{4.25}$$

The closed-loop transfer function is then given by

$$\mathbf{T}_{zw}(s) = \mathbf{G}_{zw}(s) + \mathbf{G}_{zu}(s)\mathbf{G}_c(s)\left[\mathbf{I} - \mathbf{G}_{yu}(s)\mathbf{G}_c(s)\right]^{-1}\mathbf{G}_{yw}(s) \tag{4.26}$$

The design objective is then to determine $\mathbf{G}_c(s)$ such that the closed-loop system is stable and meets the performance specifications. Although general solutions have been obtained for finite dimensional systems, the situation for infinite dimensional systems is much more complicated. As a result, only simple systems have been considered. For example, the coprime factorization technique is applied to a single torsional element in Reference 31. The extension of such an approach to complex structures would indeed be a significant achievement. Equally significant would be the extension of the characteristic gain technique, developed by MacFarlane [52], to include infinite order structural systems. This technique is a multivariable feedback version of the Nyquist stability criterion, and is well suited for systems in which a finite-dimensional state-space

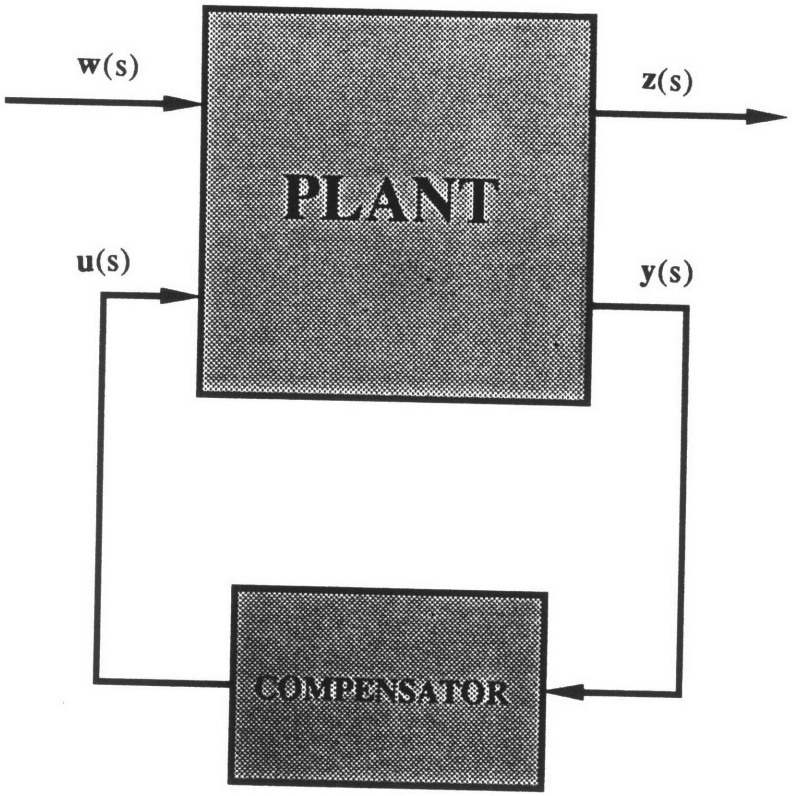

Fig. 4-10: The prototypical control problem posed in the standard form.

representation does not exist. It could potentially find use in the determination of stability criteria for the controlled system.

The control design problem can be posed more precisely if the assumtion is made that the controller has finite order. This is required if the controller is to be physically implementable. The n-th order controller has the state-space form

$$\dot{\mathbf{x}}_c(x,t) = \mathbf{A}_c\mathbf{x}_c(t) + \mathbf{B}_c\mathbf{y}(t), \quad \mathbf{u}(t) = \mathbf{C}_c\mathbf{x}_c(t) + \mathbf{D}_c\mathbf{y}(t) \tag{4.27a,b}$$

which is represented in the frequency domain by

$$\mathbf{G}_c(s) = \mathbf{C}_c(s\mathbf{I} - \mathbf{A}_c)^{-1}\mathbf{B}_c + \mathbf{D}_c \tag{4.28}$$

The objective, then, is to find the matrices $\mathbf{A}_c$, $\mathbf{B}_c$, $\mathbf{C}_c$, and $\mathbf{D}_c$, that both stabilize the closed-loop system and minimize $\mathbf{T}_{zw}(s)$ in some sense. A method of selecting the order of the controller is also required. The only data available are the partitioned transfer function matrices, which are mathematically exact at all frequencies. The optimal solution would then be valid for the exact mathematical model, rather than some truncation of it. As a result, the modelling error is restricted to the deviation of the mathematical model from the actual physical structure. This will result in a less conservative control design approach and, consequently, enhanced performance.

4.3 Limitations of the Transform Element Control Design Methodology

Although the control designs based on the TEM methodology have demonstrated remarkable performance (at least in the open-loop case), it is important to note some limitations of this approach. First, the control actuation is available only on the boundaries of the structural elements. For a small number of actuators, this may be overcome by dividing each element into smaller sub-elements at the point of control actuation. If many actuators are employed, however, this approach is clearly not feasible. Another limitation is the requirement that the initial conditions be zero. Only in this way was it possible to obtain a simple expression for the control solution.

Nonzero initial conditions introduce an extra term, $\mathbf{q}_d(s)$, in the dynamic stiffness equation for each structural element. In addition to making the optimal control expressions more complex, this term must be computed by integrating over the domain of the element, as described in Sec. 2.3.1. Consequently, the treatment of initial conditions (and distributed forcing, for that matter) increases the computation time associated with the TEM approach considerably, as a numerical integration is required for each element at each complex frequency of interest.

Some of these limitations can be overcome by working with the original PDE for the element, expressed in the time-domain. This forms the basis of the direct PDE modelling approach, which leads naturally to a different type of control theory. The direct approach is the subject of the next two chapters.

5 DIRECT PARTIAL DIFFERENTIAL EQUATION MODELLING

All physical systems are distributed in nature when viewed on a macroscopic (or continuum) level. This fact is a consequence of the underlying dynamics equations, which always take the form of a set of field equations which must be satisfied over each infinitesimal region in the spatial domain of interest. As a result, any true continuum model of a physical system must be of infinite order. Lumped parameter models are, in general, low-frequency approximations to these field equations. Examples include lumped electrical component models (such as capacitors, resistors and inductors), rigid body structural idealizations, and finite element models. In this last example, the finite order approximation is achieved by restricting the deformational degrees of freedom of the system rather than employing a low-frequency approximation directly, but the result is essentially the same: the model fails to recover the high-frequency dynamics of the system. In this chapter, we introduce the concept of a distributed, infinite-order model of a system, which retains the dynamics of the underlying equations at all frequencies. This approach, hereinafter referred to as the direct PDE modelling approach, is superior to the TEM approach when forces of a distributed nature act within the spatial domain of the structural elements. Such forces include aerodynamic and gravitational loads, inertial forces, and distributed control actuators.

Distributed system models can be characterized in either of two forms. The first is an integral form, in which the response of the system at a particular time is determined by integrating (with respect to time and/or space) the product of the distributed forcing inputs and a Green's function **kernel**. Here, the Green's function relates the response of the system at some arbitrary point and time to an impulse applied at some other point and time. Thus, this characterization is global in nature. Given this approach, it is possible to develop, for example, a distributed control theory. The work of Brogan [18] proceeds along these lines. However, the Green's function for an arbitrary system is extremely difficult to obtain. Indeed, analytical expressions are only available for the simplest of cases. The other characterization is differential in nature. Here, partial

differential equations, describing the local behavior of the system, are used to develop a system model. This characterization is much easier to obtain, as the physical laws that describe the system are always local. Consequently, more emphasis has been placed on developing the differential approach for control system design. Breakwell [53], for example, uses the differential description to obtain solutions to the boundary control of a simple flexible system. The differential description of distributed systems will be used here throughout.

5.1 One-dimensional elements

For a structural system undergoing small deformations, the underlying differential equations are, of course, the equations of elasticity. A completely rigorous and exact linear structural model must therefore account for general three-dimensional deformation. However, for long, slender structural elements, the deformation is primarily a function of position along the element. The variation in deformation with respect to the other two directions can usually be expressed in terms of a few functions of the position along the length of the element. Therefore, only one spatial coordinate is needed to describe the dynamics. This is the basis for the axial rod and Bernoulli-Euler beam models discussed in Chapter 2. While these idealizations fail to hold at extremely high frequencies (where the characteristic wavelength approaches one of the transverse dimensions), their ranges of validity tend to be greater than those of finite-order representations, such as finite element models.

5.1.1 General Formulation

We will restrict our attention to one-dimensional, linear, time-invariant distributed systems. Such systems can be written in the form

$$\dot{\mathbf{x}}(x,t) = \mathbf{L}_x(x)\mathbf{x}(x,t) + \mathbf{B}_x(x)\mathbf{u}(x,t) + \mathbf{D}_x(x)\mathbf{n}(x,t)\,, \quad x\in[0,1]\,, \quad t\in[0,\infty) \tag{5.1}$$

where $\mathbf{x}$ is the state vector, $\mathbf{u}$ is the distributed control input, and $\mathbf{n}$ is the distributed disturbance input. In contrast with lumped-parameter state space models, these vectors exhibit both spatial and

temporal dependence. Also, $\mathbf{L}_x$, $\mathbf{B}_x$ and $\mathbf{D}_x$ are linear (possibly spatially varying) matrix operators. The subscripts indicate that the operators in each matrix operate with respect to the independent variable x. Note that the spatial domain has been normalized to unity. The boundary conditions are assumed to be homogeneous, and are expressed as

$$\mathbf{x}(0,t) = \mathbf{x}(1,t) = \mathbf{0}, \quad t \in [0,\infty) \tag{5.2}$$

Most of the development presented here (and all of Chapter 6) applies only to systems with homogeneous boundary conditions. It is therefore assumed that no control or disturbance forces are applied at the boundaries of the system. The treatment of non-homogeneous boundary conditions is addressed in Appendix C. Finally, the initial conditions are expressed as

$$\mathbf{x}(x,0) = \mathbf{x}_0(x), \quad x \in [0,1] \tag{5.3}$$

5.1.2 Bernoulli-Euler Beam Example

One of the simplest examples of a one-dimensional distributed parameter system is a Bernoulli-Euler beam. A diagram of the physical system is shown in Fig. 5-1. The requirement that the boundary conditions for the mathematical model be homogeneous corresponds to pinned-pinned boundary conditions for the beam, as will be shown in the next subsection. In addition to casting the equation of motion of the beam in the form given by Eq. (5.1), the following subsections describe a method for simulating the response of the beam system to various control and disturbance forces.

5.1.2.1 Normalization of Equations of Motion

In dimensional form, the beam dynamics are described by

$$\frac{\partial^2}{\partial x_d^2}\left[EI(x) \frac{\partial^2}{\partial x_d^2} v_d(x_d,t_d) \right] + m(x) \frac{\partial^2}{\partial t_d^2} v_d(x_d,t_d) = f_d(x_d,t_d), \quad x_d \in [0,L] \tag{5.4}$$

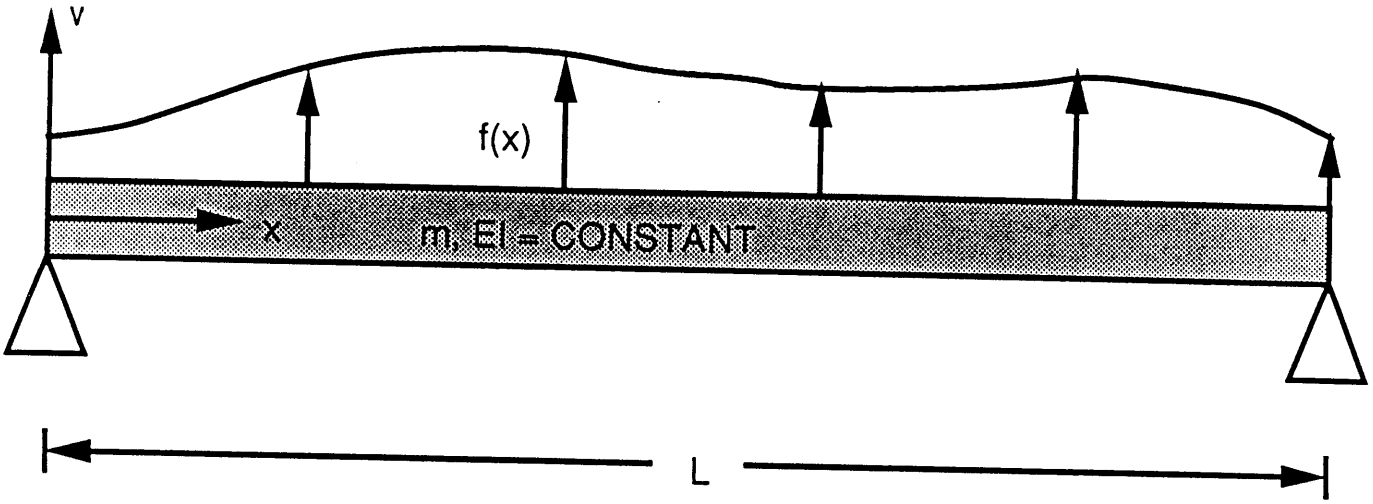

(a)

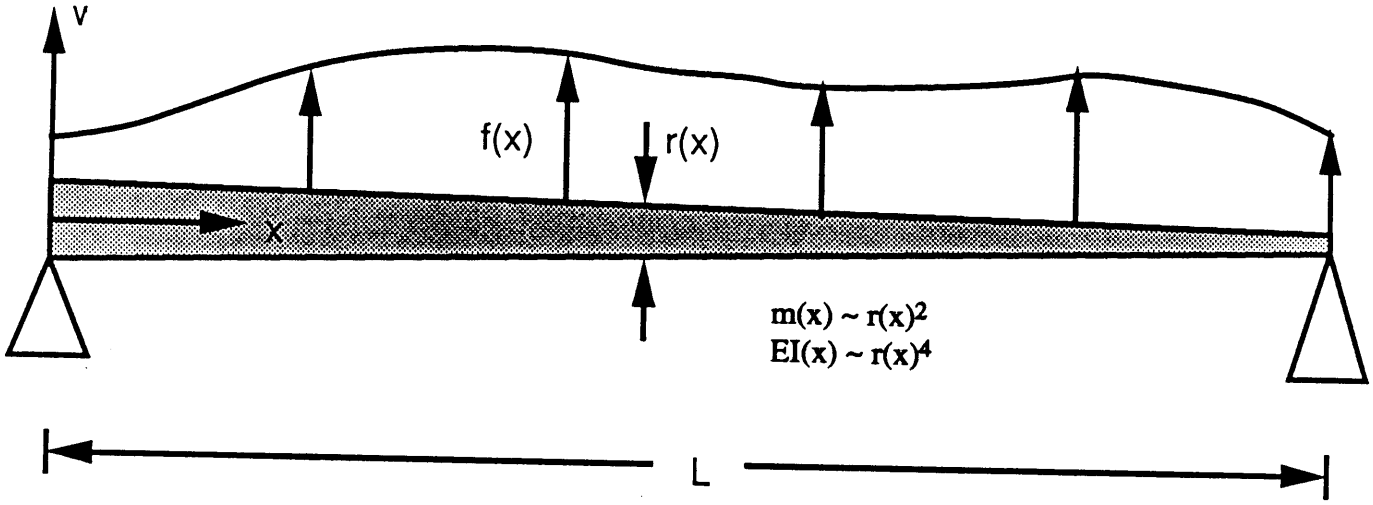

(b)

Fig. 5-1: Bernoulli-Euler beam models: (a) Uniform beam, (b) Tapered beam.

where x_d and t_d are the dimensionalized spatial and temporal variables, respectively, v_d is the transverse deflection, f_d is the applied distributed control and/or disturbance force, L is the beam length, EI(x) is the bending stiffness, and m(x) is the beam mass per unit length. To this equation we must add the boundary conditions

$$v_d(0,t_d) = \frac{\partial^2}{\partial x_d^2} v_d(0,t_d) = v_d(L,t_d) = \frac{\partial^2}{\partial x_d^2} v_d(L,t_d) = 0 \tag{5.5}$$

and the initial conditions

$$v_d(x_d,0) = v_{0d}(x_d)\,, \quad \frac{\partial}{\partial t_d} v_d(x_d,0) = \dot{v}_{0d}(x_d) \tag{5.6a,b}$$

We now introduce nondimensional independent variables according to

$$x = \frac{x_d}{L}\,, \quad t = t_d \sqrt{\frac{EI(0)}{m(0)L^4}} \tag{5.7a,b}$$

and the normalized deflection and distributed force as

$$v(x,t) = \frac{1}{L} v_d(x_d,t_d)\,, \quad f(x,t) = \frac{L^3}{EI(0)} f_d(x_d,t_d) \tag{5.8a,b}$$

We can also parametrize the bending stiffness and mass per unit length by

$$\eta(x) = \frac{EI(x)}{EI(0)}\,, \quad \beta(x) = \frac{m(0)}{m(x)} \tag{5.9a,b}$$

where η and β are nondimensional functions. These normalizations lead to the following nondimensional form of the equation of motion

$$\frac{\partial^2}{\partial x^2}\left[\eta(x) \frac{\partial^2}{\partial x^2} v(x,t)\right] + \frac{1}{\beta(x)} \frac{\partial^2}{\partial t^2} v(x,t) = f(x,t) = f_u(x,t) + f_n(x,t) \tag{5.10}$$

Here, f_u and f_n represent the normalized distributed control and disturbance forces, respectively.

To obtain the state space representation of the dynamics, we define the state vector and control and disturbance scalars by

$$\mathbf{x}(x,t) = \begin{bmatrix} \eta(x)\dfrac{\partial^2}{\partial x^2}v(x,t) \\ \dfrac{\partial}{\partial t}v(x,t) \end{bmatrix}, \quad u(x,t) = f_u(x,t), \quad n(x,t) = f_n(x,t) \qquad (5.11a\text{-}c)$$

The first and second elements of $\mathbf{x}$ correspond to the normalized curvature and velocity of the bending motion, respectively. These choices for the state vector components ensure the well-posedness of the system model, as explained by Richtmyer [54]. Equation (5.5), which is a consequence of the pinned-pinned boundary conditions, ensures that $\mathbf{x}(0,t)=\mathbf{x}(1,t)=0$ for all values of t. The equation of motion then takes the form of Eq. (5.1), with

$$\mathbf{L}_x(x) = \begin{bmatrix} 0 & \eta(x) \\ -\beta(x) & 0 \end{bmatrix}\frac{\partial^2}{\partial x^2}, \quad \mathbf{b}_x(x) = \mathbf{d}_x(x) = \begin{bmatrix} 0 \\ \beta(x) \end{bmatrix} \qquad (5.12a,b)$$

5.1.2.2 The Case of Curvature Actuation

In most active structural control applications, it is difficult to implement lightweight inertial force actuators. This is particularly challenging for space-based structures, where stringent constraints are placed on structural mass. As a result, practical structural control actuators are usually imbedded within the structure itself, and are capable of producing only relative deformation between points on the structure. For example, deLuis [55] demonstrates how an embedded piezoelectric actuator can be used to induce a local curvature in a flexible beam. Many such actuators, placed along the span of a large, beam-like structure will then approximate distributed curvature actuation.

It is therefore useful to develop the model of a beam with a distributed curvature actuator. Such is the limiting case of a beam with many embedded piezoelectric actuators distributed along its span. For this system, the equation of motion is modified to

$$\frac{\partial^2}{\partial x^2}\left[\eta(x)\frac{\partial^2}{\partial x^2}v(x,t)\right] + \frac{1}{\beta(x)}\frac{\partial^2}{\partial t^2}v(x,t) = \frac{\partial^2}{\partial x^2}m_u(x,t) \qquad (5.13)$$

where $m_u(x,t)$ represents the net action of the distributed piezoelectrics. The state vector, $\mathbf{x}$, is unchanged, as is $\mathbf{L}_x$, but $\mathbf{u}$ and $\mathbf{b}_x$ must be modified to

$$u(x,t) = m_u(x,t), \quad \mathbf{b}_x = \begin{bmatrix} 0 \\ \beta(x) \end{bmatrix} \frac{\partial^2}{\partial x^2} \tag{5.14a,b}$$

5.1.2.3 Numerical Simulation Using Laplace Transform

Given the beam dynamics model, there remains the problem of actually simulating the response of the beam to control and disturbance forces. Various methodologies exist to achieve this end. At one extreme, the dynamics equation is discretized in both space and time and then integrated forward in time. Although this method is widely used, it requires rather fine discretizations in both the temporal and spatial dimensions to achieve accurate results, and errors tend to accumulate in time. At the other extreme, one can Laplace-transform the equation into the s-domain and search for analytic solutions. However, due to the distributed nature of the control and/or disturbance forces, this transformation results in an integro-partial differential equation rather than a simple ordinary differential equation (as would be the case for boundary forcing only). Due to the generality of the distributed forces, a general analytical solution is not available.

In order to achieve accurate solutions with relatively coarse discretizations, a third alternative is proposed. The dynamics equation is Laplace-transformed, resulting in the above mentioned integro-partial differential equation. At each desired complex frequency, a finite differencing scheme is used to solve for the displacement field. The data from a set of frequencies is collected, and the numerically robust inverse Laplace transform algorithm described in Section 2.2 is used to convert the data back into the time-domain. Because the transformed equation represents a boundary value problem, it is anticipated that its approximate solution will be more stable and accurate than the corresponding solution to the mixed problem associated with time-domain integration. The stability and accuracy of the inverse transform algorithm has already been demonstrated in Chapters 2 and 3.

The development presented here corresponds to distributed force actuation only, and the case of distributed curvature actuation is addressed in Appendix D. We first transform Eq. (5.10) into the frequency-domain:

$$\frac{\partial^2}{\partial x^2}\left[\eta(x)\frac{\partial^2}{\partial x^2}\bar{v}(x,s)\right]+\frac{1}{\beta(x)}\left[s^2\bar{v}(x,s)-s\,v_0(x)-\dot{v}_0(x)\right]=\bar{f}_u(x,s)+\bar{f}_n(x,s) \quad (5.15)$$

The normalized frequency, s, is related to the dimensional frequency, s_d, by

$$s = s_d\sqrt{\frac{\rho A l^4}{EI}} \quad (5.16)$$

In this way, we can relate the transform pair $v(x,t_d) \sim \bar{v}(x,s_d)$ with the pair $v(x,t) \sim \bar{v}(x,s)$. We now assume that the feedback control law is distributed and linear, and relates the components of the state vector to the control input by

$$\begin{aligned} f_u(x,t) &= -\int_0^1 \mathbf{k}(x,y)^T\mathbf{x}(y,t)\,dy \\ &= -\int_0^1\left[k_1(x,y)\,\eta(y)\frac{\partial^2}{\partial y^2}v(y,t)+k_2(x,y)\frac{\partial}{\partial t}v(y,t)\right]dy \end{aligned} \quad (5.17)$$

In this last equation, $k_1(x,y)$ and $k_2(x,y)$ represent feedback gain kernels. This type of control law will arise in the next chapter as the optimal solution to the distributed control problem. Substituting the Laplace-transformed version of this control law in Eq. (5.15) leads to

$$\begin{aligned} &\frac{\partial^2}{\partial x^2}\left[\eta(x)\frac{\partial^2}{\partial x^2}\bar{v}(x,s)\right]+\frac{s^2}{\beta(x)}\bar{v}(x,s)+\int_0^1\left[k_1(x,y)\,\eta(y)\frac{\partial^2}{\partial y^2}\bar{v}(y,s)+s\,k_2(x,y)\,\bar{v}(y,s)\right]dy \\ &\qquad = \bar{f}_n(x,s)+\frac{1}{\beta(x)}\left[\dot{v}_0(x)+s\,v_0(x)\right]+\int_0^1 k_2(x,y)\,v_0(y)\,dy \end{aligned} \quad (5.18)$$

The term involving k_1 in this equation can be integrated by parts twice so that the derivative with respect to y operates on k_1. For homogeneous boundary conditions, the boundary term arising from this operation vanishes. The treatment of distributed control feedback for systems with non-

homogeneous boundary conditions (such as a controlled clamped-free beam) is not discussed here. By making the following associations

$$k(x,y,s) = \frac{\partial^2}{\partial y^2}\left[k_1(x,y)\,\eta(y)\right] + s\,k_2(x,y) \tag{5.19a}$$

$$\bar{f}(x,s) = \bar{f}_n(x,s) + \bar{f}_i(x,s) + \bar{f}_c(x,s) \tag{5.19b}$$

$$\bar{f}_i(x,s) = \frac{1}{\beta(x)}\left[\dot{v}_0(x) + s\,v_0(x)\right] \tag{5.19c}$$

$$\bar{f}_c(x,s) = \int_0^1 k_2(x,y)\,v_0(y)\,dy \tag{5.19d}$$

the dynamics equation reduces to

$$\frac{\partial^2}{\partial x^2}\left[\eta(x)\frac{\partial^2}{\partial x^2}\bar{v}(x,s)\right] + \frac{s^2}{\beta(x)}\bar{v}(x,s) + \int_0^1 k(x,y,s)\,\bar{v}(y,s)\,dy = \bar{f}(x,s) \tag{5.20}$$

A similar result is available for the case of curvature actuation, and can be found in Appendix D.

Equation (5.20) must be solved numerically for each value of s needed to construct the time response. To do so requires a discretization of the spatial domain into N uniform subregions. The boundaries of these subregions are given by

$$x_i = \frac{i}{N}, \quad i = 0, \ldots, N \tag{5.21}$$

We can now use the values of $\bar{f}(x,s)$ evaluated at these x_i to determine $\bar{v}(x,s)$ at these same coordinates. By defining the vectors

$$\bar{\mathbf{v}}(s) \approx \left\{\bar{v}(x_i,s)\right\}, \quad \bar{\mathbf{f}}(s) \approx \left\{\bar{f}(x_i,s)\right\} \tag{5.22a,b}$$

and the matrix

$$\mathbf{K}(s) \approx \left[k(x_i,y_j,s)\right] \tag{5.23}$$

an approximation to Eq. (5.20) is easily obtained. The first term is replaced by the finite difference approximation

$$\frac{\partial^2}{\partial x^2}\left[\eta(x)\frac{\partial^2}{\partial x^2}\bar{v}(x,s)\right] \approx N^4\,\mathbf{DHD}\,\bar{\mathbf{v}}(s) \tag{5.24}$$

where **D** is a constant banded matrix of coefficients representing the second derivative operation, and has the following form for homogeneous boundary conditions:

$$\mathbf{D} = \begin{bmatrix} -2 & 1 & & & & \\ 1 & -2 & 1 & & & \mathbf{0} \\ & 1 & -2 & 1 & & \\ & & \cdot & \cdot & \cdot & \\ \mathbf{0} & & & 1 & -2 & 1 \\ & & & & 1 & -2 \end{bmatrix} \tag{5.25}$$

For non-homogeneous boundary conditions, the elements of **D** near the upper left and lower right corners have different values. These cases are described in Appendix C. The matrix **H** is the discretized representation of $\eta(x)$:

$$\mathbf{H} = \text{diag}\left[\eta(x_i)\right] \tag{5.26}$$

The second term in Eq. (5.20) is trivially approximated by

$$\frac{s^2}{\beta(x)}\bar{v}(x,s) \approx s^2\,\mathbf{B}\,\bar{\mathbf{v}}(s) \tag{5.27}$$

where

$$\mathbf{B} = \text{diag}\left[\frac{1}{\beta(x_i)}\right] \tag{5.28}$$

Finally, the integral term is approximated using the trapezoidal rule, and leads to the following matrix-vector product:

$$\int_0^1 k(x,y,s)\,\bar{v}(y,s)\,dy \approx \frac{1}{N}\mathbf{K}(s)\,\bar{\mathbf{v}}(s) \tag{5.29}$$

Collecting terms, the discretized equation becomes

$$\left[N^4\,\mathbf{D}\mathbf{H}\mathbf{D} + s^2\,\mathbf{B} + \frac{1}{N}\mathbf{K}(s)\right]\,\bar{\mathbf{v}}(s) = \bar{\mathbf{f}}_n(s) + \bar{\mathbf{f}}_i(s) + \bar{\mathbf{f}}_c(s) \tag{5.30}$$

Thus, a single matrix inversion is required at each complex frequency. If the frequencies required for the inverse Laplace transform are given by

$$s = s_1, \ldots, s_n \tag{5.31}$$

then the solutions of Eq. (5.30) can be grouped according to

$$\bar{\mathbf{V}} = \left\{\bar{\mathbf{v}}(s_1) \ldots \bar{\mathbf{v}}(s_n)\right\} \tag{5.32}$$

The time-domain responses at each x_i are then obtained by applying the inverse transform algorithm to each row of $\bar{\mathbf{V}}$.

Figure 5-2 presents the response of a uniform and a linearly tapered beam to a sinusoidal initial displacement and zero initial velocity. (The plots display time and x-coordinate along the beam as independent variables, with transverse deflection along the vertical axis.) For the uniform beam, these initial conditions correspond to the second mode of vibration. Consequently, no other modes are excited, as can be seen in the figure. For the tapered beam, many modes are involved, as the individual mode shapes are more complicated. Figure 5-3 displays the simulation results for a uniform beam impacted with a unit transverse impulse at its center-span. The plot on the left corresponds to a long time scale, and indicates that the resulting motion is predominantly composed of a first mode vibration with odd harmonics. The plot on the right, which corresponds to a shorter time scale, accentuates the wave-like characteristics of the response. The disturbance, which begins at the center-span, quickly moves towards the boundaries and reflects. These reflections eventually set up the complex modal motion observed in the long time scale plot. Note that, for a short time following the impact, the deflection of the center-span varies as the square-root of time. This behavior agrees with the beam theory presented by Nowacki [56], where the response of a beam of infinite extent is addressed. Note also that the disturbance reaches the boundaries almost instantly, which is characteristic of the Bernoulli-Euler beam assumption of no

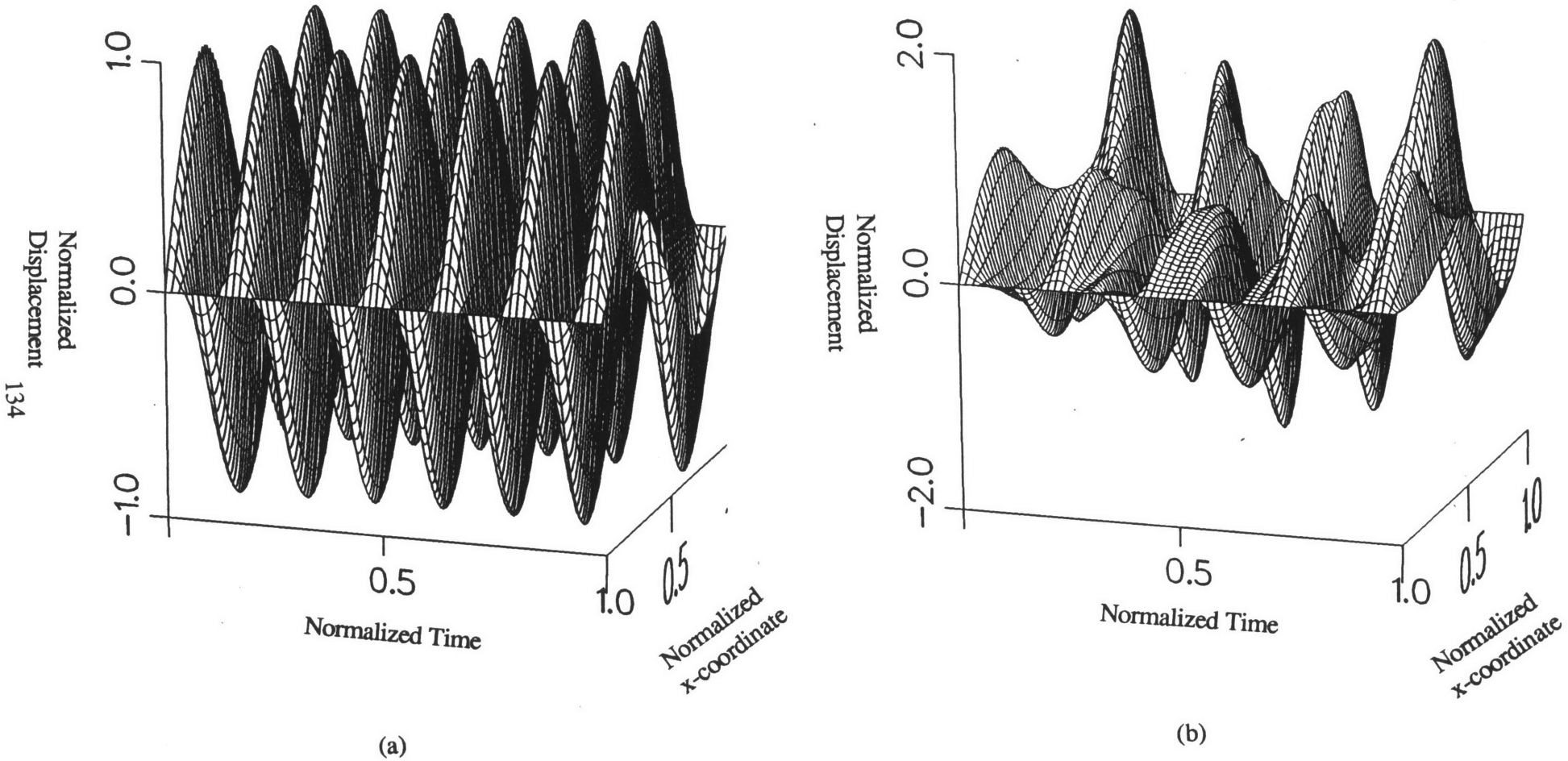

Fig. 5-2: Uncontrolled response of beam with initial displacement $v_0(x)=\sin(2\pi x)$: (a) Uniform beam, (b) Tapered beam (Beam diameter varies linearly from 1.0 at x=0 to 0.4 at x=1).

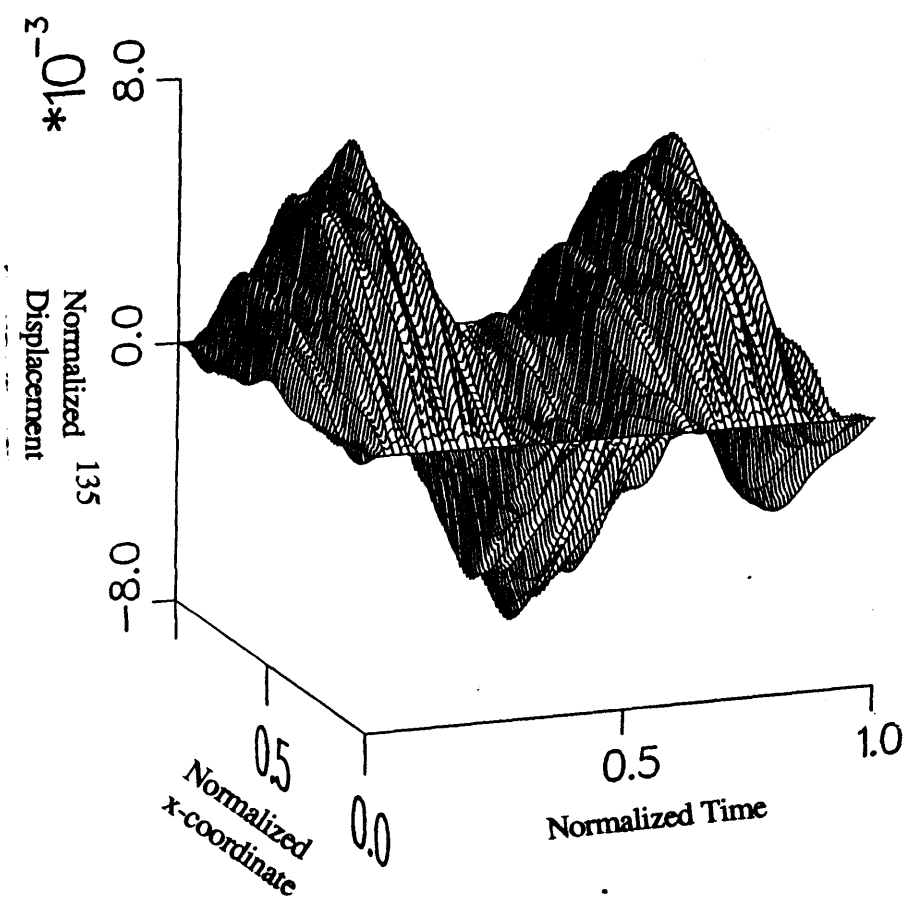

(a)

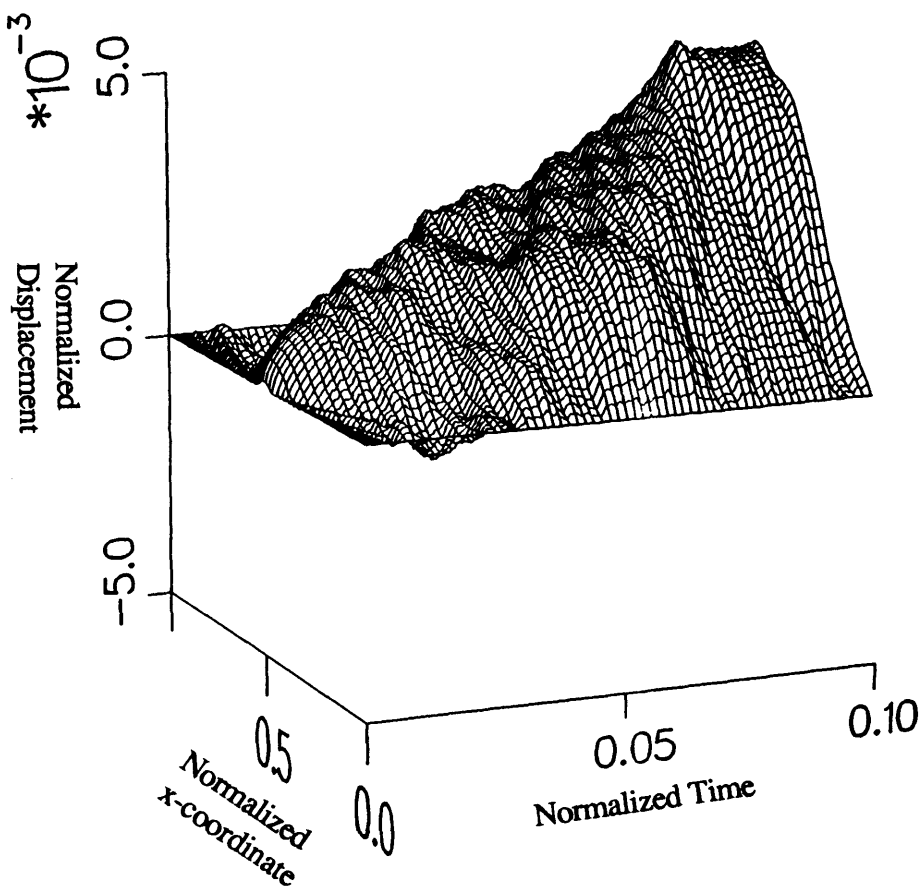

(b)

Fig. 5-3: Response of uniform beam to unit impulse applied at center-span: (a) Long time scale, (b) Short time scale.

cross section rotary inertia. That the figure does not indeed display an instantaneous response at the boundaries is a consequence of both physical and artificial effects. First we note that, from a modal analysis point of view, the excitation of the odd numbered modes due to the impulse decreases with increasing mode number. (The even modes are not excited.) Thus, the modes that travel more quickly also have smaller amplitude. The actual deflection of the beam far from the disturbance source is therefore not visible to the eye until the information carried by the lower, more highly excited modes propagates through the system. The second effect is related to the spatial discretization and temporal sampling used in simulating the response of the system. Because the modal frequencies and wavelengths are intimately related via the dispersion relation, spatial discretization necessarily affects the temporal response. However, since a fine discretization was used for this simulation (256 points in space and 512 in time), it appears as if this second effect is negligible compared to the first.

The infinite propagation speed associated with the Bernoulli-Euler beam is made more apparent in Fig. 5-4, where the beam response (on the left) is compared with that of a Timoshenko beam (on the right). (The simulation of the Timoshenko beam requires a more elaborate development than is presented above, and is therefore discussed in Appendix E.) For these simulations, free-free boundary conditions are assumed, and the impact occurs at a boundary. The effect of rotary inertia is immediately apparent, and manifests itself as a finite disturbance propagation velocity in the Timoshenko beam. Also, the reflection of the shear wave propagating through the Timoshenko beam can be seen in the plot on the right of the figure.

5.2 Two-dimensional elements

Many element models require two independent spatial coordinates to specify the domain of the element. These models include membranes, plates in bending, shells, and plane stress elements. In all cases, the third spatial dimension is of sufficiently small extent in comparison with

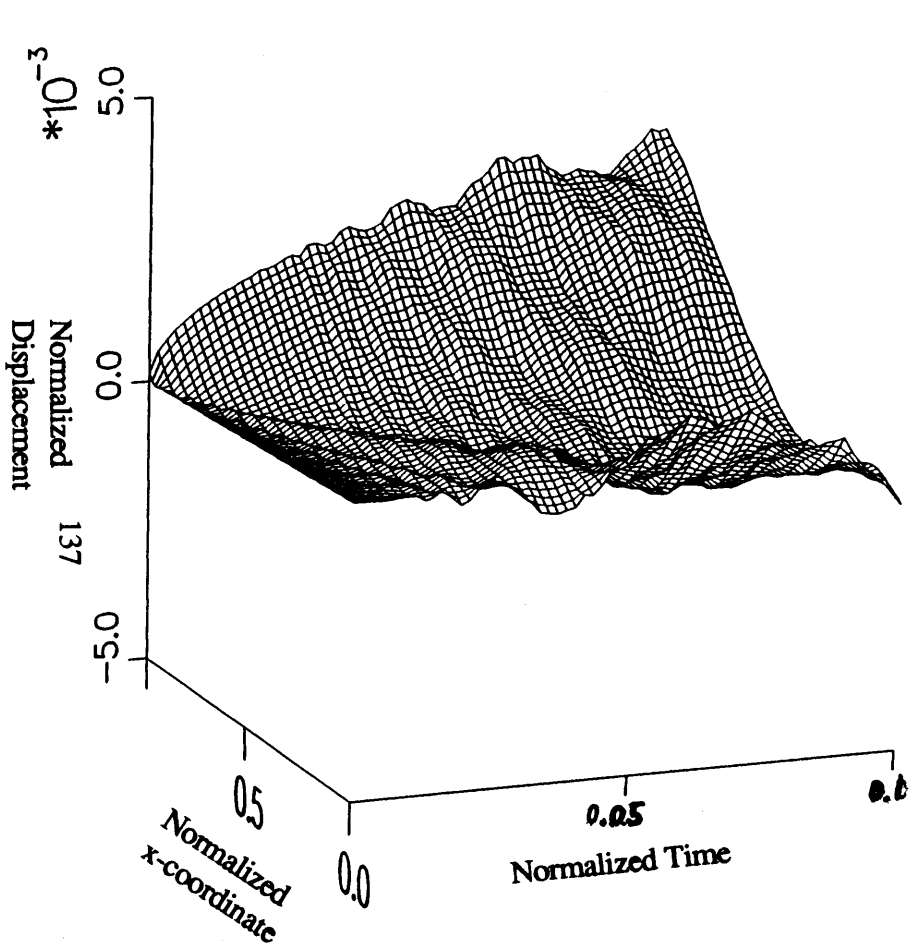

(a)

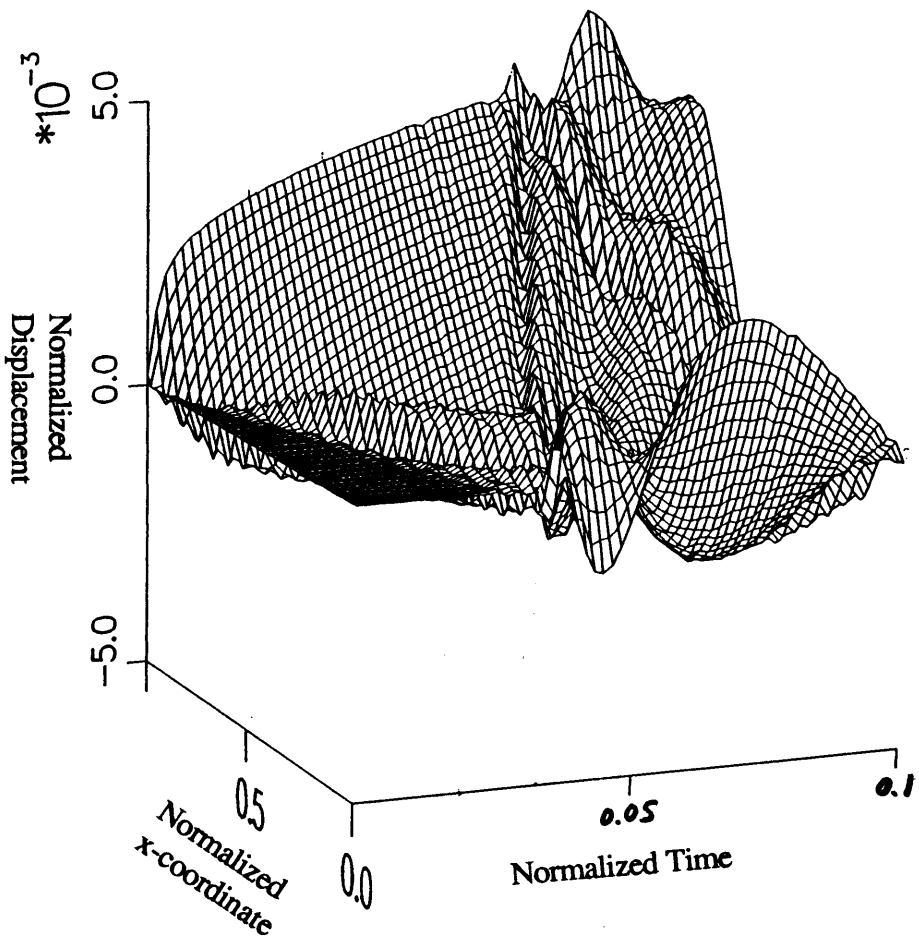

(b)

Fig 5-4: Response of free-free beam to unit impulse applied at x=0: (a) Bernoulli-Euler beam, (b) Timoshenko beam (α_I=4x10^{-4}, α_E=2.8).

the other two dimensions so that a two-dimensional idealization is reasonably accurate. These models have the general differential form

$$\dot{\mathbf{x}}(x,y,t) = \mathbf{L}_{xy}\mathbf{x}(x,y,t) + \mathbf{B}_{xy}\mathbf{u}(x,y,t)\,, \quad x,y\in[0,1]\,, \quad t\in[0,\infty) \tag{5.33}$$

where the subscripts on the operators indicate operations with respect to both x and y. Two examples of two-dimensional elements are given below.

5.2.1 Membrane model

The normalized equation of motion of a membrane is given by

$$-\nabla^2 v(x,y,t) + \ddot{v}(x,y,t) = f(x,y,t) \tag{5.34}$$

where v represents the normalized deflection, f represents a normalized force per unit area, and ∇^2 is the Laplacian operator. Taking the deflection and its velocity as the state variables:

$$\mathbf{x}(x,y,t) = \begin{bmatrix} v(x,y,t) \\ \dot{v}(x,y,t) \end{bmatrix}, \quad u(x,y,t) = f(x,y,t) \tag{5.35a,b}$$

and defining the operators $\mathbf{L}_x$ and $\mathbf{b}_x$ by

$$\mathbf{L}_x = \begin{bmatrix} 0 & 1 \\ \nabla^2 & 0 \end{bmatrix}, \quad \mathbf{b}_x = \begin{bmatrix} 0 \\ 1 \end{bmatrix} \tag{5.36a,b}$$

leads to the relation given by Eq. (5.33).

5.2.2 Plate model

Another two dimensional element is a plate in bending. Here, the equation of motion is

$$\nabla^4 v(x,y,t) + \ddot{v}(x,y,t) = f(x,y,t) \tag{5.37}$$

In this case, the following state vector and forcing input definitions are appropriate:

$$\mathbf{x}(x,y,t) = \begin{bmatrix} \nabla^2 v(x,y,t) \\ \dot{v}(x,y,t) \end{bmatrix}, \quad u(x,y,t) = f(x,y,t) \tag{5.38a,b}$$

The equation of motion then takes the form of Eq. (5.33), with

$$\mathbf{L}_x = \begin{bmatrix} 0 & \nabla^2 \\ -\nabla^2 & 0 \end{bmatrix}, \quad \mathbf{b}_x = \begin{bmatrix} 0 \\ 1 \end{bmatrix} \tag{5.39a,b}$$

5.2.3 Complexity Issues

Unfortunately, the direct simulation of two-dimensional elements is considerably more computationally intensive than the simulation of one-dimension elements. Because the spatial domain is given by two independent variables, discretization in two dimensions is required. As a result, no simulation results are currently available. A complete development of the direct simulation of two dimensional elements is the subject of future research.

5.3 Multiple Element Formulation

Distributed modelling and simulation of multiple member structures, such as space frames and trusses, is a considerably more difficult problem than the single element situation, even for one-dimensional elements. The primary difficulty is in the mathematical treatment of the boundary conditions that arise at element junctions. A rigorous, general assembly procedure for complex structures using direct PDE modelling remains to be developed. One approach currently considered is to define a normalized local coordinate system (x=0 at one end of an element and x=1 at the other end) for each structural member, as shown in Fig. 5-5, and collect the states associated with each element into a large state vector. The dynamics of the entire structure is then still represented by Eq. (5.1), and $\mathbf{L}_x$ becomes block diagonal, with each block representing the dynamics of one member. The boundary conditions then relate various elements of the state vector at x=0 and/or x=1. The difficulty in the direct modelling approach then lies in utilizing these awkward boundary

conditions for the purposes of simulation and control design. The direct multiple element formulation remains an open area of research.

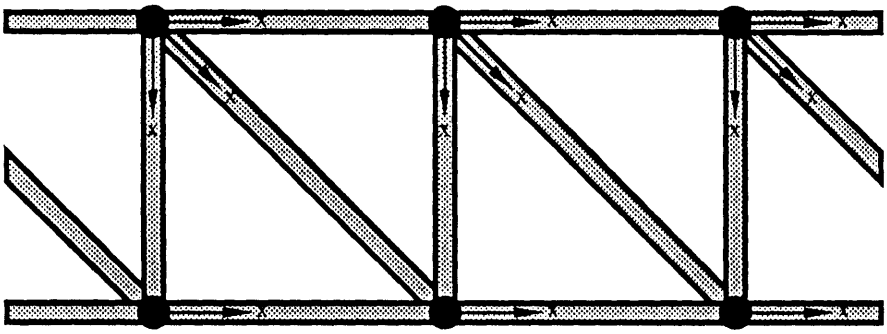

Fig. 5-5: Schematic of multi-element truss structure.

6 CONTROL DESIGN BASED ON DIRECT PARTIAL DIFFERENTIAL EQUATION MODELS

This chapter studies the properties of optimal solutions to the distributed control of systems described by direct PDE models. By distributed control, we imply that control effort is imparted to the structure in a spatially distributed sense. This can be thought of as the limiting process of employing an increasing number of actuators, all of which have a decreasing spatial domain of influence. Particular emphasis is placed on a specific example, that of a Bernoulli-Euler beam. Both finite- and infinite-length beam systems are studied, and comparisons are made between the corresponding optimal solutions. Also, two types of beam actuation are addressed. The first is force actuation, which is commonly used in theoretical studies yet is rarely achievable. The second is curvature actuation, which is more realizable (as mentioned in the previous chapter) but less often addressed in theoretical works.

Distributed control is by no means a new topic. In fact, the essential mathematical groundwork was established in the 1960's by Butkovskii [21], Wang [57], and Lions [22]. The results then obtained were analogous to the classical LQR solution (e.g., the Riccati matrix equation was replaced by a Riccati operator equation), and were derived using the principle of optimality and/or advanced functional analysis. Later works by Tzafestas [58] [59] derived the necessary conditions for optimality from a variational calculus approach. A mathematically rigorous derivation of the Riccati operator equation is performed by Gibson [23] and Balakrishnan [60]. Also, Balas [61] addresses several implementation issues, including the use of a finite set of sensors and actuators and a finite order controller. Perturbation methods are utilized to determine criteria for closed-loop stability. Until now, the complexity of the distributed control problem has rendered it a mere mathematical curiousity, rather than a practical tool. With today's computer resources, however, the solutions to simple problems, such as the Bernoulli-Euler beam system described below, are within reach.

6.1 Linear Quadratic Optimal Control Theory in the 1-D Case

The theory presented in this subsection closely resembles the work of Tzafestas [58] [59]. We restrict our attention to one-dimensional, linear, time-invariant distributed systems. Such systems can be written in the form

$$\dot{\mathbf{x}}(x,t) = \mathbf{L}_x(x)\mathbf{x}(x,t) + \mathbf{B}_x(x)\mathbf{u}(x,t)\,, \quad x\in[0,1]\,, \quad t\in[0,\infty) \tag{6.1}$$

which is identical to Eq. (5.1), except that the disturbance input has been set to zero. We will assume that $\mathbf{L}_x$ and $\mathbf{B}_x$ are matrix differential operators of orders N and M, respectively, with $M \leq N$. As before, the boundary conditions are assumed to be homogeneous, and are expressed as

$$\mathbf{x}(0,t) = \mathbf{x}(1,t) = \mathbf{0}\,, \quad t\in[0,\infty) \tag{6.2}$$

while the initial conditions are expressed as

$$\mathbf{x}(x,0) = \mathbf{x}_0(x)\,, \quad x\in[0,1] \tag{6.3}$$

The simplest optimal distributed compensator is derived under the assumption of full state feedback. That is, perfect measurements of $\mathbf{x}(x,t)$ are available in a continuous sense throughout the spatial domain at every instant of time. It is also assumed that control actuation is available in a similar distributed sense. While these assumptions are rather ideal, they serve to define an upper limit of achievable performance for the control system to be designed. The optimal distributed control problem can then be stated as follows: Given an arbitrary initial condition, determine the control required to return the system to the zero state while minimizing some cost criterion. We will assume a quadratic cost functional of the form

$$J = \frac{1}{2}\int_0^\infty\int_0^1 \left[\mathbf{x}(x,t)^T\mathbf{Q}(x)\mathbf{x}(x,t) + \mathbf{u}(x,t)^T\mathbf{R}(x)\mathbf{u}(x,t)\right] dx\, dt \tag{6.4}$$

where $\mathbf{Q}$ and $\mathbf{R}$ are symmetric (possibly spatially varying) weighting matrices. This is the distributed analogue of the classical linear-quadratic regulator (LQR) problem. Its solution is

obtained by extending the classical variational calculus approach to distributed systems. Note that the cost functional has infinite time horizon. This corresponds to the steady-state LQR problem. The finite time problem is also of interest, but provides no additional insight.

We first augment the cost functional with the system dynamics via a costate vector, $\mathbf{p}(x,t)$:

$$J_a = J + \int_0^\infty \int_0^1 \mathbf{p}(x,t)^T \left[\mathbf{L}_x(x)\mathbf{x}(x,t) + \mathbf{B}_x(x)\mathbf{u}(x,t) - \dot{\mathbf{x}}(x,t) \right] dx\, dt \tag{6.5}$$

The augmented cost functional now depends on the three vectors, $\mathbf{x}$, $\mathbf{u}$, and $\mathbf{p}$. The cost is minimized by setting the variation in cost due to independent perturbations in these three vectors to zero. Thus,

$$\delta J_a(\delta \mathbf{p}) = \int_0^\infty \int_0^1 \delta\mathbf{p}(x,t)^T \left[\mathbf{L}_x(x)\mathbf{x}(x,t) + \mathbf{B}_x(x)\mathbf{u}(x,t) - \dot{\mathbf{x}}(x,t) \right] dx\, dt = 0, \quad \forall\, \delta\mathbf{p}(x,t) \tag{6.6a}$$

$$\delta J_a(\delta \mathbf{u}) = \int_0^\infty \int_0^1 \left[\mathbf{u}(x,t)^T \mathbf{R}(x)\delta\mathbf{u}(x,t) + \mathbf{p}(x,t)^T \mathbf{B}_x(x)\delta\mathbf{u}(x,t) \right] dx\, dt$$

$$= \int_0^\infty \int_0^1 \left[\mathbf{u}(x,t)^T \mathbf{R}(x) + [\mathbf{B}_x^*(x)\mathbf{p}(x,t)]^T \right] \delta\mathbf{u}(x,t)\, dx\, dt = 0, \quad \forall\, \delta\mathbf{u}(x,t) \tag{6.6b}$$

$$\delta J_a(\delta \mathbf{x}) = \int_0^\infty \int_0^1 \left[\mathbf{x}(x,t)^T \mathbf{Q}(x)\delta\mathbf{x}(x,t) + \mathbf{p}(x,t)^T \mathbf{L}_x(x)\delta\mathbf{x}(x,t) - \mathbf{p}(x,t)^T \delta\dot{\mathbf{x}}(x,t) \right] dx\, dt$$

$$= \int_0^\infty \int_0^1 \left[\mathbf{x}(x,t)^T \mathbf{Q}(x) + [\mathbf{L}_x^*(x)\mathbf{p}(x,t)]^T + \dot{\mathbf{p}}(x,t)^T \right] \delta\mathbf{x}(x,t)\, dx\, dt = 0, \quad \forall\, \delta\mathbf{x}(x,t) \tag{6.6c}$$

Equation (6.6a) recovers the system dynamics, while Eq. (6.6b) determines the control law. The superscript (*) represents the formal adjoint operator, which is defined by

$$\int_0^1 \mathbf{a}(x)^T \mathbf{L}_x(x)\mathbf{b}(x)\,dx \;=\; \int_0^1 [\mathbf{L}_x^*(x)\mathbf{a}(x)]^T \mathbf{b}(x)\,dx \;+\; (\text{Boundary Terms}) \tag{6.7}$$

For a linear spatial differential operator, its adjoint is determined by integrating by parts with respect to the spatial dimension. The boundary terms can be made to vanish by placing the appropriate restrictions on $\mathbf{a}(x)$ and $\mathbf{b}(x)$ at $x = 0$ and $x = 1$. The nature of such restrictions is discussed in Appendix F. For this control problem, we have already assumed homogeneous boundary conditions on $\mathbf{x}(x,t)$. The remaining boundary terms vanish by requiring that

$$\frac{\partial^k}{\partial x^k}\mathbf{p}(0,t) \;=\; \frac{\partial^k}{\partial x^k}\mathbf{p}(1,t) \;=\; \mathbf{0}\,, \quad t\in[0,\infty), \quad k = 0, \ldots, N\text{-}2 \tag{6.8}$$

Because we have required that $M \le N$, these conditions suffice to eliminate the boundary terms in both Eqs. (6.6b) and (6.6c).

Solving for $\mathbf{u}$ in Eq. (6.6b) yields

$$\mathbf{u}(x,t) \;=\; -\,\mathbf{R}(x)^{-1}\mathbf{B}_x^*(x)\mathbf{p}(x,t) \tag{6.9}$$

The third term in the integrand of Eq. (6.6c) is integrated by parts with respect to time. The integrated terms go to zero due to the specification of the initial conditions for the system and the necessary condition

$$\mathbf{p}(x,\infty) \;=\; \mathbf{0}\,, \quad x\in[0,1] \tag{6.10}$$

Equations (6.1), (6.9), and the integrand in Eq. (6.6c) lead to the following equations:

$$\begin{aligned} \dot{\mathbf{x}}(x,t) &= \mathbf{L}_x(x)\mathbf{x}(x,t) - \mathbf{B}_x(x)\mathbf{R}(x)^{-1}\mathbf{B}_x^*(x)\mathbf{p}(x,t) \\ \dot{\mathbf{p}}(x,t) &= -\,\mathbf{Q}(x)\mathbf{x}(x,t) - \mathbf{L}_x^*(x)\mathbf{p}(x,t) \end{aligned} \tag{6.11a,b}$$

Equations (6.11a,b) represent the state-costate equations for the distributed control problem. Lions [22] shows that there exists a relation between the state and the costate of the form

$$\mathbf{p}(x,t) = \mathbf{P}_x(x)\mathbf{x}(x,t) \tag{6.12}$$

where $\mathbf{P}_x$ is some linear matrix operator on $\mathbf{x}$. Substituting this form in Eq. (6.11) results in a nonlinear matrix Riccati operator equation in $\mathbf{P}_x$. Such an equation is, in general, difficult to solve. Several approximate solution techniques are described in Juang [62], Schaechter [63], and Zambettakis [64]. However, it is possible to express the linear operator in a different form, so that a solution is easily attained by numerical methods. The assumed form of the solution is the same as used by Wang [57] and Tzafestas [59]:

$$\mathbf{p}(x,t) = \int_0^1 \mathbf{S}(x,y)\,\mathbf{x}(y,t)\,dy \tag{6.13}$$

where $\mathbf{S}$ is the distributed-parameter analogue of the Riccati matrix for lumped-parameter systems. Equation (6.8) automatically imposes the constraints

$$\frac{\partial^k}{\partial x^k}\mathbf{S}(0,y) = \frac{\partial^k}{\partial x^k}\mathbf{S}(1,y) = \mathbf{0}, \quad y \in [0,1], \quad k = 0, \ldots, N-2 \tag{6.14}$$

For complete generality, $\mathbf{S}$ must include generalized functions, such as Dirac delta functions and their derivatives, if necessary. Also, Wang [57] shows that $\mathbf{S}$ is symmetric in its arguments (i.e., $\mathbf{S}(x,y) = \mathbf{S}(y,x)$). Using Eqs. (6.9) and (6.13), the feedback control law becomes

$$\mathbf{u}(x,t) = -\int_0^1 \mathbf{K}(x,y)\,\mathbf{x}(y,t)\,dy\,, \quad \mathbf{K}(x,y) = \mathbf{R}(x)^{-1}\mathbf{B}_x^*(x)\mathbf{S}(x,y) \tag{6.15a,b}$$

Thus, the control law is linear and distributed.

It remains to derive a relation that enables the computation of $\mathbf{S}$. Differentiating Eq. (6.13) and introducing Eq. (6.11a) leads to

$$\dot{\mathbf{p}}(x,t) = \int_0^1 \mathbf{S}(x,y)\left[\mathbf{L}_y(y)\mathbf{x}(y,t) - \mathbf{B}_y(y)\mathbf{R}(y)^{-1}\mathbf{B}_y^*(y)\mathbf{p}(y,t)\right] dy$$

$$= \int_0^1 \left[\mathbf{S}(x,y)\mathbf{L}_y^*(y)^T\mathbf{x}(y,t) - \mathbf{S}(x,y)\mathbf{B}_y(y)\mathbf{R}(y)^{-1}\mathbf{B}_y^*(y)\int_0^1 \mathbf{S}(y,z)\mathbf{x}(z,t)\, dz\right] dy$$

$$= \int_0^1 \left[\mathbf{S}(x,y)\mathbf{L}_y^*(y)^T - \int_0^1 \mathbf{S}(x,z)\mathbf{B}_z(z)\mathbf{R}(z)^{-1}\mathbf{B}_z^*(z)\mathbf{S}(z,y)\, dz\right]\mathbf{x}(y,t)\, dy \qquad (6.16)$$

Once again, an integration by parts applied to the first term in the integral results in the adjoint operator. The last form of the equation is obtained by moving the integral on z outside that of y (thereby exchanging the order of integration for this term), and then switching the roles of y and z, since they are merely dummy variables of integration. In the process, $\mathbf{B}_y$ becomes $\mathbf{B}_z$, as the operators now operate with respect to z. The boundary terms again vanish, subject to the restriction

$$\frac{\partial^k}{\partial y^k}\mathbf{S}(x,0) = \frac{\partial^k}{\partial y^k}\mathbf{S}(x,1) = \mathbf{0}, \quad x \in [0,1], \quad k = 0, \ldots, N-2 \qquad (6.17)$$

It should be noted that the transposes of adjoint operators operate to the left in this case. Similarly, substituting Eq. (6.13) into the right side of Eq. (6.11b) yields

$$\dot{\mathbf{p}}(x,t) = -\mathbf{Q}(x)\,\mathbf{x}(x,t) - \int_0^1 \left[\mathbf{L}_x^*(x)\mathbf{S}(x,y)\mathbf{x}(y,t)\right] dy$$

$$= -\int_0^1 \left[\mathbf{Q}(x)\delta(x-y) + \mathbf{L}_x^*(x)\mathbf{S}(x,y)\right]\mathbf{x}(y,t)\, dy \qquad (6.18)$$

where $\delta(x)$ is the Dirac delta function. Note that the state vector, $\mathbf{x}$, is isolated from each term under the integral in Eqs. (6.16) and (6.18). Thus, subtracting these two equations and setting the resulting integrand to zero yields the desired relation:

$$\mathbf{L}_x^*(x)\mathbf{S}(x,y) + \mathbf{S}(x,y)\,\mathbf{L}_y^*(y)^T + \mathbf{Q}(x)\,\delta(x-y) - \int_0^l \mathbf{S}(x,z)\mathbf{B}_z(z)\mathbf{R}(z)^{-1}\mathbf{B}_z^*(z)\mathbf{S}(z,y)\,dz = 0 \qquad (6.19)$$

This relation is a *functional nonlinear matrix integro-partial differential equation* in x and y, and represents the distributed parameter analogue of the control algebraic Riccati equation. Note that we have assumed S to be time-invariant, which corresponds to the steady-state linear quadratic regulator. For a finite time problem, the zero on the right hand side of Eq. (6.19) would be replaced by $-\frac{\partial}{\partial t}\mathbf{S}(x,y)$.

6.2 Distributed Control of a Finite Beam

In this section, we apply the distributed control theory just presented to a Bernoulli-Euler beam of finite length, as described in an earlier paper [65]. Force actuation will be assumed initially, and curvature actuation will be deferred to Section 6.2.5. The feedback gains will be determined by numerical solution of the Riccati equations given by Eq. (6.19). Although these equations are quite complex, their solutions are readily attainable with the proper mix of algebraic manipulation and numerical computation. Pinned-pinned (i.e., homogeneous) boundary conditions are assumed for the example applications presented in this section, and the system model follows that developed in Chapter 5.

The solution approach presented here differs from other methodologies which are based on appoximate solutions to the mathematical model. For example, Miller and van Schoor [66] derive feedback gain kernels for a finite beam by first deriving a finite dimensional (thus approximate) state-space representation of the dynamics and then applying traditional LQR theory to obtain the feedback gains from discrete points on the beam. These spatially discrete gains are then converted into a spatially distributed feedback kernel by utilizing the interpolation functions associated with the finite element model. In the development presented below, the discretization occurs *after* the equations defining the control solution have been derived, so that the exact

dynamics dictated by the mathematical model are considered. Consequently, analytical expressions for the feedback gains are available for some limiting cases, as described below. For the general situation, however, the numerical methods which are required to solve the equations that define the control law have the same effect as the discretization that would otherwise have been performed on the dynamics model. This result will be examined in Section 6.2.3.

6.2.1 Cost Functional

The dimensionalized form of the cost functional for this system is expressed by

$$J_d = \frac{1}{2}\int_0^{\infty}\int_0^1 \left\{ q_U(x)EI(x)\left[\frac{\partial^2 v_d}{\partial x_d^2}\right]^2 + q_T(x)m(x)\left[\frac{\partial v_d}{\partial t_d}\right]^2 + r(x)\frac{L^4}{EI(x)}f_d^2 \right\} dx_d\, dt_d \qquad (6.20)$$

Thus, q_U represents a weighting on deformational potential energy, q_T represents a weighting on kinetic energy, and r weighs control effort. The physical parameters EI, m and L are introduced so that all three weights have the same units. The cost functional can then be normalized, yielding

$$J = \frac{1}{2}\int_0^{\infty}\int_0^1 \left\{ q_U(x)\eta(x)\left[\frac{\partial^2 v}{\partial x^2}\right]^2 + \frac{q_T(x)}{\beta(x)}\left[\frac{\partial v}{\partial t}\right]^2 + \frac{r(x)}{\eta(x)}f_u^2 \right\} dx\, dt \qquad (6.21)$$

where the nondimensional cost is defined by

$$J = \frac{1}{\sqrt{EI(0)m(0)L^2}}J_d \qquad (6.22)$$

Using the choice of state variables given in Chapter 5, the cost functional takes the form of Eq. (6.4), with

$$\mathbf{Q}(x) = \begin{bmatrix} q_U(x)\eta(x) & 0 \\ 0 & \frac{q_T(x)}{\beta(x)} \end{bmatrix}, \quad \mathbf{R}(x) = \frac{r(x)}{\eta(x)} \qquad (6.23)$$

6.2.2 Derivation of the Necessary Conditions

We must first determine the adjoint operators corresponding to $\mathbf{L}_x$ and $\mathbf{b}_x$. This is accomplished by using the formal definition expressed in Eq. (6.7) and integrating by parts, yielding

$$\mathbf{L}_x^*(x) = \mathbf{L}_x^T(x) = \begin{bmatrix} 0 & -\beta(x) \\ \eta(x) & 0 \end{bmatrix} \frac{\partial^2}{\partial x^2}, \quad \mathbf{b}_x^*(x) = \mathbf{b}_x^T(x) = [0\ \beta(x)] \tag{6.24a,b}$$

Using these expressions in (6.19) yields

$$\mathbf{L}_x^* \mathbf{S}(x,y) + \mathbf{S}(x,y) \mathbf{L}_y^{*T} + \mathbf{Q}(x)\,\delta(x-y) - \int_0^1 \frac{\eta(x)\beta(z)^2}{r(z)} \mathbf{S}(x,z) \begin{bmatrix} 0 & 0 \\ 0 & 1 \end{bmatrix} \mathbf{S}(z,y)\,dz = 0 \tag{6.25}$$

Also, making use of Eq. (6.15), the feedback law becomes

$$u(x,t) = -\int_0^1 \mathbf{k}(x,y)^T \mathbf{x}(y,t)\,dy, \quad \mathbf{k}(x,y) = \begin{bmatrix} k_1(x,y) \\ k_2(x,y) \end{bmatrix} = \frac{\eta(x)\beta(x)}{r(x)} \begin{bmatrix} S_{12}(x,y) \\ S_{22}(x,y) \end{bmatrix} \tag{6.26a,b}$$

The effect of the curvature feedback term (k_1) is to stiffen the beam, which reduces the settling time of the system, while the effect of the velocity feedback term (k_2) is to increase the damping of the system.

Equation (6.25) represents a system of four coupled, nonlinear, integro-partial differential equations. Due to the symmetry of $\mathbf{S}$, the fourth is redundant. Also, only S_{12} and S_{22} are needed to compute the feedback gains. The equation for S_{12}, which represents the curvature feedback gain kernel, is uncoupled from the others:

$$\frac{\partial^2}{\partial x^2}\left[\beta(x)\,S_{12}(x,y)\right] + \frac{\partial^2}{\partial y^2}\left[\beta(y)\,S_{12}(x,y)\right]$$

$$= q_U(x)\eta(x)\,\delta(x-y) - \int_0^1 \frac{\eta(x)\beta(z)^2}{r(z)} S_{12}(x,z) S_{12}(z,y)\,dz \tag{6.27}$$

Similarly, for the velocity feedback gain kernel, the relevant integro-partial differential equation is

$$\frac{\partial^2}{\partial x^2}\left[\eta(x)\, S_{12}(x,y)\right] + \frac{\partial^2}{\partial y^2}\left[\eta(y)\, S_{12}(x,y)\right]$$

$$+ \frac{q_T(x)}{\beta(x)}\,\delta(x-y) - \int_0^1 \frac{\eta(x)\beta(z)^2}{r(z)} S_{22}(x,z) S_{22}(z,y)\, dz = 0 \qquad (6.28)$$

Note that this second equation requires knowledge of $S_{12}(x,y)$, which is determined upon solving (6.27). Thus, the two equations must be solved consecutively, using approximate numerical methods.

6.2.3 Numerical Solution of the Riccati Equations

Previous attempts to obtain a numerical solution to the optimal distributed control problem for a particular system have most often dealt with the operator form of the Riccati equation, which is derived by Gibson [23] using Eq. (6.12) rather than Eq. (6.13). Usually, the solution is expressed as a series expansion of spatial differential operators of increasing order, as in Juang [62]. In some cases, the distributed control law is only solved at points where discrete controls are to be applied, which leads to a slightly suboptimal design. Balas [61] takes this approach. However, in this formulation, the functional form of the Riccati equations leads naturally to a numerical solution procedure. Because of the fundamental differences in the forms of Eqs. (6.27) and (6.28), a separate algorithm is developed for each equation, as discussed below.

6.2.3.1 Solution of the First Riccati Equation

The first Riccati equation bears some resemblance to Poisson's equation, with the exception of the nonlinear integral term. For a uniform beam, in the limit as q_U/r approaches zero, the relationship indeed reduces to Poisson's equation, with the forcing consisting of a distribution of delta functions along the line $y = x$. This represents the case of extremely low control authority, and the corresponding gain surface, S_{12}, is completely analogous to that of a stretched, square

membrane loaded with a uniform out-of-plane force over one of its diagonals. For this special case, a closed-form, exact analytical solution exists in terms of an infinite trigonometric series [67]. At the other extreme, it is easy to show that for the case of high control authority, the approximate solution is given by a distribution of delta functions along y = x. Unfortunately, the presence of the nonlinear integral term neccesitates the use of numerical techniques for all other cases. Nonetheless, these limiting cases serve as qualitative results against which the numerical solutions can be compared.

For finite values of q_U/r, Eq. (6.27) is solved by spatially discretizing the domain of S_{12} and using finite differencing and summation to approximate the derivative and integral operations, respectively. A modified relaxation algorithm is then invoked to converge upon the solution. We begin by discretizing the spatial variables according to

$$x_i = \frac{i}{N}, \quad i = 0,\ldots,N \tag{6.29}$$

and defining the mesh

$$s_{ij} = s_{12}(x_i,y_j) \tag{6.30}$$

A simple approximation to the derivative terms is then

$$\frac{\partial^2}{\partial x^2}\left[\beta(x)\, S_{12}(x,y)\right] + \frac{\partial^2}{\partial y^2}\left[\beta(y)\, S_{12}(x,y)\right] \approx N^2\left[\Delta_{ij}^{\beta} - 2(\beta_i+\beta_j)s_{ij}\right] \tag{6.31}$$

where Δ_{ij}^{β} is defined by

$$\Delta_{ij}^{\beta} = \beta_{i-1}\, s_{i-1\, j} + \beta_{i+1}\, s_{i+1\, j} + \beta_{j-1}\, s_{i\, j-1} + \beta_{j+1}\, s_{i\, j+1} \tag{6.32}$$

The forcing term in Eq. (6.27) can be approximated by

$$q_U(x)\eta(x)\,\delta(x-y) \approx N\, q_{U_i}\eta_i\,\delta_{ij} \tag{6.33}$$

and δ_{ij} is the discrete Kroneker delta function. Finally, the integral term is replaced with a summation, leading to

$$\int_0^1 \frac{\eta(x)\beta(z)^2}{r(z)} S_{12}(x,z)S_{12}(z,y)\,dz \approx \frac{1}{N}\sum_{k=0}^{N} \frac{\eta_k\beta_k^2}{r_k} s_{ik}\, s_{kj}$$

$$= \frac{1}{N}\left[I_{ij} + \left(\frac{\eta_i\beta_i^2}{r_i} s_{ii} + \frac{\eta_j\beta_i^2}{r_j} s_{jj}\right)\left(1 - \frac{1}{2}\delta_{ij}\right) s_{ij}\right] \tag{6.34}$$

where

$$I_{ij} = \sum_{\substack{k=0 \\ k\neq i \\ k\neq j}}^{N} \frac{\eta_k\beta_k^2}{r_k} s_{ik}\, s_{kj} \tag{6.35}$$

Note that, in Eqs. (6.31) and (6.34), the terms involving s_{ij} have been isolated from terms involving neighboring points. Collecting the approximate expressions, we have, for the finite difference equation

$$N^2\Delta_{ij}^{\beta} - 2N^2(\beta_i+\beta_j)s_{ij} = N\, q_{U_i}\eta_i\,\delta_{ij} - \frac{1}{N} I_{ij} - \frac{1}{N}\left(\frac{\eta_i\beta_i^2}{r_i} s_{ii} + \frac{\eta_j\beta_i^2}{r_j} s_{jj}\right)\left(1 - \frac{1}{2}\delta_{ij}\right) s_{ij} \tag{6.36}$$

Thus, given an initial estimate for the solution at each mesh point, s_{ij}^0, the entire mesh is successively iterated according to the rule

$$s_{ij}^{n+1} = s_{ij}^n - \omega e_{ij}^n, \quad 0<\omega<2 \tag{6.37}$$

In this last equation, e_{ij}^n represents the residual error at each mesh point at the n-th iteration. An expression for this error is obtained by solving Eq. (6.36) for s_{ij}, which yields

$$e_{ij} = s_{ij} - \frac{N^2\Delta_{ij}^{\beta} + \frac{1}{N} I_{ij} - N\, q_{U_i}\eta_i\,\delta_{ij}}{2N^2(\beta_i+\beta_j) - \frac{1}{N}\left(\frac{\eta_i\beta_i^2}{r_i} s_{ii} + \frac{\eta_j\beta_i^2}{r_j} s_{jj}\right)\left(1 - \frac{1}{2}\delta_{ij}\right)} \tag{6.38}$$

Also, ω is a relaxation parameter, and can be adjusted to maximize the rate of convergence towards a solution, as discussed in Press [68].

The condition for a converged solution is given by

$$\left|e_{ij}^{n}\right| < \varepsilon, \quad \forall\, i,j \tag{6.39}$$

where ε is some small positive constant. The relaxation method is guaranteed to converge when r approaches infinity (in this case, Eq. (6.27) reduces to Poisson's equation), and tests have shown that convergence is maintained over a wide range of values of q_U and r, provided ω is adjusted accordingly.

In Fig. 6-1, the gain surfaces for various r/q_U are shown for the case of constant section properties. The effect of the boundaries can be seen by observing the gain surface near (x,y) = (0,0) and (x,y) = (1,1). Qualitatively, the influence of the boundary conditions extends over a smaller domain as the control authority is increased (i.e., as the quantity r/q_U becomes smaller). A quantitative analysis indicates that the extent of this "boundary layer" is roughly proportional to $(r/q_U)^{1/4}$. This makes sense physically. As the control authority is increased (r decreasing), the system is able to suppress the majority of a disturbance before the energy reaches and reflects off the boundary. Thus, near the center of the beam, the controller models the beam as if it were infinite in length.

6.2.3.2 Solution of the Second Riccati Equation

Equation (6.28) does not have a well-behaved solution, since it requires that the integral of $S_{22}(x,y)$ cancel the delta function. We therefore make the following substitution:

$$S_{22}(x,y) = \tilde{S}_{22}(x,y) + \frac{r(x)}{\eta(x)\beta(x)^2}\, g(x)\, \delta(x-y) \tag{6.40}$$

where

$$g(x) = \sqrt{\frac{\eta(x)\beta(x)}{r(x)}\left[\eta(x)^2 q_U(x) + q_T(x)\right]} \tag{6.41}$$

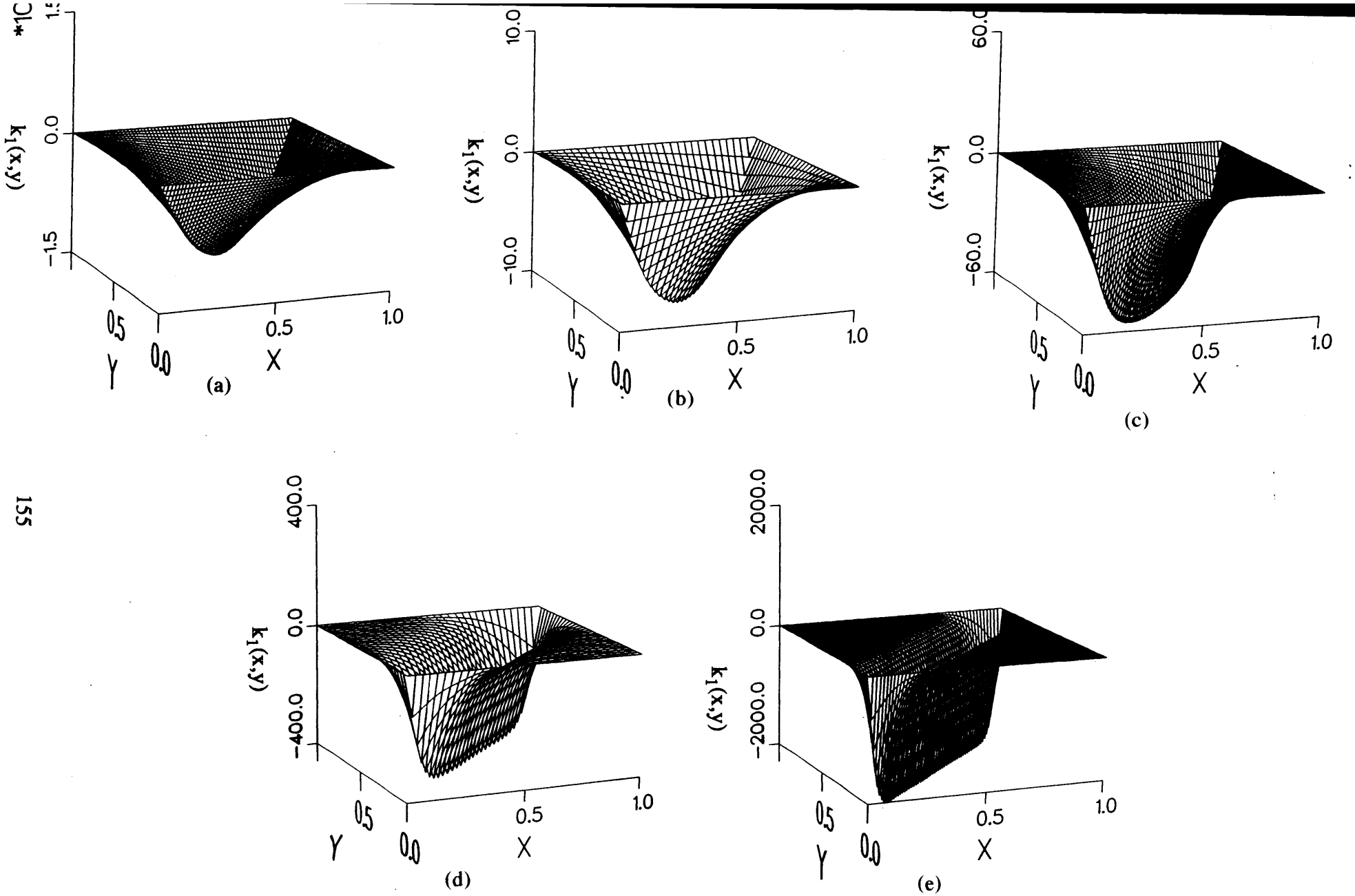

Fig. 6-1: Curvature feedback kernels for uniform beam: (a) $r/q_U=10^3$, (b) $r/q_U=10^{-2}$, (c) $r/q_U=10^{-3}$, (d) $r/q_U=10^{-4}$, (e) $r/q_U=10^{-5}$.

This is equivalent to identifying a collocated component in the velocity feedback kernel. Equation (6.28) then becomes

$$\int_0^1 \frac{\eta(z)\beta(z)^2}{r(z)} \tilde{S}_{22}(x,z)\tilde{S}_{22}(z,y)\,dz + [g(x)+g(y)]\,\tilde{S}_{22}(x,y) - c(x,y) = 0 \qquad (6.42)$$

where the known forcing term is given by

$$c(x,y) = \frac{\partial^2}{\partial x^2}\left[\eta(x)\,S_{12}(x,y)\right] + \frac{\partial^2}{\partial y^2}\left[\eta(y)\,S_{12}(x,y)\right] - q_U(x)\,\frac{\eta(x)^2}{\beta(x)}\,\delta(x-y) \qquad (6.43)$$

It is easy to show that c(x,y) is continuous (assuming $\eta(x)$ and $\beta(x)$ are continuous), as the partial differentiation terms produce delta functions that exactly cancel the term involving $\delta(x-y)$.

The solution algorithm for S_{22} is straightforward. Upon discretizing in the spatial dimension, Eq. (6.42) becomes

$$\tilde{\mathbf{S}}_{22}\mathbf{R}^{-1}\tilde{\mathbf{S}}_{22} + \tilde{\mathbf{S}}_{22}\mathbf{G} + \mathbf{G}\tilde{\mathbf{S}}_{22} - \mathbf{C} = 0 \qquad (6.44)$$

where

$$\tilde{\mathbf{S}}_{22} = \left[\tilde{S}_{22}(x_i,y_j)\right] \qquad (6.45a)$$

$$\mathbf{C} = \left[c(x_i,y_j)\right] \qquad (6.45b)$$

$$\mathbf{G} = \mathrm{diag}\left[g(x_i)\right] \qquad (6.45c)$$

$$\mathbf{R} = \mathrm{diag}\left[N\,\frac{r(x_i)}{\eta(x_i)\beta(x_i)^2}\right] \qquad (6.45d)$$

and N is the number of mesh points between x=0 and x=1. The matrix equation is solved by completing the square. After pre- and post-multiplying by $\mathbf{R}^{-1/2}$, Eq. (6.44) can be factored as

$$\left[\mathbf{R}^{-1/2}\tilde{\mathbf{S}}_{22}\mathbf{R}^{-1/2} + \mathbf{G}\right]^2 = \mathbf{R}^{-1/2}\mathbf{C}\mathbf{R}^{-1/2} + \mathbf{G}^2 \qquad (6.46)$$

The right hand side of Eq. (6.46) is symmetric and positive semidefinite. It therefore has the eigenvector decomposition

$$\mathbf{R}^{-1/2}\mathbf{C}\mathbf{R}^{-1/2} + \mathbf{G}^2 = \mathbf{W}\Lambda\mathbf{W}^T \tag{6.47}$$

where Λ is a diagonal matrix with non-negative entries. Finally, substituting Eq. (6.47) in Eq. (6.46) and solving for $\tilde{\mathbf{S}}_{22}$ gives

$$\tilde{\mathbf{S}}_{22} = \mathbf{R}^{1/2}\left[\mathbf{W}\Lambda^{1/2}\mathbf{W}^T - \mathbf{G}\right]\mathbf{R}^{1/2} \tag{6.48}$$

Typical $\tilde{k}_2(x,y)$ surfaces are shown in Fig. 6-2 ($\tilde{k}_2(x,y)$ is just $k_2(x,y)$ without the delta function corresponding to the collocated feedback component). Finally, Fig. 6-3 shows the feedback gain kernels associated with a linearly tapered beam.

6.2.3.3 Comparison With Discretized Beam Model

In this section, we will show that the application of traditional LQR to a discretized beam model yields the same discretized Riccati equations as presented above. For simplicity, we will assume uniform section properties and weighting functions. By discretizing the spatial domain and utilizing finite differences for derivative operations, it is easy to show that Eq. (5.10) can be approximated by

$$\begin{bmatrix} \dot{\mathbf{x}}_1 \\ \dot{\mathbf{x}}_2 \end{bmatrix} = \begin{bmatrix} \mathbf{0} & \mathbf{D} \\ -\mathbf{D} & \mathbf{0} \end{bmatrix} \begin{bmatrix} \mathbf{x}_1 \\ \mathbf{x}_2 \end{bmatrix} + \begin{bmatrix} \mathbf{0} \\ \mathbf{I} \end{bmatrix} \mathbf{f} \tag{6.49}$$

where the partitions of the state vector and the forcing vector are given by

$$\mathbf{x}_1(t) \approx \left\{\frac{\partial^2}{\partial x^2} v(x_i,t)\right\}, \quad \mathbf{x}_2(t) \approx \left\{\dot{v}(x_i,t)\right\}, \quad \mathbf{f}(t) \approx \left\{f(x_i,t)\right\} \tag{6.50a-c}$$

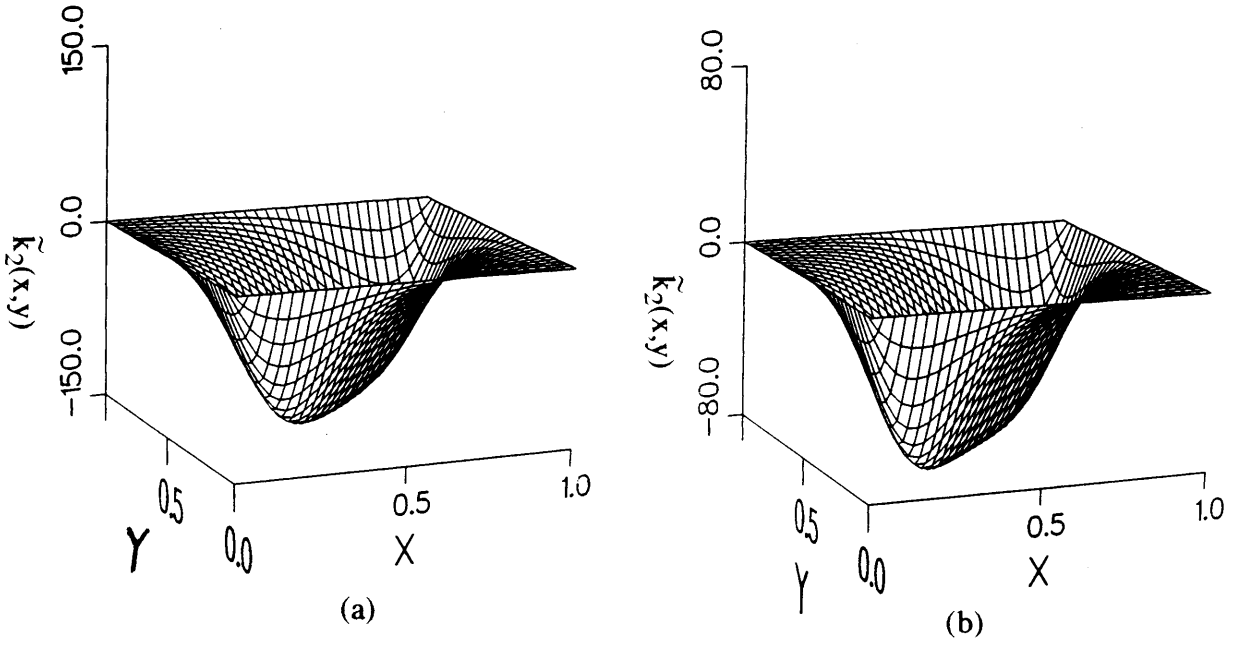

Fig 6-2: Velocity feedback kernels for uniform beam: (a) $r/q_U=10^{-4}$ and $q_T=0$, (b) $r/q_U=10^{-4}$ and $q_T=q_U$.

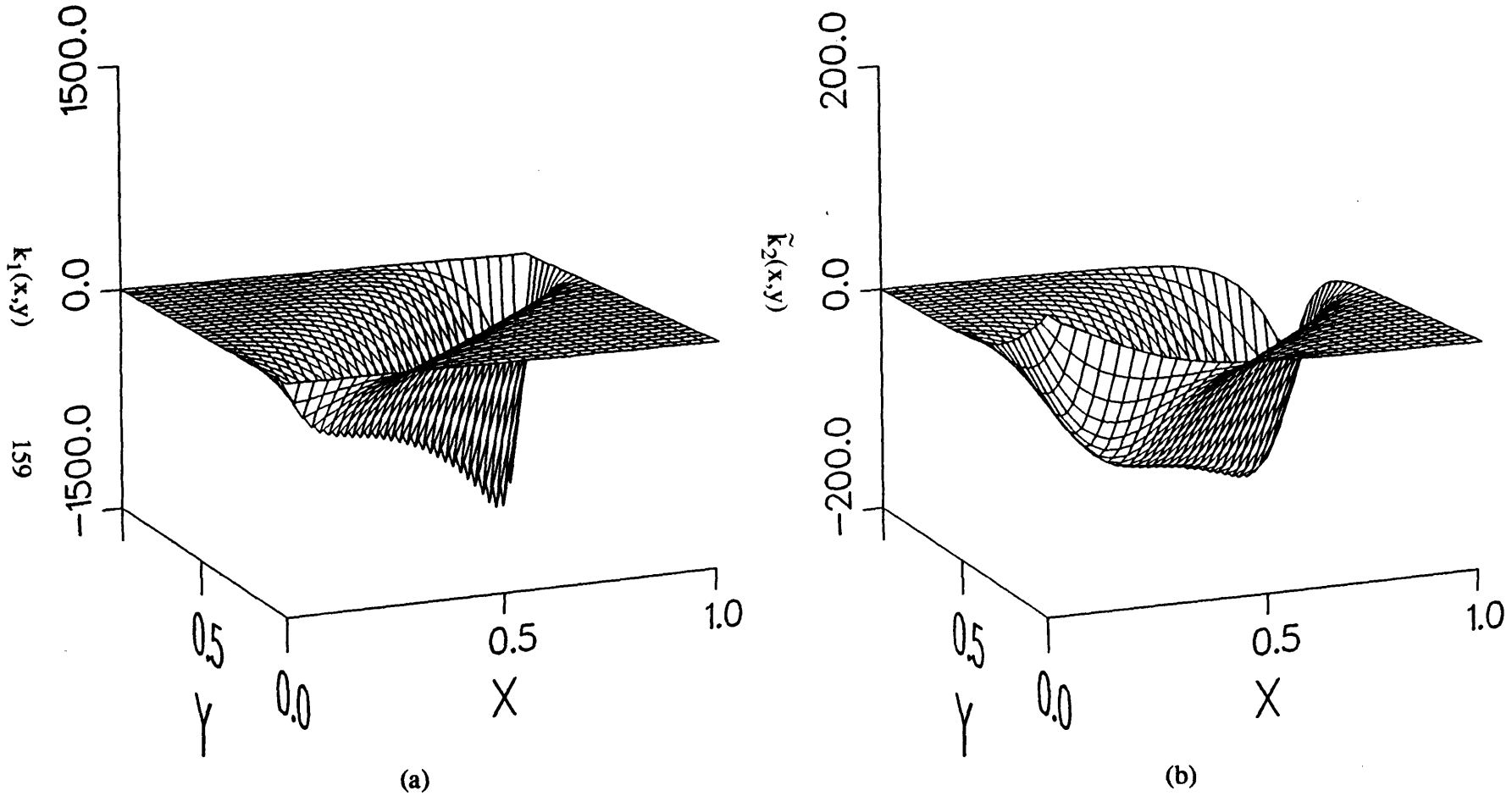

Fig 6-3: Feedback gains for tapered beam (Beam diameter varies linearly from 1.0 at x=0 to 0.75 at x=1): (a) Curvature feedback kernel, (b) Velocity feedback kernel.

and the finite difference matrix **D** is defined in Eq. (5.25). The discrete weighting matrices are likewise given by

$$\mathbf{R} = r\mathbf{I}, \quad \mathbf{Q} = \begin{bmatrix} q_1\mathbf{I} & \mathbf{0} \\ \mathbf{0} & q_2\mathbf{I} \end{bmatrix} \tag{6.51a,b}$$

and the Riccati matrix is partitioned as

$$\mathbf{S} = \begin{bmatrix} \mathbf{S}_{11} & \mathbf{S}_{12} \\ \mathbf{S}_{21} & \mathbf{S}_{22} \end{bmatrix} \tag{6.52}$$

Application of the algebraic Riccati equation then yields

$$-\mathbf{D}\,\mathbf{S}_{12} - \mathbf{S}_{12}\,\mathbf{D} + q_1\mathbf{I} - \frac{1}{r}\mathbf{S}_{12}^2 = \mathbf{0} \tag{6.53a}$$

$$\mathbf{D}\,\mathbf{S}_{12} + \mathbf{S}_{12}\,\mathbf{D} + q_2\mathbf{I} - \frac{1}{r}\mathbf{S}_{22}^2 = \mathbf{0} \tag{6.53b}$$

These equations are simply the discretized versions of Eqs. (6.27) and (6.28), respectively, with uniform section properties and weightings. Thus, in this case, discretization via finite differences at the system dynamics level is justified. In light of the preceeding development, the algorithm given by Eqs. (6.36-38) is interpreted as an iterative solution method for the first of the discrete Riccati equations shown above. For non-homogeneous boundary conditions, the elements in the corners of the **D** matrix are modified in the same manner as was discussed in Chapter 5. This is completely analogous to the integrated boundary terms present when determining the adjoint to the system dynamics operator matrix in the continuous case.

6.2.4 The Case of Curvature Actuation

For the sake of simplicity, we will assume constant section properties and weighting functions for this case. This makes it possible to obtain an analytical expression for the feedback gains. (Note that, for force actuation, a numerical solution procedure is required even in the case of constant section properties and weightings.)

The feedback gains, expressed in terms of the solutions to the Riccati equations, become

$$k_1(x,y) = \frac{1}{r}\frac{\partial^2}{\partial x^2} S_{12}(x,y), \quad k_2(x,y) = \frac{1}{r}\frac{\partial^2}{\partial x^2} S_{22}(x,y) \tag{6.54a,b}$$

and the functional Riccati equations themselves become

$$\frac{\partial^2}{\partial x^2} S_{12}(x,y) + \frac{\partial^2}{\partial y^2} S_{12}(x,y) = q_U \delta(x-y) - \frac{1}{r}\int_0^1 S_{12}(x,z)\frac{\partial^4}{\partial z^4} S_{12}(z,y)\,dz \tag{6.55a}$$

$$\frac{\partial^2}{\partial x^2} S_{12}(x,y) + \frac{\partial^2}{\partial y^2} S_{12}(x,y) + q_T \delta(x-y) - \frac{1}{r}\int_0^1 S_{22}(x,z)\frac{\partial^4}{\partial z^4} S_{22}(z,y)\,dz = 0 \tag{6.55b}$$

Integrating by parts and invoking the homogeneous boundary conditions yields

$$\frac{\partial^2}{\partial x^2} S_{12}(x,y) + \frac{\partial^2}{\partial y^2} S_{12}(x,y) = q_U \delta(x-y) - \frac{1}{r}\int_0^1 \frac{\partial^2}{\partial z^2} S_{12}(x,z)\frac{\partial^2}{\partial z^2} S_{12}(z,y)\,dz \tag{6.56a}$$

$$\frac{\partial^2}{\partial x^2} S_{12}(x,y) + \frac{\partial^2}{\partial y^2} S_{12}(x,y) + q_T \delta(x-y) - \frac{1}{r}\int_0^1 \frac{\partial^2}{\partial z^2} S_{22}(x,z)\frac{\partial^2}{\partial z^2} S_{22}(z,y)\,dz = 0 \tag{6.56b}$$

Furthermore, introducing Eqs. (6.54a,b) and exploiting the symmetry of S(x,y) yields

$$2r\,k_{12}(x,y) = q_U \delta(x-y) - r\int_0^1 k_{12}(x,z)k_{12}(z,y)\,dz \tag{6.57a}$$

$$r\int_0^1 k_{22}(x,z)k_{22}(z,y)\,dz = 2r\,k_{12}(x,y) + q_T \delta(x-y) \tag{6.57b}$$

It can easily be shown that the generalized functions

$$k_1(x,y) = \left[\sqrt{1 + \frac{q_U}{r}} - 1\right]\delta(x-y) \tag{6.58a}$$

$$k_2(x,y) = \sqrt{\frac{q_T}{r} + 2\left[\sqrt{1 + \frac{q_U}{r}} - 1\right]}\,\delta(x-y) \tag{6.58b}$$

solve the Riccati equations. The optimal control is therefore purely collocated, even though the controller has access to the state vector over the entire spatial domain.

6.2.5 Closed-Loop Simulation Results

The closed-loop simulations of a uniform beam with a sinusoidal initial condition and various control and state weightings are shown in Fig. 6-4. As expected, the response of the system becomes faster with increasing control authority. In Fig. 6-5, the response of the system to a center-span transverse impulse is shown. This figure can be compared with the open-loop case, shown in Fig. 5-3. In this case, most of the disturbance has been suppressed before it reflects from the boundaries, and the first mode of vibration is never established. This is characteristic of high-gain control systems, which provide high levels of damping augmentation. For these systems, the energy in the propagating wave is effectively absorbed as it progresses towards the boundaries of the system.

In order to compare the performance of the optimal distributed controller with the performance of discrete controllers, finite element models of the beam system were developed. These models have as state variables the same quantities that are used in the distributed model (i.e., curvature and velocity), but are only available at discrete points along the structure. Similarly, the control inputs are available at a finite number of stations along the beam. These models were used to develop full state LQR control laws for the discrete systems. Once obtained, the feedback gain matrix was separated into curvature feedback and velocity feedback partitions. In order to compare these gains to the distributed gain surfaces, the elements of the matrix partitions were plotted using their indices as x and y coordinates, and their actual values as the z coordinates. In this way, a graphical comparison was available. Figure 6-6 displays these plots for both the $r/q_U=10^{-2}$ and the $r/q_U=10^{-3}$ cases (q_T was set to zero in both cases). The figure shows excellent agreement between the discrete and the distributed curvature feedback gains, and supports the conclusion that the velocity feedback gain is primarily collocated. A numerical comparison was also performed, whereby the optimal costs required to bring the beam system to rest from initial disturbances were computed. Both the sinusoidal initial condition and the center-span impact cases were addressed. Table 6-1 summarizes the results of the numerical comparison. In all cases, the optimal cost required to return the system to rest approaches the optimal distributed cost as the discretization

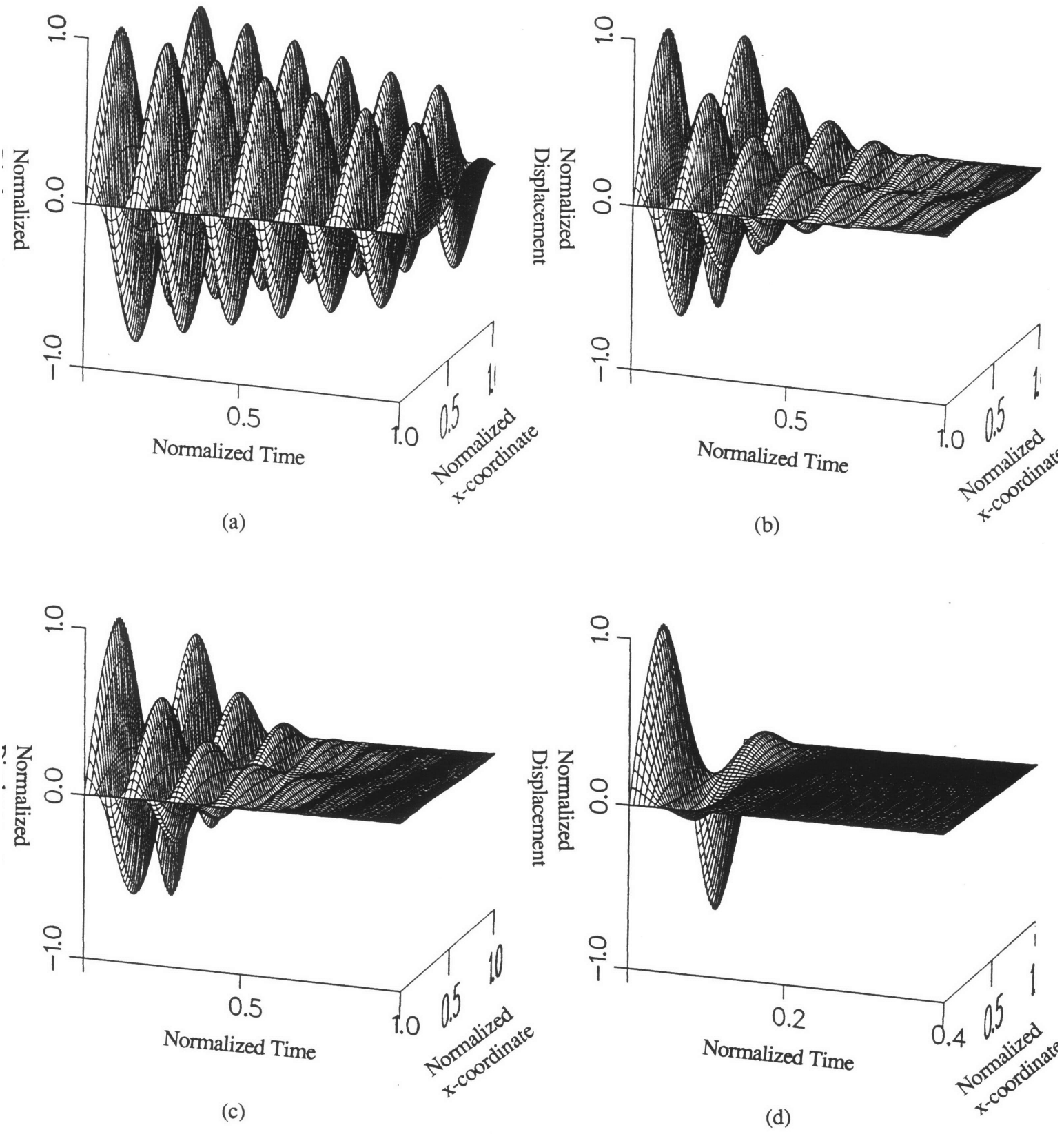

Fig. 6-4: Closed-loop simulation of uniform beam with $v_0(x)=\sin(2\pi x)$: (a) $r/q_U=10^{-2}$ and $q_T=q_U$, (b) $r/q_U=10^{-3}$ and $q_T=q_U$, (c) $r/q_U=5\times10^{-4}$ and $q_T=q_U$, (d) $r/q_U=10^{-4}$ and $q_T=q_U$.

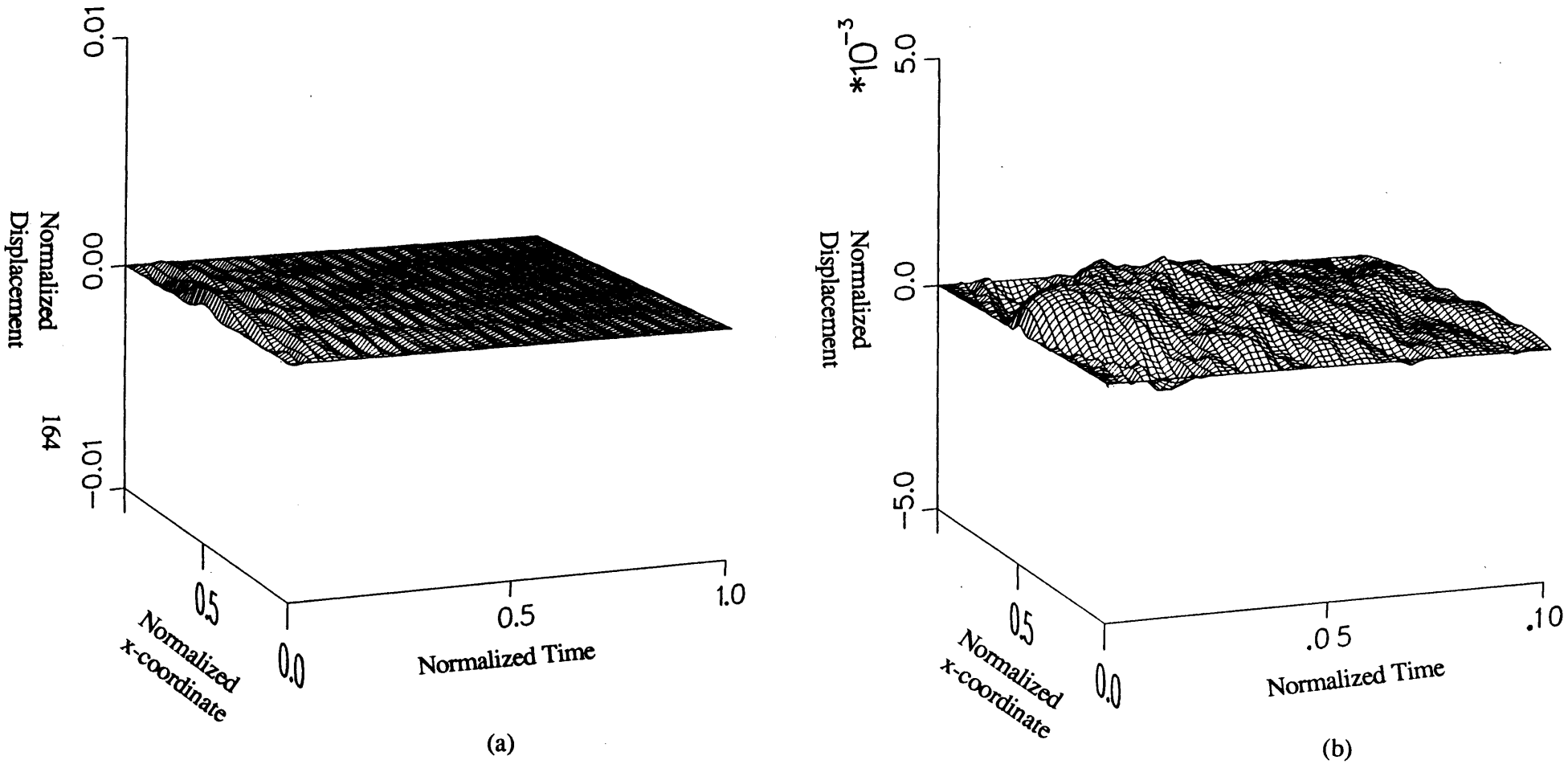

Fig. 6-5: Closed-loop simulation of uniform beam with unit impulse applied at center-span ($r/q_U=10^{-4}$ and $q_T=q_U$): (a) Long time scale, (b) Short time scale.

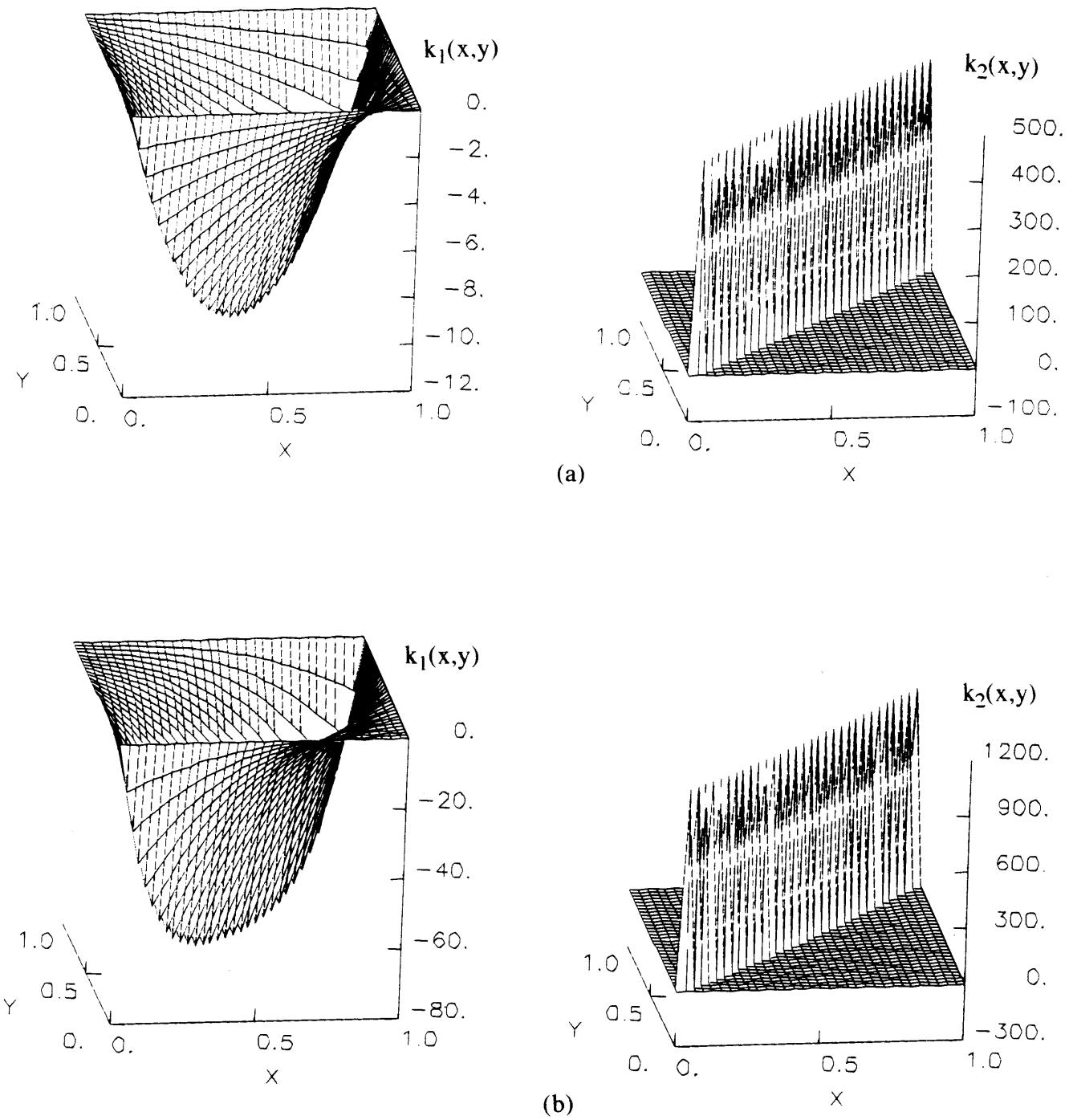

Fig. 6-6: Plots of gain matrices determined from LQR solution to discretized beam model: (a) $r/q_U=10^{-3}$, (b) $r/q_U=10^{-4}$.

	Weightings			Lumped Parameter Formulation			Distributed Formulation
	q_U	q_T	r	8 elements	16 elements	32 elements	
J_d	1	1	10^{-4}	13.68	13.28	13.19	13.15
	1	1	10^{-3}	22.02	21.72	21.65	21.64
	1	1	10^{-2}	56.79	56.67	56.64	56.63
	10	1	10^{-2}	158.48	156.62	156.18	156.13
J_v	1	1	10^{-4}	6.50×10^{-3}	6.81×10^{-3}	6.94×10^{-3}	7.07×10^{-3}
	1	1	10^{-3}	2.16×10^{-2}	2.24×10^{-2}	2.21×10^{-2}	2.24×10^{-2}
	1	1	10^{-2}	6.99×10^{-2}	7.03×10^{-2}	7.05×10^{-2}	7.07×10^{-2}
	10	1	10^{-2}	0.153	0.160	0.163	0.166

Table 6-1: Comparison between optimal costs for distributed control and conventional lumped-parameter control. In the table, J_d corresponds to an initial displacement field $v_0(x)=\sin(2\pi x)$, and J_v corresponds to an initial unit impulsive disturbance applied at the center-span of the beam.

becomes finer. (Details on determining the optimal cost for the distributed controller can be found in Appendix G.) This makes complete sense in light of the discussion in Section 6.2.3.3, where it was shown that *identical* results are obtained regardless of when the discretization takes place. The validation presented here then serves to prove that the iterative solution techniques presented in this chapter do indeed converge upon the proper solution.

6.3 Distributed Control of an Infinite Beam

In this section, we validate the results for the optimal control of finite beams by considering an infinite beam system. Most of the formulation presented in this section is based on recent work by deLuis [55]. The basic idea is to work in the spatial frequency-domain, using the spatially transformed dynamics of the beam system. This reduces the distributed control problem to a family of conventional optimal control problems, parametrized by the spatial frequency variable. The infinite model requires that the section properties and cost weightings be spatially constant, so that the spatial transform is possible. In his work, deLuis relies on functional analysis arguments to justify the form of the control law. In contrast, the approach presented here is somewhat more straightforward and intuitively satisfying.

6.3.1 Spatially Transformed Dynamics and Cost Functional

Because the beam is of infinite extent, we can take the spatial Fourier transform of (5.1). The resulting equation of motion, expressed in terms of t and the spatial frequency, ξ, is then

$$\dot{\hat{\mathbf{x}}}(\xi,t) = \mathbf{A}(\xi)\hat{\mathbf{x}}(\xi,t) + \mathbf{b}\hat{u}(\xi,t) \tag{6.59}$$

where $\mathbf{A}(\xi)$ is obtained from Eq. (5.12a):

$$\mathbf{A}(\xi) = \begin{bmatrix} 0 & -\xi^2 \\ \xi^2 & 0 \end{bmatrix} \tag{6.60}$$

The transformed state variable and the transformed control input are, in general, complex-valued. However, because $\mathbf{A}(\xi)$ and $\mathbf{b}$ are purely real for this system, the real and imaginary dynamics decouple, giving

$$\dot{\hat{\mathbf{x}}}_r(\xi,t) = \mathbf{A}(\xi)\hat{\mathbf{x}}_r(\xi,t) + \mathbf{b}\hat{u}_r(\xi,t), \quad \dot{\hat{\mathbf{x}}}_i(\xi,t) = \mathbf{A}(\xi)\hat{\mathbf{x}}_i(\xi,t) + \mathbf{b}\hat{u}_i(\xi,t) \qquad (6.61a,b)$$

Thus, for each value of ξ, we are left with two identical real-valued systems for which an optimal control solution is desired.

The cost functional to be minimized is quadratic in the normalized variables. For distributed control, we must integrate over the entire (infinite) domain. The cost functional is thus

$$J = \frac{1}{2}\int_0^{\infty}\int_{-\infty}^{\infty} \left\{ q_U \left[\frac{\partial^2 w}{\partial x^2}\right]^2 + q_T \left[\frac{\partial w}{\partial t}\right]^2 + r f_u^2 \right\} dx\, dt \qquad (6.62)$$

In this last expression, which is analogous to Eq. (6.21), q_U and q_T weigh potential and kinetic energy, respectively, while r weighs control effort. Equation (6.62) can be written

$$J = \frac{1}{2}\int_0^{\infty} J_\xi(t)\, dt \qquad (6.63)$$

where

$$J_\xi(t) = \int_{-\infty}^{\infty} \left[\mathbf{y}(x,t)^T \mathbf{y}(x,t) + r\, u(x,t)^2 \right] dx \qquad (6.64)$$

and the following definitions have been made:

$$\mathbf{y}(x,t) = \mathbf{Q}^{1/2}\mathbf{x}(x,t), \quad \mathbf{Q} = \begin{bmatrix} q_U & 0 \\ 0 & q_T \end{bmatrix} \qquad (6.65a,b)$$

By making use of Parseval's theorem, we can write

$$J_\xi(t) = \frac{1}{2\pi}\int_{-\infty}^{\infty} \left[\hat{\mathbf{x}}(\xi,t)^H \mathbf{Q} \hat{\mathbf{x}}(\xi,t) + r\, |\hat{u}(\xi,t)|^2 \right] d\xi \qquad (6.66)$$

where the superscript (^{H}) represents the complex conjugate transpose operation. Now, interchanging the order of integration in (6.63) yields

$$J = \frac{1}{4\pi} \int_{-\infty}^{\infty} J_t(\xi)\, d\xi \tag{6.67}$$

where

$$J_t(\xi) = \int_0^{\infty} \left[\hat{\mathbf{x}}(\xi,t)^H \mathbf{Q} \hat{\mathbf{x}}(\xi,t) + r\, |\hat{u}(\xi,t)|^2 \right] dt \tag{6.68}$$

At this point, the following observation can be made: J is minimized if and only if $J_t(\xi)$ is minimized for every value of ξ. We must now express $\hat{\mathbf{x}}(\xi,t)$ and $\hat{u}(\xi,t)$ in terms of their real and imaginary parts. Because $\mathbf{Q}$ and r are purely real, the (imaginary) cross-terms cancel in (6.68), and we are left with

$$\begin{aligned} J_t(\xi) = & \int_0^{\infty} \left[\hat{\mathbf{x}}_r(\xi,t)^H \mathbf{Q} \hat{\mathbf{x}}_r(\xi,t) + r\, \hat{u}_r(\xi,t)^2 \right] dt \\ & + \int_0^{\infty} \left[\hat{\mathbf{x}}_i(\xi,t)^H \mathbf{Q} \hat{\mathbf{x}}_i(\xi,t) + r\, \hat{u}_i(\xi,t)^2 \right] dt \end{aligned} \tag{6.69}$$

6.3.2 Optimal Control Solution

For each value of ξ, we have two identical dynamic systems given by Eqs. (6.61a,b) and two identical cost functionals given by Eq. (6.69). Therefore, the control laws relating $\hat{u}_r$ to $\hat{\mathbf{x}}_r$ and $\hat{u}_i$ to $\hat{\mathbf{x}}_i$ will be identical, and can be combined into the single equation

$$\hat{u}(\xi,t) = -\hat{\mathbf{k}}(\xi)^T \hat{\mathbf{x}}(\xi,t) \tag{6.70}$$

where the transformed gain vector, $\hat{\mathbf{k}}(\xi)$, is a real function of the spatial frequency. Taking the inverse transform of this equation yields

$$u(x,t) = -\int_{-\infty}^{\infty} \mathbf{k}(x-y)^T \mathbf{x}(y,t)\, dy \tag{6.71}$$

Thus, the integration kernel $\mathbf{k}(x-y)$ can be though of as a weighting from the sensed state at a location y to the control actuation at a location x. Classical LQR theory gives, as the optimal solution

$$\hat{\mathbf{k}}(\xi)^T = \left[\hat{k}_1(\xi)\ \hat{k}_2(\xi)\right] = \frac{1}{r}\mathbf{b}^T\mathbf{S}(\xi) \tag{6.72}$$

where $\mathbf{S}(\xi)$ solves the control algebraic Riccati equation

$$\mathbf{A}(\xi)^T\mathbf{S}(\xi) + \mathbf{S}(\xi)\mathbf{A}(\xi) + \mathbf{Q} - \frac{1}{r}\mathbf{S}(\xi)\mathbf{b}\mathbf{b}^T\mathbf{S}(\xi) = 0 \tag{6.73}$$

Substituting the known parameters $\mathbf{A}(\xi)$, $\mathbf{b}$, $\mathbf{Q}$ and r and solving for the elements of $\mathbf{S}$ gives

$$S_{11}(\xi) = r\xi^2\sqrt{1+\lambda_U}\sqrt{\lambda_T + 2\left[\sqrt{1+\lambda_U} - 1\right]} \tag{6.74a}$$

$$S_{12}(\xi) = -r\xi^2\left[\sqrt{1+\lambda_U} - 1\right] \tag{6.74b}$$

$$S_{22}(\xi) = r\xi^2\sqrt{\lambda_T + 2\left[\sqrt{1+\lambda_U} - 1\right]} \tag{6.74c}$$

where

$$\lambda_U = \frac{q_U}{r\xi^4}, \quad \lambda_T = \frac{q_T}{r\xi^4} \tag{6.75a,b}$$

Note that the entire behavior of the solution is parametrized by the dimensionless groupings, λ_U and λ_T. Since ξ has the units of inverse length, we can infer that $(r/q_U)^{1/4}$ and $(r/q_T)^{1/4}$ represent nondimensional distances.

Substituting Eq. (6.74b) in Eq. (6.72), we obtain, for the feedback gain relating curvature to force,

$$k_1(x) = (q_U/r)^{3/4} f_1\left[(q_U/r)^{1/4}x\right] \tag{6.76}$$

where $f_1(\bullet)$ is the inverse transform of $\hat{f}_1(\bullet)$, given by

$$\hat{f}_1(\xi) = -\left[\sqrt{\xi^4 + 1} - \xi^2\right] \tag{6.77}$$

A plot of $f_1(\bullet)$ is shown in Fig. 6-7. Some qualitative features of the feedback gain become apparent upon examination of Eq. (6.76). First, the magnitude of the feedback varies as $(q_U/r)^{3/4}$, so that increased curvature penalty and reduced control penality both increase the feedback gain, as expected. Second, the argument of $f_1(\bullet)$ indicates that the control becomes more localized with increasing state penalty and decreasing control penalty. This makes sense in terms of the nondimensional lengths described above. High control authority suggests that a disturbance can be suppressed quickly, before the majority of the energy travels very far along the beam, whereas low authority requires a longer time interval (and hence greater distance) to suppress the disturbance. These features are also observed for the finite beam system described in Section 6.2. In fact, cross sections of the finite beam gain kernels, taken near the center of the surface, have the approximate shape of the gain kernel for the infinite beam system, and the approximation gets better with increasing control authority. A quantitative analysis indicates that this is the case when $r/q_U < 10^{-3}$.

In computing $k_2(x)$, the velocity to force feedback term, an interesting feature emerges. The Riccati solution, $S_{22}(\xi)$, does not go to zero as ξ approaches infinity. As a result, the inverse transform of $\hat{k}_2(\xi)$ will include a delta function. In order to make the inverse transform continuous, this bias term is subtracted from $\hat{k}_2(\xi)$, and a delta function with magnitude equal to this bias is added to $k_2(x)$ after inversion. Thus, the velocity feedback gain kernel is expressed as

$$k_2(x) = (q_U/r)^{3/4} f_2\left[(q_U/r)^{1/4}x\,;\, q_T/q_U\right] + \sqrt{\frac{q_U}{r} + \frac{q_T}{r}}\,\delta(x) \tag{6.78}$$

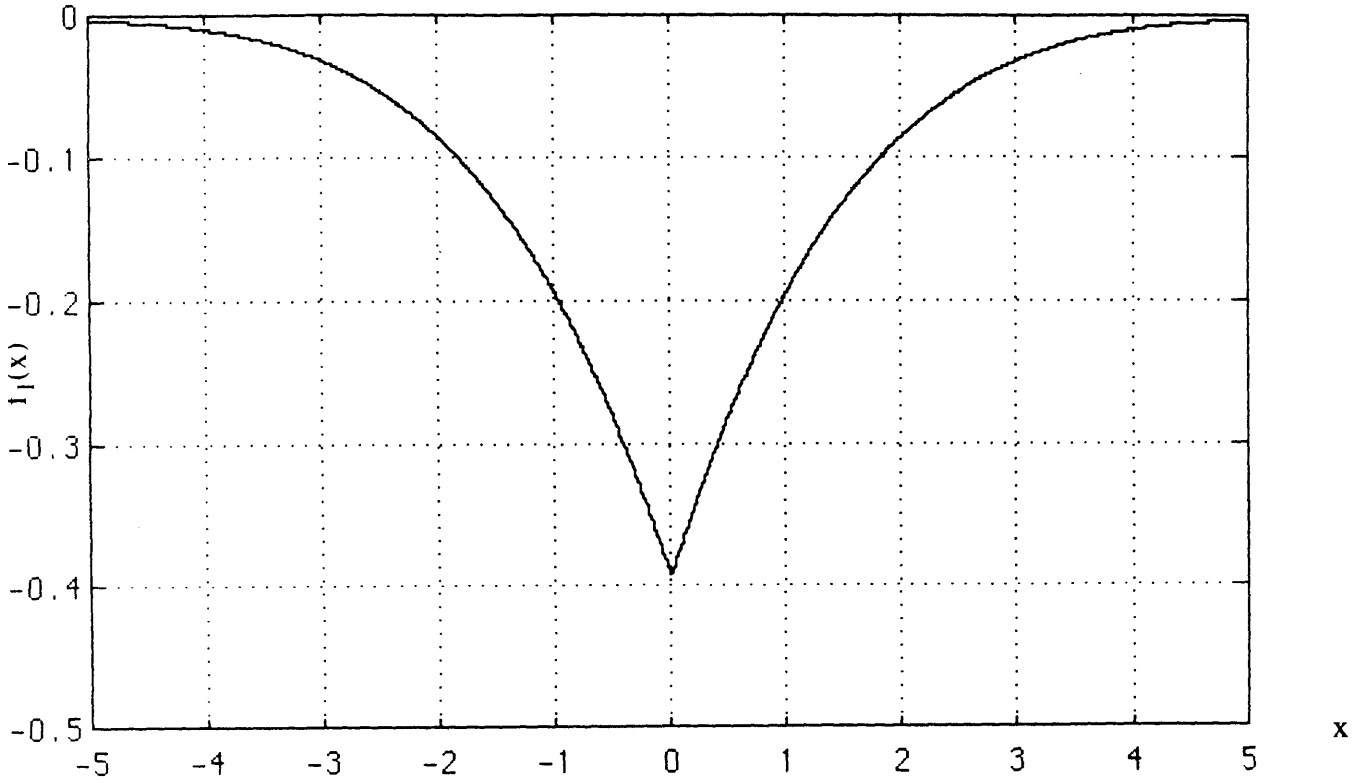

Fig. 6-7: Normalized curvature feedback gain kernel for infinite beam.

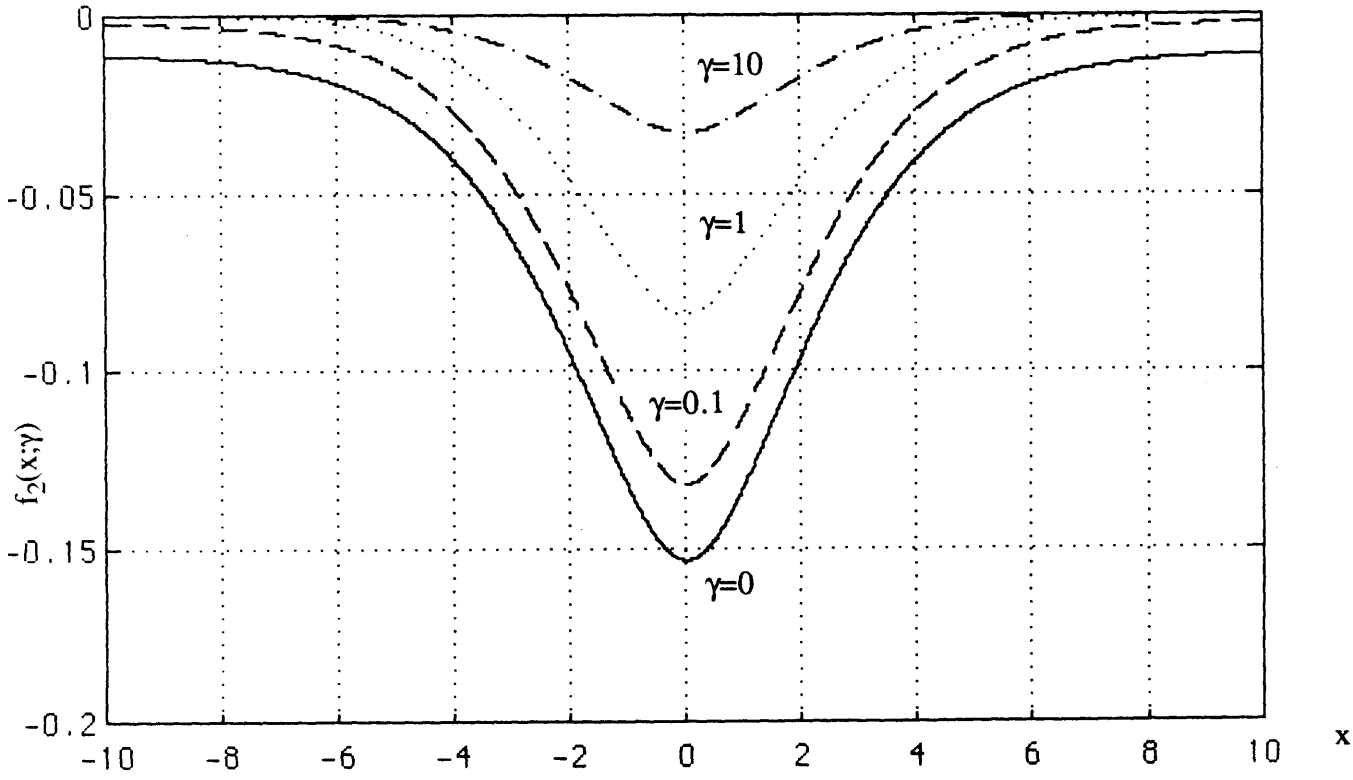

Fig. 6-8: Normalized velocity feedback gain kernel for infinite beam.

where

$$\hat{f}_2(\xi;\gamma) = \sqrt{\gamma - 2k^2 \hat{f}_1(\xi)} - \sqrt{\gamma + 1} \tag{6.79}$$

This corresponds exactly with the introduction of a collocated velocity feedback term for the finite beam system. Indeed, the magnitude of the collocated gain agrees with the finite case, with the assumption of constant section properties and weightings. Note that the velocity feedback term is parametrized by the same nondimensional length as $k_1(x)$, but an additional parameter, the ratio between kinetic and potential energy penalties, is also present. Plots of $f_2(\bullet;\gamma)$, shown for various γ, are shown in Fig. 6-8. Once again, cross sections of the velocity feedback gain kernel for the finite beam case agree quite well with the infinite beam kernel.

6.3.3 The Case of Curvature Actuation

We now study the case where a distributed actuator capable of inducing curvature in a continuous manner represents the control input. Such is the limiting case of a beam with many embedded piezoelectric actuators distributed along its span. For this system, the equation of motion is modified to

$$\frac{\partial^4}{\partial x^4} v(x,t) + \frac{\partial^2}{\partial t^2} v(x,t) = \frac{\partial^2}{\partial x^2} m_c(x,t) \tag{6.80}$$

where $m_c(x,t)$ represents the net action of the distributed piezoelectrics. By making the new definitions

$$u(x,t) = m_c(x,t), \quad \mathbf{b}(\xi) = \begin{bmatrix} 0 \\ -\xi 2 \end{bmatrix} \tag{6.81a,b}$$

the transformed equation of motion becomes

$$\dot{\hat{\mathbf{x}}}(\xi,t) = \mathbf{A}(\xi)\hat{\mathbf{x}}(\xi,t) + \mathbf{b}(\xi)\hat{u}(\xi,t) \tag{6.82}$$

This equation is identical to Eq. (6.59) except that **b** is now a function of ξ. This subtle difference has a profound effect on the control law. Following the same procedure as in the previous subsection leads to expressions for the transformed gain kernels which are independent of ξ:

$$\hat{k}_1 = \sqrt{1 + \frac{q_U}{r}} - 1, \quad \hat{k}_2 = \sqrt{\frac{q_T}{r} + 2\,\hat{k}_1} \tag{6.83a,b}$$

As a result, we have

$$k_1(x) = \hat{k}_1\,\delta(x), \quad k_2(x) = \hat{k}_2\,\delta(x) \tag{6.84a,b}$$

The optimal control is therefore purely collocated, even though the controller has access to the state vector over the entire spatial domain. This result is quantitatively identical to the finite beam case presented in Section 6.2.5, regardless of the state and control effort penalties.

6.4 Distributed Control of 2-D Systems

Another potential application of distributed control theory is in the active control of two-dimensional structures, such as plate or shell structures. These structural models are usually more representative of the actual physical structure, particularly in applications involving large antennae, solar panels, deformable mirrors and/or hull structures. Unfortunately, the increase in computational complexity for both the modelling and control of these models goes hand-in-hand with the increase in fidelity of the model, as has been demonstrated in previous chapters. An additional consideration when dealing with distributed control designs for such models is the feasibility of placing a large number of sensors and actuators on the physical structure. It is typically impossible to arbitrarily place sensors and actuators on a structure without sacrificing some performance or violating some mass constraint. If we add to this the issue of reliability in utilizing the large number of sensors and actuators required for 2-D structural control, we begin to understand the immense complexity of the problem at hand. Nevertheless, it is still useful to obtain distributed control solutions in this realm. In the first place, the distributed solution serves as a first cut approximation to any implementable design. In addition, recent advances in

embedded sensor/actuator technology, fault-tolerant design, and high-speed parallel processing may some day lead to a realizable distributed controller. With these ideas in mind, we address the issue of distributed control for 2-D structural models.

6.4.1 Structures of Finite Dimensions

Solutions to the distributed control problem for one-dimensional elements are numerically tractable because the domains over which the gains are to be determined are two-dimensional. For plate- or membrane-like structures, the dimensionality of the gain domain is increased to four, and the feedback law takes the form

$$\mathbf{u}(x,y,t) = -\int_0^1\int_0^1 \mathbf{K}(x,y,x',y')\,\mathbf{x}(x',y',t)\,dx'\,dy' \tag{6.85}$$

The associated distributed Riccati equation is then

$$\mathbf{L}^*(x,y)\mathbf{S}(x,y,x',y') + \mathbf{S}(x,y,x',y')\,\mathbf{L}'^*(x',y')^T + \mathbf{Q}(x,y)\,\delta(x-x')\,\delta(y-y')$$

$$-\int_0^1\int_0^1 \mathbf{S}(x,y,x'',y'')\mathbf{B}''(x'',y'')\mathbf{R}(x'',y'')^{-1}\mathbf{B}''^*(x'',y'')\mathbf{S}(x'',y'',x',y')\,dx''\,dy'' = 0 \tag{6.86}$$

Note that this equation assumes homogeneous boundary conditions over the entire structural boundary. The solution of such an equation represents a formidable computational task, even for the plate and membrane models discussed in Section 5.2.

If we restrict ourselves to the case of a circular plate pinned along its circumferance, we can use physical arguments to reduce the dimension of the problem by one. In polar coordinates, the feedback gain is given by

$$u(r,\theta,t) = -\int_0^{2\pi}\int_0^1 \mathbf{k}^T(r,\theta,r',\theta')\,\mathbf{x}(r',\theta',t)\,r'\,dr'\,d\theta' \tag{6.87}$$

However, due to the axial symmetry of the problem, we can deduce that the gain depends only on the relative angular position of the sensing and actuating points, in addition to the radial information. Thus, the feedback law reduces to

$$u(r,\theta,t) = -\int_0^{2\pi}\int_0^1 \mathbf{k}^T(r,r',\Delta\theta)\,\mathbf{x}(r',\theta',t)\,r'\,dr'\,d\theta' \tag{6.88}$$

where $\Delta\theta = \theta - \theta'$ is the angular separation between the sensing and actuating points. Accounting for this symmetry, and using the fact that ∇^2 is self-adjoint for homogeneous boundary conditions, we can immediately write down the distributed Riccati equation for S_{12} in polar coordinates:

$$(\nabla^2 + \nabla'^2)\,S_{12}(r,r',\Delta\theta) = \frac{1}{r}\,Q_U\,\delta(r-r')\,\delta(\Delta\theta)$$

$$-\frac{1}{R}\int_0^1 r''\int_0^{2\pi} S_{12}(r,r'',\theta-\theta'')\,S_{12}(r'',r',\theta''-\theta')\,d\theta''\,dr'' \tag{6.89}$$

where the Laplacian operators are defined as

$$\nabla^2 = \frac{1}{r}\frac{\partial}{\partial r}\left[r\,\frac{\partial}{\partial r}\right], \quad \nabla'^2 = \frac{1}{r'}\frac{\partial}{\partial r'}\left[r'\,\frac{\partial}{\partial r'}\right] \tag{6.90a,b}$$

and Q_U and R represent the curvature and control effort weightings, respectively. Note that the derivatives of S_{12} with respect to θ and θ' in the Laplacian operators exactly cancel. The feedback gain then becomes

$$k_1(r,r',\Delta\theta) = \frac{1}{R}\,S_{12}(r,r',\Delta\theta) \tag{6.91}$$

The Riccati equation for S_{22} can be determined in a similar manner. As was the case for the Bernoulli-Euler beam, S_{12} must first be determined in order to solve for S_{22}. Finally, if the optimal costs are to be determined, the equation involving S_{11} is also required. Although we have succeeded in reducing the dimension of the problem by one, it still remains computationally

untractable, given the computer resources currently available. Consequently, a numerical solution is not presented here.

6.4.2 Structure of Infinite Dimensions

As was the case with the Bernoulli-Euler beam, we can obtain qualitative information concerning the feedback gains for a structure of finite dimensions by studying the limiting case of an infinite structure. Again, the spatial Fourier transform will be employed, once for each spatial dimension. The dimension of the domain of the feedback gain will again be reduced, as the relative position between sensing and actuation points replaces their absolute positions.

We will take as the prototypical system a plate of infinite extent with spatially uniform properties. Through the Fourier transforms, the spatial variables, x and y, are related to the spatial frequencies, ξ and η, respectively. The transformed dynamics, obtained from Eq. (5.33), then take the form

$$\dot{\hat{\mathbf{x}}}(\xi,\eta,t) = \mathbf{A}(\rho)\hat{\mathbf{x}}(\xi,\eta,t) + \mathbf{b}\hat{u}(\xi,\eta,t) \tag{6.92}$$

with

$$\mathbf{A}(\rho) = \begin{bmatrix} 0 & -\rho^2 \\ \rho^2 & 0 \end{bmatrix}, \quad \mathbf{b} = \begin{bmatrix} 0 \\ 1 \end{bmatrix}, \quad \rho^2 = \xi^2 + \eta^2 \tag{6.93}$$

The feedback control law, obtained through inverse transform, is a double convolution, and is given by

$$u(x,y) = -\int_{-\infty}^{\infty}\int_{-\infty}^{\infty} \left[k_1(x',y')\nabla^2 w(x-x',y-y') + k_2(x',y')\dot{w}(x-x',y-y') \right] dx'\, dy' \tag{6.94}$$

Proceeding in a manner similar to the Bernoulli-Euler beam problem, we obtain, for the curvature feedback gain,

$$k_1(x,y) = \frac{1}{4\pi^2} \int_{-\infty}^{\infty}\int_{-\infty}^{\infty} \left[\rho^2 - \sqrt{\rho^4 + Q_U/R} \right] e^{j(\xi x+\eta y)} \, d\xi \, d\eta \tag{6.95}$$

If we now switch from rectangular (x,y) to polar (r,θ) coordinates and do the same for the variables of integration, we obtain

$$k_1(r,\theta) = \frac{1}{4\pi^2} \int_0^{\infty} \rho \left[\rho^2 - \sqrt{\rho^4 + Q_U/R} \right] \int_0^{2\pi} e^{j\rho r(\cos\theta\cos\phi+\sin\theta\sin\phi)} \, d\phi \, d\rho \tag{6.96}$$

By invoking the trigonometric identity, $\cos\theta\cos\phi+\sin\theta\sin\phi = \cos(\theta-\phi)$, and adjusting the limits of integration on ϕ accordingly, we can write

$$k_1(r,\theta) = \frac{1}{4\pi^2} \int_0^{\infty} \rho \left[\rho^2 - \sqrt{\rho^4 + Q_U/R} \right] \int_{-\pi}^{\pi} e^{j\rho r\cos\phi} \, d\phi \, d\rho \tag{6.97}$$

The integral involving ϕ is now identified as twice the value of the zero-th order Bessel function, $J_0(\rho r)$. We can therefore express the feedback gain in its final analytical form:

$$k_1(r,\theta) = k_1(r) = \frac{1}{2\pi} \int_0^{\infty} \rho \left[\rho^2 - \sqrt{\rho^4 + Q_U/R} \right] J_0(\rho r) \, d\rho \tag{6.98}$$

That the feedback gain is independent of θ makes sense physically, as one would expect the feedback gain from a sensed point to an actuation point to be solely a function of the distance between the two. In determining $k_2(x,y)$, we are again faced with a function that does not vanish

for large ξ and η. Consequently, we again have a component of collocated velocity feedback. The remaining distributed velocity feedback gain is easily shown to be

$$k_2(r) = \frac{1}{2\pi}\int_0^\infty \rho \left\{ \sqrt{Q_T/R + 2\rho^2\left[\rho^2 - \sqrt{\rho^4 + Q_U/R}\,\right]} - \sqrt{Q_T/R + Q_U/R} \right\} J_0(\rho r)\, d\rho \quad (6.99)$$

Substituting these expressions into the feedback law given by Eq. (6.94), converting the variables of integration to polar coordinates, and performing some algebraic manipulation yields, for the control law

$$u(x,y) = -\int_0^\infty \left[\tilde{k}_1(r)\,\tilde{x}_1(r) + \tilde{k}_2(r)\,\tilde{x}_2(r) \right] dr - \sqrt{\gamma+1}\, w(x,y) \quad (6.100)$$

where the following definitions have been made:

$$\tilde{x}_1(r) = \frac{1}{2\pi}\int_0^{2\pi} \nabla^2 w(x+r\cos\theta, y+r\sin\theta)\, d\theta \quad (6.101a)$$

$$\tilde{x}_2(r) = \frac{1}{2\pi}\int_0^{2\pi} \dot{w}(x+r\cos\theta, y+r\sin\theta)\, d\theta \quad (6.101b)$$

$$\tilde{k}_1(r) = 2\pi\,(Q_U/R)^{3/4}\, f_1\left[(Q_U/R)^{1/4} r\right] \quad (6.101c)$$

$$\tilde{k}_2(r) = 2\pi\,(Q_U/R)^{3/4}\, f_2\left[(Q_U/R)^{1/4} r\,;\, Q_T/Q_U\right] \quad (6.101d)$$

and the normalized gain kernels are given by

$$f_1(r) = r\int_0^\infty \rho \left[\rho^2 - \sqrt{\rho^4 + 1}\,\right] J_0(\rho r)\, d\rho \quad (6.102a)$$

$$f_2(r;\gamma) = r\int_0^\infty \rho \left\{ \sqrt{\gamma + 2\rho^2\left[\rho^2 - \sqrt{\rho^4 + 1}\,\right]} - \sqrt{\gamma+1} \right\} J_0(\rho r)\, d\rho \quad (6.102b)$$

The functions $f_1(r)$ and $f_2(r;\gamma)$ have been computed numerically and are shown in Figures 6-9 and 6-10. They represent the normalized gains to a point of actuation from the value of the state vector averaged over all points at a distance r from the actuation point. They bear some resemblance to the normalized feedback gains for the Bernoulli-Euler beam, in that they both vanish as r approaches infinity and in that f_2 has the same general dependence on γ. That both f_1 and f_2 vanish at r=0 is a consequence of the definitions of $\tilde{x}_1$ and $\tilde{x}_2$, which include $1/2\pi$ terms rather than $1/2\pi r$ terms. Had the latter terms been used in these definitions, the normalized feedback gains would have been unbounded at r=0. Consequently, it appears as if the locations and values of the minima of $f_1(r)$ and $f_2(r;\gamma)$ have no physical significance.

6.5 Discussion

The results from the distributed control theory presented above provide insights as to the qualitative nature of the feedback control laws for a controlled structure. With a distributed force actuator, the curvature feedback is purely distributed (becoming more localized with increasing control authority), while the velocity feedback has both collocated and distributed components. For a finite beam, a nondimensional length, which depends on the state and control effort penalties, indicates the extent to which the boundary conditions imposed on the finite beam affect the optimal control solution. Numerical examples for finite beam systems support this claim. The same can be inferred about the distributed control of a plate: away from the boundaries, the feedback gain approximates that of the infinite plate.

For a beam (or plate) with a distributed curvature actuator (a more realistic and implementable situation), both the curvature and velocity feedback gains are purely collocated, regardless of the nondimensional length parameter. As a result, the boundary conditions do not affect the optimal control solution for this type of actuation. The next logical step in this analysis would be to study the effect of replacing the distributed actuator with a set of discrete controls, which better reflects a physically realizable controlled structure. One way to model discrete actuation would be to let the control influence matrix, **B**, be the sum of a series of spatial delta

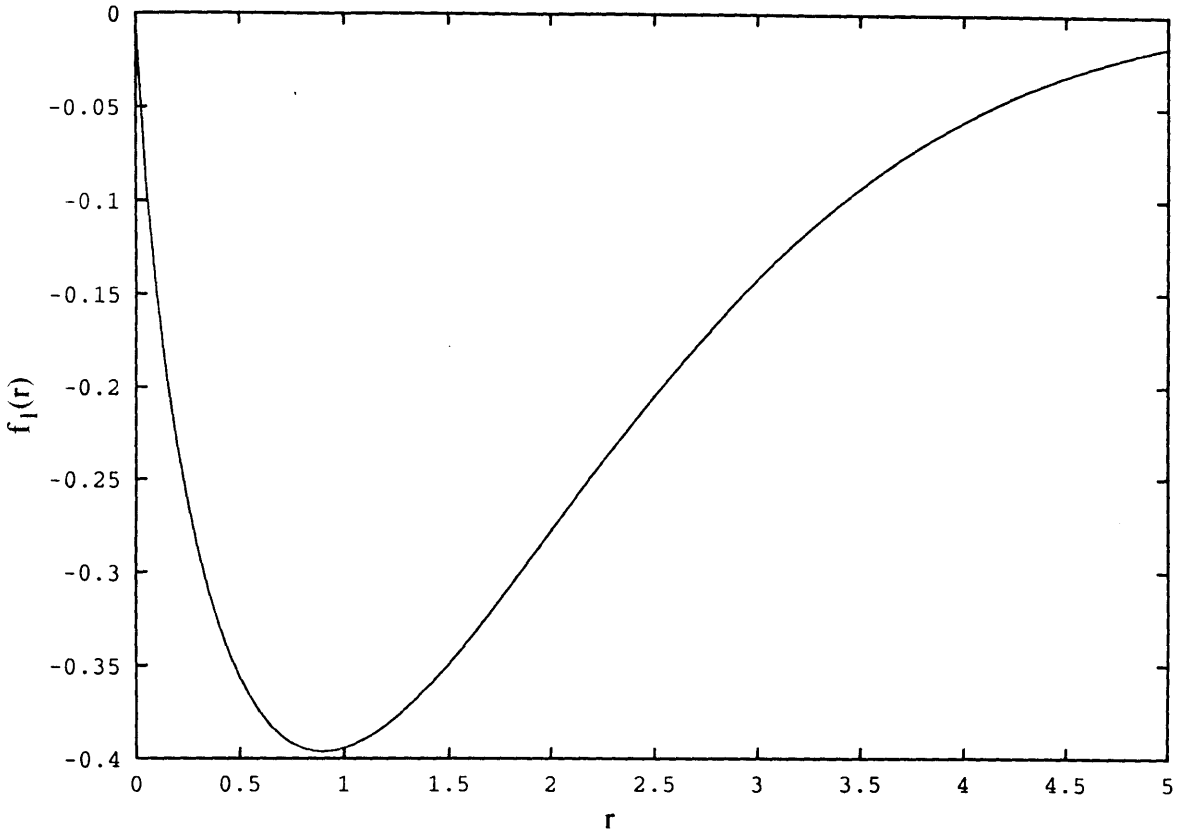

Fig. 6-9: Normalized curvature feedback gain kernel for infinite plate.

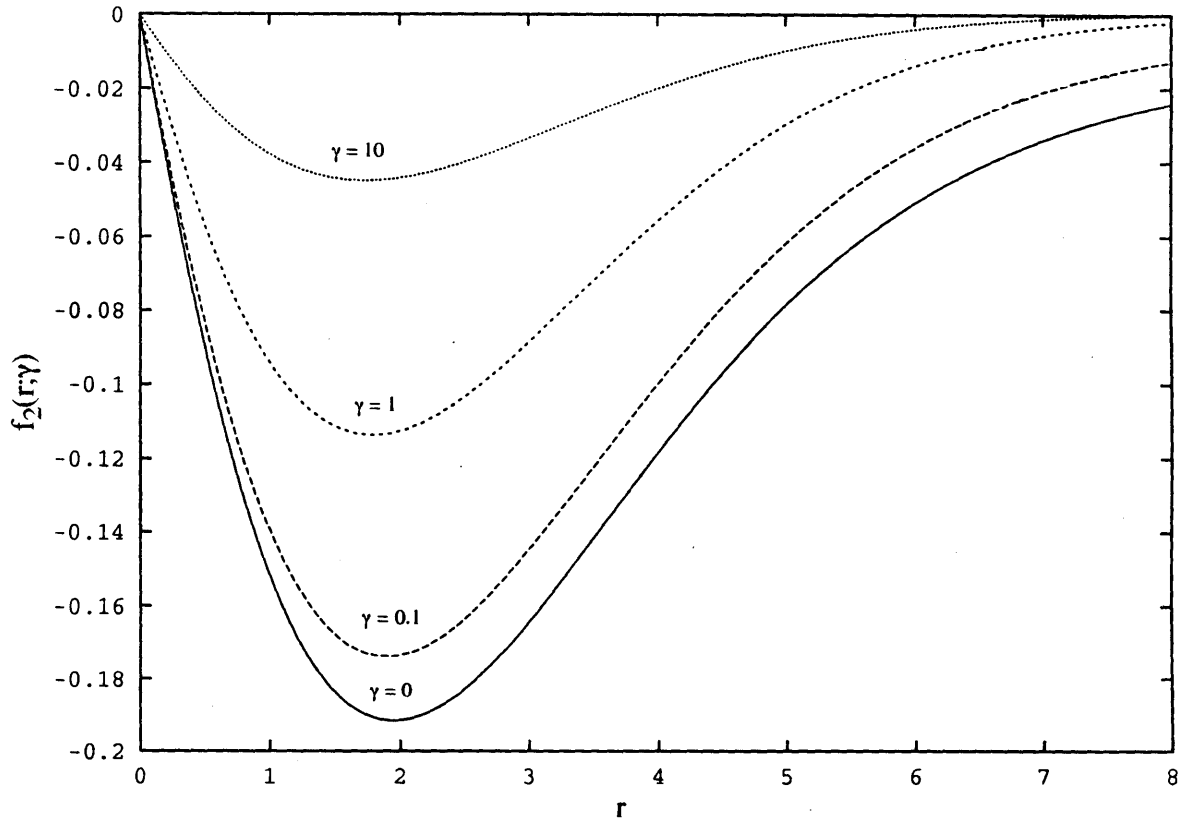

Fig. 6-10: Normalized velocity feedback gain kernel for infinite plate.

functions, each located at an actuation point. For discrete actuation, there will then always exist uncontrollable modes, so that the system as a whole would not be completely controllable. This occurs because there will always be at least one mode shape which has nodes at all actuation points. (In the limit as the mode number approaches infinity, the nodal points become infinite in number and densely spaced over the spatial domain.) Of course, this is only a mathematical issue; proper placement of a sufficiently large set of actuators based upon knowledge of the lower modes of the structure can ensure high controllability of all modes lying in the frequency range for which the mathematical model is valid. It would be interesting to observe whether or not the optimal feedback gains are still collocated for a set of discrete embedded piezoelectric actuators.

At present, no claims can be made concerning the robustness of the distributed controllers obtained above. A quantitative robustness analysis would help determine the sensitivity of the performance of the system to errors in the structural model. Also, the assumption of a truly distributed controller is rather optimistic. Any implementable system will consist of a finite set of sensors and actuators. Consequently, the theory must be extended to account for discrete sensing and actuation. It may be possible to extend the optimal output feedback approach discussed by Levine [69] or the optimal projection approach developed by Bernstein [70] in a manner amenable to the discrete sensing/actuation problem.

Another unresolved topic is the determination of optimal distributed control laws for arbitrary boundary conditions. Such a development was attempted by Tzafestas [59], but has found extremely limited application. For example, the optimal distributed control of a cantilevered beam was addressed by Bailey [71] using Tzafestas' formulation, with the conclusion that the boundary conditions could not be posed in the specific mathematical form required by the formulation. Clearly, the problem lies in dealing with the boundary conditions which arise when determining the adjoint operators in Eqs. (6.6a-c). These boundary terms result in additional necessary conditions for optimality, expressed in terms of ordinary differential equations. Currently, no general formulation exists which includes these extra conditions. The ability to

handle general boundary conditions would make it possible to develop control laws for multiple element structures, such as space frames and trusses.

7 HYBRID MODELLING APPROACH FOR HIGH AUTHORITY/LOW AUTHORITY CONTROL DESIGN

It remains to develop a control strategy that utilizes the best aspects of both the TEM and direct modelling methodologies. For example, the distributed control solutions obtained through the direct model could form the basis for a LAC design. The resulting model of the controlled structure could then be transformed, and a HAC controller could be designed by posing the problem in the standard form, as described in Section 4.2. Finally, command prefiltering of control inputs for slew maneuvers would be determined using the open-loop optimal control theory discussed in Section 4.1. The exactness of the theory makes it more attractive than modal-based approaches, such as the work of Singer [7]. The entire hierarchically controlled system would then have the general form shown in Fig. 7-1.

Inherent in this objective is a general unification of the two modelling approaches, which has not been achieved to date. Such a unification would be a profound improvement in the ability to develop exact control models for large flexible structures. Analytic TEM solutions do exist, however, for some specific controlled structural elements. Consider, for example, the Bernoulli-Euler beam with curvature feedback. The dynamics equation, expressed in dimensional form, is

$$EI\frac{\partial^4}{\partial x^4}v(x,t) + \rho A\frac{\partial^2}{\partial t^2}v(x,t) = \frac{\partial^2}{\partial x^2}m_u(x,t) \tag{7.1}$$

The optimal distributed controller is collocated in this case, with the normalized feedback law given by

$$m_u(x,t) = -k_1\frac{\partial^2}{\partial x^2}v(x,t) - k_2\frac{\partial}{\partial t}v(x,t) \tag{7.2}$$

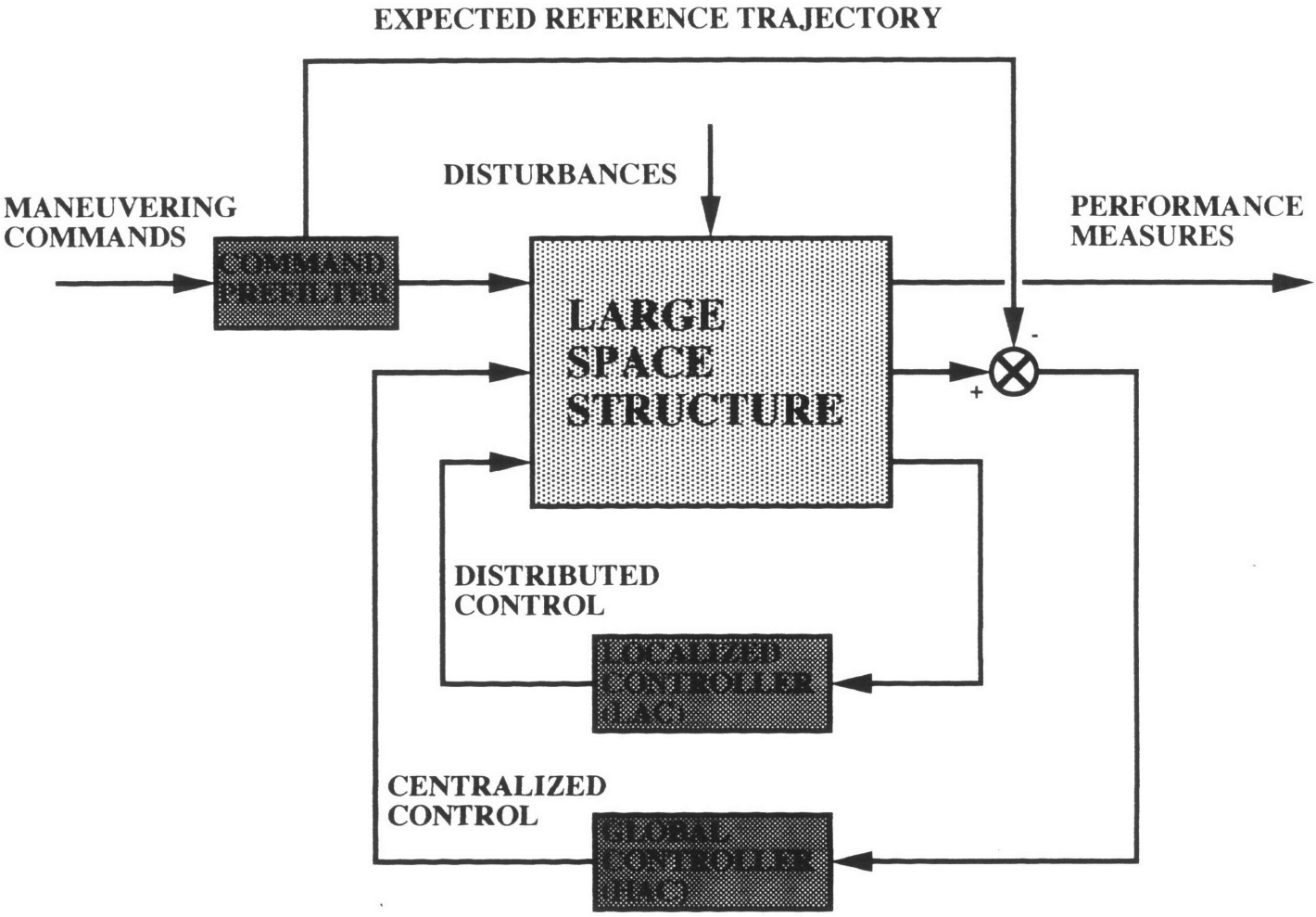

Fig. 7-1: Schematic of the complete HAC/LAC control architecture

where k_1 and k_2 are determined via Eqs. (6.58a,b). Converting this feedback law into dimensional form yields

$$m_u(x,t) = - k_1 EI \frac{\partial^2}{\partial x^2} v(x,t) - k_2 \sqrt{\rho AEI} \frac{\partial}{\partial t} v(x,t) \tag{7.3}$$

and substituting this expression in the dynamics equation produces the equation of motion for the controlled structural element. It is given by

$$EI(1+k_1) \frac{\partial^4}{\partial x^4} v(x,t) + k_2 \sqrt{\rho AEI} \frac{\partial^3}{\partial x^2 \partial t} v(x,t) + \rho A \frac{\partial^2}{\partial t^2} v(x,t) = 0 \tag{7.4}$$

It is now possible to transform the closed-loop dynamics into the frequency-domain. Assuming zero initial conditions, we have

$$(1+k_1) \frac{\partial^4}{\partial x^4} \bar{v}(x,s) - j k_2 \alpha^2 \frac{\partial^2}{\partial x^2} \bar{v}(x,s) + \alpha^4 \bar{v}(x,s) = 0 \tag{7.5}$$

where

$$\alpha^4 = - \frac{\rho A}{EI} s^2 \tag{7.6}$$

The homogeneous solution vector is then given by

$$v_H(x,s)^T = \left[e^{\alpha_1 x} \quad e^{-\alpha_1 x} \quad e^{j\alpha_2 x} \quad e^{-j\alpha_2 x} \right] \tag{7.7}$$

with

$$\alpha_1 = \sqrt{\frac{\sqrt{1 + k_1 - \left[\frac{k_2}{2}\right]^2} + j \frac{k_2}{2}}{1 + k_1}} \, \alpha$$

$$\alpha_2 = \sqrt{\frac{\sqrt{1 + k_1 - \left[\frac{k_2}{2}\right]^2} - j \frac{k_2}{2}}{1 + k_1}} \, \alpha \tag{7.8a,b}$$

The expression for the internal state vector in terms of $\bar{v}(x,s)$ remains unchanged, and is given by Eq. (2.60). The same can be said for the generalized boundary displacements and forces. The homogeneous solution vector can then be used to derive analytical expressions for the dynamic

stiffness and interpolation matrices, which will be slightly more complex than the matrices corresponding to the uncontrolled beam, discussed in Chapter 2. It is then possible to use these matrices in the assembly process of a more complex structure.

Unfortunately, if the feedback is indeed distributed rather than purely collocated, Eq. (7.5) becomes an integral equation. A general solution is therefore not available. However, the form of the gain kernels for a particular problem (e.g., beam with force feedback) may lead to some form of analytical solution, or, at least, an accurate approximate solution. Whether or not these classes of controlled structures lend themselves to analytical TEM models in the general case remains an unresolved issue.

We may, nevertheless, parametrize the solution for a controlled beam in terms of the constants associated with the distributed control cost functional. For a uniform beam, the transformed closed-loop dynamics are given by

$$\frac{\partial^4}{\partial x^4}\bar{v}(x,s) + \left[s^2 + \sqrt{\theta_U+\theta_T}\, s\right]\bar{v}(x,s) + \int_0^1 \left[\frac{\partial^2}{\partial y^2} k_1(x,y;\theta_U) + s\,\tilde{k}_2(x,y;\theta_U;\theta_T)\right]\bar{v}(y,s)\,dy = 0 \tag{7.9a}$$

$$\theta_U = q_U/r\,, \qquad \theta_T = q_T/r \tag{7.9b,c}$$

where the dependence of the gains on the control and state weightings is now explicitly shown. The homogeneous solution can then be expressed by

$$v_H(x,s;\theta_U;\theta_T) = \begin{bmatrix} v_1(x,s;\theta_U;\theta_T) \\ v_2(x,s;\theta_U;\theta_T) \\ v_3(x,s;\theta_U;\theta_T) \\ v_4(x,s;\theta_U;\theta_T) \end{bmatrix} \tag{7.10}$$

Furthermore, the stiffness matrix is generated by defining the matrices

$$\Psi(s;\theta_U;\theta_T) = \begin{bmatrix} v_1(0,s) & v_2(0,s) & v_3(0,s) & v_4(0,s) \\ \frac{\partial}{\partial x} v_1(0,s) & \frac{\partial}{\partial x} v_2(0,s) & \frac{\partial}{\partial x} v_3(0,s) & \frac{\partial}{\partial x} v_4(0,s) \\ v_1(1,s) & v_2(1,s) & v_3(1,s) & v_4(1,s) \\ \frac{\partial}{\partial x} v_1(1,s) & \frac{\partial}{\partial x} v_2(1,s) & \frac{\partial}{\partial x} v_3(1,s) & \frac{\partial}{\partial x} v_4(1,s) \end{bmatrix} \tag{7.11a}$$

$$\tilde{\Psi}(s;\theta_U;\theta_T) = \begin{bmatrix} \frac{\partial^2}{\partial x^2} v_1(0,s) & \frac{\partial^2}{\partial x^2} v_2(0,s) & \frac{\partial^2}{\partial x^2} v_3(0,s) & \frac{\partial^2}{\partial x^2} v_4(0,s) \\ \frac{\partial^3}{\partial x^3} v_1(0,s) & \frac{\partial^3}{\partial x^3} v_2(0,s) & \frac{\partial^3}{\partial x^3} v_3(0,s) & \frac{\partial^3}{\partial x^3} v_4(0,s) \\ \frac{\partial^2}{\partial x^2} v_1(1,s) & \frac{\partial^2}{\partial x^2} v_2(1,s) & \frac{\partial^2}{\partial x^2} v_3(1,s) & \frac{\partial^2}{\partial x^2} v_4(1,s) \\ \frac{\partial^3}{\partial x^3} v_1(1,s) & \frac{\partial^3}{\partial x^3} v_2(1,s) & \frac{\partial^3}{\partial x^3} v_3(1,s) & \frac{\partial^3}{\partial x^3} v_4(1,s) \end{bmatrix} \tag{7.11b}$$

and forming the product

$$\mathbf{K}(s;\theta_U;\theta_T) = \tilde{\Psi}(s;\theta_U;\theta_T) \left[\Psi(s;\theta_U;\theta_T)\right]^{-1} \tag{7.12}$$

At this point, the TEM methodology could be used to determine the transfer functions of interest for use in control design. The parameters θ_U and θ_T could then be adjusted to shape the frequency response in anticipation of the HAC loop closure. Thus, we can design a controller that meets a set of desirable performance characteristics in a systematic manner.

8 CONCLUSION

8.1 Summary of Key Results

The mathematically exact TEM and direct structural modelling representations have been developed and demonstrated. By retaining the dynamics that describe the structural model over the entire frequency range, accurate behavioral predictions are available. For example, the wave-like propagation characteristics associated with impulsive disturbances are easily observed using either exact modelling approach. In addition, new control formulations have been developed that take advantage of the information available via the exact modelling methods.

The TEM approach makes it possible to express solutions to the partial differential equations that describe the structure analytically, in terms of transcendental functions of the complex frequency. Thus, the accuracy of the solutions is limited only by the accuracy with which the computer is able to evaluate these transcendental functions. In order to avoid numerical overflow errors, asymptotic approximations of the dynamic stiffness matrics and interpolation functions must be employed at high and low frequencies. The increase in computation speed of the TEM analysis technique over a specific numerical approach in conjunction with finite element modelling has also been demonstrated. By using fewer degrees of freedom, the stiffness matrix inversion associated with the TEM representation is performed more quickly. Although this inversion must be performed at each frequency of interest, the total time required for generating a structural response still rivals that of the FEM approach. Furthermore, the frequency-domain TEM analysis incorporates general viscoelastic damping mechanisms in a very straightforward manner.

The inverse Laplace transform algorithm has been used to provide time-domain data in a computationally efficient manner, by means of the fast Fourier transform. This numerical algorithm is an approximate inversion technique, but numerous demonstrations (both in this thesis and elsewhere) have indicated that the fidelity of the model is retained. By generating the response at discrete points in time we are, in essence, filtering out all frequency components of the response above the sampling frequency. The Gibb's suppression factor, discussed in Section 2.2, ensures

that this filtering does not degrade the time-domain data in the presence of discontinuities in the response. An internal energy formulation has also been carried out within the TEM framework. The total energy due to elastic deformation is expressed in terms of a double frequency integral, which is calculated numerically.

The one-dimensional elements used to validate the TEM approach were uniform rods in compression and torsion, and uniform beams in bending. Using these elements, it was possible to assemble more complex frame-like structures, while retaining the exactness of the mathematical solutions to the dynamics equations. This was accomplished using an assembly procedure analogous to that used in FEM analysis. The exact solution to an axisymmetric system was also presented. In this case, the response of a membrane to axisymmetric forcing was determined. The ability of the TEM approach to reproduce the wave-like nature of the disturbance was apparent.

The TEM representation of two-dimensional elements can only yield approximate results, even in the frequency-domain, as the transformed equations of motion remain partial differential equations in the spatial dimensions. However, an approximate solution technique has been presented, in which the deformation in the interior of the element is expressed as a linear combination of a finite set of basis solutions whose coefficients are determined from a finite set of boundary displacements. These basis solutions are parametrized by the complex frequency and satisfy the underlying PDE's exactly for spatially uniform elements. For plane stress elements, the development of a frequency-dependent stress function was necessary, so that the in-plane displacements and stresses could be expressed in terms of a single function.

The TEM approach was generalized to include structures undergoing large angular motion. For these situations, structural deformations are expressed with respect to a frame fixed to an element boundary, and the motion is referenced to a nominal rotation rate. The resulting linearized system of integro-partial differential equations is then solved in the frequency-domain. The approach was applied to a simple mass/appendage structure and validated with a general nonlinear multibody simulation software package. As expected, the linearized and nonlinear simulations

agree quite well, provided that the angular rate does not change considerably and the angular accelerations likewise remain small.

An open-loop optimal control technique has been developed using TEM models, and has been found to virtually eliminate the residual energy associated with the slewing of flexible structures, provided that the mathematical models accurately represents the physical structures. The only approximation made concerns the control inputs themselves, which were assumed to belong to the subspace spanned by a finite set of basis functions. The algorithm has been demonstrated for two types of cost functionals. In the first, penalties are placed on deformation at discrete points on the structure, while in the other, penalties are placed on the total energy due to deformation of each structural element. While the second approach is less *ad hoc* than the first, it requires more computation time, and was applied to a simple structure only.

A primary limitation of the TEM representation as a tool for structural analysis and control design concerns situations where the initial conditions of the system are non-zero or where there exists distributed forcing within a structural element. For these cases, the computational advantages of the TEM approach are lost, as a spatial integration is required over the domain of the structural element at each frequency of interest. Moreover, this integration must be performed numerically except in rare situations. As a result, the accuracy of the TEM representation becomes dependent on the fidelity of the spatial integration, in addition to that of the inverse transform algorithm. Another limitation of the TEM representation is that it does not easily lend itself to closed-loop control design. Most control design algorithms require that the model be expressible in finite-dimensional state-space form, which is impossible in the TEM framework, as the model is of infinite order. An exception to this general rule is distributed control theory, which is well suited for infinite order systems. In order to apply the theory, however, it was necessary to use an alternative representation, which describes the same dynamics directly in the time-domain.

The direct representation of structural models uses an extended state-space formulation, where the state vector exhibits both spatial and temporal dependence. The dynamics and control influence matrices from traditional state-space become differential operator matrices in the direct

representation. A novel method of generating time-domain responses has been presented. The closed-loop equation of motion is first transformed into the frequency domain, and the resulting integro-partial differential equation is solved numerically at each frequency required to construct the time-domain response. In this thesis, only single-element systems (i.e., those described by a single PDE) have been analyzed using the direct representation, as the treatment of general boundary conditions is somewhat difficult to formulate in the direct PDE framework.

The direct analysis technique provides the framework for a distributed control theory. Having been developed, the theory has been applied to a simple Bernoulli-Euler beam system, and the feedback gain kernels have been determined. For distributed force actuation, the feedback from curvature to force is purely distributed, while the feedback from velocity to force has both a distributed and a collocated component. For distributed curvature actuation, both gain kernels are purely collocated. These kernels agree with previous results concerning the optimal distributed control of an infinite beam, as well as result from the optimal LQR control of a discrete model of the beam. The distributed control approach has also been successfully applied to a plate of infinite extent.

A simple example of the use of both the TEM and direct representations in the design of a hierarchical control system has been presented. Distributed feedback is used to achieve active damping augmentation, and the TEM representation of the system is modified to account for the distributed control. The resulting element model can then be used in the assembly of the global model in the same manner as an uncontrolled element. It is then possible to use the global TEM model for a frequency-domain control design of the high authority controller.

8.2 Contributions of this Thesis

The developments presented in this thesis have led to a number of contributions to the field of structural dynamics and control. The contributions cover a broad range of topics and issues in the field. Taken as a whole, it is felt that these contributions will enhance the current state of the art in structural control design.

The TEM representation has been presented, with provisions for nonzero initial conditions and distributed forcing within structural elements. These take the form of secular terms in the local element and global stiffness matrices for the structural model. This is in contradistinction with most formulations, which restrict the complex frequency to the imaginary-axis and usually consider only sinusoidal steady-state motion. (It should be mentioned that, for some control designs, this is all that is required.) While these extensions are not to be considered of paramount importance, they do, in fact, allow simulation of a larger class of systems under a wider range of conditions. The cost of the added capability in terms of numerical computation is an additional spatial integration at each complex frequency of interest for each mathematical element having either nonzero initial conditions or distributed forcing. In addition, the use of an existing inverse Laplace transform algorithm on global structural models of considerable complexity has been demonstrated with remarkable success. This direct method of simulation makes the TEM representation competitive with modal simulations derived from finite element models, as the (computationally costly) iterative task of determining mode shapes and frequencies from the global TEM model is avoided.

The frequency domain modelling approach has been extended to include plane stress elements. This was accomplished by developing a frequency-dependent version of the Airy stress function from the plane stress equations. All quantities of interest (in-plane displacements, extensional stresses and strains, and shear stresses and strains) are expressed as linear differential operations on this stress function. The characteristic equation which the stress function satisfies has been shown to be the product of two factors. The first supports an in-plane compression wave, while the second supports a shear wave. The propagation velocities of both wave types

have been found to be consistent with previous results concerning wave propagation in two-dimensional media. The utilization of the plane-stress formulation, in conjunction with the plate bending model, makes it possible to determine approximate dynamic stiffness matrices for planar elements undergoing general motion in three dimensions. It is believed that this capability will make the TEM approach a viable alternative to finite element modelling for realistic structural models.

The TEM approach has been used to simulate the dynamics of a simple structure undergoing large rigid angular motions. This problem is difficult in that it requires expressing small elastic deformation with respect to a moving reference frame. As a result, the dynamics of the structure are given by a system of integro-partial differential equations. Application of the Laplace transform converts the system into a set of integro-ordinary differential equations (parametrized by the complex frequency), whose solution is readily obtained. The simulation of the system has been validated by comparison with results from a nonlinear multibody dynamics software package. This demonstrates that the class of problems for which the TEM approach is applicable can be broadened to include flexible structures experiencing large rigid rotations.

A general optimal open-loop control algorithm based on the TEM representation of the structural model has been presented. This algorithm does not require *a priori* modal information concerning the structure, and is applicable to models of arbitrary complexity. Furthermore, multiple control inputs are easily handled within the framework of the formulation. The solution is carried out in a mathematically exact manner as far into the development as possible. The approximation that the control inputs belong to a space spanned by a finite set of basis functions is made in order that a numerical solution can be readily calculated. The approach has been demonstrated on a structural model of considerable complexity, and has succeeded in determining the optimal trajectory for a representative rotational slewing maneuver. It is anticipated that this algorithm will be used primarily as a command shaping tool to determine the optimal nominal input to the structural system for slewing maneuvers. Additional closed-loop control can then be utilized to damp out residual deformational energy arising from mismatches between the structure and the

model, imperfect application of control forces and/or torques, and other exogenous disturbances. The hope is that by minimizing the residual energy at the terminal time of the maneuver, the additional cost incurred to remove this energy will likewise be reduced.

A mathematically exact expression for the internal energy of structural elements of a one-dimensional spatial domain in terms of frequency-domain integrals has been developed. The internal energy at a given time is computed via numerical integration. Thus, it is possible to determine the total energy of deformation of the structure within the TEM framework. This is often not possible when dealing with transcendental functions of frequency, and often requires approximate techniques. For example, the approach used by Hagood and Crawley [45] involves replacing the exact element by an equivalent spring-mass-damper system. The physical properties are determined by minimizing the integrated error between the impedances of the exact and approximate models over some frequency range. The formulation thus makes it possible to determine values for the damped natural frequency, damping ratio, and loss factor for such approximate models, which no longer contain the infinite order structure of the original element models. Because the integration interval lies on the imaginary axis, the formulation yields steady-state damping characteristics. In contrast, the energy expression presented here (which also requires an approximate numerical evaluation in the frequency domain) is specifically suited for transient analysis, as it yields the deformational energy at a prescribed time. Because energy is often used as a performance measure in control applications, this development further reinforces the utility of the TEM representation as a control model. This internal energy expression has been utilized as part of the cost functional in the open-loop control algorithm, and yields surprisingly good nominal performance for the cases presented in this thesis.

The optimal distributed control problem has been solved for a beam of finite length with distributed force actuation. The solution approach is unique, in that the exact mathematical model is retained throughout the development. Spatial discretization is applied only after the equations from which the feedback gains are determined have been derived. Consequently, the resulting Riccati equations reflect the dynamics governed by the exact mathematical model, and their solution

can be determined to arbitrary precision. These matrix integro-partial differential Riccati equations are solved using novel iterative and direct techniques, with excellent convergence reported for many levels of discretization. The solution procedure serves as a proof of concept for further applications of distributed control. For example, the state-space representation of the Timoshenko beam, presented in Appendix E, can be used as the control model for a distributed LQR design in which feedback to the forcing input derives from measurements of transverse velocity, cross-sectional rotation rate, curvature, and shear angle. The extension of this approach to more complex PDE models should be straightforward.

The distributed control solution approach distinguishes this work from other methodologies which are based on approximate solutions to the mathematical model. For example, Miller and van Schoor [66] derive feedback gain kernels for a finite beam by first deriving a finite dimensional (thus approximate) state-space representation of the dynamics. Traditional LQR theory is then used to obtain the feedback gains from discrete points on the beam (which correspond to the boundary points of the finite elements used in the discretization) to the forcing input. These spatially discrete gains are then converted into a spatially distributed feedback kernel by utilizing the interpolation functions associated with the finite element model. Unfortunately, as reported in the research, the finite element stiffness matrix becomes ill-conditioned as the discretization becomes finer. This is, however, merely a consequence of the choice of coordinates used in the finite element model. Had curvature and velocity coordinates been used, the results would have been (numerically) identical to those presented here, as is shown in Section 6.2.3.3. By making use of displacement coordinates, Miller's work allows for general boundary conditions. (Often, curvature and velocity coordinates are bad choices, given the boundary conditions imposed.) It may be that the approach presented here cannot handle arbitrary boundary conditions and would then also require the use of displacement coordinates for the general case. It is quite possible that this change would cause the same type of ill-conditioning as was reported in the earlier research. Therefore, we can only conclude that the two approaches are numerically identical for the specific case of pinned-pinned boundary conditions, and then only if the same coordinates are used.

Furthermore, the inability to handle general boundary conditions represents a limitation of the direct PDE approach as presented in this thesis.

The optimal distributed control problem has also been solved for a beam of finite length with distributed curvature actuation. This result is interesting in that the optimal solution, obtained analytically and in closed form via rigorous application of the theory, dictates collocated feedback, even though the control system has knowledge of the state vector over the entire spatial domain. Again, this result has been obtained directly, without requiring the consideration of the limiting behavior of an approximate model of increasing fidelity. The curvature feedback solution is an extension of a similar result obtained for a beam of infinite length by de Luis [55].

A novel method of generating approximate time-domain responses of the controlled beam system has been presented. Application of the Laplace transform converts the closed-loop equation of motion, which is an integro-partial differential equation, into an integro-ordinary differential equation. This transformed equation can then be solved numerically at each complex frequency required to reconstruct the time-domain response. While this method requires spatial discretization and finite differencing, it readily handles non-homogeneous initial conditions and a large class of boundary conditions. The stability of the approach has been demonstrated for numerous test cases.

The optimal distributed control problem for a plate of infinite extent has been solved, as a demonstration of the application of the distributed control technique to a two-dimensional structure. In this case, two-dimensional spatial transform techniques are used, which represent an extension of the approach used by de Luis [55]. By utilizing polar coordinates and Bessel function-based transforms, it was possible to show that the gain from a particular sensor point to an actuator points is a function of only the distance between the two, which is consistent with our intuition.

A subtle issue must be addressed at this point. It concerns the implications of stating that a solution is "exact." Clearly, no solution involving transcendental functions can be an exact solution, since the numerical evaluation of the solution on computer requires approximations to such functions. For example, the "exact" solution to the simple harmonic oscillator equation is a

linear combination of the sine and cosine functions. Although it is impossible to evaluate these functions exactly at arbitrary points, the solution has come to be accepted as exact because much is known concerning the characteristics of these functions. In the same manner, we can state that the "exact" solution to the integral of the normal distribution function is the error function (erf), even though its exact value can be determined at only several points. In this thesis, therefore, we have made the tacit assumption that an "exact" solution is one which can be evaluated numerically to arbitrary precision. As is the case with other functions, if these solutions recur frequently, they will gradually become accepted as "exact" solutions.

8.3 Recommendations for Future Research

Several issues remain unresolved, and are recommended for future research. Although the TEM methodology has been developed for two-dimensional structures, it is incomplete in two respects. First, the selection of boundary points and their relation to element geometry and solution accuracy must be addressed. It is anticipated that the guidelines for choosing boundary points are similar to those used in approximate techniques, such as the boundary element method. Second, a rigorous method of determining the set of basis solutions for the homogeneous solution vector must be developed. Clearly, these two goals are intimately tied, as the number of basis solutions required is related to the number of the boundary points used.

An attempt should be made to develop solutions for nonuniform one-dimensional element models, such as tapered beams and rods. It is well-known that, for some particular tapers, analytical solutions exist in terms of special functions. These solutions could be used to generate dynamic stiffness matrices for such elements. For more general nonuniformities, it may be possible to develop series solutions in terms of common transcendental functions. The resulting stiffness matrices would then be approximate, as the series would be truncated at some point. Clearly, the merits of using such an approach in lieu of a finite element model would be an issue.

A comprehensive comparison between the finite element method and the TEM representation, in terms of computation speed, should be performed. Although general guidelines

have been established here concerning the conditions under which the TEM representation is favorable, a quantitative evaluation would be useful. Highly optimized versions of either code should be used for fairness, and numerous test cases, involving various topologies, should be attempted. The discretization level for the finite element models could be based on the number of points generated by the TEM simulation. Enough finite elements would be used to ensure the fidelity of the model for frequencies as high as the Nyquist frequency corresponding to the TEM time-domain samples.

The closed-loop control problem, expressed in the frequency-domain with TEM models, remains to be solved. Here, the lack of a finite state-space representation of the plant is the fundamental difficulty. While Doyle [12] has succeeded in deriving iterative state-space solutions for the H∞ control problem, the corresponding iterative solution for general (including infinite order) systems described by Francis [51] requires a coprime factorization of the system matrix. Such a factorization may not be available for infinite order systems, as the elements of the matrix are transcendental functions of frequency.

The direct PDE-based distributed control solutions developed here must be extended to include other structural elements, such as Timoshenko beams and axial and torsional rods. Two-dimensional elements of finite extent, which may represent deformable mirror surfaces or solar panels, must also be incorporated into the distributed control framework, although this extension presents a considerably more difficult computational challenge. Finally, the theory must be extended to apply to multi-element structures, which may include any of the elements mentioned. The ability to handle the complex boundary conditions that arise at element junctions is the primary difficulty here.

An evaluation of the robustness of the distributed controller to model uncertainty must also be undertaken. Discrepancies between the model and the actual physical structure, caused by tolerances in physical dimensions and material properties, structural joint dynamics, nonlinear material behavior and other unmodelled dynamics, usually result in performance degradation. A rigorous robustness evaluation would quantify the relation between modelling error and

performance. Linked to this issue are implementation considerations. Because actuators and sensors are always discrete in nature, the distributed control solution represents only a limiting case as the number of individual actuators and sensors approaches infinity. Some examples of spatially distributed sensors exist, where the response of the sensor represents the spatially integrated state over some finite domain [55]. (In fact, all real sensors perform spatial integration, whether by design or not, as it is impossible to measure the state at an infinitesimal point.) The spatial integration can even be tailored to correspond to the feedback gain kernel. It is likewise possible to manufacture a distributed actuator. However, each sensor so manufactured yields only a single output, and each actuator is controlled by a single input. A truly distributed control system relates an infinite number inputs and outputs, and is therefore not physically realizable. For any implementable control design, then, the effect of utilizing a finite set of actuators and sensors must be addressed. Also relevant would be a study of the effect of actuator and sensor dynamics and their relation to robust stability.

A combined direct/TEM control methodology for structural systems is not yet available. This hybrid technique would facilitate the development of hierarchical control schemes, such as HAC/LAC, without resorting to modal analysis and truncation. Consequently, the problems of control and observation spillover would be alleviated, at least from a mathematical perspective. (Actual implementation issues must also be addressed, as mentioned above.) Consequently, a less conservative control design would be required, resulting in enhanced nominal performance. This is the ultimate objective of all structural control designs.

APPENDIX A: HIGH FREQUENCY TRANSFORM ELEMENTS

This appendix presents the dynamic stiffness matrices for high frequency TEM elements. In particular, the Mindlin-Herrmann axial rod and the Timoshenko beam, both described in Sec. 2.3.6, are discussed.

A.1 Mindlin-Herrmann Rod

The dynamics of the Mindlin-Herrmann rod are characterized by the following set of differential equations:

$$- a^2 (\lambda+2G) \frac{\partial^2}{\partial x^2} v_1(x,s) + \rho a^2 s^2 v_1(x,s) = 2a\lambda \frac{\partial}{\partial x} v_2(x,s) \tag{A.1a}$$

$$a^2 \kappa^2 G \frac{\partial^2}{\partial x^2} v_2(x,s) - \left[8\kappa_1^2(\lambda+G) + \rho a^2 s^2\right] v_2(x,s) = 4a\kappa_1^2 \lambda \frac{\partial}{\partial x} v_1(x,s) \tag{A.1b}$$

All symbols in these equations are defined in Sec. 2.3.6. These equations apply to a rod of circular cross-section only. The Lame constants are related to the modulus of elasticity and Poisson's ratio of the material according to

$$\lambda = \frac{E\nu}{(1+\nu)(1-2\nu)}, \quad G = \frac{E}{2(1+\nu)} \tag{A.2a,b}$$

We will assume that the radial deformation, v_2, is constrained at the boundaries of the element. This is the case when the element is embedded in a structural junction. We therefore have

$$v_2(0,s) = v_2(L,s) = 0 \tag{A.3}$$

With these constraints imposed, the stiffness matrix becomes 2-by-2, and can be expressed by

$$\mathbf{K}(s) = \frac{\pi a^2 E}{\Delta(s)} \begin{bmatrix} \beta_1 s_1 c_2 - \beta_2 s_2 c_1 & -\beta_1 s_1 + \beta_2 s_2 \\ -\beta_1 s_1 + \beta_2 s_2 & \beta_1 s_1 c_2 - \beta_2 s_2 c_1 \end{bmatrix} \tag{A.4}$$

where

$$\Delta(s) = \frac{(1+\nu)(1-2\nu)}{(1-\nu)}\left[\frac{2\beta_1\beta_2(1-c_1c_2) + (\beta_1^2+\beta_2^2)s_1s_2}{\beta_1(\alpha_2 a) - \beta_2(\alpha_1 a)}\right] \tag{A.5}$$

and the following trigonometric definitions have been made:

$$\begin{aligned} c_i &= \cos(\alpha_i L) \\ s_i &= \sin(\alpha_i L) \end{aligned} \tag{A.6a,b}$$

Also, β_1 and β_2 are given by

$$\beta_i = \frac{\left[\kappa^2(1+\nu)(1-2\nu)^2\rho a^2 s^2 - 16\kappa_1^2\nu^2 E\right](\alpha_i a) + \kappa^2(1-\nu)(1-2\nu)E(\alpha_i a)^3}{4(1-\nu)(1-2\nu)\rho a^2 s^2 + 16\kappa_1^2 E} \tag{A.7}$$

and the nondimensional parameters $\alpha_1 a$ and $\alpha_2 a$ are given by

$$(\alpha_i a)^2 = -\lambda_1\left[(1+\lambda_2\sigma) \pm \sqrt{(1+\lambda_2\sigma)^2 - \frac{2}{\lambda_1}(1+\lambda_3\sigma)\sigma}\right] \tag{A.8}$$

where

$$\begin{aligned} \lambda_1 &= \frac{4\kappa_1^2(1+\nu)}{\kappa^2(1-\nu)} \qquad \lambda_2 = \frac{(1+\kappa^2)(1-2\nu)+1}{8\kappa_1^2} \\ \lambda_3 &= \frac{(1+\nu)(1-2\nu)}{4\kappa_1^2} \qquad \sigma = \frac{\rho a^2 s^2}{E} \end{aligned} \tag{A.9a-d}$$

The stiffness matrix can be shown to reduce to that of the simple axial rod either by setting ν=0 or by taking the limit as the radius, a, approaches zero.

A.2 Timoshenko Beam

The dynamics of the Timoshenko beam can be expressed either as a system of two coupled partial differential equations or as the single equation

$$EI\frac{\partial^4}{\partial x^4}v(x,t) + \rho A\ddot{v}(x,t) - \rho I\left[1+\frac{Ek}{G}\right]\frac{\partial^2}{\partial x^2}\ddot{v}(x,t) + \frac{\rho^2 Ik}{G}\ddot{\ddot{v}}(x,t) = f_d(x,t) \tag{A.10}$$

Taking the Laplace transform of this equation yields

$$\frac{\partial^4}{\partial x^4} v(x,s) + 2p_1\alpha^2 \frac{\partial^2}{\partial x^2} v(x,s) - p_2^2 \alpha^4 v(x,s) = \tilde{f}_d(x,s) \tag{A.11}$$

where the following parameters have been defined:

$$\alpha^4 = -\frac{\rho A s^2}{EI} \qquad k_1 = \frac{E}{G}\frac{k}{} \qquad r^2 = \frac{I}{A}$$
$$p_1 = \frac{1}{2}(1+k_1)(\alpha r)^2 \qquad p_2^2 = 1 - k_1(\alpha r)^4 \tag{A.12a-e}$$

The homogeneous solution vector is then

$$v_H(x,s) = \begin{bmatrix} \cosh(\alpha\beta_1 x) \\ \sinh(\alpha\beta_1 x) \\ \cos(\alpha\beta_2 x) \\ \sin(\alpha\beta_2 x) \end{bmatrix} \tag{A.13}$$

where

$$\beta_1^2 = p_3 - p_1, \quad \beta_2^2 = p_3 + p_1 \tag{A.14a,b}$$

and

$$p_3^2 = p_1^2 + p_2^2 = 1 + \frac{1}{4}(1-k_1)^2(\alpha r)^4 \tag{A.15}$$

Due to the internal shearing allowed by the Timoshenko model, the expressions for the internal state vector in terms of the homogeneous solution become considerably more complex. They are:

$$\mathbf{u}(x,s) = \begin{bmatrix} v(x,s) \\ \theta(x,s) \\ M(x,s) \\ S(x,s) \end{bmatrix} = \begin{bmatrix} 1 \\ \frac{1}{p_2^2}\left[(1+p_4^2)\frac{\partial}{\partial x} + \frac{p_4}{\alpha^2}\frac{\partial^3}{\partial x^3}\right] \\ EI\left[\frac{\partial^2}{\partial x^2} + p_4\alpha^2\right] \\ \frac{EI}{p_2^2}\left[\frac{\partial^3}{\partial x^3} + p_1\alpha^2\frac{\partial}{\partial x}\right] \end{bmatrix} v(x,s) \tag{A.16}$$

where

$$p_4 = k_1(\alpha r)^2 \tag{A.17}$$

The stiffness matrix then takes the form given by Eq. (2.66), with

$$
\begin{aligned}
K_1(s) &= \frac{p_2}{\alpha^3}(\beta_4\,sh - \beta_3\,st)\\
K_2(s) &= \frac{p_2}{\alpha^3}(\beta_3\,ch\,st - \beta_4\,sh\,ct)\\
K_3(s) &= \frac{1}{\alpha^2}(ch - ct)\\
K_4(s) &= \frac{1}{p_3\alpha^2}\left[\frac{p_2^2+p_1-p_4}{p_2}sh\,st + (p_1-p_4)(1-ch\,ct)\right]\\
K_5(s) &= \frac{1}{\alpha}(\beta_3\,sh + \beta_4\,st)\\
K_6(s) &= \frac{1}{\alpha}(\beta_4\,ch\,st + \beta_3\,sh\,ct)\\
\Delta(s) &= \frac{1}{p_3\alpha^4}\left[1 - ch\,ct - \frac{1}{2}\left(\frac{\beta_3}{\beta_4} - \frac{\beta_4}{\beta_3}\right)sh\,st\right]
\end{aligned}
\qquad \text{(A.18ag)}
$$

The trigonometric quantities must also be modified to

$$
\begin{aligned}
ch &= \cosh(\alpha\beta_1 L)\\
sh &= \sinh(\alpha\beta_1 L)\\
ct &= \cos(\alpha\beta_2 L)\\
st &= \sin(\alpha\beta_2 L)
\end{aligned}
\qquad \text{(A.19a-d)}
$$

where

$$
\beta_3 = \frac{\beta_1^2 + p_4}{\beta_1}, \quad \beta_4 = \frac{\beta_2^2 + p_4}{\beta_2} \qquad \text{(A.20a,b)}
$$

The stiffness matrix for the Bernoulli-Euler beam is recovered by setting the characteristic radius, r, to zero. Then, $p_1=p_4=0$, $p_2=p_3=1$, and $\beta_1=\beta_2=\beta_3=\beta_4=1$.

APPENDIX B: STEADY-STATE SOLUTION FOR ROTATING MASS/APPENDAGE SYSTEM

In this appendix, we derive the steady-state configuration of the mass/appendage system subject to a constant rotation rate. By neglecting all terms involving time derivatives and setting all generalized boundary forces to zero, Equations (3.12a-e) reduce to

$$M_0 A_x^{nom} - m\Omega^2 \int_0^L v_x^{nom}\, dx = \frac{1}{2} mL^2\Omega^2 \tag{B.1a}$$

$$-\frac{EA}{m}\frac{\partial^2}{\partial x^2} v_x^{nom} - \Omega^2 v_x^{nom} = \Omega^2 x - A_x^{nom} \tag{B.1b}$$

We now solve for A_x^{nom} in the first equation and substitute the result in the second. Upon re-normalizing the results in the spatial domian, we are left with

$$\frac{\partial^2}{\partial z^2} y + \alpha^2 y - \alpha^2 \gamma_M \int_0^1 y\, dz = \frac{1}{2}\alpha^2\gamma_M - \alpha^2 z \tag{B.2}$$

where

$$y(z) = \frac{1}{L} v_x^{nom}(Lz), \quad \alpha^2 = \frac{mL^2\Omega^2}{EA} \tag{B.3a,b}$$

This integro-differential equation has the general solution

$$y = A\left[\cos\alpha z + \frac{\gamma_M}{1-\gamma_M}\frac{\sin\alpha}{\alpha}\right] + B\left[\sin\alpha z + \frac{\gamma_M}{1-\gamma_M}\frac{1-\cos\alpha}{\alpha}\right] - z \tag{B.4}$$

which can be verified by direct substitution. To solve for the undetermined constants, we apply the boundary conditions

$$y(0) = 0, \quad \frac{\partial}{\partial z} y(1) = 0 \tag{B.5a,b}$$

Substituting these into Equation (B.4) we obtain, after much algebraic manipulation,

$$y = \left[\frac{\alpha(1-\gamma_M) + \gamma_M \sin\alpha}{\alpha[\alpha(1-\gamma_M)\cos\alpha + \gamma_M \sin\alpha]}\right] \sin\alpha z + \left[\frac{\gamma_M(1-\cos\alpha)}{\alpha[\alpha(1-\gamma_M)\cos\alpha + \gamma_M \sin\alpha]}\right] (1-\cos\alpha z) - z \qquad (B.6)$$

from which v_x and A_x can be derived. This solution is valid in the range $\alpha < \alpha_{crit}$, where α_{crit} is the smallest positive solution to the characteristic equation

$$\tan(\alpha_{crit}) = -\left[\frac{1-\gamma_M}{\gamma_M}\right] \alpha_{crit} \qquad (B.7)$$

Beyond this value, the axial gyroscopic forces on the rotating beam cannot be balanced by the axial stiffness, and the structure yields.

APPENDIX C: FINITE-DIFFERENCE EQUATIONS FOR THE BERNOULLI-EULER BEAM SUBJECT TO NON-HOMOGENEOUS BOUNDARY CONDITIONS

In this appendix, we derive the finite difference formulae corresponding to various boundary conditions for the Bernoulli-Euler beam. The development presented here applies to the boundary at x=0. The treatment of the other boundary is identical. We begin by discretizing the spatial domain as follows:

$$x_i = \frac{i}{N}, \qquad \left[\bar{v}(x,s)\right]_{x=x_i} \triangleq v_i \qquad (i = 0, \ldots, N) \qquad \text{(C.1a,b)}$$

In the sequel, the dependence of v on the complex frequency will be assumed and the overbar will be suppressed. The standard finite difference expressions for the various derivatives of interest are

$$\left[\frac{\partial}{\partial x}\bar{v}(x,s)\right]_{x=x_i} \approx \frac{N}{2}\left[v_{i+1} - v_{i-1}\right] \qquad \text{(C.2a)}$$

$$\left[\frac{\partial^2}{\partial x^2}\bar{v}(x,s)\right]_{x=x_i} \approx N^2\left[v_{i-1} - 2v_i + v_{i+1}\right] \qquad \text{(C.2b)}$$

$$\frac{\partial}{\partial x}\left[\eta(x)\frac{\partial^2}{\partial x^2}\bar{v}(x,s)\right]_{x=x_i} \approx \frac{N^3}{2}\left\{\eta_{i+1}\left[\frac{\partial^2}{\partial x^2}\bar{v}(x,s)\right]_{x=x_{i+1}} - \eta_{i-1}\left[\frac{\partial^2}{\partial x^2}\bar{v}(x,s)\right]_{x=x_{i-1}}\right\} \qquad \text{(C.2c)}$$

$$\frac{\partial^2}{\partial x^2}\left[\eta(x)\frac{\partial^2}{\partial x^2}\bar{v}(x,s)\right]_{x=x_i} \approx N^4\left\{\eta_{i-1}\left[\frac{\partial^2}{\partial x^2}\bar{v}(x,s)\right]_{x=x_{i-1}} - 2\eta_i\left[\frac{\partial^2}{\partial x^2}\bar{v}(x,s)\right]_{x=x_i} + \eta_{i+1}\left[\frac{\partial^2}{\partial x^2}\bar{v}(x,s)\right]_{x=x_{i+1}}\right\} \qquad \text{(C.2d)}$$

Combining Eqs. (C.2b) and (C.2d) yields the desired approximate expression for the fourth derivative at locations far from the boundaries:

$$\frac{\partial^2}{\partial x^2}\left[\eta(x)\frac{\partial^2}{\partial x^2}\bar{v}(x,s)\right]_{x=x_i} \approx N^4\left[\eta_{i-1}v_{i-2} - 2(\eta_{i-1}+\eta_i)v_{i-1} + (\eta_{i-1}+4\eta_i+\eta_{i+1})v_i - 2(\eta_i+\eta_{i+1})v_{i+1} + \eta_{i+1}v_{i+2}\right] \qquad \text{(C.3)}$$

Near the boundaries, the finite difference expression depends on the particular boundary condition enforced. We will assume that the beam is either pinned, free, or clamped at x=0, and is always pinned at x=1.

For a pinned beam, the boundary conditions are

$$\left[\bar{v}(x,s)\right]_{x=x_0} = 0 \tag{C.4a}$$

$$\left[\eta(x)\frac{\partial^2}{\partial x^2}\bar{v}(x,s)\right]_{x=x_0} = 0 \tag{C.4b}$$

Employing the previous expressions yields the particular forms

$$\frac{\partial^2}{\partial x^2}\left[\eta(x)\frac{\partial^2}{\partial x^2}\bar{v}(x,s)\right]_{x=x_1} \approx N^4\left[(4\eta_1+\eta_2)v_1 - 2(\eta_1+\eta_2)v_2 + \eta_2 v_3\right] \tag{C.5a}$$

$$\frac{\partial^2}{\partial x^2}\left[\eta(x)\frac{\partial^2}{\partial x^2}\bar{v}(x,s)\right]_{x=x_2} \approx N^4\left[-2(\eta_1+\eta_2)v_1 + (\eta_1+4\eta_2+\eta_3)v_2 - 2(\eta_2+\eta_3)v_3 + \eta_3 v_4\right] \tag{C.5b}$$

Thus, the expression for the fourth derivative at all points in the discretization can be conveniently expressed as

$$\frac{\partial^2}{\partial x^2}\left[\eta(x)\frac{\partial^2}{\partial x^2}\bar{v}(x,s)\right] \approx N^4\,\mathbf{DHD}\,\mathbf{v}(s) \tag{C.6}$$

where the second order finite difference matrix is given by

$$\mathbf{D} = \begin{bmatrix} -2 & 1 & & & \\ 1 & -2 & 1 & & \mathbf{0} \\ & 1 & -2 & 1 & \\ & & \cdot & \cdot & \cdot \\ \mathbf{0} & & & 1 & -2 & 1 \\ & & & & 1 & -2 \end{bmatrix} \tag{C.7}$$

and

$$\mathbf{H} = \mathrm{diag}\left[\eta_1\ \eta_2 \cdots \eta_{N-1}\right] \tag{C.8a}$$

$$\mathbf{v} = \left[v_1\ v_2 \cdots v_{N-1}\right]^T \tag{C.8b}$$

That this formula holds for points in the interior as well as at the boundaries can be verified by direct multiplication of the matrices. Note that v_0 and v_N do not appear, as they are constrained to zero by the boundary conditions.

For the free end of a beam, we have the natural boundary conditions

$$\left[\eta(x)\frac{\partial^2}{\partial x^2}\bar{v}(x,s)\right]_{x=x_0} = 0 \tag{C.9a}$$

$$\frac{\partial}{\partial x}\left[\eta(x)\frac{\partial^2}{\partial x^2}\bar{v}(x,s)\right]_{x=x_0} = 0 \tag{C.9b}$$

which yield the following particular finite difference expressions:

$$\frac{\partial^2}{\partial x^2}\left[\eta(x)\frac{\partial^2}{\partial x^2}\bar{v}(x,s)\right]_{x=x_0} \approx N^4\left[2\eta_1 v_0 - 4\eta_1 v_1 + 2\eta_1 v_2\right] \tag{C.10a}$$

$$\frac{\partial^2}{\partial x^2}\left[\eta(x)\frac{\partial^2}{\partial x^2}\bar{v}(x,s)\right]_{x=x_1} \approx N^4\left[-2\eta_1 v_0 + (4\eta_1+\eta_2)v_1 - 2(\eta_1+\eta_2)v_2 + \eta_2 v_3\right] \tag{C.10b}$$

The general expression can then be expressed by

$$\frac{\partial^2}{\partial x^2}\left[\eta(x)\frac{\partial^2}{\partial x^2}\bar{v}(x,s)\right] \approx N^4\,\mathbf{D}_A\mathbf{H}\mathbf{D}_B\mathbf{v}_0(s) \tag{C.11}$$

where

$$\mathbf{D}_A = \begin{bmatrix} 2 & & & & \\ -2 & 1 & & & \mathbf{0} \\ 1 & -2 & 1 & & \\ & \cdot & \cdot & \cdot & \\ \mathbf{0} & & 1 & -2 & 1 \\ & & & 1 & -2 \end{bmatrix} \qquad \mathbf{D}_B = \begin{bmatrix} 1 & -2 & 1 & & \\ & 1 & -2 & 1 & \mathbf{0} \\ & & \cdot & \cdot & \cdot \\ \mathbf{0} & & & 1 & -2 & 1 \\ & & & & 1 & -2 \end{bmatrix} \tag{C.12a,b}$$

and

$$\mathbf{v}_0 = \left[v_0\ v_1\ \cdots\ v_{N-1}\right]^T \tag{C.13}$$

Note that $\mathbf{D}_A$ has an extra row, while $\mathbf{D}_B$ has an extra column. For this case, we must include v_0, as it is not constrained by the boundary conditions.

The final case corresponds to a clamped beam. The essential boundary conditions are

$$\left[\bar{v}(x,s)\right]_{x=x_0} = 0 \tag{C.14a}$$

$$\frac{\partial}{\partial x}\left[\bar{v}(x,s)\right]_{x=x_0} = 0 \tag{C.14b}$$

and the particular finite difference expressions become

$$\frac{\partial^2}{\partial x^2}\left[\eta(x)\frac{\partial^2}{\partial x^2}\bar{v}(x,s)\right]_{x=x_1} \approx N^4\left[(2\eta_0+4\eta_1+\eta_2)v_1 - 2(\eta_1+\eta_2)v_2 + \eta_2 v_3\right] \tag{C.15a}$$

$$\frac{\partial^2}{\partial x^2}\left[\eta(x)\frac{\partial^2}{\partial x^2}\bar{v}(x,s)\right]_{x=x_2} \approx N^4\left[-2(\eta_1+\eta_2)v_1 + (\eta_1+4\eta_2+\eta_3)v_2 - 2(\eta_2+\eta_3)v_3 + \eta_3 v_4\right] \tag{C.15b}$$

The general approximation can then be expressed as

$$\frac{\partial^2}{\partial x^2}\left[\eta(x)\frac{\partial^2}{\partial x^2}\bar{v}(x,s)\right] \approx N^4 \mathbf{D_B H_0 D_A} v(s) \tag{C.16}$$

where

$$\mathbf{H_0} = \text{diag}\left[\eta_0\ \eta_1 \cdots \eta_{N-1}\right] \tag{C.17}$$

In this case, η_0 must be included, as the bending stiffness at the clamped boundary is important, while v_0 is excluded.

In summary, then, the following represent the transformed and discretized equations of motion for the Bernoulli-Euler beam subject to various boundary conditions.

$$\left[N^4\,\mathbf{DHD} + s^2\,\mathbf{I}\right]\ \mathbf{v}(s) = \mathbf{f}(s) \qquad \text{(Pinned-Pinned)} \tag{C.18a}$$

$$\left[N^4\,\mathbf{D_A H D_B} + s^2\,\mathbf{I}\right]\ \mathbf{v_0}(s) = \mathbf{f_0}(s) \qquad \text{(Free-Pinned)} \tag{C.18b}$$

$$\left[N^4\,\mathbf{D_B H_0 D_A} + s^2\,\mathbf{I}\right]\ \mathbf{v}(s) = \mathbf{f}(s) \qquad \text{(Clamped-Pinned)} \tag{C.18c}$$

APPENDIX D: SIMULATION OF BEAM WITH CURVATURE ACTUATION

In this appendix, we extend the results of Section 5.1.2.3 to the case of a beam with a distributed curvature actuator. The modified equation of motion, expressed in the time-domain, is

$$\frac{\partial^2}{\partial x^2}\left[\eta(x)\frac{\partial^2}{\partial x^2}v(x,t)\right]+\frac{1}{\beta(x)}\frac{\partial^2}{\partial t^2}v(x,t) = \frac{\partial^2}{\partial x^2}m_u(x,t)+f_n(x,t) \tag{D.1}$$

which becomes, after Laplace transformation

$$\frac{\partial^2}{\partial x^2}\left[\eta(x)\frac{\partial^2}{\partial x^2}\bar{v}(x,s)\right]+\frac{1}{\beta(x)}\left[s^2\bar{v}(x,s)-s\,v_0(x)-\dot{v}_0(x)\right] = \frac{\partial^2}{\partial x^2}\bar{m}_u(x,s)+\bar{f}_n(x,s) \tag{D.2}$$

The assumed linear feedback control law is

$$m_u(x,t) = -\int_0^1\left[k_1(x,y)\,\eta(y)\frac{\partial^2}{\partial y^2}v(y,t)+k_2(x,y)\frac{\partial}{\partial t}v(y,t)\right]dy \tag{D.3}$$

which transforms into

$$\bar{m}_u(x,s) = -\int_0^1\left[k_1(x,y)\,\eta(y)\frac{\partial^2}{\partial y^2}\bar{v}(y,s)+k_2(x,y)\,s\,\bar{v}(y,s)\right]dy + \int_0^1\left[k_2(x,y)\,v_0(y)\right]dy \tag{D.4}$$

Substituting this expression into Eq. (D.2) leads to

$$\frac{\partial^2}{\partial x^2}\left[\eta(x)\frac{\partial^2}{\partial x^2}\bar{v}(x,s)\right]+\frac{s^2}{\beta(x)}\bar{v}(x,s)+\frac{\partial^2}{\partial x^2}\left[\int_0^1\left[k_1(x,y)\,\eta(y)\frac{\partial^2}{\partial y^2}\bar{v}(y,s)+s\,k_2(x,y)\,\bar{v}(y,s)\right]dy\right] = \bar{f}_n(x,s)+\frac{1}{\beta(x)}\left[\dot{v}_0(x)+s\,v_0(x)\right]+\frac{\partial^2}{\partial x^2}\left[\int_0^1 k_2(x,y)\,v_0(y)\,dy\right] \tag{D.5}$$

Employing the same discretization technique used in Section 5.1.2.3, we obtain, for the finite-difference equation

$$\left[N^4\,\mathbf{DHD} + s^2\,\mathbf{B} + N\,\mathbf{DK}(s)\right]\,\bar{v}(s) = \bar{f}_n(s) + \bar{f}_i(s) + N^2\,\mathbf{D}\,\bar{f}_c(s) \qquad \text{(D.6)}$$

All terms in this last equation are as defined in Section 5.1.2.3.

APPENDIX E: SIMULATION OF A TIMOSHENKO BEAM

In this appendix, we discuss the direct simulation of a Timoshenko beam. For simplicity, we will assume that the initial conditions are zero and that the section properties are constant, although other situations can be treated in a manner similar to the Bernoulli-Euler beam model. The dimensional form of the equation of motion is

$$EI\frac{\partial^4}{\partial x_d^4}v_d(x_d,t_d) + \rho A\frac{\partial^2}{\partial t_d^2}v_d(x_d,t_d) - \rho I\left[1+\frac{Ek}{G}\right]\frac{\partial^4}{\partial x_d^2\partial t_d^2}v_d(x_d,t_d) + \frac{\rho^2 Ik}{G}\frac{\partial^4}{\partial t_d^4}v_d(x_d,t_d) = f_d(x,t) \qquad (E.1)$$

which can be normalized (using the same groupings as in Section 5.1.2.1) to

$$\frac{\partial^4}{\partial x^4}v(x,t) + \frac{\partial^2}{\partial t^2}v(x,t) - \alpha_I\left[1+\alpha_E\right]\frac{\partial^4}{\partial x^2\partial t^2}v(x,t) + \alpha_I^2\alpha_E\frac{\partial^4}{\partial t^4}v(x,t) = f(x,t) \qquad (E.2)$$

where

$$\alpha_I = \frac{I}{AL^2}, \quad \alpha_E = \frac{Ek}{G} \qquad (E.3a,b)$$

Taking the Laplace transform (neglecting initial conditions) yields

$$\frac{\partial^4}{\partial x^4}\bar{v}(x,s) - \alpha_I\left[1+\alpha_E\right]s^2\frac{\partial^2}{\partial x^2}\bar{v}(x,s) + s^2\bar{v}(x,s) + \alpha_I^2\alpha_E s^4\bar{v}(x,s) = \bar{f}(x,s) \qquad (E.4)$$

Finally, the spatial discretization yields

$$\left[N^4\mathbf{D}^2 + s^2\left(\mathbf{I} - \alpha_I(1+\alpha_E)N^2\mathbf{D}\right) + \alpha_I^2\alpha_E s^4\mathbf{I}\right]\bar{\mathbf{v}}(s) = \bar{\mathbf{f}}(s) \qquad (E.5)$$

The preceding equation holds for pinned-pinned boundary conditions only. The treatment of non-homogeneous boundary conditions is discussed in Appendix C.

It is interesting to note that the dynamics of the Timoshenko beam also has a state-space representation. Rather than using Eq. (E.1) directly, we begin with the simpler second order equations from which it was derived:

$$\frac{\partial^2}{\partial x^2} v(x,t) - \alpha_I \alpha_E \frac{\partial^2}{\partial t^2} v(x,t) = \frac{\partial}{\partial x} \theta(x,t) - \alpha_I \alpha_E f(x,t) \tag{E.6a}$$

$$\frac{\partial^2}{\partial x^2} \theta(x,t) - \alpha_I \frac{\partial^2}{\partial t^2} \theta(x,t) = -\frac{1}{\alpha_I \alpha_E} \left[\frac{\partial}{\partial x} v(x,t) - \theta(x,t) \right] \tag{E.6b}$$

where θ is the rotation of the cross section of the beam, and is related to the shear angle, ψ, via

$$k\,\psi(x,t) = \frac{\partial}{\partial x} v(x,t) - \theta(x,t) \tag{E.7}$$

The choice of state variables is determined from energy considerations. By making the assignment

$$\mathbf{x}(x,t) = \left[\frac{\partial^2}{\partial x^2} v(x,t) \quad k\psi(x,t) \quad \frac{\partial}{\partial t} v(x,t) \quad \frac{\partial}{\partial t} \theta(x,t) \right]^T \tag{E.8}$$

we relate the first and second elements of $\mathbf{x}$ with the potential energy due to bending and shearing, respectively. Likewise, we associate the third and fourth elements of $\mathbf{x}$ with the kinetic energy due to transverse deflection and cross section rotation, respectively. Using this definition and the previous equations allows us to determine the dynamics operator matrix and the forcing influence matrix. They follow as

$$\mathbf{L}_x = \begin{bmatrix} 0 & 0 & D^2 & 0 \\ 0 & 0 & D & -1 \\ 0 & \frac{1}{\alpha_I \alpha_E} D & 0 & 0 \\ \frac{1}{\alpha_I} D & \frac{1}{\alpha_I} \left[\frac{1}{\alpha_I \alpha_E} - D^2 \right] & 0 & 0 \end{bmatrix}, \quad \mathbf{b} = \begin{bmatrix} 0 \\ 0 \\ 1 \\ 0 \end{bmatrix}, \quad D = \frac{\partial}{\partial x} \tag{E.9a-c}$$

The dynamics equation can now be posed in the form given by Eq. (5.1).

APPENDIX F: DERIVATION OF ADJOINT OPERATORS

In this appendix, we derive an expressioon for the adjoint of a general linear spatial differential operator, and the associated conditions that cause the boundary terms to vanish. We begin by applying successive integration by parts to a single differential operator of order n:

$$\int_0^1 \mathbf{a}(x)^T \mathbf{A}_n(x) \frac{\partial^n}{\partial x^n} \mathbf{b}(x)\, dx = (-1)^n \int_0^1 \frac{\partial^n}{\partial x^n} \left[\mathbf{a}(x)^T \mathbf{A}_n(x) \right] \mathbf{b}(x)\, dx - \left[\sum_{k=1}^{n} (-1)^n \frac{\partial^{k-1}}{\partial x^{k-1}} \left[\mathbf{a}(x)^T \mathbf{A}_n(x) \right] \frac{\partial^{n-k}}{\partial x^{n-k}} \mathbf{b}(x) \right]_{x=0}^{x=1} \tag{F.1}$$

where **A** is a (generally) spatially varying matrix. By repeatedly applying the product rule to the bracketed terms, we obtain

$$\int_0^1 \mathbf{a}(x)^T \mathbf{A}_n(x) \frac{\partial^n}{\partial x^n} \mathbf{b}(x)\, dx = (-1)^n \int_0^1 \sum_{k=0}^{n} \binom{n}{k} \frac{\partial^{n-k}}{\partial x^{n-k}} \mathbf{a}(x)^T \frac{\partial^k}{\partial x^k} \mathbf{A}_n(x)\, \mathbf{b}(x)\, dx - \left[\sum_{k=1}^{n} (-1)^n \sum_{m=0}^{k-1} \binom{k-1}{m} \frac{\partial^m}{\partial x^m} \mathbf{a}(x)^T \frac{\partial^{k-m-1}}{\partial x^{k-m-1}} \mathbf{A}_n(x) \frac{\partial^{n-k}}{\partial x^{n-k}} \mathbf{b}(x) \right]_{x=0}^{x=1} \tag{F.2}$$

We now let the operator $\mathbf{L}_x$ have the general form

$$\mathbf{L}_x(x) = \sum_{n=0}^{N} \mathbf{A}_n(x) \frac{\partial^n}{\partial x^n} \tag{F.3}$$

Applying Eq. (F.2) then yields

$$\int_0^1 \mathbf{a}(x)^T \mathbf{L}_x(x)\mathbf{b}(x)\,dx = \int_0^1 \sum_{n=0}^{N}\sum_{k=0}^{n} (-1)^n \binom{n}{k} \frac{\partial^{n-k}}{\partial x^{n-k}} \mathbf{a}(x)^T \frac{\partial^k}{\partial x^k} \mathbf{A}_n(x)\, \mathbf{b}(x)\,dx$$

$$- \left[\sum_{n=0}^{N}\sum_{k=1}^{n} (-1)^n \sum_{m=0}^{k-1} \binom{k-1}{m} \frac{\partial^m}{\partial x^m} \mathbf{a}(x)^T \frac{\partial^{k-m-1}}{\partial x^{k-m-1}} \mathbf{A}_n(x) \frac{\partial^{n-k}}{\partial x^{n-k}} \mathbf{b}(x) \right]_{x=0}^{x=1} \qquad \text{(F.4)}$$

From this last expression, we identify the adjoint operator as

$$\mathbf{L}_x^*(x) = \sum_{n=0}^{N}\sum_{k=0}^{n} (-1)^n \binom{n}{k} \frac{\partial^k}{\partial x^k} \mathbf{A}_n(x)^T \frac{\partial^{n-k}}{\partial x^{n-k}}$$

$$= \sum_{k=0}^{n} \left[\sum_{n=0}^{N} (-1)^n \binom{n}{k} \frac{\partial^{n-k}}{\partial x^{n-k}} \mathbf{A}_n(x)^T \right] \frac{\partial^k}{\partial x^k} \qquad \text{(F.5)}$$

Note that it has the same general form as $\mathbf{L}_x$, since the bracketed term in the last expression is simply the spatially varying matrix corresponding to the k-th differential operator. The last term in Eq. (F.4) is the expression we would like to have vanish. If we assume the following for $\mathbf{b}(x)$

$$\mathbf{b}(0) = \mathbf{b}(1) = 0 \qquad \text{(F.6)}$$

then the boundary term is zero whenever n = k. Therefore, the second summation in this term need only run from k = 1 to k = n-1. Consequently, the index k always lies within the range $0 \le k \le N-1$, and the index m always lies within the range $0 \le m \le N-2$. Thus, by imposing the additional constraints

$$\frac{\partial^m}{\partial x^m} \mathbf{a}(0) = \frac{\partial^m}{\partial x^m} \mathbf{a}(1) = \mathbf{0}, \quad m = 0, \ldots, N-2 \qquad \text{(F.7)}$$

the boundary term is identically zero at either endpoint. In the special case where N=1, no constraints need be placed on $\mathbf{a}(x)$.

APPENDIX G: OPTIMAL COSTS FOR DISTRIBUTED CONTROL SYSTEMS

This appendix discusses the computation of the optimal cost required to bring a one-dimensional distributed system to rest from an arbitrary initial condition using a distributed controller. We will restrict attention to the force actuation case, and we will assume uniform cross section properties. The formulation is analogous to the discrete case, for which the optimal cost is expressed by

$$J^* = \frac{1}{2}\mathbf{x}_0^T\mathbf{S}\mathbf{x}_0 \tag{G.1}$$

where $\mathbf{x}_0$ is the initial condition on the state vector and $\mathbf{S}$ is the Riccati matrix. Wang [57] shows that, for the distributed case, the optimal cost has the form

$$J^* = \frac{1}{2}\int_0^1\int_0^1 \mathbf{x}_0(x)^T\mathbf{S}(x,y)\mathbf{x}_0(y)\,dx\,dy \tag{G.2}$$

where $\mathbf{x}_0(x)$ is the distributed initial condition and $\mathbf{S}(x,y)$ is the Riccati matrix function associated with Eq. (6.19). Thus, for the case of an initial displacement, $v_0(x)=\sin(2\pi x)$, the optimal cost is

$$J^* = \frac{1}{2}\int_0^1\int_0^1 \frac{\partial^2}{\partial x^2}v_0(x)\; S_{11}(x,y)\; \frac{\partial^2}{\partial y^2}v_0(y)\,dx\,dy$$

$$= 8\pi^4\int_0^1\int_0^1 \sin(2\pi x)\; S_{11}(x,y)\; \sin(2\pi y)\,dx\,dy \tag{G.3}$$

The Riccati equations for $S_{11}(x,y)$ follow directly from Eq. (6.25). For constant section properties, they are given by

$$\frac{\partial^2}{\partial x^2} S_{11}(x,y) - \frac{\partial^2}{\partial y^2} S_{22}(x,y) - \frac{1}{r}\int_0^1 S_{22}(x,z)S_{12}(z,y)\,dz = 0 \qquad \text{(G.4a)}$$

$$-\frac{\partial^2}{\partial x^2} S_{22}(x,y) + \frac{\partial^2}{\partial y^2} S_{11}(x,y) - \frac{1}{r}\int_0^1 S_{12}(x,z)S_{22}(z,y)\,dz = 0 \qquad \text{(G.4b)}$$

Adding these two equations yields

$$\nabla^2 S_{11}(x,y) = \nabla^2 S_{22}(x,y) + \frac{1}{r}\int_0^1 \left[S_{22}(x,z)S_{12}(z,y) + S_{12}(x,z)S_{22}(z,y)\right] dz \qquad \text{(G.5)}$$

Thus, S_{11} is computed using a simple relaxation algorithm. For the case of an initial velocity, $\dot{v}_0(x)=\delta(x-1/2)$, which is equivalent to a center-span impulse, the cost is simply

$$J^* = \frac{1}{2}\int_0^1\int_0^1 \dot{v}_0(x)\, S_{22}(x,y)\, \dot{v}_0(y)\, dx\, dy = \frac{1}{2} S_{22}(1/2,1/2) \qquad \text{(G.6)}$$

REFERENCES

[1] Plunkett, R., and Lee, C.T., "Length Optimization for Constrained Viscoelastic Layer Damping," *J. Acoustical Society of America*, Vol. 48, No.1, 1970, pp. 150-161.

[2] Balas, M.J., "Feedback Control of Flexible Systems," *IEEE Trans. Automatic Control*, Vol. AC-23, No.4, 1978, pp. 673-679.

[3] Bernstein, D.S., and Hyland, D.C., "The Optimal Projection Equations for Finite-Dimensional Fixed-Order Dynamic Compensation of Infinite-Dimensional Systems," *SIAM J. Control and Optimization*, Vol. 24, No.1, 1986, pp. 122-151.

[4] Kosut, R.L., "Suboptimal Control of Linear Time-Invariant Systems Subject to Control Structure Constraints," *IEEE Trans. Automatic Control*, Vol. AC-15, No.5, 1970, pp. 557-563.

[5] Yousuff, A., and Skelton, R.E., "Controller Reduction by Component Cost Analysis," *IEEE Trans. Automatic Control*, Vol. AC-29, No.6, 1984, pp. 520-530.

[6] Gupta, N.K., Lyons, M.G., Aubrun, J.N., and Margulies, G., "Modelling, Control and System Identification Methods for Flexible Structures," NATO document, AGARDograph-AG-260, 1981.

[7] Singer, N.C., and Seering, W.P., "Preshaping Command Inputs to Reduce System Vibration," *J. Dynamic Systems, Measurement and Control*, Vol. 112, 1990, pp. 76-82.

[8] Aubrun, J.N., "Theory of the Control of Structures by Low-Authority Controllers," *AIAA J. Guidance, Control and Dynamics*, Vol. 5, No.3, 1980, pp. 444-451.

[9] MacMartin, D.G., and Hall, S.R., "An H∞ Power Flow Approach to Control of Uncertain Structures," *Proc. American Controls Conference*, San Diego, CA, May 23-25, 1990, pp. 3073-3080.

[10] Miller, D.W., and Hall, S.R., "Experimental Results Using Active Control of Travelling Wave Power Flow," *AIAA J. Guidance, Control and Dynamics*, Vol. 14, No.2, 1991, pp. 350-358.

[11] Stein, G., and Athans, M., "The LQG/LTR Procedure for Multivariable Feedback Control Design," *IEEE Transactions on Automatic Control*, Vol. AC-32, No.2, 1987, pp. 105-114.

[12] Doyle, J.C., et al, "State-Space Solutions to Standard H2 and H∞ Control Problems," *IEEE Trans. Automatic Control*, Vol. AC-34, No.8, 1989, pp. 831-847.

[13] Meirovich, L., and Norris, M.A., "Sensitivity of Distributed Structures to Model Order in Feedback Control," *Journal of Sound and Vibration*, Vol. 144, No.3, 1991, pp. 365-380.

[14] Ramnath, V., *Non-Linear Systems Analysis and Design*, ASME Publication, 1981.

[15] Ramnath, V., "Stability and Control Analysis of a Class of Distributed Parameter Systems," *NASA Langley Conf. on Flexible Space Structures*, (Date unknown).

[16] Ramnath, V., and Jenie, "Non-Linear Dynamics of the Electrostatically Controlled Membrane Mirror," (Conference and date unknown).

[17] Ramnath, V., and Jenie, "Stability and Dynamic Analysis of the Electrostatically Controlled Membrane Mirror," *Proc. IAF Congress*, Lucerne, Switzerland, 1984.

[18] Brogan, W.L., "Optimal Control Theory Applied to Systems Described by Partial Differential Equations," *Advances in Control Systems*, C.T. Leondes, ed., Vol. 6, Academic Press, N.Y., 1968, pp. 221-316.

[19] Brogan, W.L., "Theory and Application of Optimal Control for Distributed Parameter Systems - I," *Automatica*, Vol. 4, Pergamon Press, 1967, pp. 107-120.

[20] Brogan, W.L., "Theory and Application of Optimal Control for Distributed Parameter Systems - II," *Automatica*, Vol. 4, Pergamon Press, 1967, pp. 121-137.

[21] Butkovskii, A.G. and Lerner, A.Y., "The Optimal Control of Systems With Distributed Parameters," *Automation and Remote Control*, Vol. 21, No.6, 1960, pp. 472-477.

[22] Lions, J.L., *Optimal Control of Systems Governed by Partial Differential Equations*, Springer-Verlag, N.Y., 1971.

[23] Gibson, J.S., "The Riccati Integral Equations for Optimal Control Problems on Hilbert Spaces," *SIAM J. Control and Optimization*, Vol. 17, No.4, 1979, p. 537-565.

[24] Mace, B.R., "Wave Reflection and Transmission in Beams," *Journal of Sound and Vibration*, Vol. 97, No. 2, 1984, pp. 237-246.

[25] Mace, B.R., "Active Control of Flexural Vibrations," *Journal of Sound and Vibration*, Vol. 114, No. 2, 1987, pp. 253-270.

[26] von Flotow, A.H., and Schafer, B., "Wave Absorbing Controllers for a Flexible Beam," *J. Guidance, Control and Dynamics*, Vol. 9, No.6, 1986, pp. 673-680.

[27] Miller, D.W., and von Flotow, A.H., "A Travelling Wave Approach to Power Flow in Structural Networks," *Journal of Sound and Vibration*, Vol. 128, No. 1, 1989, pp. 145-162.

[28] Miller, D.W., Hall, S.R., and von Flotow, A.H., "Optimal Control of Power Flow at Structural Junctions," *Proc. ACC*, 1989, pp. 212-220.

[29] MacMartin, D.G., and Hall, S.R., "Structural Control Experiments Using an H∞ Power Flow Approach," *Proc. AIAA GN&C Conf.*, Portland, OR., Aug. 20-22, 1990, pp. 1634-1644.

[30] Signorelli, J., and von Flotow, A.H., "Wave Propagation, Power Flow, and Resonance in a Truss Beam," *Journal of Sound and Vibration*, Vol. 126, No. 1, 1988, pp. 127-144.

[31] Piché, R.A., "Analysis of Structural Control Problems Using Frequency-Domain Continuum Methods," PhD Thesis, Univ. of Waterloo, Waterloo, Ontario, 1986, pp. 197-214.

[32] Wittrick, W.H. and Williams, F.W., "A General Algorithm for Computing Natural Frequencies of Elastic Structures," *Quarterly Journal of Mechanics and Applied Mathematics*, Vol. 24, No.3, 1971, pp. 263-284.

[33] Piché, R.A., "Analysis of Structural Control Problems Using Frequency-Domain Continuum Methods," PhD Thesis, Univ. of Waterloo, Waterloo, Ontario, 1986, pp. 48-52.

[34] Langley, R.S., "Analysis of Power Flow in Beams and Frameworks Using the Direct Dynamic Stiffness Method," *Journal of Sound and Vibration*, Vol. 136, No. 3, 1990, pp. 439-452.

[35] Hagood, N.W., and Crawley, E.F., *Development and Experimental Verification of Damping Enhancement Methodologies for Space Structures*, MIT Space Systems Laboratory Report No. 18-88, Sept., 1988, pp. 18-49.

[36] Hughes, P.C., and MacTavish, D.J., "Dynamics Modelling of Viscoelastic Space Structures," *Proc. ESTEC Workshop on Modal Representation of Flexible Structures by Continuum Methods*, Noordwijk, The Netherlands, June 15-16, 1989, pp. 193-215.

[37] Bagley, R.L., and Torvik, P.J., "Fractional Calculus - A Different Approach to the Analysis of Viscoelastically Damped Structures," *AIAA Journal*, Vol. 21, No.5, 1983, pp. 741-748.

[38] Bellman, R., *Numerical Inversion of the Laplace Transform*, Elsevier Publishing Co., New York, 1966, pp. 32-47.

[39] Weeks, W.T., "Numerical Inversion of Laplace Transforms Using Laguerre Functions," *J. of the Assoc. for Comp. Mach.*, Vol. 13, No.3, 1966, pp. 419-426.

[40] Wing, O., "An Efficient Method of Numerical Inversion of Laplace Trransforms," *Computing*, Vol. 2, No.2, 1967, pp. 153-166.

[41] Davies, B., and Martin, B., "Numerical Inversion of the Laplace Transform: a Survey and Comparison of Methods," *J. Computational Physics*, Vol. 33, 1979, pp. 1-32.

[42] Wilcox, D.J., "Numerical Laplace Transform and Inversion," *Int. J. Elec. Eng. Education*, Vol. 15, 1978, pp. 246-265.

[43] Cooley, J.W., Lewis, P.A.W., and Welch, P.D., "The Fast Fourier Transform Algorithm: Programming Considerations in the Calculation of Sine, Cosine and Laplace Transforms," *J. Sound and Vibration*, Vol. 12, No.3, 1970, pp. 315-337.

[44] Lanczos, C., *Applied Analysis*, Prentice Hall, Englewoods Cliffs, N.J., 1956, pp. 219-229.

[45] Hagood, N.W., and Crawley, E.F., "Approximate Frequency Domain Analysis for Linear Damped Space Structures," *AIAA Journal*, Vol. 28, No. 11, Nov. 1990, pp. 1953-1961.

[46] Abramowitz, M., and Stegun, I., "Handbook of Mathematical Functions," 9th ed., Dover, N.Y., N.Y., 1972, p. 360.

[47] Kulla, P.H., *Dynamic Stiffness of Rectangular Plates*, Final Report, ESTEC Contract 7814/88/NL/JG(SC), RESSULT, Research and Consulting, 1990.

[48] Poelaert D., "A Distributed Element Program for Dynamic Modelling and Response Analysis of Flexible Structures," *Proc. Fourth VPI&SU Symposium on the Dynamics and Control of Large Structures*, Blacksburg, VA., June 6-8, 1983.

[49] Taylor, L.W., and Balakrishnan, A.V., "A Mathematical Problem and a Spacecraft Control Laboratory Experiment (SCOLE) Used to Evaluate Control Laws for Flexible Spacecraft .... NASA/IEEE Design Challenge," NASA Technical Memorandum 89075, Nov. 17-18, 1986, pp. 386-412.

[50] Skaar, S.B., "Closed Form Optimal Control Solutions for Continuous Linear Elastic Systems," *Journal of the Astronautical Sciences*, Vol. 32, No.4, 1984, pp. 447-461.

[51] Francis, B.A., *A Course in H∞ Control Theory*, Springer-Verlag, New York, NY., 1987.

[52] MacFarlane, A.G.J., and Kouvaritakis, B., "A Design Technique for Linear Multivariable Feedback Systems," *Int. J. Control*, Vol. 25, No. 6, 1977, pp. 837-874.

[53] Breakwell, J.A., "Optimal Control of Distributed Systems," *J. of the Astronautical Sciences*, Vol. 29, No.4, 1981, pp. 343-372.

[54] Richtmyer, R.D., *Difference Methods for Initial Value Problems*, Wiley (Inter-Science), N.Y., 1957.

[55] deLuis, J., "Design and Implementation of Optimal Controllers for Intelligent Structures Using Infinite Order Structural Models," Ph.D. Thesis, Massachusetts Institute of Technology, Cambridge, MA., 1989.

[56] Nowacki, W., *Dynamics of Elastic Systems*, John Wiley & Sons, Inc., N.Y., 1963, pp. 114-118.

[57] Wang, P.C., "Control of Distributed Parameter Systems," *Advances in Control Systems*, C.T. Leondes, ed., Vol. 1, Academic Press, N.Y., 1964, pp. 75-172.

[58] Tzafestas, S.G. and Nightingale, J.M., "Optimal Control of a Class of Linear Stochastic Distributed-Parameter Systems," *Proc. IEE*, Vol. 115, No. 8, Aug. 1968, pp. 1213-1220.

[59] Tzafestas, S.G. and Nightingale, J.M., "Optimal Distributed Parameter Control Using Classical Variational Calculus," *Int. J. Control*, Vol. 12, No.4, 1970, pp. 593-608.

[60] Balakrishnan, A.V., *Applied Functional Analysis*, Springer-Verlag, N.Y., 1976.

[61] Balas, M.J., "Toward a More Practical Control Theory for Distributed Parameter Systems," *Control and Dynamic Systems: Advances in Theory and Applications*, C.T. Leondes, ed., Vol. 18, Academic Press, N.Y., 1982, pp. 361-421.

[62] Juang, J.N. and Dwyer, T.A.W., "First Order Solution of the Optimal Regulator Problem for a Distributed Parameter Elastic System," *J. of the Astronautical Sciences*, Vol. 31, No.3, 1983, pp. 429-439.

[63] Schaechter, D.B., "Estimation of Distributed Parameter Systems," *J. Guidance, Control and Dynamics*, Vol. 5, No.1, 1982, pp. 22-26.

[64] Zambettakis, I., Duaphin-Tanguy, G., and Rotella, F., "An Analytical Approach of Optimal Control for Multi-Scale Distributed Parameter Systems," *IFAC Control of Distributed Parameter Systems*, Perpignan, France, 1989, pp. 295-301.

[65] Lupi, V.D., Chun, H.M., and Turner, J.D., "Distributed Control and Simulation of a Bernoulli-Euler Beam," to appear in the *J. Guidance, Control and Dynamics.*, 1991.

[66] Miller, D.W., and van Schoor, M.C., "Formulation of Full State Feedback for Infinite Order Structural Systems," *First Joint U.S./Japan Conference on Adaptive Structures*, Maui, Hawaii, Nov. 1990.

[67] Hildebrand, F. B., *Advanced Calculus for Applications*, 2nd ed., Prentice Hall, N.J., 1976, p. 515.

[68] Press, W.H., Flannery, B.P., Teukolsky, S.A., and Vetterling, W.T., *Numerical Recipes*, Cambridge Univ. Press, N.Y., 1986, pp. 652-659.

[69] Levine, W.S., Johnson, T.L., and Athans, M., "Optimal Limited State Variable Feedback Controllers for Linear Systems," *IEEE Trans. Automatic Control*, Vol. AC-16, No.6, 1971, pp.785-793.

[70] Bernstein, D.S., and Hyland, D.C., "Optimal Projection Approach to Robust Fixed-Structure Control Design," *Mechanics and Control of Large Flexible Structures*, J.L. Junkins, ed., AIAA, Washington, D.C., 1990, pp. 237-293.

[71] Bailey, T.L., "Distributed-Parameter Vibration Control of a Cantilever Beam Using a Distributed-Parameter Actuator," S.M. Thesis, Massachusetts Institute of Technology, Cambridge, MA., 1984.